# Nitric oxide and Temperature in the Thermosphere: MIPAS observations


Tesis Doctoral realizada por:

Diego Bermejo Pantaleón


Granada, 2011


Instituto de Astrofísica de Andalucía, CSIC

Universidad de Granada




ugr Universidad de Granada

DEPARTAMENTO DE FÍSICA APLICADA
UNIVERSIDAD DE GRANADA

INSTITUTO DE ASTROFÍSICA DE ANDALUCÍA
CONSEJO SUPERIOR DE INVESTIGACIONES CIENTÍFICAS

# NITRIC OXIDE AND TEMPERATURE IN THE THERMOSPHERE: MIPAS OBSERVATIONS

Diego Bermejo Pantaleón

**Memoria de Tesis**
presentada para optar al grado de
Doctor en Ciencias Físicas por la Universidad de Granada

Dirigida por:

Manuel López Puertas
Prof. Investigación del CSIC

Bernd Funke
Científico Titular del CSIC

Granada, septiembre 2011

*A mis padres, a mi hermana, a mi abuela y a Cathy*

*All the pieces matter.*

Lester Freamon

Caminante, son tus huellas
el camino y nada más;
Caminante, no hay camino,
se hace camino al andar.
Al andar se hace el camino,
y al volver la vista atrás
se ve la senda que nunca
se ha de volver a pisar.

A. Machado

# Agradecimientos

Quiero dar las gracias en primer lugar a Manuel López Puertas por haberme dado la oportunidad de hacer este trabajo. Su apoyo, su ánimo, su consejo, su rigurosidad científica, su sabiduría en el campo de la física atmosférica y su valiosísima ayuda al final ha sido excepcional y admirable. Por supuesto, quiero darle las gracias a Bernd Funke, que me ha guiado de una forma brillante en el recorrido de esta tesis, y que sin él, el resultado no habría sido el mismo. Gracias a Maya y a Sergio, por lo que he aprendido de ellos (y de sus tesis) y por haberme prestado su ayuda y consejo científico siempre que lo necesité. Gracias también a los marcianos.

Gracias al Instituto de Astrofísica de Andalucía, a los científicos que lo habitan, al personal administrativo, al centro de cálculo, la biblioteca, a Paco Navarro, por haberme facilitado las cosas en mi tiempo aquí. Gracias por la peña de fútbol. Mi válvula de escape. Gracias también al grupo de IMK, que me acogieron como a uno más y que me ayudaron tanto profesional como personalmente en los 4 meses que pasé con ellos. Gracias a Sylvi por la bici y a Swappi por la casa.

Muy especialmente quiero acordarme de todos los que habeis hecho posible que mi estancia en Granada haya sido lo más parecido a estar en casa. Antonio y Víctor, por darme cobijo en el pisito cuando llegué, y luego por la estupenda convivencia que compartimos. Walter por enseñarme a tocar la guitarra (¡artista!). Giuseppe, Carmen, Juande, Andrés, Joni, Toño, el zulo y los que estaban dentro. Marquitos, al que le debo conocer la preciosa Móstoles. Y los de Madrid, Fernandito, Dani, Rubén, Víctor, María, Montse, Laura, Mª Cruz, que conseguisteis que pensara que en Madrid seguía teniendo mi casa.

Belén, Marta, Mar, Javier, Vicent, David: no sé cómo expresar mi agradecimiento por tantos y tantos buenos momentos.

Termino dando las gracias a mis padres, a mi hermana y la familia, por su amor y apoyo incondicional. Y a Cathy, gracias por darle sentido a todo esto.

x

# Resumen

La termosfera es la región menos explorada de la atmósfera de la Tierra hasta la fecha. No fue hasta la década de los noventa cuando el avance en las técnicas de sondeo remoto (o teledetección) permitieron abordar misiones de observación global de esta región con instrumentación en satélites. Gracias a éstas se pueden obtener medidas de temperatura y abundancias de gases con amplia cobertura espacial y temporal. La disponibilidad de estas medidas ha permitido aumentar nuestro conocimiento sobre el balance energético, la dinámica y la composición, así como sobre las tendencias a medio y largo plazo y las variabilidades naturales, de la región atmosférica en cuestión.

Precisando un poco, el conocimiento de la distribución espacial y temporal de la temperatura en la termosfera permite estudiar el balance energético de esta región, gobernado principalmente por la energía procedente del Sol, tanto mediante la absorción de radiación de alta energía (rayos X, ultravioleta) como de la energía depositada por partículas cargadas (electrones, protones) que interaccionan con el campo magnético terrestre. La energía transportada por ondas de gravedad que se propagan desde regiones inferiores y el enfriamiento radiativo por la emisión infrarroja de moléculas como el óxido nítrico, el dióxido de carbono y el oxígeno atómico, son también mecanismos importantes que determinan el estado energético de la termosfera. De hecho, el óxido nítrico (NO) juega un papel muy importante en el balance energético y la temperatura de la termosfera. Por un lado, es el principal contribuyente al enfriamiento radiativo a partir de 140 km. Por otro lado, debido a su bajo potencial de ionización, controla la composición de la región E de la ionosfera. Además, su distribución geográfica y variabilidad temporal dependen fuertemente de la entrada de energía procedente del Sol. Esto hace que sea un gas clave para el estudio de la conexión Sol-Tierra. La importancia del NO en la atmósfera no se restringe únicamente a la termosfera. Se sabe que el NO es transportado por la circulación meridional desde la baja termosfera hasta la estratosfera en las regiones polares durante el invierno, lo que afecta directamente al aporte de $NO_y$ en la estratosfera y, en consecuencia, a la química del ozono.

La atmósfera presenta emisiones infrarrojas originadas por las tran-

siciones vibro-rotacionales de las moléculas de los gases que la constituyen. Por este motivo, se construyen preferentemente instrumentos para la observación de la atmósfera en este intervalo espectral. Es el caso del instrumento MIPAS a bordo de ENVISAT (ESA). En el contexto científico presentado arriba, las medidas globales (de polo a polo, durante día y noche) de temperatura y concentración de óxido nítrico en la termosfera tomadas por MIPAS en el período 2005-2009 vienen a llenar un importante hueco, especialmente en las medidas de NO de noche en la termosfera, que no ha sido medido hasta ahora.

Esta memoria recoge el análisis de las medidas tomadas por MIPAS en la media y alta atmósfera. El primer objetivo de este trabajo versa sobre la viabilidad de la inversión de temperatura y razón de mezcla de NO en la termosfera a partir de la medidas de MIPAS de la emisión de la banda fundamental del NO en 5.3 $\mu$m. La dificultad de esta tarea radica en: 1) la emisión del NO está afectada por el No-(Equilibrio Termodinámico Local) (no-ETL), lo que hace necesario incluir un modelo preciso de poblaciones vibracionales, rotacionales y de espín responsables de la emisión medida; y 2) la propia inversión conjunta de temperatura y concentración de NO, pues la dependencia de la radiancia medida con estos parámetros es no lineal. Además, puesto que se pretende invertir la temperatura y la razón de mezcla de NO (no simplemente la densidad), es esencial tener un conocimiento preciso del estado hidrostático (presión y temperatura) de la atmósfera debajo de la termosfera. Por esta razón, la temperatura y la altura de apuntado de MIPAS son invertidos en la estratosfera y mesosfera previamente. Para ello, se utiliza la emisión en 15 $\mu$m del $CO_2$ que también está afectada de no-ETL típicamente por encima de los 70 km.

El segundo objetivo de este trabajo se centra en el estudio de la física y la química de la termosfera valiéndose de las medidas de MIPAS previamente procesadas. Se pretende estudiar y entender la distribución en altura y latitud y la variabilidad temporal y estacional de la temperatura y el NO en la termosfera. Dada la época en la que MIPAS ha realizado las medidas, la fase descendente del ciclo solar 23, el estudio está enfocado en condiciones de mínimo solar. Además, tanto la temperatura como el NO han sido comparados con medidas previas, así como con simulaciones de modelos.

Los principales resultados obtenidos es este trabajo se pueden resumir en los siguientes puntos:

- Primero, se ha adaptado el esquema de inversión desarrollado en un principio para inversiones de temperatura a partir de observaciones nominales de MIPAS (hasta 70 km) a las medidas de los modos de observación de MIPAS que alcanzan la baja termosfera (100 km). Para ello, se ha incluido un modelo actualizado de no-ETL para las poblaciones de los niveles vibracionales de $CO_2$ responsables de las emisiones medidas. Además se han incluido regiones espectrales

(micro-ventanas) que muestran una fuerte emisión en la mesosfera y baja termosfera. Estas micro-ventanas adicionales incluyen líneas de la rama R de la banda fundamental ($01^10$-$00^00$) y de la rama Q de la primera banda "caliente" ($10^00$-$01^10$). El esquema de inversión se ha aplicado a las medidas de MIPAS y se han caracterizado los errores debidos al ruido instrumental así como los errores sistemáticos debidos principalmente a incertidumbres en parámetros de no-ETL y en la abundancia de oxígeno atómico. La temperatura invertida hasta la baja termosfera ha sido validada con medidas de instrumentos independientes, mostrando en general buen acuerdo hasta la alta mesosfera (mejor que 3 K), donde el acuerdo empeora por el incremento del efecto de no-ETL hasta unos 10 K.

- A continuación, se ha desarrollado un esquema de inversión conjunta de la temperatura y la razón de mezcla de NO en la termosfera. Este esquema tiene en cuenta la pronunciada inhomogeneidad espacial, particularmente cerca de las regiones aurorales, de la distribución de NO, mediante la inversión del $ln$(NO) y adicionalmente, de los gradientes horizontales (latitudinales y longitudinales) del NO. Este esquema de inversión incluye un modelo de no-ETL para las poblaciones de los niveles vibracionales de NO responsables de la emisión medida, ya que están afectados de no-ETL vibracional, rotacional y de espín. La calidad de la inversión, en términos de errores aleatorios (error instrumental) y de resolución vertical, ha sido optimizada para proporcionar el mejor compromiso entre una óptima precisión y una alta resolución vertical, así como una distribución vertical similar de la información independiente del NO y de la temperatura, y un alto porcentaje de convergencia del código de inversión. Al aplicar el esquema de inversión a las medidas de MIPAS, se ha encontrado que la calidad de la inversión mejora significativamente con la relación señal-ruido. Se ha encontrado también que la abundancia de oxígeno atómico es el principal factor de incertidumbre en la inversión de NO, lo que hace necesario introducir una corrección a la hora de comparar el NO de MIPAS con los resultados de los modelos. De la caracterización del esquema de inversión de NO y $T_k$ se ha podido comprobar la influencia de la elección de la información *a priori* en los parámetros invertidos. Así, la forma del perfil de NO *a priori* para condiciones nocturnas y de baja relación señal-ruido (regiones extra-polares y baja actividad auroral principalmente) induce un error de suavizado sistemático traducido en una anti-correlación entre el NO y la $T_k$ invertidos. No obstante, las observaciones de MIPAS pueden ser comparadas con las simulaciones de los modelos mediante la aplicación de los "averaging kernels" de MIPAS a estas últimas.

- Con la aplicación de los esquemas de inversión sobre las medidas de MIPAS disponibles entre 2005-2009 se ha creado una atmósfera de re-

ferencia para la temperatura en la atmósfera media y otra atmósfera de referencia para la temperatura y la razón de mezcla de NO de día para la termosfera en condiciones de mínimo solar. Las medidas de noche no forman parte de la atmósfera de referencia debido al sesgo encontrado en la temperatura y el NO para medidas en condiciones de baja relación señal-ruido. La atmósfera de referencia para la temperatura en la atmósfera media puede ser utilizada para mejorar nuestro conocimiento de la física atmosférica, particularmente en la mesosfera y baja termosfera, siendo además esencial para llevar a cabo la inversión de otras especies a partir de sus emisiones infrarrojas medidas por MIPAS.

- La atmósfera de referencia obtenida para el NO y la $T_k$ en la termosfera ha sido estudiada en este trabajo. Se ha analizado la distribución en altura, latitud, y su variación estacional, encontrando un desplazamiento de fase estacional para el máximo de temperatura del polo de verano hacia el equinoccio precedente que no aparece en la atmósfera de referencia de MSIS. La distribución de temperatura se ha comparado con la atmósfera de referencia de MSIS, mostrando un buen acuerdo en general, excepto el mencionado desplazamiento de fase y la detección del sesgo frío de MSIS a 120-125 km encontrado en otros estudios. El NO de MIPAS se ha comparado con dos atmósferas de referencia: una correspondiente a un período de máximo solar (NOEM), con la que tiene buen acuerdo, excepto en regiones polares donde MIPAS es menor un 20-60 %; y otra correspondiente a un período de mínimo solar (HALOE+SME), en la que MIPAS siempre es mayor (10-40 % en las regiones aurorales y un factor 1.6-2 en regiones ecuatoriales).

- La atmósfera de referencia obtenida (MIPAS es el primer instrumento que mide concentraciones de NO en condiciones nocturnas), permite atacar diversos aspectos de la alta atmósfera. Por ejemplo, pueden estudiarse por vez primera las diferencias día/noche del NO y mejorar el conocimiento de la foto-química del NO. Aunque las medidas de noche no se incluyen en la atmósfera de referencia, las diferencias día/noche medidas encajan bastante bien, tanto cualitativa como cuantitativamente, con las simulaciones de modelos. Otra aplicación de la atmósfera de referencia ha sido la de estudiar la variabilidad de la temperatura y el NO con la actividad geomagnética y solar, encontrando claras correlaciones para el NO y para la temperatura en las regiones aurorales con el índice $A_p$, y también en latitudes bajas con el índice de actividad solar $F_{10.7}$.

- Dicha atmósfera de referencia también ha permitido estudiar fenómenos esporádicos que afectan a la termosfera, como es el caso de eventos de protones solares (SPE). En este caso, MIPAS ha medido aumentos de hasta 100 K en la temperatura y de 20 a 120 % en el NO.

Simulaciones de modelos arrojan un buen acuerdo con las medidas de MIPAS en el NO, aunque sobreestima el tiempo de respuesta en la producción de NO, mientras que, para la temperatura, el modelo subestima la respuesta y sobreestima el tiempo de relajación post-tormenta. Por otro lado, la atmósfera de referencia de MIPAS ha permitido encontrar la primera evidencia experimental de acoplamiento dinámico de la baja atmósfera con la termosfera a partir de medidas de satélite, durante un período de calentamiento súbito de la estratosfera (SSW).

La atmósfera de referencia obtenida de las medidas de MIPAS deja unos puntos de trabajo futuro, que en algún caso, ya están en marcha:

- La mejora de la inversión de la temperatura y del NO en la termosfera en condiciones nocturnas, incluyendo una concentración de NO *a priori* más realista.
- La explotación de las atmósferas de referencia de temperatura y de NO obtenidas. Ya está en marcha la comparación de los datos de MIPAS con simulaciones de modelos 3D como TIME-GCM y WACCM y en ello se profundizará en un futuro cercano.
- Además, como actualmente MIPAS continúa midiendo regularmente en la alta atmósfera, y la misión ENVISAT ha sido extendida hasta finales de 2013, se planea aplicar el esquema de inversión desarrollado en esta memoria a los nuevos datos y poder así construir una atmósfera de referencia que incluya también una fase ascendente de la actividad del ciclo solar.

# Contents

# List of Figures

# List of Tables

# Chapter 1

# Introduction

*Abstract*

This introductory chapter gives an overview of the importance of observing the upper atmosphere, being historically the less explored region of the atmosphere. The main properties of the atmosphere, such as its temperature structure and composition, are briefly described. Also, the main processes that drive the energetics of the middle and upper atmosphere are posed. To this respect, the temperature and the NO abundance arise as key atmospheric parameters that allow to get a better understanding of the physics of the upper atmosphere. At the end of the chapter, the main objectives of this thesis work are unfolded.

## 1.1. Context

Since the industrial revolution (second half of $18^{th}$ c.), the human activity has influenced the Earth environment with an unprecedented intensity. The fossil fuel combustion, the intensive agricultural practices or the biomass burning are examples of activities that have changed the chemical composition of the atmosphere by inundating it with carbon and nitrogen oxides, methane, hydrocarbons, aerosols, halogenated compounds, etc.

Among other significant consequences, such as the degradation of air quality or the acidification of precipitations, changes in the Earth's climate are also produced in response to modified absorption and emission of radiation by atmospheric trace constituents. These changes are more evident near the Earth's surface, where life is more directly affected. However, as the experience of the Earth's ozone layer illustrates, changes higher up in the atmosphere might also be important. For instance, whereas the increase in global surface air temperature during the $20^{th}$ century has been attributed mainly to the increasing atmospheric concentrations of greenhouse gases (a 25% in the case of $CO_2$,

see Figure 1.1), the radiative effect of the greenhouse gases become more pronounced and of opposite sign in the upper atmosphere, above 100 km, as it has been modelled by *Rishbeth and Roble* (1992) and *Akmaev* (2002).

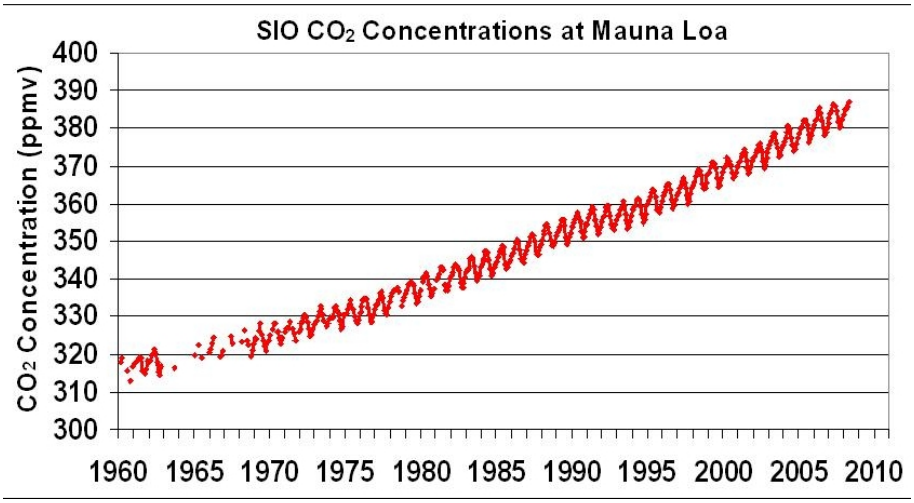


Figure 1.1: Change in $CO_2$ concentration (ppmv) from 1958 to 2008 at Mauna Loa, Hawaii (taken from http://cdiac.ornl.gov/trends/co2/sio-keel.html).

Modeling studies from *Roble and Dickinson* (1989) and more recently from *Akmaev and Fomichev* (1998) have estimated that doubling the amount of $CO_2$ in the middle and upper atmosphere produces a response of cooling: an average of 14 K at the stratopause, decreasing to around 8 K at the mesopause and then increasing up to 40-50 K at thermospheric altitudes. The cooling should cause the upper atmosphere to contract, thus a substantial decline in thermospheric density is expected, as well as a downward displacement of ionospheric layers (*Rishbeth*, 1990). A perturbation in the radiative exchange produces, therefore, a response in the thermal structure of the atmosphere. Needless to say, these response may bring other changes in the atmosphere, such as perturbations of the meridional circulation, or changes in the polar mesospheric clouds (PMCs) occurrence (*Roble*, 1995).

A comprehensive review of temperature trends between 50 and 100 km (*Beig et al.*, 2003) reveals the following trends: (i) moderate negative trends of about 2 to 3 K per decade between 50-70 km, with largest magnitude in the tropics; (ii) slightly larger cooling trends of 70 to 80 km in the low and mid-latitudes; and (iii) essentially zero temperature trends between 80 and 100 km. Over the past three decades, the global temperature at Earth's surface has increased by 0.2 to 0.4 K, compared with a 5 to 10 K decrease in the lower and middle mesosphere. Thus, the magnitude of the trends is much larger in the mesosphere. In the thermosphere, estimated neutral temperatures at 350 km reveal a negative long-term trend of near -50 K per decade (*Holt and Zhang*, 2008), while *Semenov* (1996)

inferred a decrease of 30 K per decade based on downward movement of the atomic oxygen red-line emission layer near 270 km at a rate of 10 km per decade.

Besides, thermospheric drag causes measurable decay of orbits of satellites, and this information can be used to derive long-term changes in thermospheric density. Studies from *Emmert et al.* (2004) and *Marcos et al.* (2005) indicate that the thermospheric density has declined during the past decades at a rate of 2-3% per decade, increasing this rate at higher altitudes, which is qualitatively consistent with model predictions (*Rishbeth and Roble*, 1992). Further, model simulations also show that the impact of long-term changes in stratospheric ozone and water vapour on atmospheric density may extend into the thermosphere (*Akmaev et al.*, 2006). *Laštovička and Bremer* (2004) found positive long-term trends in the electron density at fixed heights, confirming the downward displacement of the lower ionosphere, and *Bremer* (2001) found a slight decrease in the height of the electron density maximum of the E-layer, in qualitative agreement with *Rishbeth and Roble* (1992). These ionospheric trends accelerated after 1980, providing support for their anthropogenic origin (*Bremer*, 2005).

The paragraphs above try to give an overview of the influence of the increasing greenhouse forcing on the observed trend pattern of global change in the upper atmosphere above 50 km (see Figure 1.2). Complementarily to the greenhouse gases influence, there may be contributions from secular changes in solar and geomagnetic activity. During the 20$^{th}$ century, the geomagnetic activity has increased and stabilized towards its end (*Clilverd et al.*, 1998). Likewise, the solar variability[1] has also increased during the first half of the past century and it has stagnated afterwards. *Laštovička* (2005) analyzed the possible effects of long-term variations in both solar and geomagnetic activity on long-term trends, e.g., density in the thermosphere. The study reveals that the role of the solar and geomagnetic activity on the long-term trends decreases with decreasing altitude and from the beginning of the century towards its end. The cause is found both in the continuous increase of concentration of greenhouse gases and in the weaker trend of the solar and geomagnetic activity towards the end of the century.

In addition, the 11 year solar activity cycle, i.e., changes in its radiation and energetic particle flux also produces cyclical responses in the upper atmosphere, heating and expanding it at solar maximum, cooling and contracting it at solar minimum. This cyclical response must be taken into account in the process of finding long-term trends. Furthermore, the evolution of the Earth magnetic field (the dipole strength

[1]The solar variability is usually studied by using the sunspot numbers. The troposphere is affected by the variability of the total solar irradiance, the stratosphere by solar ultraviolet (UV) radiation and the mesosphere and thermosphere (and ionosphere), by solar X-rays and extreme UV (EUV) variability.

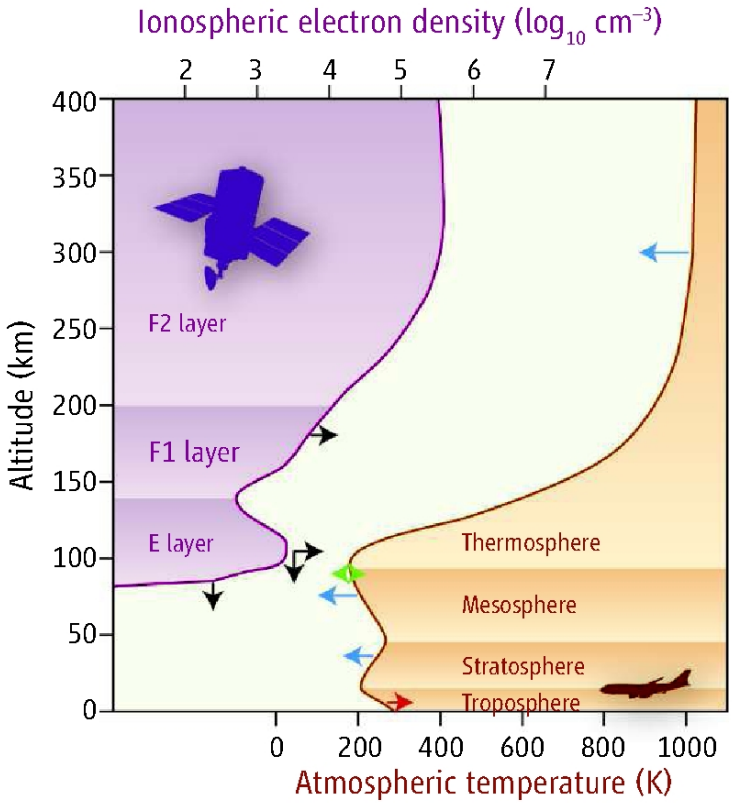


Figure 1.2: Observed over-all long-term trends. Atmospheric layers (orange, right) are defined by the temperature profile. Ionospheric layers (purple, left) are defined by the electron density profile (shown here at midnight at the equator). Arrows denote the direction of observed changes in the past three to four decades: Red, warming; blue, cooling; green, no temperature change; black, changes in maximum electron density (horizontal) and the height of ionospheric layers (vertical). Most spacecraft fly at altitudes above 300 km. The aircraft and satellite shown are not to scale. After *Laštovička et al.* (2006).

has decreased about 6 % over the past century) has also influence in the upper atmosphere. The strength and orientation of the geomagnetic dipole determine how the solar wind and the interplanetary magnetic field interact with the magnetosphere, and therefore how they influence the auroral particle precipitation and the high-latitude Joule heating in the thermosphere (*Cnossen and Richmond*, 2008).

The upper atmosphere is, as high-lightened in the studies mentioned above, of high interest, and thanks to the development of remote sensing techniques on space platforms and the development of powerful numerical models during the last 40 years, the knowledge on this region of the atmosphere has increased strikingly. Still, the upper atmosphere is the least explored region of Earth's atmosphere. Its altitude range is too high for in situ measurements from aircraft or balloons. Besides, rocket or ground based measurements do not provide the suite of measure-

ments required for a complete characterization of this region. It is since middle 1990's when remote sensing technology became sufficiently advanced to enable comprehensive satellite observations of this region of the atmosphere. This observation technique allows to perform measurements of temperature and abundances of key gases with large spatial and temporal coverage so that: (i) natural variabilities and trends can be quantified; (ii) the general circulation models can be validated and, in short, the understanding of the energetics, dynamics and composition of this region is improved.

Since the atmosphere emits radiation mostly in the infrared part of the spectrum, instruments on satellite platforms preferably observes in this spectral range. The remote sensing can be performed in three different ways: *1)* limb, by which the instrument points to the atmosphere horizon and measures the radiance coming out in the tangent direction; *2)* nadir, by which the instrument points downwards, perpendicular to the Earth's surface, and measures the radiance in the vertical direction coming out from the atmosphere and also from the surface; and *3)* occultation, by which the instrument measures the absorption spectrum from a emitting source, such as the Sun, the Moon or any other star, when it travels through the atmosphere. Out of these three observation techniques, the limb observation is the most suitable for the study of the upper atmosphere. On the one hand, it provides high sensitivity to small amounts of gas since the geometric path tracked by the radiance is longer than in the case of nadir observations and hence, the measured signal is greater. On the other hand, it provides high vertical resolution since most of the received signal usually comes from the atmospheric layer right above the tangent point of the line of sight between the instrument and the atmosphere[2]. Further, the limb observation technique avoids additional emitting sources, like the occultation or nadir (Earth's surface) have. Additionally, in the infrared spectral region, the effect of the cosmic background on the measured radiance is negligible.

The choice of the remote sensing techniques entails the previous knowledge of how the information is transferred from the observed region to the instrument, and also that what is actually measured is not directly the physical parameters but a complex function of them. Therefore an inversion process is necessary to be applied to the measurements in order to retrieve the wished atmospheric parameters.

The nitric oxide (NO) infrared emissions at $5.3\,\mu$m are a source of information on the upper atmosphere. From its measurement, abundances of NO and kinetic temperature can be derived (*Funke et al.*, 2001). Further, the NO infrared emissions in the upper atmosphere are affected by non

[2]There are exceptions in which the measured radiance does not come mainly from nearby the tangent point. For example, the thermospheric contribution of the NO emission at $5.3\,\mu$m at stratospheric and mesospheric tangent altitudes reaches up to 55%.

local thermodynamic equilibrium (non-LTE[3]), that is, the populations of energy levels responsible for the emission are not described by the local temperature and, hence, a detailed model to describe these populations is needed.

The knowledge of the thermal structure is essential in order to undertake any study of the atmosphere. In the upper atmosphere, the temperature field is governed by solar-UV absorption, auroral heating by particles and Joule dissipation of ion currents, release of chemical energy, winds, deposited energy by gravity wave breaking and radiative cooling mainly from $CO_2$, NO, and O infrared emissions.

Nitric oxide is a minor but key constituent in the upper atmosphere. Its infrared emission at 5.3 $\mu$m contributes to the cooling above 110 km, and its distribution and variability in this region depends strongly on the energy input from the Sun. Hence, it can provide information on the solar and auroral variability. Further, the low ionization potential of the NO turns it into an important source of ionization in the atmosphere.

MIPAS instrument on board ENVISAT satellite (*Fischer et al.*, 2008), has been measuring on a regular basis since 2005 the NO 5.3 $\mu$m limb emission in the upper atmosphere with high spectral resolution. In this work, these emissions have been analyzed for the period 2005-2009, allowing to construct a climatology for kinetic temperature and NO abundance in the upper atmosphere.

## 1.2. Structure and composition of the atmosphere

### 1.2.1. Vertical structure

The vertical structure of the Earth's atmosphere is highly variable in temperature, dynamics and composition and hence, there is not an unique criterium to divide the atmosphere into different regions.

The first divisions of the atmosphere were made in the early 20$^{th}$ century taking into account the presence of charged particles, electrons and ions. The propagation of radio waves (e.g., Marconi transmitted radio signal from Europe to America in 1901) were explained by the existence of a conducting layer (eventually named the ionosphere) near 80 km that reflected such waves. Then, with the criterium of the presence of charged particles, the atmosphere is divided into two regions: neutral atmosphere and ionosphere. Within the ionosphere, several layers are distinguished based on the vertical profile of the concentration of charged particles which depends on variations in ion production rates. These layers are known as the D, E and F layers. The D region extends from

[3]The nature of the non-LTE is explained in Section 3.3.1.

50 to 90-100 km, and it disappears at night; the E region ranges between 100 and 150 km. The F region is divided into the $F_1$ and $F_2$ layers. The electron densities of the E and $F_1$ layers are greatly reduced at night. The $F_2$ region is present day and night. In the D and E layers, mostly $N_2$ and $O_2$ are ionized, while in the F region it is mainly O.

Today it is widely accepted the temperature structure as a way to divide the atmosphere. With this criterium, the atmosphere is divided into different regions (*spheres*), where the boundaries (*pauses*) between them are defined by inversions of the temperature gradient (see Figure 1.3).

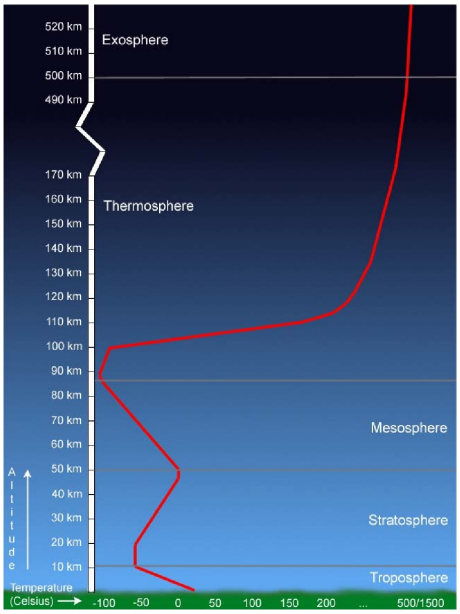


Figure 1.3: Temperature structure of the atmosphere.

The atmosphere is transparent to the visible part of the solar spectrum. This radiation propagates to the ground unless absorbed or scattered by clouds or aerosols. On average, 30 % of the total energy from the Sun is reflected back to space, 21 % is absorbed in the atmosphere before reaching the ground and 49 % is absorbed at the ground. The energy absorbed by the ground is transferred back to the atmosphere, mostly by infrared radiation and latent heat, which is absorbed in the lowest layers of atmosphere. Hence, a negative vertical temperature gradient arises which, added to the negative vertical pressure gradient given by the hydrostatic equilibrium, leads to convective instability with a nearly constant lapse rate (*Houghton*, 1986) of around -8 K/km. The convection extends up to 10-15 km, defining the atmospheric region so-called *troposphere*, from the greek "tropos", i.e., turning or changing atmosphere. Due to the larger solar irradiance at low latitudes, the convective instability is maintained up to higher altitudes (18 km) than

at high latitudes, where the incoming energy from the Sun is lower (8 km at the poles). Its upper boundary, where the convection ends, is the tropopause. The troposphere contains around 85 % of the total mass of the atmosphere, it is characterized by the vertical motion of air masses, and it is the region where most of the weather phenomena occur. It is also called the lower atmosphere.

Above the tropopause, the decrease in the air density allows the emitted radiation to escape to space turning into a radiative cooling. Then, the atmospheric layers are heated by absorption of upwelling radiation coming from below and are cooled in the same proportion. This makes that the temperature right above the tropopause is nearly constant, which defines the beginning of the next region, the *stratosphere*. This radiative equilibrium is broken from around 20 km, where the thermal gradient becomes positive due to the absorption of UV by ozone in the Hartley (200-300 nm) and Huggins (300-335 nm) bands. The heating rate peaks at near 50 km, defining the stratopause. The positive temperature gradient in the stratosphere does not favor vertical motions of air (so the region is stratified), then, the horizontal motions (latitudinal and longitudinal) become much more important.

Above 50 km, the air density is low enough so that the radiative heating by upwelling radiation or by solar irradiance is not efficient, and the radiative cooling, specially by $CO_2$, governs the temperature structure. This negative gradient defines the *mesosphere*, which extends up to between 87 km (summer pole) and 100 km (winter pole). At its upper boundary (mesopause), the coldest temperature in the whole atmosphere is reached (around 130 K in the summer pole). The combination of the stratosphere and the mesosphere together is frequently referred to as the middle atmosphere.

Above the mesopause, the temperature gradient becomes again positive due to the strong absorption of solar UV by $O_2$ in the Schumann-Runge bands (175-200 nm) and the Schumann-Runge continuum (100-180 nm) and, above 150 km, due to dissociation and ionization of $O$, $O_2$ and $N_2$ by absorption of solar extreme-UV fluxes and by energetic particles. This region is called *thermosphere* (also the upper atmosphere), and highest temperatures of the atmosphere are reached here, between 700 and 2000 K, depending on the solar activity. The temperature increases with altitude until the molecular heat conduction, which cools by transferring heat downwards, becomes sufficiently large that makes the temperature to be efficiently constant. This happens from around 200 km to about 500-600 km. Above, the density of the atmosphere is so low that neutral particles are unaffected by collisions and move on ballistic trajectories, and even the slowest particles may escape to space. This last region is the *exosphere*, extending up to near 10000 km, the outer limit of the atmosphere.

In addition, an alternative division of the atmosphere is based on changes in composition and mixing. In the lower and middle atmosphere, the major constituents, $N_2$ and $O_2$, are uniformly mixed by turbulence and its proportion with respect the total number density (around 78 % and 21 %, respectively) hardly changes. Then, the molecular weight of air varies little with altitude. This region is referred to as the *homosphere*. The upper limit of turbulent diffusion is at around 90-100 km (homopause). Above, the proportion of $N_2$ and $O_2$ decreases due to dissociation processes, while the proportion of O increases. In this region, called *heterosphere*, the molecular mean weight of air varies with altitude because the molecular diffusion dominates over turbulence, and the constituents are vertically distributed according their molecular weight.

### 1.2.2. Composition

The chemical composition of the Earth's atmosphere has evolved since its origin. At its early stages, it is believed that the atmosphere was composed of a few number of species, such as water vapor, carbon dioxide, sulfur dioxide and nitrogen, which were released in volcanic eruptions. These gases pushed lighter constituents out of the atmosphere, such as molecular hydrogen, helium, neon and other inert gases. The first stable atmosphere was mainly oxidized. As the Earth eventually formed, i.e., the accretionary phase had ended, the surface heat flux would have dwindled and hence the atmosphere would have cooled, producing the condensation of water vapor and the origin of the oceans. On the other hand, UV radiation photolyzed water vapor producing molecular oxygen. However, the current amount of molecular oxygen cannot be explained without taking into account the presence of life, for which the existence of liquid water was indispensable.

The photosynthetic activity, i.e., the production of molecular oxygen favored the appearance of ozone, essential for the evolution of living beings. Since approximately $10^9$ years, the atmospheric composition has barely changed: 78 % of $N_2$, 21 % of $O_2$, and the remaining 1 % includes minor gases, such as argon, $CO_2$, $O_3$, $H_2O$, $CH_4$ and nitrogen oxides (NO, $N_2O$, $NO_2$). Figure 1.4 shows the composition of a typical atmosphere for daytime and mid-latitude conditions.

$N_2$ and $O_2$ are the most abundant constituents. They are long lived, well mixed and they have constant relative abundance until photodissociation becomes important above around 90 km.

$H_2O$ has a large variability. Its volume mixing ratio peaks near the surface due to the oceans' contribution, decreasing rapidly up to the tropopause and then being practically constant up to 70-80 km. Then it decreases again because of photodissociation. Its radiatively very ac-

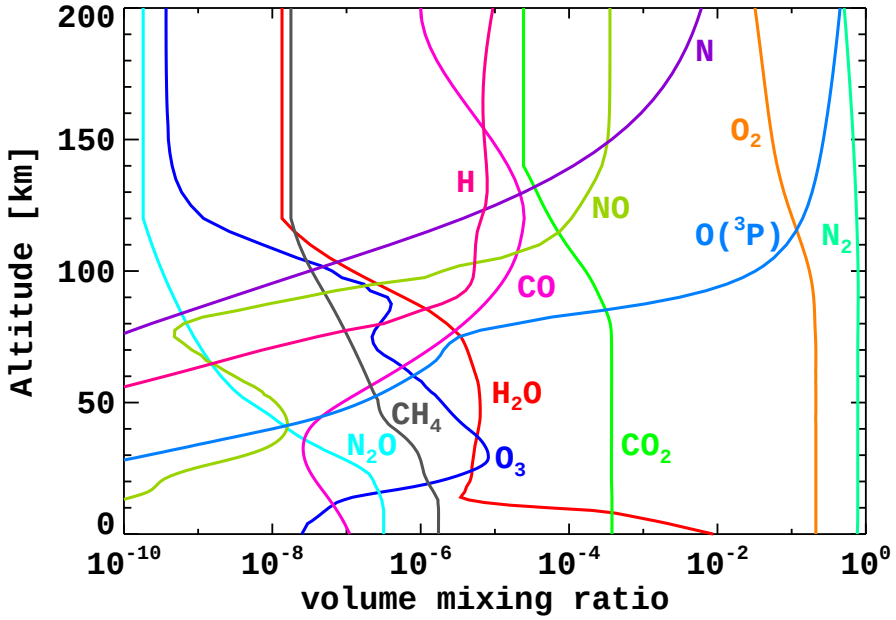


Figure 1.4: Mixing ratio profiles of the main constituents of the Earth's atmosphere for typical daytime and mid-latitude conditions. After *López-Puertas et al.* (2009a).

tive vibrational bands make it the most important greenhouse gas in the atmosphere.

$CO_2$ has a nearly constant abundance up to 70-80 km, where it decreases due molecular diffusion and photodissociation. Its role on the radiative transfer in the infrared is very important up to 130 km, and it is a key species concerning the global warming.

$O_3$ plays a major role in the thermal structure of the atmosphere. It is produced by photodissociation of $O_2$ followed by recombination of $O_2$ and O. Its abundance peaks at 25 km, then decreasing upwards due to fast photodissociation and it reaches a secondary maximum near 80 km due to the increasing abundance of O.

$CH_4$ and $N_2O$ are greenhouse gases which are abundant in the troposphere. They have natural but also anthropogenic sources (industry, fossil fuel), and their concentrations decrease with altitude via oxidation and photodissociation. Measurements confirm that their tropospheric abundances have increased in the last two centuries.

CO plays an important role in the chemistry of the troposphere and stratosphere, where it is destroyed by reactions with OH. CO is produced on ground by fuel and biomass burning processes, in the middle atmosphere it is produced from methane oxidation and in the thermosphere its major source is the photolysis of $CO_2$.

NO and $NO_2$ are the most important compounds of active nitrogen. In the

middle atmosphere, they are related by chemical processes (oxidation and photodissociation) and therefore they are considered as a single group, $NO_x$. They play a major role in a catalytic cycle of $O_3$ destruction in the stratosphere. Besides, NO gives the main contribution to radiative cooling in the thermosphere.

Atomic oxygen is produced in the middle atmosphere by photodissociation of $O_2$ and $O_3$. In the upper atmosphere, its distribution follows the molecular diffusion. It takes part in the radiative cooling in the thermosphere, by its emission at 63 $\mu$m, and by transferring its kinetic energy to internal energy of $CO_2$ and NO.

The halogenated compounds, and specially, those of anthropogenic source with long photochemical life, e.g. chlorofluorocarbons (CFC's), are a dominant source of ozone depletion in the stratosphere. The production and use of CFC's have been strongly limited by international agreements (Montreal Protocol, 1987) as well as by national regulations.

As it is seen, chemical reactions are a key factor in driving the abundances of atmospheric constituents. For example, the photodissociation processes by solar illumination can cause large diurnal variability in some species, such as the ozone (more abundant at nighttime) or atomic oxygen (more abundant at daytime). Atmospheric dynamics also plays an important role in the distribution of gases. For example, zonal winds in the middle atmosphere tend to distribute homogeneously the constituents in the direction of parallels, while meridional winds, slower than zonal winds, distribute the gases in the latitudinal direction typically showing larger variabilities than in the longitudinal direction.

## 1.3. Middle and Upper atmosphere

The understanding of the energy balance of the Earth's atmosphere requires to take into account the various physical and chemical processes that heat and cool the atmosphere. Absorption of solar radiation, storage and release of chemical energy, energy transport, dissipation of wave disturbances, auroral heating and cooling by radiative emissions account for the energy budget, and, as a result, produce the temperature structure.

### 1.3.1. Energy balance

The heating of the thermosphere is driven by several process: (1) virtually all solar photons at wavelengths less that 102.5 nm are absorbed by thermospheric $N_2$, $O_2$ and O, leading them to photodissociation and ionization; (2) $O_2$ absorbs solar UV in the Schumann-Runge continuum (100-180 nm) and in the Schumann-Runge bands (175-200 nm); (3) exothermic

ion-neutral and neutral-neutral chemical reactions (see, e.g., tables of neutral and ion chemistry involving nitrogen and oxygen from *Roble* (1995)); (4) collisions between ambient electron, ion and neutrals[4]; (5) quenching of metastable species, such as $O(^1D)$ by $N_2$ and $O_2$; (6) atomic oxygen recombination; (7) heating by fast photoelectrons and auroral electron precipitation; (8) Joule dissipation of ionospheric currents in auroral region[5]; and (9) heating by dissipation of tides, planetary waves and gravity waves generated in the lower atmosphere that reach thermospheric heights.

Also, the main cooling processes of the thermosphere are: (1) NO emission at 5.3 $\mu$m, which is the most important radiative cooling mechanism between 120 and 200 km; (2) $CO_2$ emission at 15 $\mu$m up to 140 km; (3) downward molecular heat conduction, which becomes the primary cooling mechanism above 140 km; (4) and, to a lesser extent, the 63 $\mu$m infrared emission from the fine structure of atomic oxygen (see, e.g., *López-Puertas and Taylor* (2001)).

In addition, the heating mechanisms: a) absorption of solar UV irradiance (in situ solar forcing), b) Joule dissipation at auroral latitudes and c) tides propagating from below, generate pressure gradients that force the gas of the thermosphere into motion following negative temperature gradients (*Fuller-Rowell*, 1995). The dynamics of the thermosphere also contributes to the energy balance in this region by means of transport of energy, like: cooling (heating) due to expansion (contraction) of gas; viscous heating due to relative motion between gas parcels; or thermal conduction, represented by temperature gradient, and heat carried by electric currents.

Below, the mesosphere is heated by (1) absorption of solar UV by $O_3$ in Hartley bands (242-310 Å); (2) quenching of $O(^1D)$ produced by photolysis of $O_3$ and $O_2$; (3) release of chemical energy from the recombination of O and from exothermic reaction between H and $O_3$; (4) dissipation of gravity waves and tides; (5) heating by adiabatic compressions caused by vertical motions. The cooling of the mesopause is driven mainly by radiative mechanisms, i.e., $CO_2$ 15 $\mu$m emission and, to a lesser extent, the $O_3$ 9.6 $\mu$m emission.

[4] In the thermosphere (neutral), the kinetic temperature of ions and electrons is always higher than the kinetic temperature of neutrals, due to their additional heating sources by photoelectrons production and electric fields (see *Roble et al.* (1987) and *Rees* (1989)). Hence, the collisions of neutrals with ions and electrons results in the heating of neutrals.

[5] The Joule heating is the frictional heating associated to collisions between neutral and ions moving at different velocities due to the presence of electric fields. The electric fields in the thermosphere can have different origins: 1) the interaction between solar wind and the geomagnetic field causes electrons and ions to drift in different directions, creating a polarization field; 2) the thermospheric neutral winds drag ions across the geomagnetic field, producing an effective electric field (see *Rees* (1989)).

Dynamical processes play a decisive role in the temperature structure of the middle atmosphere. It is well known that the cold summer mesopause and the warm winter stratopause are caused by the meridional circulation in the mesosphere and lower thermosphere. The forcing of the meridional circulation in the middle atmosphere is mainly provided by gravity waves. That is, the filtering of gravity-waves phase speeds by the mean zonal winds in the stratosphere through which they propagate, and which has different sign in the summer and winters hemispheres, produces the meridional circulation in the mesosphere (*Andrews et al.*, 1987).

Planetary waves are stationary, or slowly westward propagating oscillations that are formed in the lower atmosphere by the interaction of winds with large scale topographic and thermal features (large landmasses and land-ocean heating contrasts) and propagate upwards. Planetary waves are also responsible for the so-called stratospheric sudden warmings (SSWs). During these events, the interaction between the wave and mean flow lead to decelerate and even reverse the eastward winter stratospheric polar jet, inducing a downward circulation in the stratosphere that causes adiabatic heating and an upward circulation in the mesosphere that causes adiabatic cooling (*Matsuno*, 1971).

Atmospheric solar tides are planetary-scale oscillations in winds, temperature and pressure with periods that are harmonics of a 24-hour day. These tides play an important role in the dynamics, energetics and composition of the middle and upper atmosphere. Tides generated by periodic heating of the atmosphere are termed thermal tides and migrate westward with the apparent motion of the sun. Tides arising from gravitational forcing through the moon and sun are described as gravitational tides. Thermal tides dominate over gravitational tides in the Earth's atmosphere. Tides generated in the lower and middle atmosphere have components which are able to propagate vertically into the thermosphere. Observations of tidal amplitudes in the mid to high latitude thermosphere reveal a dependency on the geomagnetic activity (*Müller-Wodarg et al.*, 2001).

### 1.3.2. Sun-Earth connection

The Earth's atmosphere, and especially the thermosphere-ionosphere system, depends strongly on the radiation and energetic particles coming out from the Sun.

#### 1.3.2.1. Solar cycle and solar emissions

The activity of the Sun varies over an approximately 11 years cycle, called the solar cycle. When the Sun is active, it is brighter and emits more radiation. The variation in irradiance over the solar cycle is of

the order of 0.1 % near the peak of the spectrum (in the visible domain), but can exceed 100 % in the UV and EUV.

The $F_{10.7}$ index is a measure of the 10.7 cm solar radio flux, and it is a good indicator of the solar activity. Besides, it is strongly correlated to the solar X-ray flux in the 2-7 nm wavelength range (*Bailey et al.*, 2000). $F_{10.7}$ is measured in solar flux units (SFU[6]), and varies from 70 SFU at solar minimum to 230 SFU at solar maximum. In addition to electromagnetic radiation, the Sun also continuously emits charged particles (plasma) from its corona, which is called the solar wind. As the solar wind moves out into space, it carries with it the magnetic field of the Sun, forming the interplanetary magnetic field (IMF). The solar wind encounters the Earth's magnetosphere, producing a shock wave that release heat. It may happen that the IMF field lines connect the field lines of the Earth's magnetic field, causing the so-called magnetic reconnection. When this happens, magnetic energy is released and it is partly transformed into kinetic energy of particles than may eventually fall towards the Earth, following the magnetic lines.

Energetic particles entering the Earth's atmosphere from the magnetosphere, i.e., particle precipitation, transfer their kinetic energy to atmospheric molecules through collisions, being an important heat source at high latitudes. Also Joule heating by ionospheric electric currents can be important at high latitudes.

#### 1.3.2.2. Geomagnetic activity

The interaction of energetic particles with the atmosphere and the flow of currents arising from plasma convection in the ionosphere can cause perturbations in the magnetic field close to the surface. The level of disturbance of the magnetic field depends on the irregularities in the solar wind, and is referred to as the geomagnetic activity level.

A measure of geomagnetic activity level is the planetary 3-hour $K_p$ index (*Bartels*, 1949). The index is obtained from the mean value of the disturbance levels in the north-south geomagnetic field, observed at 13 stations. Levels at each station are determined by measuring the range of disturbance, relative to an assumed quiet-day curve, during three-hourly time intervals. The range is then converted into a local $K_p$ index taking values from 0 to 9 according to a quasi-logarithmic scale. The three-hourly $A_p$ index is a linear scale, directly related to the $K_p$ index. $A_p$ is a daily index obtained from the average of the $A_p$ indices for that day.

[6] 1 SFU (Solar Flux Units) = $10^{-22}\,\mathrm{nW\,m^{-2}\,Hz^{-1}}$

## 1.4. Nitric oxide

Nitric oxide is a heteronuclear molecule, that is, it has a permanent dipole moment. Therefore it is able to radiate in the infrared region. Since it is a diatomic molecule, it only has one vibration mode, with a fundamental frequency $\nu = 1875\,\mathrm{cm}^{-1}$. The vibrational levels of NO are separated approximately by this energy gap. Then, a transition between two consecutive vibrational energy levels implies the emission (from a higher to a lower energy level) or absorption (vice-versa) of a photon in the range of $5.3\,\mu$m. The transition between two vibrational levels defines a vibrational band. Within a vibrational level, the molecule has also rotational levels, $J$, hence, the vibrational band has a structure given by the transitions from a given upper level $(\nu, J)$ to a lower level $(\nu', J')$. For diatomic molecules, the selection rules allow ro-vibrational transitions with change in the rotational quantum number of $\Delta J = +1, -1$, defining the P and R branches, respectively. The molecule of NO is somewhat different from typical diatomic molecules since it has an unpaired electron. This contributes to the total angular momentum and modifies the selection rules allowing ro-vibrational transitions with $\Delta J = 0$ (Q branch). Additionally, its spin produces a splitting of the NO states in two folds: S=1/2 and S=3/2, which turns into a two-folded ro-vibrational band.

### 1.4.1. NO in the upper atmosphere

Nitric oxide is a very important trace gas throughout the atmosphere. In the middle atmosphere, its role in the chemistry of odd nitrogen ($NO_x$) is essential for the catalytic destruction of ozone (*Brasseur and Solomon*, 2005). In the upper atmosphere, its $5.3\,\mu$m emission contributes to the cooling the middle thermosphere (120-200 km), particularly during auroral events (*Kockarts*, 1980), when temperature increases due to the Joule heating. It is, therefore, very important in the energetic balance of the thermosphere (*Roble et al.*, 1987; *Mlynczak et al.*, 2010). Nitric oxide plays also an important role in the ionosphere, since its low ionization potential (lower than molecular nitrogen, molecular oxygen and atomic oxygen) turns it into an important source of ionization for the D and E regions.

In the thermosphere, nitric oxide is chemically produced due to the action of energetic photons (ultraviolet and X rays) and auroral electrons (1-10 keV) (*Gerard and Barth*, 1977) that dissociate molecular nitrogen and produce excited atomic nitrogen, subsequently reacting with molecular oxygen. Explicitly,

$$N(^2D) + O_2 \rightarrow NO(v, J, S) + O \tag{1.1}$$

$$N(^4S) + O_2 \rightarrow NO(v, J, S) + O. \tag{1.2}$$

Reaction 1.1 is the dominant source of thermospheric NO below 130 km during daytime (*Sharma et al.*, 1998), but vanishes at nighttime due to the negligible nighttime N($^2$D) concentrations (*Rusch et al.*, 1991). Reaction 1.2 is the main source of NO above 130 km and below that altitude during nighttime. It has been demonstrated that it produces highly vibrationally and rotationally excited NO detectable in the NO dayglow emission at 5.3 $\mu$m (*Gérard et al.*, 1997; *Duff et al.*, 1994). Since this reaction has an activation energy of $\sim$0.3 eV, N($^4$S) atoms with kinetic energy higher than the activation energy are needed to produce NO. In the daytime thermosphere, the N($^4$S) kinetic energy distribution function (EDF) is super-thermal (*Sharma et al.*, 1998), that is, the proportion of "hot" N($^4$S) atoms with energies higher than $\sim$0.3 eV is higher than at nighttime, when the EDF is thermal (*Sharma et al.*, 1996a). Hence, the production of NO via reaction 1.2 increases during daytime, while at nighttime only the "hot" N($^4$S) atoms found in the tail end of the thermal EDF contributes to the production of NO (*Sharma et al.*, 1996b). During geomagnetically active periods, the NO production via 1.1 and 1.2 pathways can become important due to the enhancement of atomic nitrogen abundance even as low as in the mesosphere and lower thermosphere.

The major losses of NO in the thermosphere come mainly from photodissociation produced by solar far ultraviolet radiation,

$$NO + h\nu \ (\lambda = 181 - 192\,\mathrm{nm}) \rightarrow N(^4S) + O, \tag{1.3}$$

followed by the chemical reaction with N($^4$S), often called 'cannibalistic' reaction,

$$NO + N(^4S) \rightarrow N_2 + O. \tag{1.4}$$

The lifetime of a NO molecule to chemical destruction (or e-folding[7] time in the NO density) under illuminated conditions is 19 hours (*Barth et al.*, 2001). The lifetime of the NO molecule to diffusive transport is approximately one day (*Barth*, 1992). Given that the solar illumination varies throughout the day, the abundance of NO at any time is then representative of the level of solar energy deposition (solar irradiance and auroral energy) over the past day. During polar winter, NO is rather long-lived (lifetimes of weeks to months) throughout the middle and upper atmosphere, since photo-chemical losses are minimized. It is then transported downwards by the residual circulation, increasing the $NO_x$ reservoir in the stratosphere (*Solomon et al.*, 1982; *Funke et al.*, 2005a).

The geographical distribution and variability of NO depends strongly on the energy input from the Sun, in the form of energetic photons at low latitudes (*Barth et al.*, 1988; *Siskind et al.*, 1990) or precipitation of charged particles (with the subsequent Joule heating events) at mid and

[7] A decrease by a factor $e$.

high latitudes (*Siskind et al.*, 1989a,b; *Dobbin and Aylward*, 2008; *Barth et al.*, 2009).

Therefore, the density distribution of nitric oxide may be used as an indicator of the temporal and spatial distribution of energy deposition into the thermosphere. For example, in *Barth et al.* (1988) and *Barth et al.* (2003), using SME and SNOE data, respectively, it is demonstrated that the NO variability in the equatorial region at 105-110 km is controlled by the variability in the energetic solar variation. That is, there is a correlation between the solar activity and the NO production. In conditions of high geomagnetic activity, the high-latitude heating is proved to cause adiabatic compressional heating at low and mid-latitudes, produced as a response of the thermosphere to the auroral heating (*Roble et al.*, 1987; *Siskind et al.*, 1989a). In consequence, the heating produced by the particle precipitation on the one hand, and by the ionization and dissociation of molecular nitrogen on the other hand, produce an enhancement in the NO concentration, as recorded by observations from SME (*Siskind et al.*, 1989b) and SNOE (*Barth et al.*, 2003).

## 1.5. Measurements of temperature and NO in the thermosphere

### 1.5.1. Temperature

Temperature in the thermosphere can be measured using different techniques. For instance, using ground-based instruments, such as Fabry-Perot interferometers, that measures airglow emissions from atomic oxygen (*Griffin et al.*, 2008), or incoherent scatter radars (*Maeda et al.*, 2002), that allow the derivation of neutral temperatures. Neutral temperature in the lower thermosphere can be also derived from rotational temperature of $N_2$, as described in *Kurihara et al.* (2006) using rocket-borne instruments. Thermospheric temperature has also been obtained by measuring the rotational structure of the UV airglow emission of NO (*Barth and Eparvier*, 1993). *Zachor and Sharma* (1985) developed an algorithm for retrieving the kinetic temperature in the lower thermosphere from a spectrally resolved profile of infrared limb radiance. In particular, they demonstrate the usefulness of the method for the case of $CO_2$ 15 $\mu$m emission in the 80-130 km interval. Later, CIRRIS-1A observations allowed retrieval of kinetic temperature from the rotational distribution of NO($v$ = 1), taking into account rotational thermal and non-thermal components (*Sharma and Duff*, 1997).

More recently there is also another (yet short) dataset from an experiment on the International Space Station (ISS) called the Remote At-

mospheric Ionospheric Detection System (RAIDS) (*Budzien et al.*, 2010). RAIDS measures temperature from 90–150 km using the near-IR spectra of the $O_2$ A-band. These data start in fall of 2009. Since it is the ISS, which has a relatively low inclination orbit, the data are limited to equatorwards of 50° and there are no polar measurements.

### 1.5.2. NO

Thermospheric nitric oxide has been remotely observed since 1964 using different measurement techniques. Fluorescent scatter of ultraviolet solar radiation by NO gamma bands has been applied by instruments on board rockets (*Barth*, 1964; *Eparvier and Barth*, 1992) and on satellite platforms both looking in the nadir and limb, e.g. OGO-4 (*Rusch and Barth*, 1975), the Atmosphere Explorer satellites (*Barth et al.*, 1973), the Solar Mesosphere Explorer (SME) (*Barth et al.*, 1988), and the Student Nitric Oxide Explorer (SNOE) (*Barth et al.*, 2003). With this technique, thermospheric NO number densities were obtained although restricted to daytime and twilight conditions. In addition, NO slant column densities were measured by occultation in the infrared by the Atmospheric Trace Molecule Spectroscopy instrument (ATMOS) on board Spacelab 3 (*Russell III et al.*, 1988) and NO number density by the Halogen Occultation Experiment (HALOE) on board UARS (*Russell III et al.*, 1993).

Another observation technique for NO consists in the measurement of its infrared emission at 5.3 $\mu$m, as used in the analysis of the Spectral Infrared Rocket Experiment (SPIRE) (*Zachor and Sharma*, 1985), the Improved Stratospheric and Mesospheric Sounder (ISAMS) (*Taylor et al.*, 1993), the Cryogenic Infrared Radiance for Shuttle (CIRRIS-1A) instrument (*Armstrong et al.*, 1994), the Sounding of the Atmosphere using Broadband Emission Radiometry (SABER) radiometer (*Russell III et al.*, 1999; *Gardner et al.*, 2007; *Mlynczak et al.*, 2010) and the Michelson Interferometer for Passive Atmospheric Sounding (MIPAS) (*Funke et al.*, 2005b). If the radiance is spectrally resolved in thermospheric observations, as in SPIRE and CIRRIS-1A, the temperature and the number density of the vibrationally excited NO(1) can be retrieved, as well as the NO 5.3 $\mu$m cooling rate. If not, only the latter can be obtained.

It is well known that the NO 5.3 $\mu$m emissions are affected by non-LTE at altitudes as low as the stratosphere (*Kaye and Kumer*, 1987; *López-Puertas and Taylor*, 2001) hence, this has to be taken into account when analyze them.

## 1.6. Motivation of this work and objectives

The thermosphere is the least explored region of the atmosphere. It was only with the advent of remote sensing during the 1960's that began the observation of this region globally.

On one hand, there are very few temperature measurements from satellite (e.g. global) above 100 km, yet the knowledge of the temperature structure is essential to study the energy balance, and it is also needed in order to accurately model this atmospheric region.

On the other hand, the NO in the upper thermosphere is a key piece in the energy balance because it contributes to cool the thermosphere by its infrared emission. Besides, its distribution depends strongly on the energy input in the atmosphere, as from energetic photons as from precipitation of energetic charged particles. NO plays a major role not only in the thermosphere but also in lower atmospheric regions, since it can be transported from the thermosphere down into the stratosphere in the polar regions during winter dark conditions and can affect the global $NO_y$ budget of the stratosphere. Actually, there is an important international effort dedicated to quantify this descent and study its variability along the solar cycle, e.g. the HEPPA working group and associated meetings (http://heppa2011.iaa.es). In spite of its importance, NO has not been yet (prior to MIPAS) measured in the nighttime thermosphere.

In this context, MIPAS measurements of thermospheric temperature and nitric oxide has come to fill a very important gap. Since 2005, MIPAS on board ENVISAT has been measuring on a regular basis the NO 5.3 $\mu$m limb emission in the upper atmosphere with high spectral resolution. MIPAS also has large spatial and temporal coverage, allowing to measure the NO limb radiance from pole to pole and at day and nighttime.

The major objective of this work is the analysis of those measurements, from which two major aims are pursed. The first, rather technical yet scientifically important, is to retrieve the kinetic temperature and NO vmr from MIPAS spectra. This is a very difficult and complex task because: a) non-LTE modelling for the vibrational, rotational and spin populations of NO have to be included; and b) because of the inherent difficulty of retrieving temperature and NO vmr simultaneously from the spectra. That aim comprises, of course, the characterization of the quality of the measurements, and the validation, whenever possible, with independent measurements. In addition to those difficulties, and because NO vmr's are retrieved (and not just the NO number density), accurate information on the temperature and pointing below the thermosphere, i.e., in the stratosphere and mesosphere, is required. Hence the retrieval of those quantities from the $CO_2$ 15 $\mu$m emission, not from the NO 5.3 $\mu$m emission, was also carried out, prior to the thermospheric temperature and NO

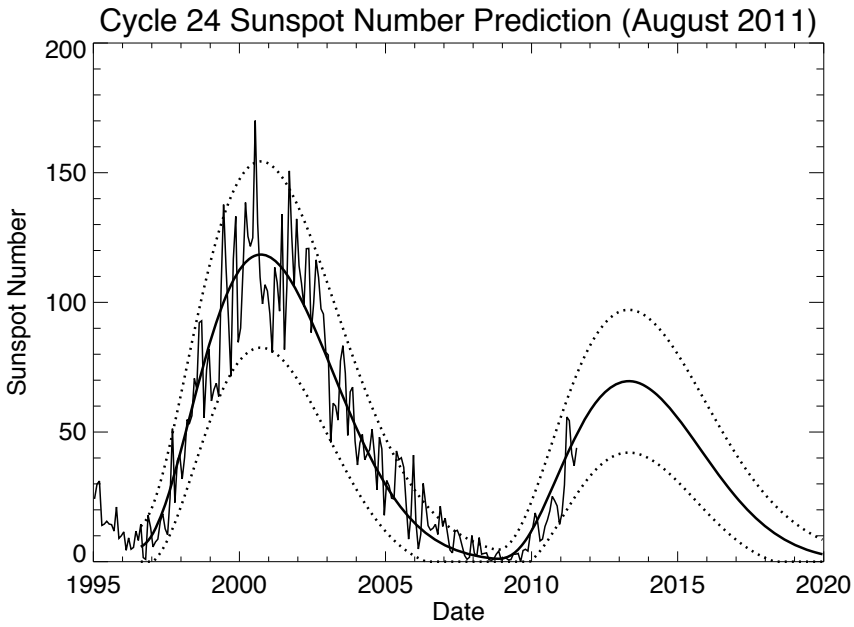


Figure 1.5: Sunspot cycle measurements and predictions. Solid: The International Sunspot Number as compiled by the Solar Influences Data Analysis Center in Belgium. Solid and dashed smooth curves: prediction for sunspot cycle 24 by MSFC Solar Physics Branch members Wilson, Hathaway, and Reichmann. After Wilson, Hathaway, and Reichmann, (2011).

inversions. Similarly to these retrievals, the characterization of the quality of the stratospheric and mesospheric temperature measurements and their validation were also performed.

The second major aim is to study the physical and chemicals aspects of the thermosphere by using those measurements. Among those, to study and understand the altitude, latitude, seasonal and temporal distributions of temperature and NO vmr in the thermosphere. Because of MIPAS operation, this study is mainly focused in the declining phase of solar cycle 23, typical of solar minimum conditions. Comparison with previous measurements and models, both for temperature and NO, have also been performed. Among other findings, the retrieved MIPAS data has allowed us to: (i) establish a climatology of thermospheric temperatures and NO abundances typical of solar minimum conditions; (ii) to study, for the first time, the diurnal variations of thermospheric NO; (iii) to find the first experimental evidence of a dynamical coupling of the lower atmosphere and the thermosphere in the 120–150 km range by means of satellite data (during an stratospheric-warming event); and (iv) to analyze in detail the changes in thermospheric temperature and NO induced by a solar proton event.

Yet the important findings achieved, this work is expected to be continued in the future. The important database of temperature and NO generated during this Thesis (see, e.g., the IMK-IAA database web site) is

still far beyond being fully exploited. In that sense ongoing studies to compare the data with 3D simulations as the TIME-GCM (*Roble*, 1995; *Liu and Roble*, 2002) and WACCM (*Garcia et al.*, 2007) models is currently under progress.

In addition, MIPAS is still measuring routinely in the upper atmospheric (*UA*) mode with the current baseline of 1/10 days and the Envisat mission has been extended until the end of 2013. It is then planned to apply the retrieval scheme developed in this Thesis to those data and in this way to extent the thermospheric temperature and NO database to the rising phase of solar cycle 24 and have then a database for a nearly complete solar cycle (see Figure 1.5).

# Chapter 2

# The MIPAS instrument

*Abstract*

An overall view of the ENVISAT mission and the MIPAS instrument is given: motivation, scientific aims and technical characteristics are introduced. The measurement strategy, as well as the calibration and characterization of the data is also described. Finally, a list of the measurement days used in this work is presented.

## 2.1. Introduction

MIPAS, the Michelson Interferometer for Passive Atmospheric Sounding (*Fischer et al.*, 2008), is a high spectral resolution emission spectrometer designed for the limb scanning of the Earth atmosphere in the near and mid-infrared. It is part of the core payload of the ENVISAT mission by ESA (Figure 2.1), successfully launched on 1$^{st}$ March 2002 into a sun-synchronous polar orbit (98.55$^{\circ}$ inclination at a mean altitude of 800 km). The ENVI(ronment) SAT(ellite) was devised to provide a capability for remote sensing observation of the Earth from space that allows to study and monitor its environment. The list of scientific objectives addressed by ENVISAT is wide and various disciplines are covered: atmosphere, oceans, ice, natural resources, etc (please visit the ENVISAT web site for detailed information).

MIPAS takes part in the ENVISAT Atmospheric-Chemistry experiment, together with GOMOS (Global Ozone Monitoring by Occultation of Stars) and SCIAMACHY (Scanning Imaging Absorption Spectrometer for Atmospheric Cartography), which were designed to shed light on the highly concerning issue during the nineties about of the Earth, its environment and mankind's impact on it. Climate warming, tropospheric pollution or ozone depletion in the stratosphere were examples of the necessity of improving the understanding of the role of the atmosphere in the Earth system.

Three major scientific areas were established to assess the utility

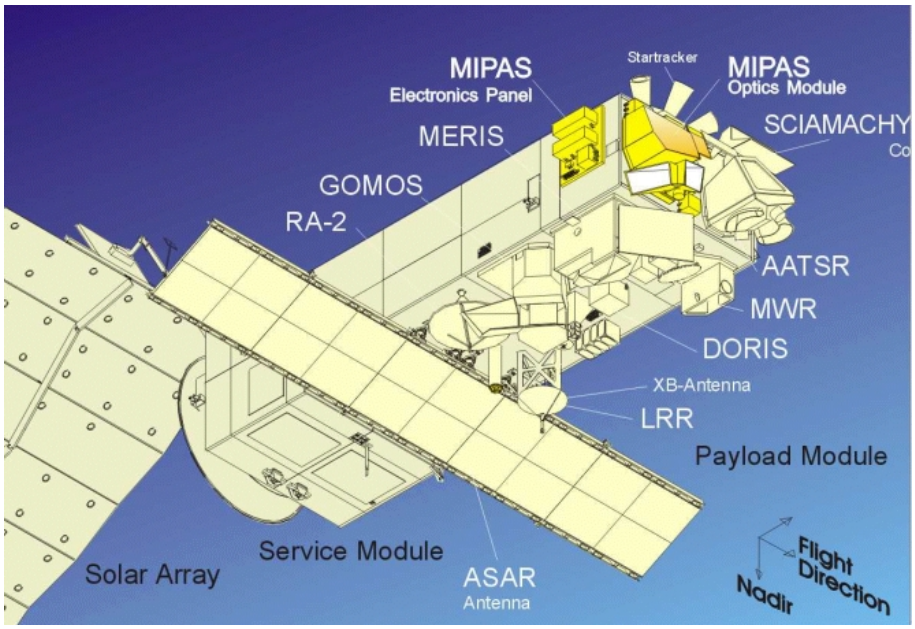


Figure 2.1: Envisat satellite and all its instruments on board with MIPAS at the top in bright yellow (ESA picture).

of an instrument like MIPAS:

> *Atmospheric Chemistry*: out of the necessity of a better understanding the photochemical processes which control the distribution of trace species in the atmosphere.
>
> *Climatology*: by monitoring trace gases which temporal variability modify the radiative transfer and may influence the Earth's climate.
>
> *Meteorology*: as the study of the influence of dynamic and radiative processes at lower atmosphere on the rest of atmosphere.

To achieve these requirements, MIPAS needed to be capable of measuring several gases simultaneously. In this sense, previous instruments: MIPAS-B (balloon) and ATMOS (Atmospheric Trace Molecular Spectroscopy) influenced strongly on the design of MIPAS as an interferometer centered in the mid-infrared. Because:

i) A large number of important gases, i.e. $CO_2$, $O_3$, $NO_x$, etc, present vibration-rotation lines in this part of the spectrum, making them suitable to be detected by MIPAS.

ii) The atmospheric signal is higher than in other parts of the spectrum, since the Planck function maximum at atmospheric temperatures peaks near 10 $\mu$m. This allows MIPAS to measure signal independently of sunlight conditions.

iii) The instruments operating in the mid-infrared can be smaller than those working in longer wavelengths. This is determined by the diffraction limits and the high spectral resolution (which depends upon the maximum distance between the two retro-reflectors of the interferometer) necessary to observe trace species of interest.

iv) The calibration of instruments operating in the mid-infrared can be done by observing the cold space or black bodies, which means a clear advantage over instruments that works in visible or ultraviolet windows.

In addition, MIPAS scans the atmosphere horizontally, allowing to measure radiance coming from long optical paths and hence being able to observe low-concentration trace gases. The limb observing geometry of MIPAS also provides an interesting vertical resolution of few kilometers for the targets down to upper tropospheric altitudes and its high sensitivity allow to detect signal up to the lower thermosphere. The ability of MIPAS to make global and simultaneous measurements makes it a very powerful instrument to study the energetics, the dynamics and the chemistry of the atmosphere.

First of all, information on temperature structure is fundamental to undertake any study in the atmosphere. MIPAS is capable of measuring temperature at all its altitude range, from troposphere to thermosphere (*Bermejo-Pantaleón et al.*, 2011; *Chauhan et al.*, 2009; *von Clarmann et al.*, 2003a, 2009; *García-Comas et al.*, 2011). Since the beginning of the mission to current days, the database of MIPAS temperature is huge (please visit the IMK-IAA database web site for detailed information).

In the upper troposphere, MIPAS can measure trace gases like formaldehyde (HCHO) (*Steck et al.*, 2008), acetone ($CH_3COCH_3$) (*Moore et al.*, 2010), PAN (peroxyacetyl nitrate) (*Glatthor et al.*, 2007), $C_2H_6$ (*von Clarmann et al.*, 2007) and CO (*Funke et al.*, 2009). Elevated concentrations of HCHO, acetone and PAN in the upper troposphere indicate upward transport of air from below. In addition, enhancements of tropospheric $C_2H_6$, HCN and ozone originated in biomass burning events have been measured by MIPAS (*von Clarmann et al.*, 2007; *Glatthor et al.*, 2009). Also, injections of polluted air and biomass burning products in the upper troposphere can be tracked by MIPAS by observing global CO (*Funke et al.*, 2009).

The troposphere to stratosphere interactions are a very important issue at a global scale. Let's name some examples of the importance of this interaction. The exchange of mass through the tropopause and the upwards and downwards propagation of wave disturbances may affect the dynamics of the stratosphere (like the breakdown of the polar vortex) and the tropospheric weather. Tropospheric ozone at mid and high latitudes depends strongly on the stratospheric ozone transported downward. The chemical

composition of the stratosphere is affected by the input of air from upper troposphere; of particular interest is the TTL (Tropical Transition Layer). Also, upward and downward propagating radiative fluxes are modified as a consequence of atmospheric composition changes. MIPAS contributes to study the interaction between troposphere and stratosphere by providing observations of concentration profiles with high vertical resolution of numerous species like $H_2O$ (*Milz et al.*, 2005) or $CH_4$, $N_2O$ and $O_3$ (*Glatthor et al.*, 2005), whose vertical gradients vary rapidly. Other interesting species is $SF_6$, which injection in the stratosphere from tropical troposphere allows to assess the mean age of air of the stratosphere (*Stiller et al.*, 2008).

In the stratosphere, there are still many open questions regarding its chemistry and dynamics, specially within the polar regions. MIPAS measurements of temperature and trace gases like $N_2O$, CO or $CH_4$ are useful for the better understanding of circulation patterns, such as the descending branch of the meridional circulation which manifests in the downward transport of $NO_x$ during polar winters (*Funke et al.*, 2005a). Out of the polar regions, the Brewer-Dobson circulation can be traced by $SF_6$ (*Stiller et al.*, 2008). MIPAS temperature and $O_3$ distributions allowed to study the dynamics of the Antarctic vortex split in September-October 2002 during a major stratospheric warming event (*Wang et al.*, 2005) and related mixing processes were studied on basis of MIPAS $CH_4$, $N_2O$, CFC-11 and $O_3$ (*Glatthor et al.*, 2005). The most interesting topic related to stratospheric chemistry is the chemistry of ozone and all the chemically active families involved, $Cl_y$, $NO_y$ and $HO_y$[1] , together with the polar stratospheric clouds. MIPAS global and continuous measurements of these species (*von Clarmann et al.*, 2005; *Glatthor et al.*, 2004; *Höpfner et al.*, 2004, 2009a; *López-Puertas et al.*, 2005a,b, 2007a; *Mengistu Tsidu et al.*, 2004, 2005; *Stiller et al.*, 2005, 2007), and PSC's (*Spang et al.*, 2005a,b; *Höpfner et al.*, 2006a,b, 2009b) allow to figure out their sources and sinks and temporal distribution.

The high sensitivity of MIPAS makes it capable of measuring abundances of key gases in the mesosphere and lower (and mid) thermosphere: CO (*Funke et al.*, 2009), NO (*Funke et al.*, 2005b; *Bermejo-Pantaleón et al.*, 2011), $CH_4$ and $CO_2$ (*Fischer and Oelhaf*, 1996; *von Clarmann et al.*, 2009; *Payan et al.*, 2009), $H_2O$ (*Milz et al.*, 2005; *García-Comas et al.*, 2010) and $O_3$ (*Gil-López et al.*, 2005). About energetics, the infrared radiative cooling in this region by $CO_2$, $H_2O$, $O_3$ and NO (*López-Puertas and Taylor*, 2001) can also be addressed by MIPAS measurements. Regarding chemistry, water vapour is a representative species, as an OH source (important cooler of the upper mesosphere) or a $CH_4$ sink (*Brasseur and Solomon*, 2005), and also as an signal of PMC occurrence (*Hervig et al.*, 2003; *López-Puertas et al.*, 2009b). Moreover, ozone's secondary maximum

[1] $Cl_y$ family: Cl, $ClNO_3$, $ClONO_2$, ClO, HOCl, $Cl_2O_2$. $HO_y$ family: H, OH, $HO_2$, $CH_3OOH$, HONO, $HO_2NO_2$. $NO_y$ family: $NO_x$(NO + $NO_2$), $N_2O_5$, $HNO_3$, $ClONO_2$.

is known to be affected by tides, hence, a relation between chemistry and dynamics can be stated (*Smith and Marsh*, 2005). CO and $CO_2$ MIPAS measurements can yield understanding on the molecular and vertical eddy diffusions in the upper mesosphere and lower thermosphere (*López-Puertas and Taylor*, 2001). CO, besides, provide information on meridional circulation, specially on downward motion at winter pole and transition equinox to solstice and vice versa (*López-Valverde et al.*, 1996). The dynamical coupling between middle and upper atmosphere during a major stratospheric warming could be studied on basis of MIPAS temperature (*Funke et al.*, 2010). MIPAS can also be used to study the impact on middle and upper atmosphere chemistry by incoming radiation and particle flux from sun, like the solar proton event in October-November 2003 (*Funke et al.*, 2008a, 2011; *Höpfner et al.*, 2004; *López-Puertas et al.*, 2005a,b; *von Clarmann et al.*, 2005) or by major warming events, like that occurred in the Antarctic on 2002 (*Funke et al.*, 2008b; *Glatthor et al.*, 2004; *López-Puertas et al.*, 2007a; *Mengistu Tsidu et al.*, 2005).

MIPAS has been measuring since 2002, allowing to study the interannual variability of important species, like the $Cl_y$, $NO_y$ and $HO_y$ families, all of the of importance to understand the variation of ozone levels. Also, the long-term $H_2O$ measurements by MIPAS in the upper troposphere and stratosphere can yield information on the monitoring of the cooling of the atmosphere. Therefore, MIPAS entails a great demand of data to create climatologies and to be part of weather forecast and assimilation.

Furthermore, the infrared emission measured by MIPAS, specially that coming from the upper atmosphere, is affected by non local thermodynamic equilibrium (non-LTE) (*Funke et al.*, 2007; *López-Puertas et al.*, 2005c,d, 2007b). The high sensibility and high spectral resolution of the instrument allow to study this effect with accuracy and this is crucial when concentration of species are retrieved from its non-LTE emission (*Bermejo-Pantaleón et al.*, 2011; *Funke et al.*, 2005b, 2009; *García-Comas et al.*, 2011; *Gil-López et al.*, 2005), besides its fundamental role on the infrared radiative cooling.

## 2.2. The Instrument

Some of the characteristics of MIPAS have been already briefly mentioned. Now, the instrument is described with more detail.

MIPAS is a Fourier transform infrared (FTIR) spectrometer. It offers the advantage over dispersive spectrometers of putting less limitations on the input signal, which means a high sensitivity and a wide field of view. By the time it was designed, it meant the best option for measuring IR spectra with high resolution and a good sensitivity.

The FTIR instruments, on the other hand, entail a mechanical complexity. The optical elements need to move very precisely and a stable alignment is required for them. Besides, the optical system has to be cooled in order to reduce its thermal background emission. In the case of MIPAS, the optics is kept at 210 K.

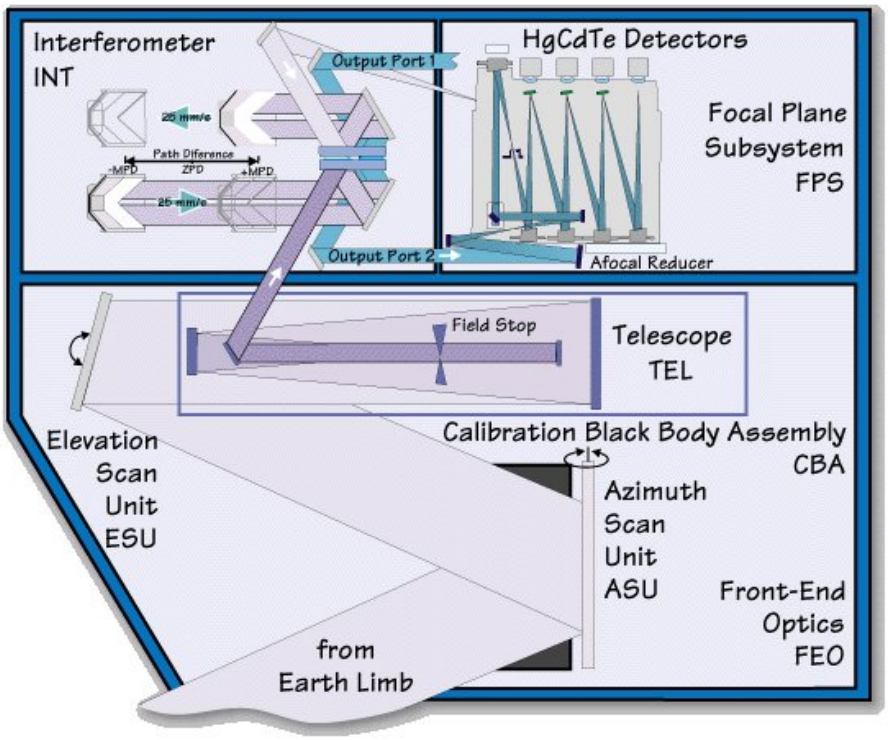


Figure 2.2: MIPAS optical system (ESA picture).

The atmospheric limb radiance enters MIPAS (Figure 2.2) through the Front-End Optics subsystem, where it is reflected by azimuth (to select the orientation of target) and elevation (to select the altitude of the target) mirrors and directed to the input telescope. Then, the radiation is collimated and redirected to the Michelson interferometer where it is split in two beams. Two movable retro-reflectors give these two beam fractions back to the splitter and they are recombined producing an interference pattern. Once again, the signal is divided in two beams and they are sent this time to the infrared detectors through two output ports. Each signal enters the Focal Plane subsystem and it is filtered into four spectral channels (eight in total) and analyzed by respective MCT (Mercury Cadmium Telluride) detectors, which are actively cooled down to 70 K in order to minimize their thermal emission and their contribution to internal noise. The detectors are optimized to cover the spectral range between 4.15 to 14.6 $\mu$m (685 to 2410 $cm^{-1}$). Combining the channels from each output port, five spectral bands are obtained for

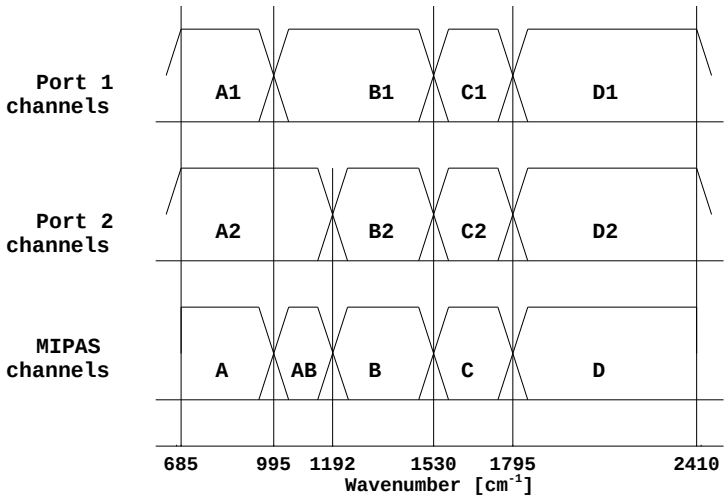


Figure 2.3: Spectral bands covered by the infrared detectors for each output port and the MIPAS filters at the bottom.

MIPAS (Figure 2.3).

The infrared detectors collect a succession of interference patterns of different intensity called interferogram. This happens because of the varying optical path created by the movement of the retro-reflectors. The intensity spans from zero (destructive interference) to maximum signal (constructive interference). The interference pattern depends upon the optical path defined by the retro-reflectors and upon the wavelength of the incoming light. Also, the amplitude of the interferogram carries information on the radiance energy. All this information is retrieved by applying the Fourier transform on the interferogram, converting it into a spectrum. Fourier transform spectrometers produce a spectral resolution which is determined by the optical path difference (OPD) between the two retro-reflectors, about 0.6/OPD. MIPAS has a OPD of 20 cm and hence it determines a spectral resolution of 0.035 $cm^{-1}$ for an unapodized spectrum. Such a precision is difficult to achieve by other types of spectrometer. However, the failure of an interferometer drive unit (*QWG*, 2004) on March 2004 made the OPD to be reduced to 8 cm, which meant a reduction of the spectral resolution to 0.0625 $cm^{-1}$. As a consequence, the observation modes of MIPAS were redefined (Section 2.6).

## 2.3. Data calibration and characterization

The interferogram recorded by the detectors is pre-processed on board in order to reduce the amount of data to be sent to ground station. Amplification, digitalization, complex filtering, compression and formatting is applied to the interferogram, configuring the *Level 0* data.

This data, together with auxiliary information for further calibration, is sent to the Envisat spacecraft and finally transmitted to the ground, including information on the telemetry.

Once in ground, the interferograms are transformed into calibrated and geolocated spectra, the so-called *Level 1b* data, from which profiles of atmospheric parameters will be eventually obtained (*Level 2* data). The process begins with a radiometric calibration of the measurements, consisting of two steps:

1. Offset calibration. Measurements looking at the cold space are taken (this is called a "cold" measurement). The obtained interferogram is produced by the instrument's thermal emission since the infrared radiance from the space is the 3 K cosmic background and it is considered negligible. Thus, the radiometric offset can be determined.

2. Gain calibration. The instrument takes "warm" measurements when looking at an internal source well characterized by a black body with known temperature.

In both calibrations, the measurements are performed by reducing the spectral resolution by a factor 10 in order to make them faster (0.4 s). Since the instrument offset is much more sensitive to changes in the instrument temperature than the gain function, the gain calibration is performed once per day and the "deep space" offset is carried out every 800 s (*Niro*, 2011). The gain function can be expressed as:

$$G = \frac{L_{BB}}{S_{BB} - S_{DS}}. \tag{2.1}$$

Thus, the radiometric calibration is:

$$L_{atm} = G\left(S_{atm} - S_{DS}\right), \tag{2.2}$$

where $S_{BB}$, $S_{DS}$, $S_{atm}$ are, respectively, the measured spectrum of the black body, the deep space and the atmosphere, and $L_{BB}$ is the known radiance of the black body and $L_{atm}$ is the radiometrically calibrated spectrum.

It then follows the spectral calibration. It consists of a correction of the Doppler shift caused by the relative motion of the satellite with respect to the atmosphere. Reference line positions in the measured spectrum are identified and compared to known theoretical positions in each MIPAS channel. Ozone (802.5074 $cm^{-1}$, 1125.2085 $cm^{-1}$) and water vapour (1409.9686 $cm^{-1}$, 1672.475 $cm^{-1}$, 1966.2615 $cm^{-1}$) lines are used for this purpose. An assignment of wavenumbers to spectral data points is then established. In order to ensure stability, the spectral calibration is performed every 4 limb sequences (*Nett et al.*, 2002;

*Kleinert et al.*, 2007).

During the radiometric and spectral calibration process, auxiliary procedures are employed for cleaning the interferogram. For instance, the presence of spurious spikes due to cosmic rays or errors in the transmission are detected and corrected. Another example is the detection and correction of different sampling of an interferogram of a measurement with respect to the sampling of interferograms corresponding to gain and offset calibrations. An important issue is the non-linear response of the MIPAS detectors, which can be a source of significant radiometric errors. This effect appears with high photon fluxes and it is stronger at shorter wavenumbers (detectors A1, A2, B1, B2) (*BOMEM*, 1996). The non-linear behaviour is characterized on ground by a polynomial function ($k = 1 + d_0\,F + d_1\,F^2 + d_2\,F^3 + d_3\,F^4$), being $k$ the black body emission at a known temperature, $F$ the total flux on a given detector and $d_i$ the coefficients determined by the non-linearity characterization for each detector; and it is cross-checked in flight. The non-linearity effect is corrected by scaling the interferogram with this function, before the equations 2.1 and 2.2 are applied.

At the end of the day, the accuracy achieved in the radiometric calibration is around 1-2 %, being the most critical issue the non-linearity corrections (*Kleinert et al.*, 2007).

The radiometric calibrated spectrum is stored in a complex variable. The real part represents the *Level 1b* data and the imaginary part contains information on noise and it is used for computing the noise equivalent spectral radiance (NESR). The noise of the MIPAS spectra is quantified by the NESR. For each calibrated spectrum a NESR is calculated. This NESR is derived from the imaginary part of the calibrated spectrum, by taking the standard deviation of all data points within a spectral interval of $10\,\mathrm{cm}^{-1}$. The $\mathrm{NESR}_0$ is the NESR in absence of signal radiation, therefore, it is the minimum NESR possible. The $\mathrm{NESR}_0$ ranges from 3 to $50\,\mathrm{nW/(cm^2\,sr\,cm^{-1})}$, depending on the MIPAS channel. It is evaluated from deep space measurements at 210 km altitude. The most important effect on the NESR is the ice accumulation on the detector system, which may degrade it by up to a 20 %.

The presence of ice on the detectors produces strong infrared absorption bands (specially in the MIPAS A band) and a consequent decrease of the signal. As a result, the gain factor increases. Decontamination plans are periodically carried out every $\sim$8 months, and more frequent towards the beginning of the mission. In the last months the slope of the gain increase is progressively decreasing, demonstrating that detector is more and more "ice-free" (*Niro*, 2011).

The radiance measured by an instrument is not the actual radiance coming from the atmosphere, but the response of the instrument to the latter. An ideal spectrometer responds to a monochromatic signal with

a *sync* function (Figure 2.4). This is the definition of the instrumental line shape, ILS. The ILS of a real spectrometer is more complex, as the input radiance is not monochromatic and there are mis-alignments or the angular aperture is irregular. Thus, a measured spectrum will be a convolution of an atmospheric spectrum with the ILS. A good characterization of the MIPAS ILS is important because it gives the actual spectral resolution, defined as the full width at half maximum. MIPAS ILS was modeled before the launch and this model is adjusted with measurements in order to get a more realistic ILS (*BOMEM*, 1992a,b). This process is performed after the radiometric and spectral calibration in order to reduce errors.

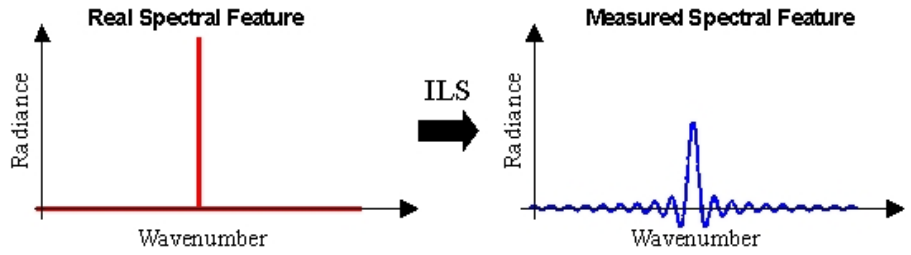


Figure 2.4: Effect of the convolution of an 'ideal' atmospheric signal (left) with the instrumental line shape (ILS): the measurement (right).

It is interesting to remark that before performing the *Level 2* retrieval, the spectrum is apodized. As mentioned before, the measured spectra is the convolution of atmospheric spectrum with the ILS. The ILS is characterized by 'side-lobes' decreasing linearly in amplitude (Figure 2.4) and hence, the atmospheric signal at a given wavenumber affects the measured signal in a broad spectral interval. The apodization is a convolution of the observed spectrum with a function that reduces the amplitude of the side lobes of the ILS (Figure 2.5). This is very useful in order to make smaller the necessary spectral intervals for the retrieval of atmospheric parameters. The counterpart of using apodization is a slight loss of spectral resolution.

For a limb instrument like MIPAS, it is essential to get accurate knowledge of where the atmospheric radiance comes from. Hence, the elevation pointing or line of sight (LOS) is calibrated. The calibration is carried out by a dedicated measurement mode in which the interferometer acts as a radiometer, that is, with the retro-reflectors at their stop end, creating the maximum path difference. Then, incoming radiance from bright infrared stars are measured (MIPAS D band is used). The trajectory of the star along the field of view (FOV) can be predicted using orbital information of ENVISAT. The difference between the expected time for the star to cross the FOV and the actual time of crossing is directly the MIPAS mis-pointing and the MIPAS engineering pointing is then esti-

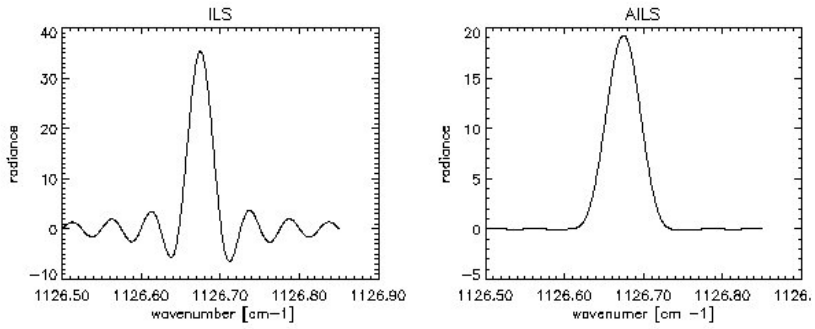


Figure 2.5: Example of ILS at left and Apodized ILS (AILS) at right.

mated. The line of sight is calibrated weekly (*Niro*, 2011) in order to correct it from deviations in platform altitude, misalignments between platform and instrument or misalignments between azimuth and elevation mirrors. From the studies by *von Clarmann et al.* (2003a) it was found that MIPAS engineering tangent altitude had a bias with respect to the real tangent altitude of up to 3 km, but after an upgrade of the MIPAS pointing system this bias was reduced within the accuracy specification, i.e. 900 m (*Raspollini et al.*, 2006). In addition, a seasonal and latitudinal bias was found in the engineering line of sight with respect to that retrieved (*Kiefer et al.*, 2007). The information on the corrected elevation pointing and measured azimuth angles are used to compute the geolocation of a measurement defined as the latitude and longitude of the corresponding tangent point.

## 2.4. Spectral coverage

As previously mentioned, MIPAS operates in the spectral range between 4.15 and 14.6 $\mu$m, shared out in five channels or filters (Table 2.1 and Figure 2.6). This distribution optimizes the sensitivity in all the spectral bands. Besides, the two set of detectors assure redundant information in spectral regions of maximum interest (Figure 2.3). The shorter wavelength limit is fixed by the low sensitivity, yet allowing to measure $CO_2$ radiance at 4.3 $\mu$m, which is essential for the study of energy balance at middle and upper atmosphere. The longer wavelength limit was set for the accurate derivation of temperature from $CO_2$ emission at 15 $\mu$m.

Concerning the spectral resolution, the history of MIPAS has two parts: an initial period of maximum spectral resolution (full resolution, FR) of 0.025 $cm^{-1}$ apodized, from September 2002 to March 2004, and a period of optimized spectral resolution (OR) of 0.0625 $cm^{-1}$ apodized, from January 2005 to present. This decrease is proportional to the reduction of the OPD from 20 to 8 cm because of the interferometer drive system problem.

Table 2.1: MIPAS filters. The spectral range (in $cm^{-1}$), the average noise (in $nW/(cm^2\,sr\,cm^{-1})$) and the most important absorbing or emitting species are specified for each filter.

| Band | Spectral range | NESR | Species |
|---|---|---|---|
| A | 685 - 970 | 30 | $CO_2$, $O_3$ CFCs, $HNO_3$ $ClONO_2$, $HNO_4$, $C_2H_2$, $C_2H_6$ $CCl_4$, OCS, $SF_6$, aerosols |
| AB | 1020 - 1170 | 24 | $O_3$, $N_2O$, CFC12, aerosols |
| B | 1215 - 1500 | 12 | $N_2O$, $H_2O$, $CH_4$, $HNO_3$, $N_2O_5$ $ClONO_2$, $CF_4$, $COF_2$, HCN |
| C | 1570 - 1750 | 4 | $H_2O$, $NO_2$, $O_3$, $HNO_3$, NO |
| D | 1820 - 2410 | 4 | $CO_2$, CO, NO, $O_3$ $N_2O$, OH, $NO^+$ $H_2O$, OCS, $COF_2$ |

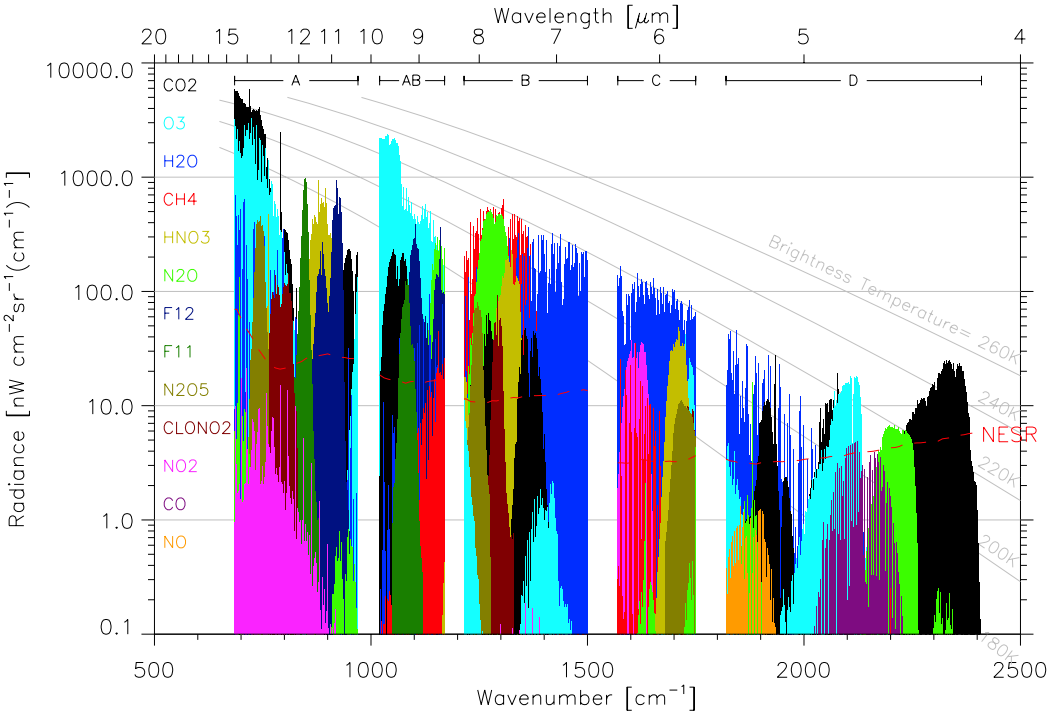


Figure 2.6: Contribution of different atmospheric constituents within MIPAS filters at a tangent height of 12 km. The typical NESR is represent by the red dashed line (*Fischer et al.*, 2008).

The NESR ranges from 3 to 50 $nW/(cm^2\,sr\,cm^{-1})$, increasing with decreasing wavenumbers. Within each MIPAS band the NESR is also variable and its averaged value is shown on Table 2.1.

## 2.5. Observation capability and strategy

MIPAS observes the infrared emission of the limb of the atmosphere. The instrument points at a minimum altitude called tangent altitude, selected by the elevation mirror and which geographical location is determined by the azimuth mirror. Moreover, the elevation mirror corrects for platform attitude, orbital altitude and Earth's geoid geometry.

When the tangent point is fixed, the elevation mirror is actively controlled in order to keep the tangent altitude constant and then an interferometer sweep is acquired. A discrete variation of the elevation mirror orientation generates a limb sequence at different steps in tangent altitude. The limb sequence is performed scanning down from high to low altitudes, since the movement of the platform compensates that, the lower the tangent point is, the farther from the platform is (Figure 2.7) and, hence, an almost vertical sequence of tangent altitude points is obtained. There is a difference of about 500 km (this depends on the observation mode, see Table 2.2), in the direction of the satellite track (rearward direction) between the uppermost and lowermost measurements within a limb sequence. Roughly speaking, MIPAS can observe in an altitude range from 5 to 170 km with minimum and maximum steps of 1 and 8 km, respectively.

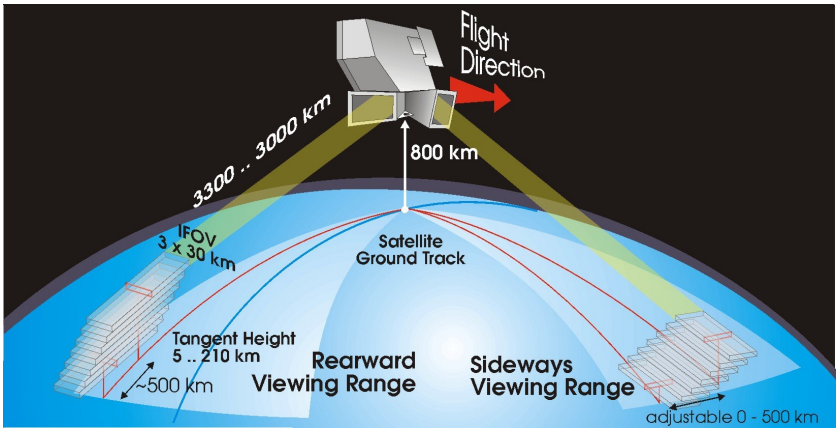


Figure 2.7: MIPAS observation geometry (ESA picture).

Operationally, MIPAS observes in the rearward direction, allowing the complete pole to pole coverage. This is achieved by changing the azimuth angle with respect to the rearward direction, moving the altitude point location away from the satellite ground track[2]. The observation in the sideways direction (cross-track) is reserved for special events, such as volcanic eruptions or for viewing parallel to the terminator. The

[2]The satellite ground track is limited to the region between, approximately, 80ºN to 80ºS, due to the inclination of the orbit.

spatial resolution, i.e., the field of view of the instrument is 30 km in the horizontal (perpendicular to the line of sight) and 0.9 mrad in the vertical direction, resulting in about 3 km width at the tangent point. This gives an air mass of around 400 km along the line of sight. The horizontal spacing between single measurements depends on the observation mode (see Table 2.2), ranging between 200-500 km.

ENVISAT follows a sun-synchronous orbit, with an orbital period of 100.6 minutes, i.e., more than 14 orbits per day (Figure 2.8). While a single full resolution (FR) spectrum was recorded in 4.5 s, the time for recording a optimized resolution (OR) spectrum is shortened to 2.1 s. The number of limb sequences (scans) is usually larger than 1000 per day. The temporal resolution that MIPAS offers is optimal for time scales of days, seasons and years, allowing to study short and mid term radiative, chemical and dynamical atmospheric processes. Time scales of hours are difficult to be resolved, since there are only two local times sampled per latitude and day.

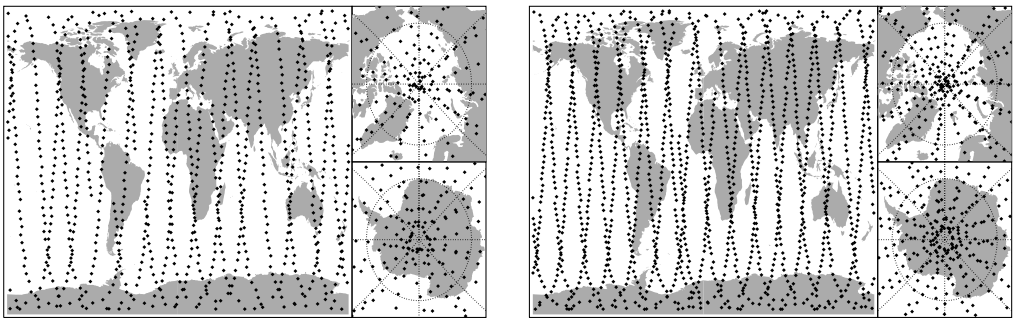

Figure 2.8: MIPAS spatial coverage for 1 day of measurements for *UA* (left) and *NLC* (right) observation modes. The smaller number of sweeps per scan in the *NLC* mode is reflected in more scans per orbit, i.e., a denser number of scans (profiles).

MIPAS measured its first interferogram on March 2002 and from September 2002 until the end of March 2004, it has been measuring almost continuously. Then, the measurements ceased due to the problem with the drive unit and they were resumed on January 2005 with the optimized spectral resolution and shorter measurement time. Along the year 2005, MIPAS duty cycle was restricted to 35 % and then increased gradually up to 100 % by December 2007 to present. Today, MIPAS is still measuring; the ENVISAT mission has been extended until end of 2013.

MIPAS spectra (*Level 1b*) are inverted to obtained atmospheric parameters (*Level 2*). The European Space Agency (ESA) carries out a near real time data processing, delivering profiles for pressure, temperature, water vapour, ozone, nitric acid, methane, nitrous oxide and nitrogen

dioxide for the nominal observation mode (*Raspollini et al.*, 2006). Complementary to this, there are other off-line data processors, such as the IMK/IAA processor developed at the Institut für Meteorologie und Klimaforschung (IMK) in collaboration with the Instituto de Astrofísica de Andalucía (IAA) (*von Clarmann et al.*, 2003b,a), the MORSE code developed at Oxford University and the GMTR code developed at Bologna University (*Carlotti et al.*, 2006). These off-line processors allow to derive atmospheric parameters beyond the ESA operational products[3]: extension of the altitude range for operational species, extension of number of species retrieved (see Table 2.1) and application to special observation modes (Section 2.6).

## 2.6. Observation modes

In order to achieve the numerous objectives of MIPAS, different modes of observation have been defined, attending to the altitude coverage or the vertical and horizontal spacing. Then, the modes are defined focused on specific atmospheric regions, like the upper troposphere, the middle atmosphere or the lower thermosphere, with an intended vertical sampling, the higher the better vertical resolution of the parameter profile. The optimized spectral resolution brought a redefinition of the observation modes (*Oelhaf*, 2008), since the time gained with faster scan records can be used for a finer vertical sampling, a larger coverage of altitude ranges or a finer along-track sampling. Following, a enumeration of observation modes for the 'OR' period is shown (see also Table 2.2).

*Nominal* (*NOM*). Its goal is to study the chemistry and transport of the upper troposphere and stratosphere, and to provide a data basis for climatology and trend analyses issues. It covers the upper troposphere, the stratosphere and the lower mesosphere (boundaries 6 - 70 km). A variable altitude grid is proposed, finer at the UTLS region (1.5 km) where the variability of the atmosphere is higher, and wider above (4 km), with 27 sweeps in total, in order to keep an along-track sampling of 410 km.

*Upper Troposphere Lower Stratosphere* (*UTLS*). Aimed to study processes at the UTLS region. As the nominal mode, the vertical sample grid is finer at the bottom (1.5 km) and wider above (5 km), but the altitude range is shorter, from upper troposphere to upper stratosphere (8-50 km). The amount of sweeps is 19, providing an along-track sample of only 290 km. There exists another UTLS sub-mode,

[3] Obtained with the Near Real Time retrieval processor developed by ESA, ORM, (*Ridolfi et al.*, 2000).

Table 2.2: MIPAS observation modes for optimized spectral resolution. Horizontal spacing and tangent heights are specified.

| **Mode** | **Nominal** | **UTLS-1** | **UTLS-2** | **MA** | **UA** | **NLC** | **AE** |
|---|---|---|---|---|---|---|---|
| **Horiz. spacing** | 410 km | 290 km | 180 km | 430 km | 515 km | 375 km | n/a |
| **Sweeps/Scan** | 27 | 19 | 11 | 29 | 35 | 25 | 12 |
| Scan #1 | 72 | 49 | 42 | 102 | 172 | 102 | 38 |
| Scan #2 | 67.5 | 44.5 | 37 | 99 | 167 | 99 | 33.5 |
| Scan #3 | 63 | 40 | 33 | 96 | 162 | 96 | 29 |
| Scan #4 | 59 | 35.5 | 29 | 93 | 157 | 93 | 24.5 |
| Scan #5 | 55 | 31 | 26 | 90 | 152 | 90 | 20 |
| Scan #6 | 51 | 28 | 23 | 87 | 147 | 87 | 17 |
| Scan #7 | 47 | 25 | 20 | 84 | 142 | 85.5 | 15 |
| Scan #8 | 44 | 23 | 18 | 81 | 137 | 84 | 13 |
| Scan #9 | 41 | 21 | 16 | 78 | 132 | 82.5 | 11.5 |
| Scan #10 | 38 | 19 | 14 | 75 | 127 | 81 | 10 |
| Scan #11 | 35 | 17.5 | 12 | 72 | 122 | 79.5 | 8.5 |
| Scan #12 | 32 | 16 | | 69 | 117 | 78 | 7 |
| Scan #13 | 30 | 14.5 | | 66 | 112 | 75 | |
| Scan #14 | 28 | 13 | | 63 | 107 | 72 | |
| Scan #15 | 26 | 11.5 | | 60 | 102 | 69 | |
| Scan #16 | 24 | 10 | | 57 | 99 | 66 | |
| Scan #17 | 22 | 8.5 | | 54 | 96 | 63 | |
| Scan #18 | 20.5 | 7 | | 51 | 93 | 60 | |
| Scan #19 | 19 | 5.5 | | 48 | 90 | 57 | |
| Scan #20 | 17.5 | | | 45 | 87 | 54 | |
| Scan #21 | 16 | | | 42 | 84 | 51 | |
| Scan #22 | 14.5 | | | 39 | 81 | 48 | |
| Scan #23 | 13 | | | 36 | 78 | 45 | |
| Scan #24 | 11.5 | | | 33 | 75 | 42 | |
| Scan #25 | 10 | | | 30 | 72 | 39 | |
| Scan #26 | 8.5 | | | 27 | 69 | | |
| Scan #27 | 7 | | | 24 | 66 | | |
| Scan #28 | | | | 21 | 63 | | |
| Scan #29 | | | | 18 | 60 | | |
| Scan #30 | | | | | 57 | | |
| Scan #31 | | | | | 54 | | |
| Scan #32 | | | | | 51 | | |
| Scan #33 | | | | | 48 | | |
| Scan #34 | | | | | 45 | | |
| Scan #35 | | | | | 42 | | |

with less sweeps and a subsequently reduced along-track sampling of 180 km, conceived to test 2D retrievals.

*Middle Atmosphere* (*MA*). It covers most part of the stratosphere, the mesosphere and the lower thermosphere (from 18 to 102 km) with 29 steps at a constant 3 km step size. The along-track sampling is about 430 km. This mode is dedicated to study linkages between the upper atmosphere and the stratosphere, i.e. the global circulation and transport from CO and $NO_x$ from the mesosphere down to the stratosphere in polar winter hemispheres, as well as Solar Proton Events affecting both the upper atmosphere and the stratosphere. The mode is also used to monitor the quality of operational retrievals that are neglecting non-LTE effects, such as the water vapour or ozone. The chemistry involved in the stratosphere and mesosphere can be also addressed.

*Upper Atmosphere* (*UA*). The *UA* mode covers the altitude region from 42 to 172 km with 35 scans. The step size is 3 km from 42 to 102 km, and 5 km above. The along-track sampling is about 515 km. This mode is mainly dedicated to measurements of the thermosphere, mainly temperature, NO and $CO_2$.

*Noctilucent Clouds* (*NLC*). This mode corresponds to the *UA* mode but is truncated at 102 km altitude. Instead, three additional layers at 79.5 km, 82.5 km, and 85.5 km are inserted (25 sweeps in total) in order to optimize the detection of noctilucent clouds which appear regularly in the polar summer mesopause region.

*Aircraft Emission* (*AE*). It is dedicated to the detection of aircraft emissions and their effects on the chemistry in the upper troposphere and lowermost stratosphere.

Currently, the nominal mode covers the 80% of the duty cycle and the *MA*, *NLC* and *UA* modes have a permanent presence in the MIPAS schedule (1 day each out of 10 for *MA* and *UA*, and 3 consecutive days in each solstice for *NLC*). The rest of modes are occasionally used.

## 2.7. MIPAS measurements analyzed in this work

The IMK/IAA retrieval processor (Section 4.3) has been applied to MIPAS measurements taken in its middle and upper atmosphere observation modes during the period of optimized spectral resolution. Thus, measurements from *MA*, *NLC* and *UA* modes between 2005 and 2009 have been processed. A list of days for each observation mode is summarized in Tables 2.3, 2.4, and 2.5. For the *MA* mode, there are 117 days, spread in 1452 orbits, i.e., 124168 scans (∼86 scans per orbit). In the case of *NLC* mode, there are 16 days, distributed in 219 orbits, turning into 21791 scans (∼100 scans per orbit). Finally, for the *UA* mode, there are

103 days, spread in 1233 orbits, resulting in 88155 scans (∼71 scans per orbit).

Table 2.3: MIPAS measurements in the *MA* mode for the period 2005-2009.

| | 2005 | 2006 | 2007 | 2008 | 2009 |
|---|---|---|---|---|---|
| January | 10, 11, 12, 13 | - | - | 8, 16, 26 | 1, 11 |
| February | - | - | - | 5, 15, 25 | 5, 15, 25 |
| March | 13, 14 | 19, 20 | 23 | 6, 16, 26 | 7, 17, 27 |
| | 27, 28, 29, 30 | - | - | - | - |
| April | - | - | 2, 12, 22 | 5, 15, 25 | 6, 16 |
| May | - | - | 4, 14, 25 | 25 | 6, 16, 26 |
| June | - | 21, 22 | 6, 7, 22 | 3, 25 | 5, 15, 25 |
| July | - | - | 25 | 15, 25 | 15, 25 |
| August | - | - | 4, 14, 24 | 4, 14 ,24 | 1, 11, 21 |
| September | - | 19, 20 | 3, 13 | 3, 13 | 10, 20, 30 |
| October | 29, 30, 31 | - | 3, 13 | 3, 13, 23 | 10, 20, 30 |
| November | - | - | 4, 14, 24 | 2, 12, 22 | 29 |
| December | 29, 30 | 19, 20, 21 | 9, 19, 29 | 2, 12, 22 | 15, 25 |

Table 2.4: MIPAS measurements in the *NLC* mode for the period 2005-2009.

| | 2005 | 2006 | 2007 | 2008 | 2009 |
|---|---|---|---|---|---|
| January | - | - | - | - | 5, 6, 7 |
| July | 19, 20, 21 | - | 4, 5, 14, 15 | 5, 6, 7 | 5, 6, 7 |

Table 2.5: MIPAS measurements in the *UA* mode for the period of 2005-2009.

| | 2005 | 2006 | 2007 | 2008 | 2009 |
|---|---|---|---|---|---|
| January | 21, 22 | - | - | 9, 17, 27 | 2, 12, 19, 20[†] |
| February | - | - | - | 6, 16, 26 | 6, 16, 26 |
| March | - | 21 | 22 | 7, 17 | 8, 18, 28 |
| April | 12, 13 | - | - | 6, 16, 26 | 7, 17 |
| May | - | - | - | 16, 26, 31 | 7, 17, 27 |
| June | - | 23 | 20, 21 | 9, 22 | 6, 16, 26 |
| July | 22 | - | - | 16, 26 | 16, 26 |
| August | - | - | - | 5, 15, 25 | 2, 12, 22 |
| September | - | 21 | 21, 22, 23 | 4, 14, 24 | 1, 11, 21 |
| October | 31 | - | - | 4, 14, 24 | 1, 11, 21, 31 |
| November | 1 | - | 5, 15, 25 | 3, 13, 23 | 30 |
| December | 31 | 22 | 10, 20, 30 | 3, 13, 23 | 10, 20, 30 |

[†]Days 14-18 and 21-27 have only 3 *UA* orbits (Delta-2 Campaign, see Section 6.6.2).

# Chapter 3

# Basics

*Abstract*

In this chapter, a theoretical treatment of the radiative transfer through the Earth atmosphere in the infrared part of the spectrum is presented. The notion of non-local thermodynamic equilibrium (non-LTE) is introduced and the inverse problem is addressed. Solutions for the forward and the inverse problems are posed.

## 3.1. Radiative transfer in the atmosphere

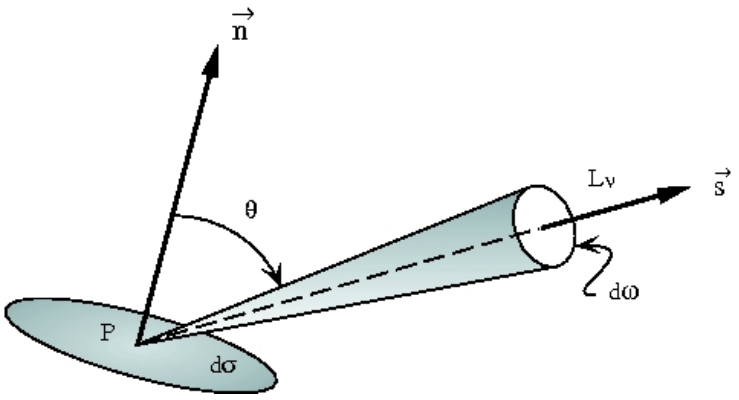


Figure 3.1: Radiance, $L_\nu$, at a point P.

The radiative field can be defined at a given point $P$ in the space as photons of all wavelengths travelling in all directions. The radiative field can be described with the concept of *radiance* (or *specific intensity*). The radiance, $L_\nu$, is just the amount of energy, $\mathrm{d}E_\nu$, within the frequency interval $(\nu, \nu + \mathrm{d}\nu)$, transported by the radiative field across an infinitesimal area, $\mathrm{d}\sigma$ (centered at $P$), along a direction $\vec{s}$ (that forms an angle $\theta$ with $\vec{n}$) and confined at a solid angle $\mathrm{d}\omega$ during

an infinitesimal time, $\mathrm{d}t$ (Figure 3.1 and Equation 3.1).

$$\mathrm{d}E_\nu = L_\nu(P,\vec{s})\cos\theta\,\mathrm{d}\sigma\,\mathrm{d}\omega\,\mathrm{d}\nu\,\mathrm{d}t \tag{3.1}$$

The amount of energy along the $\vec{n}$ direction is called the *radiative flux*, obtained by integrating the travelling pencils of radiation contained in $\mathrm{d}\omega$ over all $\vec{s}$ directions:

$$F_{\nu,n}(P) = \int_\omega L_\nu(P,\vec{s})\,(\vec{n}\cdot\vec{s})\,\mathrm{d}\omega \tag{3.2}$$

Since the flux depends on the direction of $\vec{n}$, it is a vector quantity. Considering a three-dimensional cartesian coordinate system $(x_1,x_2,x_3)$ of unit vectors $\{\vec{u}_1,\vec{u}_2,\vec{u}_3\}$, the flux is:

$$\vec{F}_\nu(P) = \sum_{i=1}^{3} F_{\nu,i}(P)\,\vec{u}_i, \tag{3.3}$$

with

$$F_{\nu,i}(P) = \int_\omega L_\nu(P,\vec{s})\,(\vec{s}\cdot\vec{u}_i)\,\mathrm{d}\omega. \tag{3.4}$$

The divergence of the radiative flux gives the net rate at which the energy per unit volume of the radiation field is increased or decreased. The latter is usually referred as the heating rate, $h_\nu$, since it is the amount of energy gained by the matter interacting with the radiative field:

$$h_\nu = -\vec{\nabla}\cdot\vec{F}_\nu(P) = -\int_\omega \left[\sum_{i=1}^{3}\frac{\partial L_\nu}{\partial x_i}\,(\vec{s}\cdot\vec{u}_i)\right]\mathrm{d}\omega = -\int_\omega \frac{\mathrm{d}L_\nu}{\mathrm{d}s}\,\mathrm{d}\omega. \tag{3.5}$$

In the presence of matter, the radiative field can be strengthened (by emission), weakened (by absorption), or redistributed (by scattering), although the latter can be considered negligible in the infrared part of the spectrum. In this context, the decrease of radiance when travelling across a medium along an infinitesimal path $\mathrm{d}s$ is, by virtue of Lambert's law, given by the absorption of radiation by matter:

$$\frac{\mathrm{d}L_\nu}{\mathrm{d}s} = -k_\nu\,n_a L_\nu, \tag{3.6}$$

and the increase in the radiance across the path $\mathrm{d}s$ is given by the emission:

$$\frac{\mathrm{d}L_\nu}{\mathrm{d}s} = j_\nu\,n_a, \tag{3.7}$$

where $n_a$ is the density of molecules along $\mathrm{d}s$ and $k_\nu$ and $j_\nu$ are, respectively, the absorption and emission coefficients, both characterizing the interaction between radiation and matter. These coefficients are related by the so-called *source function*, $J_\nu = \dfrac{j_\nu}{k_\nu}$, which allows to write

the change in radiance travelling in the direction of $\vec{s}$ at point $P$:

$$\frac{\mathrm{d}L_\nu(P,\vec{s})}{\mathrm{d}s} = -k_\nu\, n_a\, \left[L_\nu\left(P,\vec{s}\right) - J_\nu(P,\vec{s})\right]. \tag{3.8}$$

This is the *Radiative Transfer Equation* (RTE). Making use of the expression for the heating rate 3.5 and the definition of the radiative flux as a function of the radiance, the Equation 3.8 integrated over all solid angles can be written as:

$$h_\nu(P) = 4\pi k_\nu n_a \left(\bar{L}_\nu(P) - \bar{J}_\nu(P)\right), \tag{3.9}$$

being $\bar{L}_\nu$ and $\bar{J}_\nu$ the incident radiance and the source function averaged over all solid angles:

$$\bar{L}_\nu(P) = \frac{1}{4\pi}\int_\omega L_\nu(P,\vec{s})\,\mathrm{d}\omega \tag{3.10}$$

$$\bar{J}_\nu(P) = \frac{1}{4\pi}\int_\omega J_\nu(P,\vec{s})\,\mathrm{d}\omega. \tag{3.11}$$

Now, let's consider the optical path as shown in Figure 3.2. The RTE can be simplified by defining the *optical thickness* between two points, $s$ and $s'$ in the direction of $\vec{s}$:

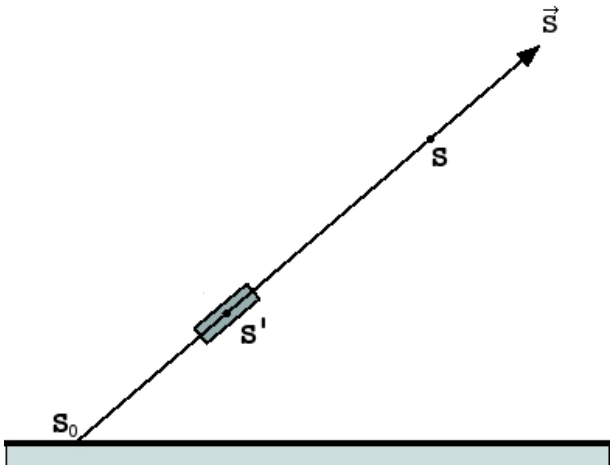


Figure 3.2: Optical path.

$$\tau_\nu(s,s') = \int_{s'}^{s} k_\nu(s'')\, n_a(s'')\, ds'', \tag{3.12}$$

where $s > s'$ by geometrical definition (Figure 3.2) and hence $\tau_\nu(s,s')$ is defined as a positive quantity. Besides, it is meaningful to choose the origin of $\tau_\nu$ at the top of the atmosphere. In consequence, the quantity

$\frac{\mathrm{d}\tau_\nu}{\mathrm{d}s}$ has a negative sign. Then, RTE can be written as:

$$\frac{\mathrm{d}L_\nu(s',s)}{\mathrm{d}\tau_\nu} = L_\nu(s',s) - J_\nu(s',s). \tag{3.13}$$

Now, the RTE admits an integrating factor $\mathrm{e}^{-\tau_\nu}$ and the equation can be, therefore, integrated between $s_0$ and the observation point,$s$, in the direction $\vec{s}$, giving the following **formal solution**:

$$L_\nu(s,\vec{s}) = L_\nu(s_0,\vec{s})\,\mathrm{e}^{-\tau_\nu(s_0,s)} + \int_{s_0}^{s} J_\nu(s',\vec{s})\,\mathrm{e}^{-\tau_\nu(s',s)}\,k_\nu(s')\,n_a(s')\,ds'. \tag{3.14}$$

Let's see the physical meaning of the solution. The first term represents the radiance from the boundary (the deep space, the Sun, the stars or the surface), $L_\nu(s_0,\vec{s})$, attenuated by the absorbing material between $s_0$ and the observation point, $s$; the second term stands for the emission from all the volume elements at positions $s'$ along the path, also attenuated by the matter between $s'$ and $s$.

Then, an accurate knowledge of the emitting and absorbing properties of the matter (the source function and the absorption coefficient), as well as its density, from the boundary to the observation point will allow to determine the monochromatic radiance. The formulation of analytical expressions for the source function and the absorption coefficient will be addressed in Section 3.3.2.

## 3.2. RTE for limb observations: the *forward problem*

It is of interest in the context of this work to characterize the general expression of RTE (Equation 3.14) in the particular case of remote sensing of limb atmospheric emission (Figure 3.3) by an instrument on a satellite platform like MIPAS. The limb radiance coming from a given tangent point measured by an instrument would be:

$$L(x_{obs},\vec{x}\,) = \int_{\Delta\nu} L_\nu(x_{obs},\vec{x}\,)\,f(\nu)\,\mathrm{d}\nu, \tag{3.15}$$

where $L_\nu(x_{obs},\vec{x}\,)$ is the monochromatic limb radiance emitted by the atmosphere and later measured at a given observation point $x_{obs}$, with $\vec{x}$ indicating the limb view direction. $f(\nu)$ is the instrumental response function over a finite range of frequency, $\Delta\nu$. For the case of limb viewing, the monochromatic radiance is derived from the formal solution (Equation 3.14) as follows: on the one hand, the radiance at the origin point, $x_0$, is just that coming from the space, therefore it can be considered negligible; on the other hand, the monochromatic *transmittance*

between $x$ and $x_{obs}$ is defined as:

$$\mathcal{T}_\nu(x, x_{obs}) = \exp\left[-\tau_\nu(x, x_{obs})\right] = \exp\left(-\int_x^{x_{obs}} k_\nu(x')\, n_a(x') dx'\right). \tag{3.16}$$

Then, the RTE in its integral form can be written as:

$$L_\nu(x_{obs}, \vec{x}\,) = \int_{x_0}^{x_{obs}} J_\nu(x)\, \mathrm{e}^{-\tau_\nu(x, x_{obs})}\, k_\nu(x)\, n_a(x)\, dx = \int_{x_0}^{x_{obs}} J_\nu(x) \frac{d\mathcal{T}_\nu(x, x_{obs})}{dx} dx, \tag{3.17}$$

again, dependent on the source function and the absorption coefficient.

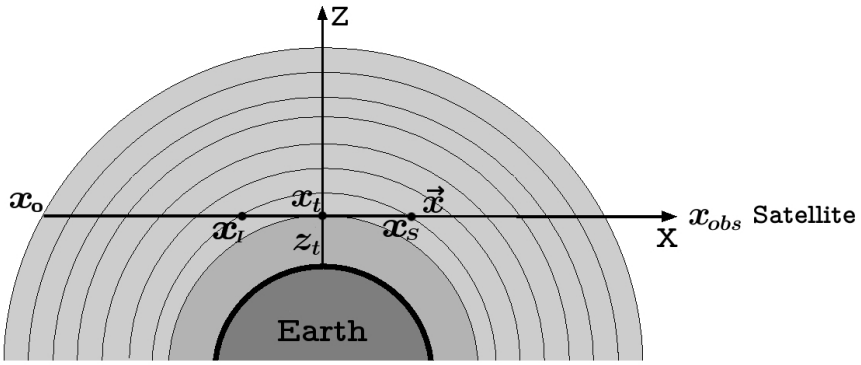


Figure 3.3: Geometry for limb observations.

Eventually, the limb radiance measured by an instrument on a satellite platform needs to be modelled by a numerical code. That is the so-called *forward problem*. In this case, it is helpful to divide the atmosphere in homogeneous concentric layers characterized by equivalent temperature, pressure, and density. There are different methods for calculating those equivalent quantities from the inhomogeneous atmosphere. One of the most commonly used is the Curtis-Godson approximation (*Curtis*, 1956; *Godson*, 1953). Under this homogeneous assumption, the density of the absorbing gas, $n_l$, the absorption coefficient, $k_{\nu,l}$ and the source function, $J_{\nu,l}$, remains constant along every atmospheric layer $l$, between $x_I$ and $x_S$ (see Figure 3.3). Then, defining the optical mass or absorbing amount, $u_l$, in the direction of $\vec{x}$ as:

$$u_l(\vec{x}) = n_l\ (x_S - x_I)\,, \tag{3.18}$$

the optical thickness (Equation 3.12) of the layer $l$ in the direction of $\vec{x}$ can be written as:

$$\tau_{\nu,l}(\vec{x}) = \tau_{\nu,l}(x_I, x_S) = k_{\nu,l}\, u_l(\vec{x}) \tag{3.19}$$

With this approximation, the integral in the limb radiance equation (Equation 3.17) can be replaced by a sum over the atmospheric layers

and the monochromatic limb radiance measured by an instrument at $x_{obs}$ is:

$$L_\nu(x_{obs}, \vec{x}\,) = \sum_{l=0}^{N} \left[ J_{\nu,l} \left(1 - \exp\left(-k_{\nu,l}\, u_l(\vec{x})\right)\right) \prod_{j>l} \exp\left(-k_{\nu,j}\, u_j(\vec{x})\right) \right], \qquad (3.20)$$

where the layer $l = 0$ corresponds to $x_0$ in the Figure 3.3.

Note that for solving the forward model problem the source function $J_\nu$ needs to be known. In many practical problems it can be considered to be the Planck function at the local kinetic temperature but, for the general case, when non-LTE occurs, it has to be calculated previously. In the next section, all these concepts are described, as well as how the source function can be calculated.

## 3.3. The source function

An ideal, closed and isolated atmospheric gas parcel composed of atoms and molecules eventually becomes to a state of *Thermodynamic Equilibrium* (TE) and its macroscopic properties can be described solely by its temperature, $T_k$. A situation of TE fulfill the following statements:

* the atomic and molecular motion follows the classical Maxwellian statistics, with:

$$n\,\mathrm{d}v = 4\pi N \left(\frac{m}{2\pi k T_k}\right)^{3/2} v^2 \exp\left(-\frac{m v^2}{2 k T_k}\right) \mathrm{d}v \qquad (3.21)$$

and

$$E_k = \frac{3}{2}\, k T_k, \qquad (3.22)$$

where $n\,\mathrm{d}v$ is the number of particles with a velocity between $v$ and $v+\mathrm{d}v$, $N$ is the total number of particles, $m$ is the mass of a single particle, $E_k$ is the mean kinetic energy of the molecules and $k$ is the Boltzmann constant;

* the distribution of the atomic and molecular populations within the energy states (electronic, vibrational and rotational) is given by the *Boltzmann's law*:

$$\frac{n_i}{n_j} = \frac{g_i}{g_j} \exp\left(-\frac{E_i - E_j}{k T_k}\right), \qquad (3.23)$$

where $i$ and $j$ are states with respective populations $n_i$ and $n_j$, degenerations[1] $g_i$ and $g_j$ and energies $E_i$ and $E_j$;

* the radiative field, $L_\nu$, equals the source function, $J_\nu$, i.e., the

[1] An energy level is said to be degenerate when it has more than one associated state.

absorbed monochromatic radiance is entirely emitted (*Kirchhoff's law*). Planck gave an analytical expression for it, the *Planck function*:

$$J_\nu = B_\nu(T_k) = \frac{2h\nu^3}{c^2}\frac{1}{\exp\left(\frac{h\nu}{kT_k}\right) - 1}, \tag{3.24}$$

being $h$ the Planck's constant and $c$ the speed of light.

The TE ensures that the radiative properties of the matter depends solely on the kinetic temperature, and that the translational energy of particles responds to an external change faster than the internal energy states, so that the Maxwellian distribution of the particles in the gas parcel is kept.

It is clear that the Earth atmosphere is not in TE, since it is in constant change, by exchanging radiation and matter, or energy through collisions between molecules or chemical processes. Thus, the temperature $T_k$ given by the TE cannot be constant with altitude. However, **locally**, TE may be defined assuming a kinetic temperature, $T_k(z)$, at each atmospheric altitude, $z$. This is the so-called *Local Thermodynamic Equilibrium* (LTE) approach. Under this hypothesis, the properties acquired by the TE are preserved, in particular the *Boltzmann's law* (Equation 3.23), except that the radiative field is not necessarily described by the Planck function ($L_\nu \neq B_\nu$). As a consequence, the monochromatic radiative equilibrium is not imposed, and a net gain (heating) or loss (cooling) of radiative energy is possible, as it is demonstrated by the heating rate expression (Equation 3.9).

In practice, LTE conditions can be assumed when the collisions between atmospheric molecules are so frequent that any change in the internal energy of the molecules is responded by a redistribution of their kinetic energy among their states. Hence, their energy level populations are controlled by the local kinetic temperature, as defined by the Maxwellian statistics of motion (Equations 3.21 and 3.22). The energy levels are, then, thermalized.

### 3.3.1. LTE breakdown

Actually, in a real atmosphere, collisions with transfer of kinetic energy, i.e., *thermal collisional processes*, those that lead to the LTE, are not the only kind of processes that molecules undergo. Apart from the *radiative processes*, i.e., spontaneous and induced emissions and absorption, there exists *non-thermal processes* that also contribute to populate or depopulate the energy levels (Figure 3.4). Processes of this nature are: *a)* collisions involving exchange of vibrational energy (so-called V-V processes); *b)* collisions involving electronic relaxation

for one molecule and vibrational excitation for the partner (E-V processes); *c)* chemical recombination, i.e., the production a vibrational excited molecule from released energy in a chemical reaction, like the NO production in the thermosphere; *d)* photochemical reaction, like the $NO_2$ photolysis as a source of stratospheric NO; *e)* dissociative recombination (e.g. $O_2^+ + e^- \rightarrow O^* + O$); and *f)* collisions with charged particles, like during auroral or proton events. When the radiative and/or non-thermal processes become comparable to thermal collisions or more important than them, the energy level (vibrational or rotational) populations are not controlled by the kinetic temperature anymore, but by an *excitation* temperature, $T_{\nu,r}$. Under these conditions the populations of the energy level are also given by the Boltzmann equation 3.23 but replacing $T_k$ by $T_{\nu,r}$, and it is said that the energy level is in *Non-Local Thermodynamic Equilibrium* (non-LTE), i.e.,

$$\frac{n_{\nu,r}}{n_0} = \frac{g_{\nu,r}}{g_0} \exp\left(-\frac{E_{\nu,r}}{kT_{\nu,r}}\right), \tag{3.25}$$

where index $0$ denotes the fundamental vibrational level.

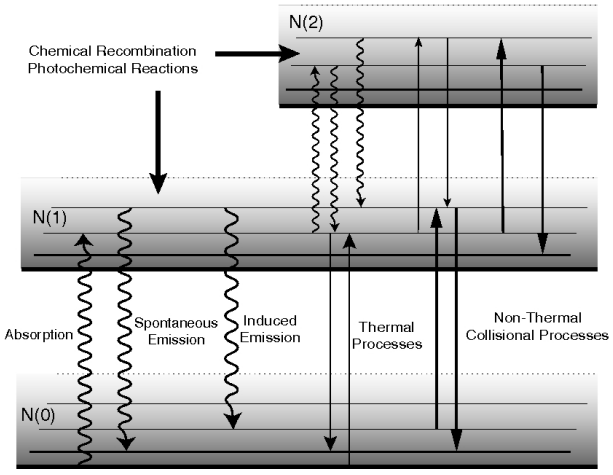


Figure 3.4: Processes affecting the populations of vibrational levels in the atmosphere.

The classic scenario for a non-LTE situation is an atmospheric region with such a pressure that the thermal collisions do not compensate the energy loss by spontaneous emission and a given excited level is populated under its LTE values. It is expected, then, that non-LTE effects become important at increasing low-pressure altitudes. Usually, the non-LTE affects the high-energetic (i.e., vibrational, electronic) levels of atmospheric molecules. There are numerous examples, like the $CO_2$ 15 $\mu$m fundamental band above 90 km, the $H_2O$ 6.3 $\mu$m band above 40 km, the $O_3$ 10 $\mu$m hot bands at 30-40 km or NO 5.3 $\mu$m fundamental band from 20 km. In

addition, higher up, at thermospheric altitudes, the non-LTE effect may be present also in rotational levels populations, despite the fact that a rotational transition implies small energy jumps. In such scenario, the density (pressure) is so low that thermal collisions cannot compensate the radiative losses. Other non-LTE scenarios are given when an excited level is overpopulated due to absorption of radiation (coming from the Sun or from other warmer regions of the atmosphere) or due to chemical production (like NO excited ro-vibrational levels in the thermosphere). Further information on non-LTE situations can be found in *López-Puertas and Taylor* (2001).

The atmospheric infrared emissions from vibrational bands of important molecules may be affected by non-LTE, specially at mesospheric and thermospheric altitudes. Since these emissions are analyzed in order to derive temperature and gas abundances, the processes that populate the vibrational and rotational levels need to be known, understood and modelled as accurate as possible.

### 3.3.2. Solving the radiative transfer and statistical equilibrium equations

It has been said in Section 3.1 that, in order to calculate the radiance emitted from the atmosphere (and eventually measured by an instrument in the space), it is necessary to have previous knowledge on the source function and the absorption coefficient (see Equations 3.14 and 3.17). These quantities are characterized in this section.

Since the purpose of this section is to be illustrative, let's consider a simple case[2]: a sample of gas interacting with a radiative field $L_\nu$. This gas is composed of molecules characterized by an emission (or absorption) band centered at $\nu_0$, which connects two vibrational levels (subindices 1 and 2 denote lower and upper vibrational level, respectively) with a rotational structure. The interaction between the radiative field and the molecules is described by three processes: spontaneous emission, induced emission and absorption, characterized by their respective Einstein coefficients: $A_{21}$, $B_{21}$ y $B_{12}$. These coefficients depend upon the quantum properties of the molecules and transition and they are independent of the radiative field. Therefore, if a LTE state is assumed, the following statements are satisfied: *a)* the rate of photons emitted per volume in the frequency interval $[\nu, \nu + \mathrm{d}\nu]$ by the molecules equals that of absorbed photons,

$$n_2\, A_{21}\, q_{r,s}(\nu - \nu_0) + n_2\, B_{21}\, \bar{L}_\nu\, q_{r,i}(\nu - \nu_0) = n_1\, B_{12}\, \bar{L}_\nu\, q_{r,a}(\nu - \nu_0), \qquad (3.26)$$

being $q_{r,s} = \dfrac{n_{2,J}}{n_2}$, $q_{r,i} = \dfrac{n_{2,J'}}{n_2}$ and $q_{r,a} = \dfrac{n_{1,J''}}{n_1}$ normalized factors for ro-

[2] *López-Puertas and Taylor* (2001) contemplates a multilevel case.

tational distributions of the involved vibrational levels, with $n_{\nu,J}$ the population of the rotational level $J$ of the vibrational level $\nu$; *b)* the ratio of the vibrational populations is given by Boltzmann law and *c)* the radiative field, $\bar{L}_\nu$, is determined by the Planck function, $B_\nu$. Then, the Einstein coefficients are related as:

$$\frac{A_{21}\, q_{r,s}}{B_{21}\, q_{r,i}} = \frac{2h\nu_0^3}{c^2} \quad \text{and} \quad \frac{B_{12}\, q_{r,a}}{B_{21}\, q_{r,i}} = \frac{g_2}{g_1}\exp\left(\frac{h(\nu-\nu_0)}{kT}\right). \tag{3.27}$$

Now, assuming that the rotational transitions have the same frequency $\nu_0$ (the band does not extend over a long spectral interval) and that the two vibrational levels have the same rotational state distribution, i.e., $q_{r,s} = q_{r,i} = q_{r,a}$, the usual **Einstein relations** are obtained:

$$\frac{A_{21}}{B_{21}} = \frac{2h\nu_0^3}{c^2} \quad \text{and} \quad \frac{B_{12}}{B_{21}} = \frac{g_2}{g_1} \tag{3.28}$$

When a radiative field $L_\nu$ interacts with matter, the difference between the photons emission rate (proportional to the upper level population) and the photons absorption rate (proportional to the lower level population) can be written as the change in the radiance (in number of photons) along a path $\mathrm{d}s$ and over a solid angle $\mathrm{d}\omega$ as:

$$\frac{1}{h\nu}\frac{\mathrm{d}L_\nu}{\mathrm{d}s}\mathrm{d}\omega = \left(n_2 A_{21} + n_2 B_{21} L_\nu - n_1 B_{12} L_\nu\right)\frac{\mathrm{d}\omega}{4\pi}, \tag{3.29}$$

which is analogue to Equation 3.8. If the Einstein relations (Equation 3.28) are used in Equation 3.29 and then compared to Equation 3.8, expressions for the absorption coefficient, $k_\nu$, and for the source function, $J_\nu$, at a given frequency $\nu$ are found:

$$k_\nu = \frac{h\nu}{4\pi}\frac{n_1}{n_a}B_{12}\left(1 - \frac{g_1}{g_2}\frac{n_2}{n_1}\right) \tag{3.30}$$

$$J_\nu = \frac{2h\nu^3}{c^2}\left(\frac{g_2}{g_1}\frac{n_1}{n_2} - 1\right)^{-1}. \tag{3.31}$$

In situations where the width of the ro-vibrational band cannot be considered negligible, its corresponding absorption coefficient is defined by the *band strength*:

$$S = \int_{\Delta\nu} k_\nu \,\mathrm{d}\nu \tag{3.32}$$

It is clearly seen, for both absorption coefficient and source function, their dependence on the ratio of the populations of two vibrational levels. In LTE conditions, the population ratio is a function of kinetic temperature, by Boltzmann's law (Equation 3.23). Therefore, the absorption coefficient depends solely upon the kinetic temperature and the source function identifies with the Planck function. But when non-LTE

arises, the population ratio needs to be characterized by taking into account the processes that populates and depopulates the vibrational levels involved. These are:

i) radiative: spontaneous and induced emission and absorption. The number of molecules radiatively excited up to level 2 from level 1 per unit volume is expressed as: $B_{12}\, n_1\, \bar{L}_\nu$, and those de-excited to level 1 are: $A_{21}\, n_2 + B_{21}\, n_2\, \bar{L}_\nu$.

ii) thermal collisions (or vibrational-translational, V-T, processes) of the form:

$$k_t: \quad n_2 + M \rightleftharpoons n_1 + M + h\nu_0, \tag{3.33}$$

being $M$ any molecule (typically $O_2$, $N_2$ or O in Earth atmosphere) and $k_t$ the collisional rate. The number of molecules de-excited from level 2 to level 1 by thermal collisions are: $l_t = k_t\,[M]$, while the excitations from 1 to 2 are: $p_t = k'_t\,[M]$. $k'_t$ is just the inverse collisional rate, given by:

$$k'_t = k_t\, \frac{g_2}{g_1} \exp\left(-\frac{h\nu_0}{kT}\right) \tag{3.34}$$

iii) non-thermal collisional processes; for example, V-V processes:

$$k_{vv}: \quad n_2 + M(\nu) \rightleftharpoons n_1 + M(\nu') + \Delta E, \tag{3.35a}$$

being $\nu$ and $\nu'$ two vibrational levels of the molecule $M$ separated by a vibrational energy gap $E_{\nu'} - E_\nu$, and $\Delta E = E_2 - E_1 + (E_{\nu'} - E_\nu)$; or chemical productions:

$$k_c: \quad A + B + M \rightarrow n_2 + M. \tag{3.35b}$$

The molecules excited in level 2 due to these non-thermal processes can be written as: $p_{nt} = k'_{vv}\,[M(\nu')] + \dfrac{1}{n_1} k_c\,[A][B]$, and the de-excitations to level 1 by: $l_{nt} = k_{vv}\,[M(\nu)]$.

Then, a conservative principle of steady state conditions is imposed for the populations of $n_1$ and $n_2$, by which the level excitations must be balanced with the de-excitations (see Figure 3.4). This is the *Statistical Equilibrium Equation* (SEE) or *Detailed Balance*, given by:

$$n_1 \left(B_{12}\bar{L}_\nu + p_t + p_{nt}\right) = n_2 \left(B_{21}\bar{L}_\nu + A_{21} + l_t + l_{nt}\right), \tag{3.36}$$

where the left (right)-hand term denotes the production (losses) rate referred to the level $n_2$. Hence, the population ratio can be generally written as:

$$\frac{n_2}{n_1} = \frac{B_{12}\bar{L}_\nu + p_t + p_{nt}}{A_{21} + B_{21}\bar{L}_\nu + l_t + l_{nt}}. \tag{3.37}$$

The RTE (Equation 3.14) and SEE (Equation 3.37) form a system of coupled equations. Since the posed problem is generally non-linear, there is no analytical solution and the system needs to be linearized.

The solution of the RTE is a very complicated task. Even for the simple case of 2 vibrational levels it has been seen above that in non-LTE conditions the population of the excited state, $n_2$, depends on the radiation field, $\bar{L}_\nu$ (Equation 3.37), which in turns depends on $n_2$ (Equations 3.14, 3.17), through the source function and, to a lesser extent, through the absorption coefficient. The general case takes into account: *(i)* the radiation exchange between different atmospheric layers and whenever is required, external radiation fields (terrestrial and solar); *(ii)* the frequency dependence of the absorption coefficient, which includes a large number of ro-vibrational lines with shapes that vary with temperature and pressure; and *(iii)*, all the processes, thermal and non-thermal, that affect the ro-vibrational states of the molecules. Therefore, the full solution of the RTE requires its integration over frequency, solid angle and altitude.

A very common technique that deals with these integrations is called *flux formulations*[3]. It is based on the calculation of net exchange of radiation between atmospheric layers, which enters into the calculation of the heating rates and the excitation of the upper state by radiative exchange. The **Curtis matrix method** is a flux formulation by which the coupled system RTE+SEE is solved over altitude by matrix inversion.

The method divides the atmosphere in homogeneous layers characterized by mean values for density, pressure and temperature, i.e., by using the Curtis-Godson approximation. For each layer, the RTE and SEE are posed, as well as the heating rate.

Considering the two-level approach, the source function for the band, $2 \rightarrow 1$, centered in $\nu_0$ is re-written by substituting the SEE in Equation 3.31 and using the Einstein relations (Equation 3.28) and the Planck function (Equation 3.24):

$$J_{\nu_0} = \frac{\bar{L}_{\Delta\nu} + \varepsilon_1 B_{\nu_0}}{1 + \varepsilon_2}, \tag{3.38}$$

where

$$\varepsilon_1 = \frac{p_t + p_{nt}}{A_{21}} \frac{g_1}{g_2} \left[ \exp\left(\frac{h\nu}{kT_k}\right) - 1 \right] \quad \text{and} \quad \varepsilon_2 = \frac{l_t + l_{nt}}{A_{21}} \left( 1 - \frac{p_t + p_{nt}}{l_t + l_{nt}} \frac{g_1}{g_2} \right), \tag{3.39}$$

and $\bar{L}_{\Delta\nu}$ is the mean radiance within the band (extended $\Delta\nu$). With the definition of the band strength, $S$ (Equation 3.32), the heating rate for the band is:

$$h_{12} = 4\pi S n_a \left( \bar{L}_{\Delta\nu} - J_{\nu_0} \right). \tag{3.40}$$

[3] See more details on this technique and others in *López-Puertas and Taylor* (2001).

Using this equation and substituting the mean radiative field in the Equation 3.38, the source function for the $i^{\text{th}}$ layer is expressed as:

$$J_{\nu_0,i} = \frac{\varepsilon_{1,i}}{\varepsilon_{2,i}} B_{\nu_0,i} + \frac{1}{4\pi S_i n_{a,i}\, \varepsilon_{2,i}} h_{12,i}. \tag{3.41}$$

On the other hand, the Curtis matrix method let the RTE to be expressed in terms of the heating rate as:

$$h_{12,i} = \sum_j C_{12,ij} J_{\nu_0,j} + \gamma_{12,i}\,, \tag{3.42}$$

where $C_{12,ij}$ is the ***Curtis matrix*** element. The off-diagonal element represents the radiative contribution of a given atmospheric layer $j$ to the net heating rate of the $i^{\text{th}}$ layer. The diagonal elements mean the cooling to space of the $i^{\text{th}}$ layer. $\gamma_{12,i}$ stands for the heating of $i^{\text{th}}$ layer by the outer limits of the atmosphere, i.e., Earth surface brightness or solar radiation.

The Equations 3.41 and 3.42 form the linear system to be solved for each atmospheric layer, being the heating rate (radiative transfer) and the source function (the population of the emitting level) the unknown quantities. Re-arranging for all altitudes:

$$\begin{aligned} \vec{h} &= \mathcal{C}\,\vec{J} + \vec{\gamma} \\ \vec{J} &= \mathcal{E}\,\vec{B} + \mathcal{D}\,\vec{h}, \end{aligned} \tag{3.43}$$

where $\mathcal{C}$ is the Curtis matrix and $\mathcal{E}$ and $\mathcal{D}$ are diagonal matrices: $\mathcal{E}_{i,i} = \dfrac{\varepsilon_{1,i}}{\varepsilon_{2,i}}$ and $\mathcal{D}_{i,i} = \dfrac{1}{4\pi S_i n_{a,i}\, \varepsilon_{2,i}}$. The boundary conditions for the system are: *1)* the lowermost layer's source function is Planck function at local $T_k$, and *2)* the gradient of the source function at the uppermost layer is considered negligible. From this system, the heating rate and the source function are solved simultaneously by inverting the Curtis matrix.

Curtis matrix inversion method is very useful when the atmospheric layers are radiatively coupled, i.e., the exchange of photons between layers is important; or when there are strong vibrational coupling between vibrational levels (V-V coupling) and the radiative transfer must be calculated accurately. For example, *López-Puertas et al.* (1986a,b, 1998a,b) use this technique for $CO_2$ vibrational bands. Alternately, an iterative technique is used in situations where the degree of coupling, radiative or V-V is weak or negligible. An example of the iterative technique is the **Approximate (or Accelerated) Lambda Iteration (ALI)** method, which defines an operator, $\Lambda$, so that when it is applied to the source function, $J_\nu$, the radiance, $L_\nu$ is obtained:

$$L_{\mu,\nu} = \Lambda_{\mu,\nu}\left[J_{\mu,\nu}\right], \tag{3.44}$$

where $\mu$ stands for the direction of a ray path and $[]$ means 'applied-to'. The method is based on the splitting of the lambda operator, i.e.

$$\Lambda_{\mu,\nu} = \Lambda^*_{\mu,\nu} + \left(\Lambda_{\mu,\nu} - \Lambda^*_{\mu,\nu}\right) \tag{3.45}$$

where the approximate lambda operator, $\Lambda^*_{\mu,\nu}$ is chosen so it can be quickly calculated while retaining most of the radiative exchange. With this approach, the iterative scheme is given by:

$$L^i_{\mu,\nu} = \Lambda^*_{\mu,\nu}\left[J^i_{\mu,\nu}\right] + \left(\Lambda_{\mu,\nu} - \Lambda^*_{\mu,\nu}\right)\left[J^{i-1}_{\mu,\nu}\right], \tag{3.46}$$

where $J^{i-1}_{\mu,\nu}$ is the source function of the previous iteration. In this way, a lambda operator can be chosen so that the RTE+SEE system can be solved *locally* at every altitude, using in each iteration the radiative field obtained in the previous iteration. A more thorough description of this method can be seen in *Rybicki and Hummer* (1991) and *Kutepov et al.* (1991).

Furthermore, a combination of Curtis matrix and lambda iteration methods can be used. For example, an iterative scheme can be proposed to calculate the populations of the emitting vibrational levels locally at every altitude, while the full radiative transfer in the form of Curtis matrix elements is calculated only in the first step or every few iterations.

In summary, the solution of the system RTE+SEE, necessary for knowing the radiative properties of the atmosphere (the source function and the absorption coefficient), also requires (as seen for the forward problem) an accurate treatment of the radiative transfer. Once the *forward problem* has been described and we know how to compute the source function and the absorption coefficient, the *inverse problem* is described in the next Section. The actual codes for modelling the radiative transfer (KOPRA), for calculating the non-LTE populations (GRANADA), and the retrieval code use to invert the MIPAS measurements are described later in Sections 4.1, 4.2 and 4.3, respectively.

## 3.4. The inversion

In the previous sections the forward problem has been described, that is, the calculation of the radiance emitted by any parcel in the atmosphere and eventually measured by an instrument on a satellite platform. There, the physical properties of the atmosphere are assumed to be known. The inverse problem deals with the opposite issue. The aim is to derive the physical properties of the atmosphere: density, pressure, temperature, gases abundances, when the measured radiance is known. Usually, the quantities to be retrieved are continuous functions, while the mea-

surements are always discrete quantities. Thus, most of the inverse problems are formally ill-posed (under-constrained). The degree of accuracy and the spatial resolution required for the scientific use of the retrieval will determine whether the problem is still under-constrained or not.

Let the RTE for limb observations (Equation 3.17) be expressed in a general form:

$$\vec{y} = \mathbf{F}(\vec{x}) + \vec{\varepsilon}, \tag{3.47}$$

being $\vec{y}$ a vector of measurements, for example, a spectra profile of dimension $m$; $\vec{x}$ is a vector with the physical parameter to retrieve, typically a profile of dimension $n$; $\mathbf{F}$ is a function, generally non-linear, representing the forward problem (radiance calculation), which depends on the retrieval parameter and encapsulates the physics of the measurement; and $\vec{\varepsilon}$ stands for the random (instrumental) errors of the measurement.

The theory of inversion (*Rodgers*, 2000) proposes a linearization of the radiative transfer problem with respect to a reference state, $\vec{x}_0$:

$$\vec{y} = \mathbf{F}(\vec{x}_0) + \frac{\partial \mathbf{F}(\vec{x})}{\partial \vec{x}}(\vec{x} - \vec{x}_0) + \vec{\varepsilon}, \tag{3.48}$$

where $\frac{\partial \mathbf{F}(\vec{x})}{\partial \vec{x}}$ is the so-called *Jacobian*, usually denoted as a matrix: $\mathbf{K} \equiv \frac{\partial \mathbf{F}(\vec{x})}{\partial \vec{x}}$ of dimensions $m \times n$. In this linear frame, $\mathbf{K}$ represents the mapping from the state space, $\vec{x}$, into the measurement space, $\vec{y}$, i.e., the act of measurement apart from the measurement error (the forward problem). The physical meaning of $\mathbf{K}$ is that it provides information on the dependence of the radiance on the retrieval parameters. The inverse problem is, therefore, that of finding an inverse mapping from the measurement space back into the state space. In the process of determining if there is a solution (unique or infinite) or not for the inverse problem, the rank of $\mathbf{K}$ is taken into account. Denoted by $p$, it represents the number of linearly independent rows (or columns) of $\mathbf{K}$, that is, there exists a state subspace of dimension $p$ so that only the components of the state vector which lie in it contribute to the measurement vector; in other words, there are only $p$ independent quantities or pieces of information that can describe the state. If it happens that $p < n$, there exists another state subspace, called *null space*, of dimension $n - p$, so that the components of the state vector that lie in it make no contribution to the measurement vector and therefore they cannot be determined by the measurements and they can take any value. When the dimension of the null space is greater than 0 it is said that the problem is undetermined. This is one of the most important aspects of the inverse problem.

A common way to proceed in the solution of the inverse problem is

to minimize the sum of the squares of the difference between the actual measurements and the forward problem using the solution, weighted with the measurement errors through its covariance matrix, $S_y$[4]:

$$\frac{\partial}{\partial \vec{x}} \left( [\vec{y} - \mathrm{F}(\vec{x})]^{\mathrm{T}} \; S_y^{-1} \; [\vec{y} - \mathrm{F}(\vec{x})] \right) = 0. \tag{3.49}$$

This minimization leads to an iterative solution for the retrieval parameter (or state vector):

$$\vec{x}_{i+1} = \vec{x}_i + \left( \mathbf{K}^{\mathrm{T}} \mathbf{S}_y^{-1} \mathbf{K} \right)^{-1} \times \left[ \mathbf{K}^{\mathrm{T}} \mathbf{S}_y^{-1} (\vec{y} - \mathbf{F}(\vec{x}_i)) \right]. \tag{3.50}$$

Knowledge on the components of the state vector lying in the null space is provided by the so-called *a priori* information, $\vec{x}_a$. It generally comes from climatological data (numerical models or datasets from instruments) and it is implemented in Equation 3.50:

$$\vec{x}_{i+1} = \vec{x}_i + \left( \mathbf{K}^{\mathrm{T}} \mathbf{S}_y^{-1} \mathbf{K} + \mathbf{R} \right)^{-1} \times \left\{ \mathbf{K}^{\mathrm{T}} \mathbf{S}_y^{-1} (\vec{y} - \mathbf{F}(\vec{x}_i)) - \mathbf{R} \; (\vec{x}_i - \vec{x}_a) \right\}, \tag{3.51}$$

where $\mathbf{R}$ is the *regularization* matrix. The regularization matrix can be chosen according to how accurate and close to the real solution the *a priori* information is. For instance, if there is certain *a priori* knowledge on the retrieval parameter, it is common to use the *maximum a posteriori* or *optimal estimation* method (*Rodgers*, 2000), where $\mathbf{R}$ is given by: $\mathbf{R} = \mathbf{S}_a^{-1}$, being $\mathbf{S}_a$ the covariance matrix of the *a priori* information (errors of the *a priori* values). This method constrains the solution to take values within the range of variability given by $\mathbf{S}_a$ and provides the best trade-off between the noise-induced retrieval errors (see Equation 3.57) and the smoothing errors (see Equation 3.59).

Another method for setting the regularization matrix is the Tikhonov formalism (*Tikhonov*, 1963), which express $\mathbf{R}$ as: $\gamma \mathbf{B}^{\mathrm{T}} \mathbf{B}$, where $\gamma$ is a factor that adjusts the weight of the measurements against the *a priori* information, and $\mathbf{B}$ is a matrix whose values depend on the order of the regularization. That is, a zero-order regularization (i.e., $\mathbf{B} = \mathbf{I}$) minimizes the square mean differences between the retrieved parameter, $\vec{x}$, and the *a priori*, $\vec{x_a}$. This order is useful when the inversion parameters are known to be close to the *a priori* values. A first-order regularization minimizes the derivative of the square mean differences between $\vec{x}$ and $\vec{x_a}$, so that:

$$\mathbf{B} = \begin{pmatrix} -1 & 1 & 0 & \dots \\ 0 & -1 & 1 & 0 \\ 0 & 0 & -1 & 1 \\ \dots & \dots & \dots & \dots \end{pmatrix}. \tag{3.52}$$

This order is preferable when the solution profile shape is expected to be

[4] The covariance matrix of a vector of random variables, $\vec{X} = \{X_1, \dots, X_n\}$ is defined as: $S_{ij} = cov\,(X_i, X_j) = \langle (x_i - \langle x_i \rangle)\,(x_j - \langle x_j \rangle) \rangle$, where $\langle\,\rangle$ denotes mean.

similar to the *a priori*'s. A second-order regularization, subsequently, minimizes the second derivative of the square mean differences between $\vec{x}$ and $\vec{x_a}$, and:

$$\mathbf{B} = \begin{pmatrix} -1 & 2 & 1 & \dots \\ 0 & -1 & 2 & 1 \\ 0 & 0 & -1 & 2 \\ \dots & \dots & \dots & \dots \end{pmatrix}. \tag{3.53}$$

This order ensures that the change in the profile shape of the solution (convexity) is like the *a priori*'s.

It should be noted that a zero-order regularization might introduce a bias of the retrieved quantity towards the *a priori* values, while Tikhonov regularizations of higher order avoid such a bias, at least on the scale of the expected vertical resolution of the retrieval. The regularization can be seen as a 'completion' function that uses the *a priori* information for filling the gaps or the space regions where there is no measurement, contributing to transform a discrete set of measurements into a continuous profile of a retrieved quantity.

The influence of the measurements, $\vec{y}$, on the retrieval parameters, $\vec{x}$, i.e., the mapping of a variation of the measurement $\vec{y}$ onto the vector of retrieved parameters $\vec{x}$ within the linear approximation is given by the *gain* matrix (*Rodgers*, 2000):

$$\mathbf{G} = \left(\mathbf{K}^{\mathrm{T}}\mathbf{S}_y^{-1}\mathbf{K} + \mathbf{R}\right)^{-1}\mathbf{K}^{\mathrm{T}}\mathbf{S}_y^{-1}. \tag{3.54}$$

The gain matrix allows to define the *Averaging Kernel* matrix, $\mathbf{A} = \mathbf{GK}$. In the case that $\vec{x}$ and $\vec{y}$ vectors represent vertical (altitude) profiles, the rows of the averaging kernel can be considered as 'smoothing' functions. They give the contribution to the information on $\vec{x}$ at a given altitude point coming from every point of $\vec{y}$. They are peaked functions, which full width at half maximum gives the vertical resolution of the observing system, thus providing a simple characterization of the relationship between the retrieval and the true state; in an ideal inversion, $\mathbf{A}$ would be the unit matrix. Averaging kernel rows enclose an area normalized to 1; in consequence, the retrieval is considered accurate at those altitudes where the averaging kernel is close to this value. In other words, $\mathbf{A}$ rows give a rough measure of the fraction of the information on the retrieved parameter that comes from the measurement rather than from the *a priori*. $\mathbf{A}$ columns represent the retrieval response at a given altitude point to a delta perturbation of the retrieval parameter profile. The amount of independent pieces of information on the retrieved parameter, or *degrees of freedom*, is quantified by the trace of the $\mathbf{A}$ matrix.

After a calculation of $\vec{x}_i$, the fit residuals are characterized by the

chi-square parameter, $\chi^2$:

$$\chi^2 = [\vec{y} - \mathbf{F}(\vec{x})]^{\mathrm{T}} \mathbf{S}_y^{-1} [\vec{y} - \mathbf{F}(\vec{x})] + (\vec{x} - \vec{x}_a)^{\mathrm{T}} \mathbf{R} (\vec{x} - \vec{x}_a) . \tag{3.55}$$

The closer to unity this parameter is, the more accurate the retrieval is.

In general, the solution of a linearized inverse problem which indeed is non-linear can be hard to reach. The Levenberg-Marquardt relaxation (*Levenberg*, 1944; *Marquardt*, 1963) forces the solution $\vec{x}$ to stay within the linear approximation by including a damping term, $\lambda\mathbf{I}$, in the Equation 3.51:

$$\vec{x}_{i+1} = \vec{x}_i + \left(\mathbf{K}^{\mathrm{T}}\mathbf{S}_y^{-1}\mathbf{K} + \mathbf{R} + \lambda\mathbf{I}\right)^{-1} \times \left[\mathbf{K}^{\mathrm{T}}\mathbf{S}_y^{-1}(\vec{y} - \mathbf{F}(\vec{x}_i)) - \mathbf{R}(\vec{x}_i - \vec{x}_a)\right] . \tag{3.56}$$

The convergence of the problem is accelerated. In every iteration, the parameter $\lambda$ is tuned as follows: if $\chi^2$ decreases $\lambda$ is decreased, otherwise, keeping $\vec{x}_i$ constant, $\lambda$ is increased until $\chi^2$ decreases; then, a new iteration starts and $\lambda$ is decreased.

From this formulation, retrieval errors due to instrumental noise are described by the random error covariance matrix:

$$\mathbf{S}_x = \mathbf{G}\mathbf{S}_y\mathbf{G}^{\mathrm{T}}, \tag{3.57}$$

which accounts for the contribution of the noise measurement at any altitude onto the random error of the state parameter at any other altitude. Retrieval errors due to uncertainties $\epsilon$ of the parameter $a_j$ used in the forward calculation are estimated by:

$$\Delta\vec{x}_j = \mathbf{G} \cdot [\mathbf{F}(\vec{x}, a_j + \epsilon) - \mathbf{F}(\vec{x}, a_j)] . \tag{3.58}$$

In addition, the choice of a suitable *a priori* information may influence the retrieved state parameter, particularly in cases where the information from the measurement is scarce. The mapping of the difference between the *a priori* assumption and the true state is the retrieval smoothing error. Its covariance matrix is defined as:

$$\mathbf{S}_s = (\mathbf{A} - \mathbf{I})\, \mathbf{S}_a\, (\mathbf{A} - \mathbf{I})^{\mathrm{T}} , \tag{3.59}$$

where $\mathbf{S}_a$ is the covariance matrix of the climatological *a priori* information. It was stated in the previous section that the discretization of the atmosphere is a very useful tool for the solution of the direct problem, and so it is for the inverse problem. In *Rodgers* (2000), various retrieval techniques are proposed. In this work, it has been applied a *Global Fitting*, which consists of a simultaneous retrieval in all the atmospheric layers where there is a measurement.

As seen above, in order to perform retrieval of atmospheric param-

eters it is necessary to have a precise inversion code that makes the best fit between measurements and calculations. This implies to have comprehensive radiative transfer and non-LTE models.

# Chapter 4

# Inversion scheme of MIPAS measurements

*Abstract*

In this chapter, the retrieval strategies to derive on the one hand, temperature profiles in the middle atmosphere, and on the other hand, temperature and nitric oxide mixing ratio jointly in the thermosphere from MIPAS spectra at 15 $\mu$m and 5.3 $\mu$m, respectively, are presented. Spectral windows selection, constraints, *a priori* information and NLTE modelling of the vibrational populations of $CO_2$ and NO responsible for the emissions at 15 $\mu$m and 5.3 $\mu$m, respectively, are described in detail. The chapter starts with the description of the numerical codes required for the simulation of the spectra, for the non-LTE modelling and for the retrieval of atmospheric parameters from MIPAS spectra.

## 4.1. A radiative transfer code: KOPRA

The retrieval of atmospheric state parameters from remote measurements depends on the accurate modeling of the atmospheric radiative transfer (forward problem). When the MIPAS experiment was launched it was decided in the Institut für Meteorologie und Klimaforschung (IMK), Karlsruhe, Germany, to develop a new radiative transfer code specially suited for the analysis of the data measured by MIPAS (*Stiller*, 2000). The Karlsruhe Optimized and Precise Radiative transfer Algorithm (KOPRA) was designed having in mind the observation scenarios and instrument characteristics of MIPAS. Also it was required to be flexible and well structured to make it easy to be integrated into an automated retrieval system. The Instituto de Astrofísica de Andalucía (IAA) has participated in the development of KOPRA mainly by the implementation of non-LTE.

KOPRA is able to calculate the infrared monochromatic radiance through the atmosphere for a wished spectral interval by using a line-by-line technique and using many observational geometries (e.g., limb,

nadir, balloon-looking, etc.). It can also compute quasi-analytically the jacobians (i.e., the derivatives of the radiance with respect to the atmospheric and instrumental parameters). In the context of MIPAS measurements of limb radiance, KOPRA discretizes the Equation 3.17 layer by layer in the way of Equation 3.20 (assuming the Curtis-Godson approximation) as follows:

$$L_\nu(x_{obs}) = \sum_{l=0}^{L} \frac{\sum_{ig} J_{l,ig} k_{l,ig} u_{l,g}(x)}{\sum_{l,ig} k_{l,ig} u_{l,g}(x)} \left[1 - \exp\left(-\sum_{ig} k_{l,ig} u_{l,g}(x)\right)\right] \prod_{j>l} \exp\left(-\sum_{ig} k_{j,ig} u_{j,g}(x)\right), \quad (4.1)$$

where $u_{l,g}$ is the absorbing amount of gas $g$, $k_{l,ig}$ is the absorption coefficient at frequency $i$ for gas $g$, and $J_{l,ig}$ is the source function at frequency $i$ for gas $g$, referred to the atmospheric layer $l$.

KOPRA is a very complete code. It calculates the ray tracing along the line of sight of the instrument MIPAS, taking into account the change in the refraction index and the oblateness of the Earth. It is also capable of accounting for the spectral response of the instrument (AILS) as well as its field of view with a selectable degree of accuracy. The spectral lines are modelled by a Voigt profile and the line-mixing effect in the $CO_2$ bands can also be included. The spectroscopic information comes from external databases, typically in HITRAN format (*Rothman et al.*, 2005). The most recent HITRAN database is normally used. The infrared emission of the terrestrial atmosphere is dominated by ro-vibrational lines, but there are other features considered by KOPRA: *1)* collision-induced absorption bands by interaction of pairs $N_2$-$N_2$ and $O_2$-$O_2$; *2)* superposition of line wings from strongly absorbing bands like $H_2O$ 6.3 $\mu$m or $CO_2$ 4.3 $\mu$m; *3)* the continuum-like contribution of heavy molecules: CFCs, acetone, PAN, $N_2O_5$ or formaldehyde, among others. All these contributions are treated as *continuum*.

KOPRA admits a large number of options, like the choice of the spectral resolution or the thickness of the atmospheric layers, the inclusion of horizontal inhomogeneities in temperature or gas abundances, the consideration of isotopes and non-LTE effects, different geometries or the accuracy in the calculation of absorption coefficients. The code allows to calculate the contribution of wished species and selected vibrational bands to the radiance for a given spectral region. KOPRA has also been validated against other forward codes (*von Clarmann et al.*, 2002). More details about KOPRA can be found on the KOPRA-IMK web site.

## 4.2. A non-LTE code: GRANADA

As mentioned above, KOPRA is able to calculate the contribution to the radiance of ro-vibrational bands which are affected by non-LTE. To do this, KOPRA needs the non-LTE populations of the emitter levels as input data. For this purpose, an additional and complementary numerical code was created.

The Generic RAdiative traNsfer AnD non-LTE population Algorithm (GRANADA) is a numeric code that calculates the non-LTE populations of the molecular vibrational and rotational levels. More precisely, it provides vibrational temperatures (excitation temperatures for vibrational levels) and population ratios, $n_{\nu,J}^{non-LTE}/n_{\nu,J}^{LTE}$. The input data are gas abundances and temperature profiles, as well as kinetic rates.

GRANADA solves the system RTE+SEE for the wished ro-vibrational levels and the bands generated between them. As exposed in Section 3.3.2, depending on the degree of coupling of the vibrational levels with the radiative field or with other vibrational levels through V-V exchange, one technique or another may be selected for solving the system of equations. This is supported by GRANADA, allowing to choose between inversion (Curtis matrix) or iteration (lambda iteration) techniques, or a combination of both. GRANADA allows the radiative transfer to be calculated either line-by-line or by statistical band methods.

The system RTE+SEE is solved along a selected altitude range and altitude grid, allowing flexibility on the processes involved (collisional, chemical, radiative, thermal or non-thermal), the participating species (and isotopes), their ro-vibrational energy levels, the bands to be included and the coupling between vibrational levels from different species like, for instance, the influence of vibrational exchange of $O_2$ or $N_2$ with $CO_2$, $H_2O$ or $CH_4$. The calculation of the RTE is based on the KOPRA code.

GRANADA also plays an important role in the retrieval of atmospheric state parameters, since it considers the possibility that the non-LTE populations, $n$, depend on the retrieval parameters $\vec{x}$. This is implemented by correction to the Jacobians calculated by KOPRA, as:

$$\mathbf{K} = \frac{\partial \mathbf{F}(\vec{x})}{\vec{x}} \mid_{n=constant} + \frac{\partial \mathbf{F}(\vec{x})}{\partial n} \times \frac{\partial n}{\partial \vec{x}}, \tag{4.2}$$

where the term $\frac{\partial n}{\partial \vec{x}}$ is calculated by GRANADA and $\frac{\partial \mathbf{F}(\vec{x})}{\partial n}$ is calculated by KOPRA.

In this work, GRANADA has been used for the analysis of the $CO_2$ and NO emission at 15 and 5.3 $\mu$m, respectively, measured by MIPAS, which are affected by vibrational (and rotational and spin in the case of NO) non-

LTE. The specifications of the non-LTE treatment for each species are described in detail in Sections 4.4.1 for $CO_2$ and 4.5.1 for NO.

Some aspects of the radiative processes, however, are common to both species. Thus, solar incoming fluxes at the top of the atmosphere are adapted from the SOLAR2000 solar irradiance model (*Tobiska et al.*, 2000), including modulations due to temporal variations of the Sun-Earth distance. Attenuation of the solar flux by Fraunhofer lines[1] is taken into account (*Hase et al.*, 2006). Tropospheric upwelling fluxes are calculated under consideration of surface emissions, tropospheric absorbing species and clouds, the latter characterized by the mean cloud top altitude and cloud coverage. Surface and cloud emissions are treated as blackbody radiation at the temperature of their respective height level.

## 4.3. The retrieval code: RCP

The Retrieval Control Program (RCP) is the inversion algorithm developed at IMK and complemented with the non-LTE treatment at IAA, designed for the retrieval of atmospheric parameters from MIPAS measurements. RCP requires the forward calculations from KOPRA (and from GRANADA if non-LTE processes are considered), the *a priori* information and the regularization matrix as input.

The diagram shown in Figure 4.1 constitutes the *IMK-IAA non-LTE retrieval scheme*. It comprises the forward calculations, i.e, the radiance calculation by KOPRA and, if necessary, the non-LTE populations of the vibrational states by GRANADA, the inversion algorithm described in Section 3.4 and the specifications on *a priori* information and on regularization constraints. It was developed as complementary to the retrieval algorithm used by the European Space Agency (ESA) for so-called operational near-real time data processing with the requirement to deliver pressure, temperature, and volume mixing ratio profiles of H2O, O3, HNO3, CH4, N2O, and NO2 within 3 hours after measurement taken in the MIPAS *Nominal* observation mode (*Ridolfi et al.*, 2000). The purpose of the IMK-IAA retrieval processor is to derive atmospheric parameters beyond the ESA operational data product, by extending the altitude of the operational products and the number of species to be retrieved, and being applicable to the special modes of MIPAS observations.

Back into the characteristics of RCP, it follows the least squares algorithm with a Levenberg-Marquardt relaxation technique (see Section 3.4), with the $\lambda$ parameter forced to be 0 in the last iteration. Given the initial solution (*initial guess*), which in some cases coin-

[1] Absorption lines present in the visible part of the solar spectrum, mainly produced in the solar atmosphere, although absorption lines of $O_2$ coming from Earth atmosphere are also found.

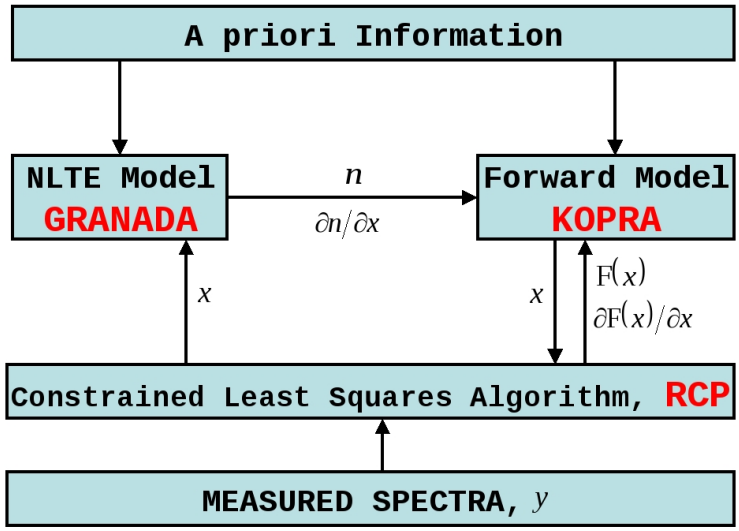


Figure 4.1: IMK/IAA non-LTE retrieval processor scheme.

cides with the *a priori*, the retrieval parameter is iterated by means of the Equation 3.56 until convergence is reached, i.e., when the difference between the measurement and the forward calculation using the result of the last iteration is lower than a fraction of the expected noise-induced retrieval error.

The type of regularization, as well as the *a priori* information used in the retrieval process depend on the specific atmospheric parameter to be retrieved. They are addressed in Sections 4.4 and 4.5 for the temperature in the middle atmosphere, and for temperature and NO in the thermosphere, respectively.

The retrieval processor is applied to MIPAS data, focused on specific small spectral regions called *microwindows*. Two reasons support this strategy: on the one hand, using small spectral regions saves computing efforts in the simulation of radiance with the forward model; and on the other hand, the high spectral resolution given by MIPAS allows to isolate the most prominent and the most useful transition lines that contain information on the retrieval parameter.

The use of these small windows also contributes to reduce the systematic errors, by avoiding important errors of this type, for example, temperature uncertainty through optically thick lines, abundances of other gases uncertainty through their contribution to the radiance or uncertainties in non-LTE parameters through spectral lines affected by non-LTE. On the other hand, the exclusion of spectral grid points worsens the random errors since the signal to noise ratio decreases.

An optimized tool for the selection of microwindows that minimizes the total retrieval error at each altitude has been developed, the *Karlsruhe*

*Occupation Matrix Algorithm* (KOMA) (*Echle et al.*, 2000; *von Clarmann and Echle*, 1998). Its basic requirement is to allow an optimal trade-off between random measurement errors and systematic errors. The selected microwindows have a typical width of 0.1-0.5 $cm^{-1}$. The width and the extension in altitude of every microwindow vary with tangent altitude in order to account for the variability of the sensitivity of spectral lines to the retrieval parameter. The collection of selected microwindows built up the so-called *occupation matrix* (OM).

Once the MIPAS measurements and the tools developed for their analysis have been described, one the major aims of this work is addressed: the inversion of kinetic temperature and nitric oxide volume mixing ratio (*vmr*) at thermospheric altitudes (100-170 km) from MIPAS *UA* observation mode measurements. Prior to this, and because it is wanted to retrieve NO *vmr* (not just number density), it is needed to retrieve the temperature in the region below, in the stratosphere and mesosphere. Hence, it will be first described the inversion of temperature an pointing (line of sight, LOS) in the next section, followed by the inversion for temperature and NO *vmr* in the thermosphere in Section 4.5.

There are, however, some common steps to both retrievals, aiming at minimizing the systematic errors, which need to be performed in an earlier stage. Thus, the retrieval process starts with a second spectral calibration of the *Level-1b* data, after that performed in the *Level-1b* processing (*Kleinert et al.*, 2007). Version 4.61/4.62 *Level-1b* have been used in this work. The spectral wavenumber shift is retrieved from spectra at around 40 km by using lines of $H_2O$, $CO_2$, $O_3$, $N_2O$, $CH_4$ and $HNO_3$, in the spectral range of 690 to 1800 $cm^{-1}$.

## 4.4. Temperature and pointing retrieval scheme

The retrieval scheme to derive temperature profiles and MIPAS altitude pointing (or Line of Sight), hereafter called TLOS retrieval scheme, was first applied to the *Nominal* observation mode on the full spectral resolution period, between 2002 and 2004 (*von Clarmann et al.*, 2003a). In this scheme, the used microwindows in the 15 $\mu$m spectral region contain $CO_2$ lines for a double reason: within the altitude range of the observation mode (6-70 km), $CO_2$ abundance is well known (*López-Puertas et al.*, 2000) and its emission can be assumed in LTE.

With the availability, since 2005, of new MIPAS observations in the middle atmosphere in optimized spectral resolution (see Section 2.6), the TLOS retrieval scheme has been reviewed (*von Clarmann et al.*, 2009). Among other improvements, the joint retrieval of horizontal temperature gradients in latitudinal and longitudinal directions has been incorporated. This approach avoids significant retrieval errors due to tem-

perature inhomogeneities along the line of sight (*Kiefer et al.*, 2010) and it has improved the accuracy of the retrieval as well as reduced the number of convergence failures.

Additional modifications to the retrieval setup of nominal observations are required in order to account for the extended altitude range of new (*MA*, *NLC* and *UA*) observation modes. These include: (i) the extension of the occupation matrix to altitudes up to 100 km; (ii) the inclusion of non-LTE modelling of $CO_2$ vibrational populations emitting near 15 $\mu$m, since they are not negligible at mesospheric altitudes (see Section 4.4.1); (iii) the adaptation of the microwindows to the new spectral resolution (see Section 4.4.2); (iv) a modified grid of the retrieval parameter vector; and (v) a modified *a priori* information on temperature and its horizontal gradients. Hence, nominally, the retrieval parameter vector includes, besides the temperature profile and the line of sight (LOS), the zero-offset radiometric calibration, the continuum contribution and the horizontal temperature gradients.

The temperature retrieval is performed on a 0-120 km altitude grid of 1 km step up to 50 km, 2 km steps between 50 and 100 km and 2.5-5 km above. The retrieval altitude grid is fine enough to provide a good trade-off between computational cost and the best accuracy in the radiative transfer calculations. A more precise altitude grid of 1 km step has been tested, yielding no improvement in the quality of the retrieval in terms of the $\chi^2$ (Equation 3.55). Due to the over-sampled retrieval compared to the tangent height spacing, the retrieval is regularized by a first-order Tikhonov-type constraint which adds to the objective function of the least squares fit a penalty keeping the temperature differences at adjacent altitudes reasonably small (*Tikhonov*, 1963; *Steck*, 2002). The strength of the regularization is altitude-dependent, allowing the best trade-off between the vertical resolution and retrieval error in every height.

The line of sight of MIPAS is retrieved as in the nominal setup, that is, the retrieval vector consists of the tangent altitudes of each limb scan. The LOS retrieval is constrained to engineering pointing information from ESA (and its uncertainties, i.e., 300 m between two successive tangent altitudes and $<$1.92 km in the absolute pointing (*Pellegrini*, 2003)) using a *maximum a posteriori* approach (*Rodgers*, 2000). Since independent spectral information on pressure (and hence LOS) is not available at mesospheric tangent heights, the retrieved relative tangent altitude spacing above 70 km is identical to that provided by the engineering pointing information. The pressure profile is hydrostatically adjusted within each iteration from the current guess of temperature profile and using a pair of pressure and geometrical altitude values, calculated from the European Center of Medium range Weather Forecast (ECMWF) meteorological analysis data. The reference altitude is usually

selected close to the lowermost tangent height of the given observation mode: ∼20 km for *MA* mode and ∼40 km for *NLC* and *UA* modes.

It has been noticed that the spectra below 32 km are affected by a continuum-like background contribution, mainly due to $H_2O$, $N_2$, $O_2$, $CO_2$, aerosols and clouds. This background may not be perfectly reproduced by the forward model and therefore it is retrieved in each microwindow for every altitude of the retrieval grid up to 32 km. The continuum is hard constrained to 0 above 32 km and regularized below by a Tikhonov-type constraint. For the *NLC* and *UA* observation modes, since their lowermost tangent height is near 40 km, the contribution of the continuum is not retrieved.

The zero-offset radiometric calibration is not perfectly known and therefore it is also retrieved. At lower altitudes, the offset information is largely correlated with the continuum but at tangent altitudes above 32 km, where the continuum is assumed to be zero, it is unambiguously contained in the spectra. For every microwindow, a value for the offset is retrieved at 40 km and assumed to be constant with altitude. The retrieval of this quantity is constrained to 0 with a zero-order regularization matrix.

The assumption of an homogeneous temperature field along the line of sight may not represent a realistic atmosphere. Regions where strong horizontal gradients in temperature may be expected, such as polar summer mesopauses, do need to take temperature gradients into account in the retrieval, otherwise large errors would be incurred. The latitudinal and longitudinal temperature gradients are retrieved on the same altitude grid as temperature. These zonal and meridional gradients are defined as a relative temperature change per kilometer in easterly and southerly directions, respectively, at the center of scan location and a given altitude. Temperatures along the LOS are corrected accordingly to these gradients during the ray-tracing process performed within the forward calculation of each retrieval iteration.

A priori temperature information below 60 km is taken from ECMWF reanalysis data. At higher altitudes, the *a priori* profiles are merged with NRLMSIS-00 model data (*Picone et al.*, 2002) extracted at the location and local time of the MIPAS observations and taking into account the actual solar-geomagnetic conditions. A priori profiles for latitudinal and longitudinal temperature gradients are calculated from ECMWF data below 60 km and are set to zero above. $CO_2$ abundances are assumed to be vertically constant below 35 km with a volume mixing ratio of 376 ppmv at the beginning of 2004 and a linear trend of 1.9 ppmv per year. This has been extracted from the monthly mean carbon dioxide data globally averaged over marine sites, as issued in September 2007 by NOAA (Pieter Tans, NOAA/ESRL, www.esrl.noaa.gov/gmd/ccgg/trends). Above 35 km, monthly zonal mean $CO_2$ abundances from WACCM simulations

(*Garcia et al.*, 2007), averaged over 2003-2004, are interpolated to the latitude and day of the year of the MIPAS observations. The same trend correction as above is then applied.

To conclude, the *initial guess* for all the retrieval parameters is equal to their respective *a priori* values.

### 4.4.1. Non-LTE model for $CO_2$

The radiance at 15 $\mu$m measured by MIPAS is caused mainly by deexcitations of vibrational levels of $CO_2$ molecules. It is essential, therefore, to know with the best accuracy as possible the population of such vibrational levels in order to retrieve accurate temperatures. In *von Clarmann et al.* (2003a) it is justified the assumption of LTE for MIPAS temperature and line of sight (TLOS) retrievals below 60 km, since the difference in the retrieved temperature when non-LTE is introduced remains smaller than 1 K. However, higher up, the processes (radiative and collisional) that populate and de-populate the vibrational levels can lead them to depart from LTE, and they must be taken into account in the MIPAS TLOS retrievals.

The calculations of $CO_2$ populations needed in the TLOS retrieval are performed with GRANADA (Section 4.2), which is run in every iteration during the retrieval process. The code calculates vibrational populations of the six most abundant $CO_2$ isotopes.

The setup of GRANADA for $CO_2$ populations used here takes into account 134 vibrational levels, including $O^{16}C^{12}O^{16}$ (isotope 626) levels up to $(070)$[2], $(061)$, $(032)$, and $(013)$; $O^{16}C^{12}O^{17}$ (isotope 627) levels up to $(040)$ and $(041)$; $O^{16}C^{12}O^{18}$ and $O^{16}C^{13}O^{16}$ (isotopes 628 and 636) levels up to $(030)$ and $(011)$; and $O^{16}C^{13}O^{17}$ and $O^{16}C^{13}O^{18}$ (isotopes 637 and 638) levels up to $(010)$ and $(001)$. Because of the strong collisional coupling of $CO_2$ with $N_2(v{=}1)$ via V-V energy transfer, the vibrational population of the latter is also included in the model. The $CO_2$ levels are connected by 695 radiative transitions, 39 of them considering full radiative transfer in the atmosphere. These 39 transitions involve vibrational states up to $(041)$ for the 626 isotope, $(030)$ and $(021)$ for the 627 isotope, and $(011)$ for the 628 and 636 isotopes. Above 20 km, radiative transfer is calculated using statistical band methods in the Curtis matrix formalism. Upwelling tropospheric fluxes at 20 km are calculated line-by-line, taking into account absorption by $H_2O$, $CO_2$, $O_3$ and $N_2O$. For the remaining 656 transitions (without consideration of atmospheric radiative trans-

[2]The Herzberg notation is used hereafter to refer to the $CO_2$ vibrational levels, i.e., $(v_1,v_2^l,v_3)$, where $v_1, v_2, v_3$ designate the level excited in the symmetric stretching, the bending and the asymmetric stretching modes, respectively, and $l$ is the vibrational angular momentum quantum number. Also the $CO_2$ isotopes are denoted with the last digit of the atomic weight of each atom, for example, 626 isotope for $^{12}C^{16}O_2$.

port), the radiative field is constrained by a top-of-the-atmosphere solar component and a tropospheric upwelling component at an estimated emission altitude.

The collisional scheme of $CO_2$ levels is based on *López-Puertas and Taylor* (2001) (see Table 6.2 therein). The current GRANADA setup for $CO_2$ has undergone important updates as a result of several analysis of SABER and MIPAS data (*López-Puertas et al.*, 2004, 2005c; *Kutepov et al.*, 2006; *García-Comas et al.*, 2008). These updates are discussed below.

The collisional deactivation of $CO_2(v_2)$ level by O, $k_O$,

$$CO_2(v_2) + O(^3P) \rightleftharpoons CO_2(v_2 - 1) + O(^3P),$$

is still a major uncertainty in the calculation of the populations of $CO_2(010)$ in the upper atmosphere and lower thermosphere. *García-Comas et al.* (2008) summarizes the existing literature about the values of the $CO_2$-O collisional rate. Values at 300 K range from 1.5 to $6 \times 10^{-12}$ $cm^3s^{-1}$, being the larger values deduced from atmospheric observations and the smaller obtained from laboratory measurements. In this work, this rate constant takes the value of $6 \times 10^{-12}$ at 300 K (*Sharma and Wintersteiner*, 1990), maintaining its temperature dependency:

$$k_O(v_2 = 1 \rightarrow 0) = 3.5 \times 10^{-13} \left[\sqrt{T} + 2.32 \times 10^{-9} \exp\left(\frac{-76.75}{T^{1/3}}\right)\right],$$

This rate is also being used in the current version of temperature retrieval from SABER (*García-Comas et al.*, 2008).

Another aspect which has been deeply revised here is the vibrational-vibrational (V-V) energy transfer of $CO_2$ $v_2$ quanta among the $CO_2$ levels of the same isotope,

$$CO_2(0, v_{2,e}, v_3) + CO_2(00^00) \rightleftharpoons CO_2(0, v_{2,e} - 1, v_3) + CO_2(01^10) + \Delta E,$$

where $v_{2,e}$ is the effective $v_2$ of the group (i.e. $v_{2,e} = 2v_1 + v_2$ ); and among different $CO_2$ isotopes $i$ and $j$:

$$CO_2^i(01^10) + CO_2^j(00^00) \rightleftharpoons CO_2^i(00^00) + CO_2^j(01^10).$$

A new V-V $v_2$ collisional scheme has been included which is based on the rate constants found by *Dang et al.* (1983) for the V-V exchange among $v_2 = 2$ and $v_2 = 1$. The scheme takes into account V-V exchange for levels with $v_{2,e} > 1$ within an isotope, with:

$$k_{vv}(v_{2,e}) = v_{2,e}\, 2.394 \times 10^{-11} \exp\left(\frac{-9.788\, c_1\, \Delta E}{T}\right),$$

with $c_1 = 1.439$. And for the V-V exchange between two different isotopes involving $v_2 = 1$: $k_{vv} = 2.35 \times 10^{-11}$ $cm^3s^{-1}$, consistent with the values

of *Dang et al.* (1983). The update in this V-V exchange results in a two times faster net exchange rate of $\upsilon_2$ quanta in $CO_2$-$CO_2$ V-V collisions (*López-Puertas et al.*, 2009a).

The values used for the V-T collisional relaxation of $CO_2$ $(0\upsilon_20)$ with $N_2$ and $O_2$, $k_{air}$,

$$CO_2(\upsilon_{2,e}) + N_2, O_2 \rightleftharpoons CO_2(\upsilon_{2,e} - 1) + N_2, O_2,$$

are taken from *Wintersteiner et al.* (1992), including their temperature dependence:

$$N_2: \; k_{air} = A\left[7 \times 10^{-17}\sqrt{T} + 6.7 \times 10^{-10}\exp\left(\frac{-83.8}{T^{1/3}}\right)\right]$$
$$O_2: \; k_{air} = A\left[7 \times 10^{-17}\sqrt{T} + 1.0 \times 10^{-9}\exp\left(\frac{-83.8}{T^{1/3}}\right)\right],$$

with $A = 1, 1.5, 1.5, 9/8$ for $\upsilon_2 = 1, 2, 3, 4$, respectively. However, no measurements were reported at temperatures below 150 K and the extrapolated values from measurements at higher temperatures resulted in very low values and hence very cold temperatures around the polar mesopause. Hence, a constant value of $10^{-15}\,cm^3s^{-1}$ has been assumed for temperatures below 150 K.

Further, the updated setup for $CO_2$ includes: 1) new rates for the relaxation of $CO_2$ 2.7 $\mu$m Fermi levels obtained from the analysis of MIPAS spectra (*López-Puertas et al.*, 2005c); 2) new rates for the V-V coupling of $CO_2(\upsilon_3)$ with $N_2$, including a larger excitation of $(001)$ at night through V-V exchange with $N_2(1)$ from the $OH(\upsilon)$ vibrationally excited (*López-Puertas et al.*, 2004); and 3) a new scheme for the relaxation of $CO_2(001)$ in collisions with $N_2$ and $O_2$ (see details of these updates in *García-Comas et al.* (2011)).

These updates in the collisional scheme for $CO_2$ in the current GRANADA setup introduce changes in the $CO_2$ vibrational populations which can be summarized as:

- Larger $k(CO_2(010)\text{-}O)$ collisional deactivation rate turns into more thermalized (larger) populations for $CO_2(\upsilon_2)$ levels at higher altitudes (above 90 km).
- The populations of the 15 $\mu$m hot and isotopic levels in the summer mesopause are generally closer to LTE and, hence, smaller because of the larger $k_{v v}(\upsilon_2)$ value used now.
- $CO_2(001)$ is more populated now in the daytime mesosphere because of weaker collisional reaction of $CO_2(001)$ with $M(N_2$ and $O_2)$ to relax to lower $CO_2$ $\upsilon_2 = 1, 2, 3, 4$ levels.
- Because of the process above, the $CO_2(040)$ levels have also changed

significantly their populations in the daytime mesosphere, being now significantly smaller.

The calculation of $CO_2$ vibrational populations requires additional information on atmospheric abundances of $H_2O$, $O_3$, $N_2O$, O, and $O(^1D)$, as well as tropospheric cloud conditions. $H_2O$ and $N_2O$ abundances are taken from the MIPAS IG2 climatology (*Raspollini et al.*, 2006). $O_3$ and O abundances are taken from 2D model calculations (*Garcia*, 1983) and are interpolated in latitude and day of the year to MIPAS measurement locations. O abundances above 80 km are taken from NRLMSIS-00 (*Picone et al.*, 2002). The sum of $O_3$ and O is then used in simple photochemical box model for the calculation of O and $O(^1D)$ abundances adjusted to the local time of MIPAS measurements. National Centers for Environmental Prediction (NCEP) clear-sky and all-sky OLR, and cloud fraction data, sampled at the measurement locations, are used for the determination of the effective cloud coverage and top height.

Figure 4.2 shows the excitation (vibrational) temperatures, $T_v$, (see Equation 3.25) of the most important $CO_2$ vibrational states that contribute to the MIPAS radiance spectra at 15 $\mu$m. On the one hand, the state $(01^10)$ responsible for the $\nu_2$ fundamental band, FB, $(01^10\text{-}00^00)$ for the main isotope (626) and the isotope 628. On the other hand, the states $(02^20)$ and $(10^00)$[3], responsible for the first hot bands, FH, $02^20\text{-}01^10$ and $10^00\text{-}01^10$, respectively, of the main isotope. Four typical scenarios are shown: mid-latitudes (day and night) and polar summer (day) and polar winter (night). These vibrational temperatures have been calculated with the non-LTE model for $CO_2$ described above. The behavior of such vibrational temperatures deserves a brief discussion.

Below the stratopause, around 50 km (not shown in the figures), the atmospheric density is high enough to make the thermal collisions (V-T) to be the dominant process and therefore, the populations of the vibrational levels are well described by the Boltzmann distribution at the corresponding $T_k$ and $T_v = T_k$. Higher up, in the mesosphere and lower thermosphere, the decrease of the density leads to less thermal collisions making the contribution of radiative processes and collisions with exchange of vibrational energy to become important in populating the vibrational levels.

The mid-latitude daytime case shows that the V-T processes are still important up to 70 km for the levels represented. The $(01^10)$ of the main isotope is quite close to LTE up to 90 km, while 626-(020) levels depart from LTE at 75 km and 628-(020) at 70 km. The population over LTE of the latter levels can be explained by the absorption of upwelling radiative

[3]This two states plus $(02^00)$ form the triad (020). These three states have very close energy levels and are considered in LTE among themselves since their V-T collisions with $N_2$ and $O_2$ are two orders of magnitude more efficient than V-V exchange (*López-Puertas and Taylor*, 2001). Hence, they show very similar populations.

flux coming from the warmer low mesosphere. The level 628-$(01^10)$ gives rise to an emission band weaker than that produced by 626-(020). This means that the former band becomes optically thin at lower altitudes in the mesosphere (at higher temperatures) than the latter. In consequence, the upwelling radiation due to the 628-FB comes from lower and warmer layers than that due to 626-FH and then the excitation by absorption of radiation is larger for 628-$(01^10)$ than for 626-(020). This is reflected in a larger $T_v$ for 628-$(01^10)$ compared to $T_v$ for 626-(020). The absorption of upwelling radiation from 626-FB hardly affects the $T_v$ of 626-$(01^10)$, rising it up near 2 K over $T_k$ at near 85 km. Above the mesopause at 90 km, all the plotted $T_v$ have a similar tendency: the difference with respect to $T_k$ becomes larger (in absolute values). At this altitudes, the excitation of vibrational levels by V-T collisions with atomic oxygen becomes important, although they cannot compensate the radiative loss to space. This explains that vibrational populations are depleted relative to their LTE values. The mid-latitude night case shows the same pattern described for the daytime. The only difference is the slightly smaller amplitude of the $T_v$-$T_k$ difference. In the nighttime non-LTE calculations, the daytime $T_k$ profile has been used. The larger daytime vibrational populations is due to vibrational energy exchange with level $(00^01)$, directly pumped by absorption of solar radiation at 4.3 $\mu$m (see *López-Puertas and Taylor* (2001)).

The vibrational temperatures for the polar summer case shows a similar behaviour than for mid-latitude but the non-LTE effects in the higher mesosphere are stronger. This is because: 1) the temperature at the stratopause is larger and hence, the absorption of upwelling radiation is larger, and 2) the temperature along the mesosphere is smaller and then the LTE values of the levels' populations are also smaller. The net effect is a larger deviation from the LTE populations for all vibrational levels shown.

The polar winter case is somewhat different from the other scenarios. First, the temperature at the lower mesosphere is colder, the $T_k$ negative gradient upwards is more irregular and less steep, and the mesopause is located at near 100 km. At the lower mesosphere, the colder temperatures makes the V-T collisions unable to compensate for the radiative loss in the case of 628-$(01^10)$, leading it to have under-LTE populations. Also, the upward radiative flux generated at these altitudes is smaller due to the lower temperatures, which, together with a smaller negative $T_k$ gradient, makes the absorption of upwelling radiation above 70 km smaller and, in consequence, the populations of 626-$(01^10)$ and 626-(020) to be under LTE. Above 85 km, the $T_v$-$T_k$ differences become less negative (or even positive) due to the excitation by V-T collisions with atomic oxygen, as explained above.

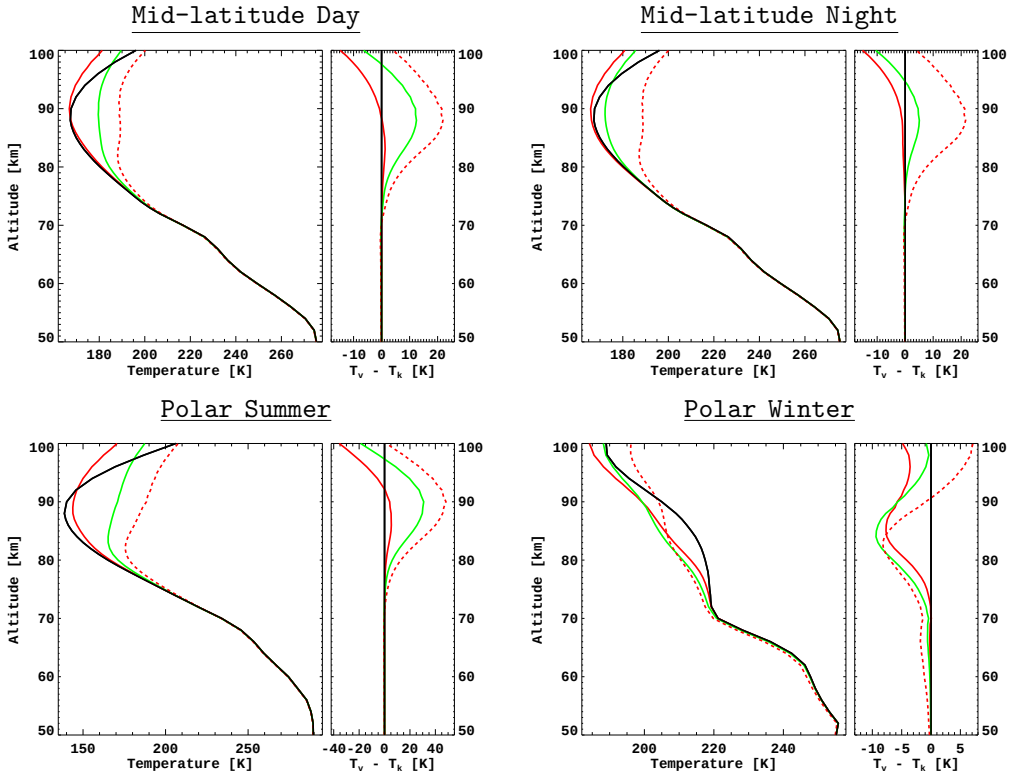


Figure 4.2: Vibrational temperatures of the main $CO_2$ vibrational levels responsible for the 15 $\mu$m emission falling into the selected microwindows. Four typical atmospheric cases are shown: mid-latitudes, day- and nighttime, polar summer and polar winter. Left panels show absolute profiles of the vibrational temperatures ($T_v$) for the levels: 626-($01^10$) (red); 626-(020) (green); 628-($01^10$) (red-dashed). Kinetic temperature, $T_k$, is also plotted (black). Right panels show the deviation of the $T_v$ with respect to $T_k$. Note the different scales used in the absolute profiles and in the $T_v$-$T_k$ differences for every scenario.

### 4.4.2. Occupation matrix

MIPAS channel A (685-970 $cm^{-1}$) contains plenty of information on $CO_2$ emission at 15 $\mu$m, therefore, the occupation matrix (OM) will be created out of this spectral range. The OM used in the TLOS retrieval from optimized resolution spectra (OR) for the *Nominal* and *UTLS* mode was created with KOMA, avoiding microwindows that contain spectral lines affected by non-LTE (OM-IMK) (*von Clarmann et al.*, 2009). Likewise, another OM was generated with KOMA for the middle and upper atmospheric modes, but this time assuming no LTE restriction (OM-IAA). The OM-IAA wisely keeps most of the microwindows from the OM-IMK for stratospheric altitudes but above, OM-IAA contains new microwindows with very strong emission features that ensures a good signal-to-noise ratio at upper mesospheric and lower thermospheric altitudes. In this way, the new microwindows include lines of $CO_2$ main isotope from the R-branch of its fundamental

band ($01^10$-$00^00$) in the 686-703 $cm^{-1}$ range (FB690) and from the strong Q branch[4] of hot bands emissions located at 720 $cm^{-1}$ (Q720, $10^00$-$01^10$), 740 $cm^{-1}$ (Q740, $03^10$-$02^20$) and 791 $cm^{-1}$ (Q791, $03^10$-$02^00$).

Table 4.1: Occupation matrix for TLOS retrieval scheme.

| Microwindow [$cm^{-1}$] | Altitude range [km] | Original OM | Strongest line[†] |
|---|---|---|---|
| (686.9375, 687.3750) | 45 - 50 | non-LTE | $01^10$-$00^00$ R24 |
| (687.0000, 687.3125) | 50 - 100 | non-LTE | $01^10$-$00^00$ R24 |
| (688.5000, 689.0625) | 42 - 100 | non-LTE | $01^10$-$00^00$ R26 |
| (690.1250, 690.6250) | 45 - 100 | non-LTE | $01^10$-$00^00$ R28 |
| (691.7500, 692.2500) | 40 - 100 | non-LTE | $01^10$-$00^00$ R30 |
| (699.8750, 700.2500) | 40 - 100 | non-LTE | $01^10$-$00^00$ R40 |
| (700.4375, 700.6875) | 60 - 70 | non-LTE | $01^10$-$00^00$ R40 |
| (701.5625, 701.8750) | 50 - 100 | non-LTE | $01^10$-$00^00$ R42 |
| (719.6250, 720.6875) | 32 - 40 | non-LTE | $10^00$-$01^10$ Q10-32 |
| (720.8125, 721.0000) | 32 | non-LTE | $10^00$-$01^10$ Q2-10 |
| (719.6250, 721.0625) | 40 - 100 | non-LTE | $10^00$-$01^10$ Q2-32 |
| (731.2500, 731.3750) | 20 - 40 | LTE | $01^10$-$00^00$ R78 |
| (731.5000, 731.8125) | 20 - 40 | LTE | $10^00$-$01^10$ R13 |
| (741.2500, 741.7500) | 32 - 40 | non-LTE | $11^10$-$02^20$ Q3-19 |
| (741.1875, 741.8125) | 32 - 70 | non-LTE | $11^10$-$02^20$ Q3-21 |
| (744.3125, 744.5000) | 20 - 40 | LTE | Continuum |
| (745.0625, 745.5000) | 20 - 40 | LTE | $10^00$-$01^10$ R31 |
| (748.9375, 749.1250) | 18 - 40 | LTE | Continuum |
| (749.5000, 749.8125) | 18 - 40 | LTE | $10^00$-$01^10$ R37 |
| (765.8750, 766.0000) | 20 - 40 | LTE | $11^10$-$02^20$ R32 |
| (766.1250, 766.1875) | 20 - 40 | LTE | $11^10$-$02^20$ R32 |
| (766.3750, 766.5625) | 20 - 40 | LTE | $11^10$-$02^20$ R31 |
| (780.4375, 780.6250) | 18 - 40 | LTE | $11^10$-$02^00$ P14 |
| (791.3750, 791.7500) | 20 - 62 | non-LTE | $11^10$-$02^00$ Q4-12 |
| (798.1250, 798.1875) | 20 - 35 | LTE | Continuum |
| (798.4375, 798.5000) | 20 - 40 | LTE | $11^10$-$02^00$ R8 |
| (810.8125, 811.0625) | 18 - 40 | LTE | $11^10$-$02^00$ R24 |
| (812.2500, 812.5625) | 18 - 40 | LTE | $11^10$-$02^00$ R26 |

[†]Of $CO_2$ main isotope.

Table 4.1 summarizes the set of microwindows used for TLOS retrieval, showing the most prominent transitions of the $CO_2$ main isotope, and Figure 4.3 illustrates the regions covered by the microwindows on MIPAS spectra. The microwindows which contain information on FB690 (686-701) are contaminated by hot bands contribution, like $02^20$-$01^10$ and $11^10$-$10^00$, and FB690 of $CO_2$ minor isotopes.

The resulting OM-IAA optimizes the altitudes where the microwindows are applied. This is achieved by the inspection of the jacobians of the temperature, that provide information on the sensitivity of the spectral

[4]Ro-vibrational transitions with no change in the rotational quantum number.

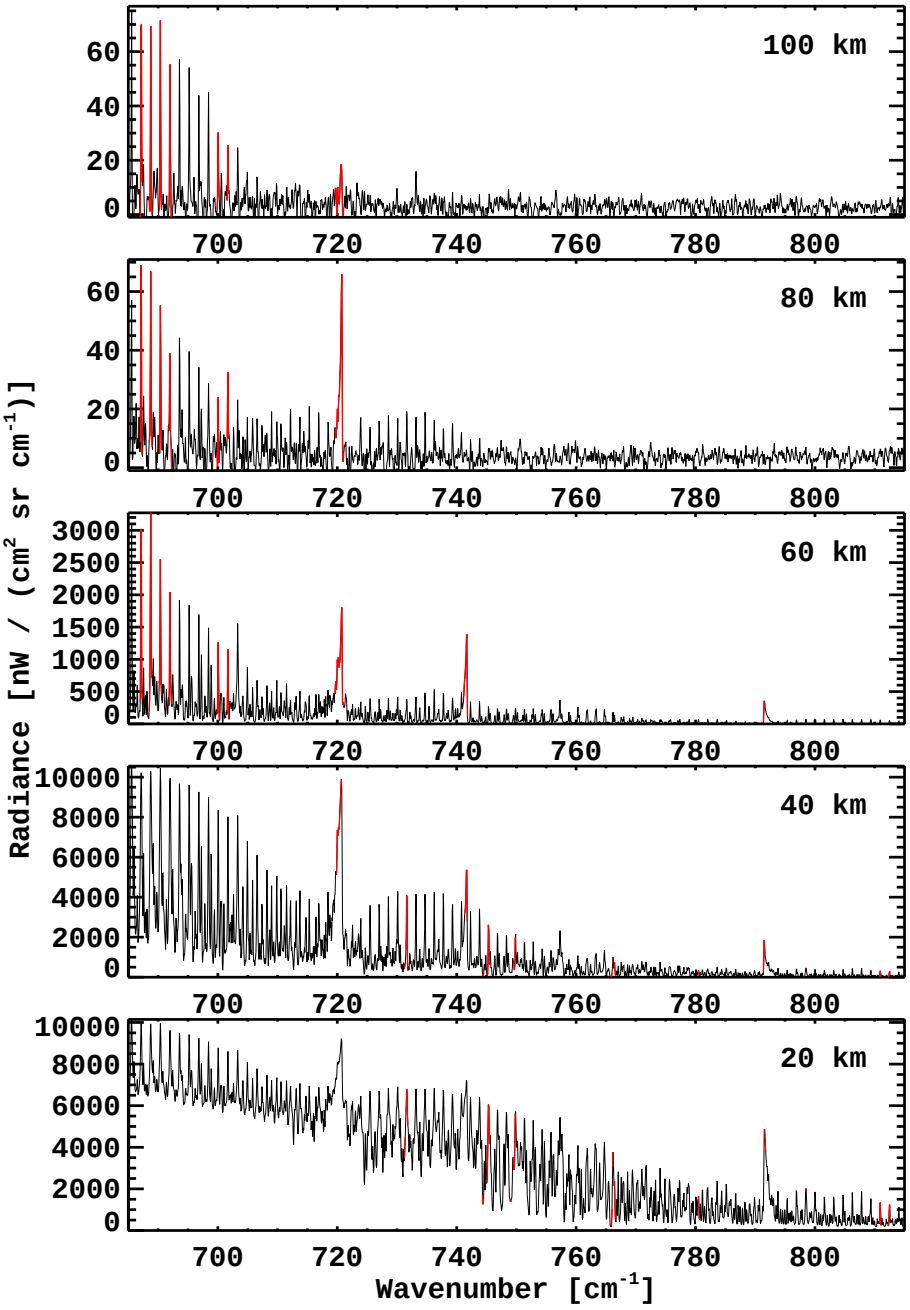


Figure 4.3: Co-added MIPAS spectra from *MA* observations on January 2005 for polar summer. The red-coloured regions denote the selected microwindows.

window to temperature at a given tangent altitude For example, most of the microwindows labeled 'ETL', except those at 740 and 791 $cm^{-1}$, provide little information on temperature above 40 km and they are therefore removed higher up. At upper mesospheric altitudes, only the new 'non-LTE' microwindows contain information on temperature. Figure 4.4 shows

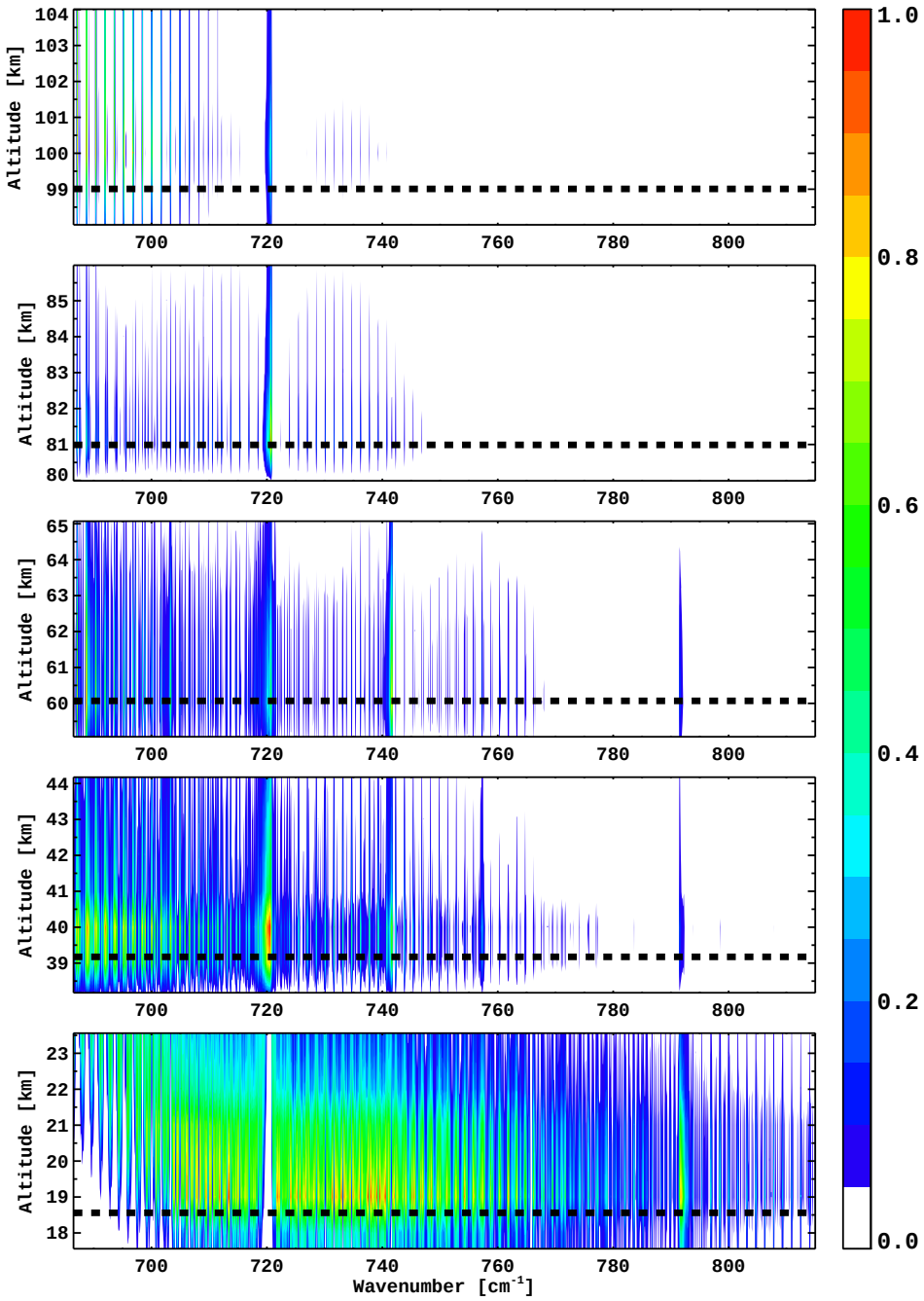


Figure 4.4: Simulated temperature jacobians for a single MIPAS scan of polar summer conditions at tangent heights: 19, 39, 60, 81 and 99 km (from bottom to top). For every tangent height, the jacobians are normalized to a 0-1 scale. Warmer (colder) colours denote stronger (weaker) information content on temperature. White regions mean no information. Dashed black line stands for the tangent height.

the spectral regions that contain more information on temperature, i.e., larger jacobians. It can be seen that the jacobians in the spectral re-

gion of the OM-IMK microwindows, 730-812 $cm^{-1}$, decrease with altitude, while the microwindows at 690-720 $cm^{-1}$ are the only ones that provides information on temperature at higher altitudes. An interesting feature observed in the lowermost tangent height panel is the saturation of the FB690 and Q720 lines captured by the jacobians. They show that, for these lines, the information on temperature comes from higher altitudes.

The width of the larger microwindows at 720 and 740 $cm^{-1}$ (see Figure 4.5) have also been optimized by using the jacobians. At lower altitudes, the good signal to noise ratio lead to very narrow microwindows. Besides, the jacobians are a very useful tool to avoid saturation, such as that observed in the 720 $cm^{-1}$ microwindow at 32 km (Figure 4.5, bottom left panel), and in constraining the microwindow to the spectral region where the information is optimal, i.e., larger jacobians (Figure 4.5, mid panels). Higher up, the microwindows become wider in order to increase of the signal to noise ratio (Figure 4.5, upper panels).

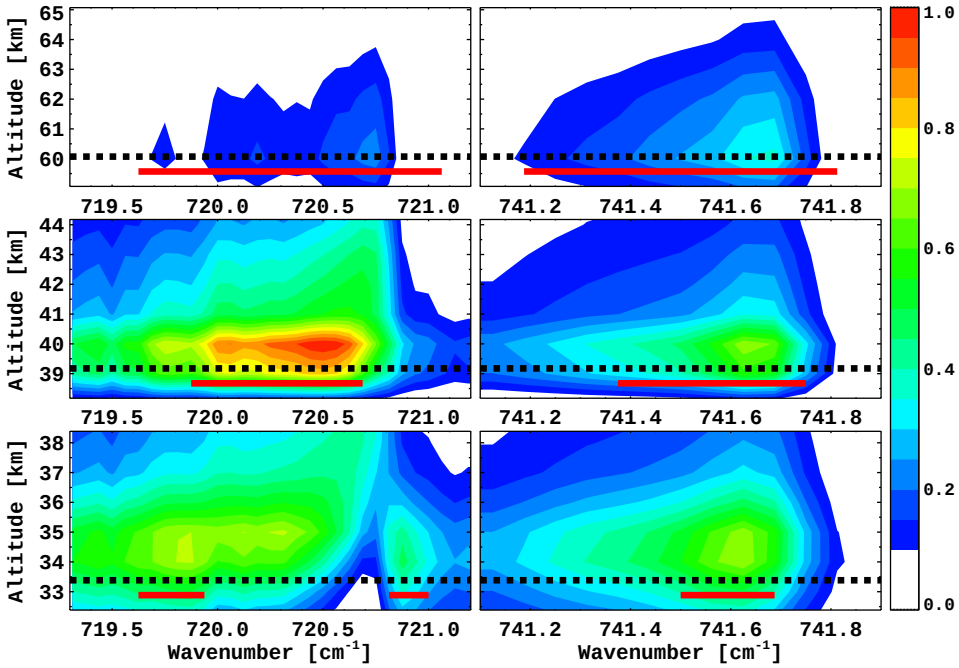


Figure 4.5: Jacobians of temperature for a single MIPAS scan of polar summer conditions at tangent heights: 33, 39, 60 km (from bottom to top), focused on the microwindows 720 (left) and 740 (right) $cm^{-1}$. For all heights, the values of the jacobians are normalized to a 0-1 scale. Black dashed lines denote the tangent height and red solid lines stand for the sub-microwindows.

Synthetic spectra corresponding to the MIPAS *MA* observation mode have been generated with the forward model KOPRA for typical atmospheric conditions (polar summer, polar winter and mid-latitudes). Subsequently,

Table 4.2: Degrees of freedom for temperature and line of sight (LOS) for three atmospheric conditions using the OM-IAA and OM-IMK MWs.

| | Polar Winter | | Polar Summer | | Mid-latitude | |
|---|---|---|---|---|---|---|
| | OM-IAA | OM-IMK | OM-IAA | OM-IMK | OM-IAA | OM-IMK |
| $T_k$ | 20.8 | 14.2 | 22.4 | 16.2 | 22.1 | 16.1 |
| LOS | 4.0 | 1.9 | 5.7 | 3.3 | 5.5 | 3.3 |

Table 4.3: Vertical resolutions at representative altitudes for retrieved kinetic temperature profiles for three typical atmospheric conditions obtained with OM-IAA and OM-IMK.

| | Polar Winter | | Polar Summer | | Mid-latitude | |
|---|---|---|---|---|---|---|
| z [km] | OM-IAA | OM-IMK | OM-IAA | OM-IMK | OM-IAA | OM-IMK |
| 80 | 3.3 | 6.0 | 5.3 | 7.7 | 5.0 | 8.1 |
| 70 | 4.7 | 5.8 | 3.2 | 4.8 | 4.2 | 5.4 |
| 60 | 5.5 | 6.7 | 4.1 | 6.0 | 3.4 | 6.2 |
| 50 | 3.3 | 4.2 | 5.3 | 5.8 | 4.4 | 6.1 |
| 40 | 3.3 | 3.8 | 3.2 | 3.3 | 3.1 | 3.2 |

Table 4.4: Noise errors at representative altitudes for retrieved kinetic temperature profiles for three typical atmospheric conditions obtained with the IAA and IMK Occupation matrices.

| | Polar Winter | | Polar Summer | | Mid-latitude | |
|---|---|---|---|---|---|---|
| z [km] | OM-IAA | OM-IMK | OM-IAA | OM-IMK | OM-IAA | OM-IMK |
| 80 | 5.4 | 7.5 | 5.0 | 8.2 | 4.8 | 7.6 |
| 70 | 2.5 | 3.1 | 2.9 | 3.4 | 2.7 | 3.5 |
| 60 | 0.7 | 1.4 | 0.8 | 1.3 | 0.9 | 1.4 |
| 50 | 0.5 | 0.7 | 0.4 | 0.6 | 0.4 | 0.6 |
| 40 | 0.3 | 0.5 | 0.3 | 0.4 | 0.3 | 0.4 |

TLOS retrievals have been performed by using OM-IAA and OM-IMK occupation matrices. Figure 4.6 shows clearly that the averaging kernels are better for the OM-IAA above 50 km. The degrees of freedom (*dof*) obtained for the most important retrieval targets, temperature and line of sight, are compared in Table 4.2, showing a difference of up to 6 *dof* in the retrieved kinetic temperature between the OMs. If the vertical resolutions for the retrieved temperature profile are compared (Table 4.3), no signficant difference is observed below 50 km (3-4 km), but above, OM-IAA provides better vertical resolutions than OM-IMK, 3-5 km against values higher than 5 km. To conclude this study, the noise retrieval error for kinetic temperature is much lower when OM-IAA is applied (see Table 4.4).

The ideal microwindow would isolate the emission of the wished

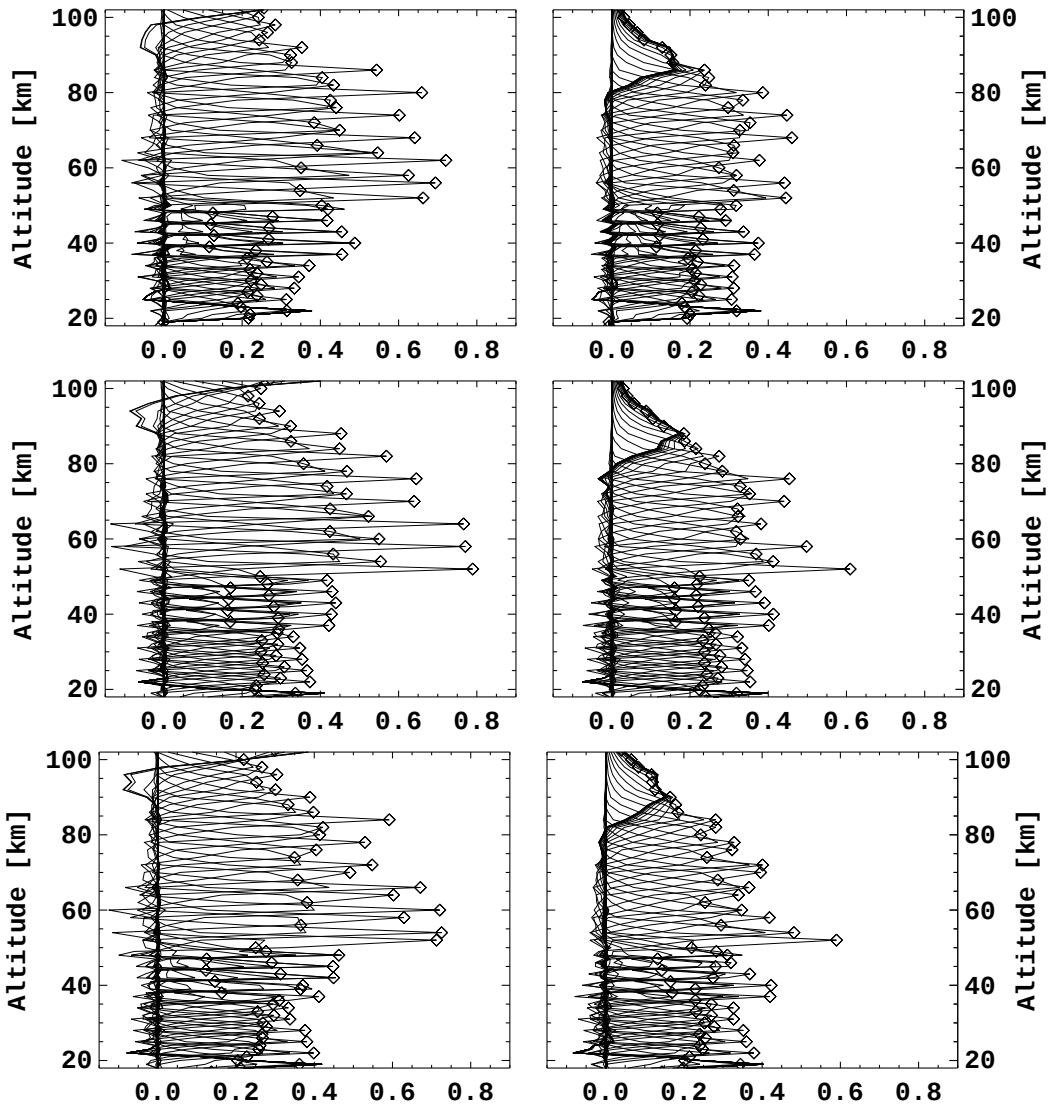


Figure 4.6: Averaging Kernels of temperature retrieval for different atmospheric conditions: polar winter (top), polar summer (mid) and mid-latitudes (bottom), using OM-IAA (left column) and OM-IMK (right).

species, making the spectral fitting easier. Unfortunately, in the real atmosphere, it is very difficult to avoid emissions from other gases. Ozone and water vapour up to 60 km, and $N_2O_5$ and $NO_2$ to a lesser extent below 30 km, are the main interfering species within the selected microwindows and therefore, their contribution must be taken into account. Their abundances are taken from the MIPAS IG2 climatology (*Raspollini et al.*, 2006) except for $O_3$ that are taken from the 2D model (*Garcia*, 1983), and their uncertainties are taken into account in the systematic error budget (see Section 5.1.1).

An important issue to bear in mind is the line mixing effect (also

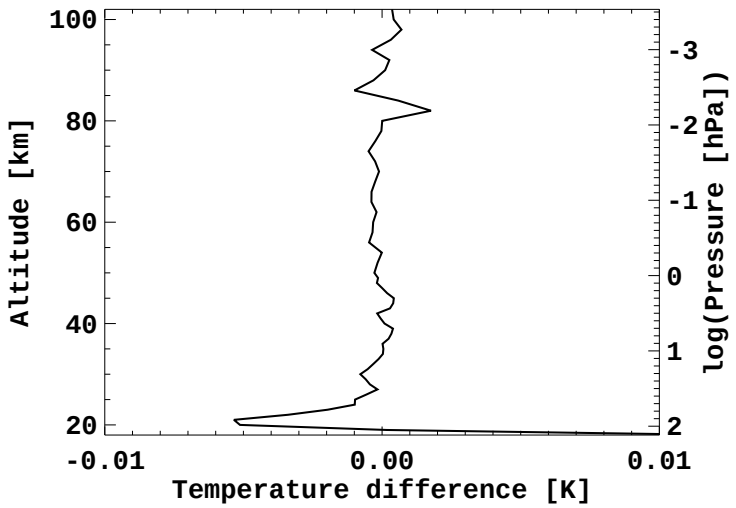


Figure 4.7: Difference in retrieved temperature using different parameterization of line mixing: Rosenkranz minus direct (note the small scale).

known as collisional narrowing) that affect the $CO_2$ emission at 15 $\mu$m. Line-mixing consists of a redistribution of ro-vibrational states populations within a band. It is caused by collisions between emitting molecules and it is proportional to the gas density. The $CO_2$ Q branches (Q720, Q740 and Q791) included in the microwindow selection requires the modeling of line-mixing effects in spectral simulations. KOPRA allows to include the exact calculation of the line-mixing, but also can use the Rosenkranz approximation, much less time consuming (see further information in *Funke* (2000)). In the altitude range of interest, the use of the Rosenkranz parameterization is acceptable, since negligible difference in the retrieved temperature has been observed by using the exact calculation or the Rosenkranz parameterization. Figure 4.7 shows the difference in retrieved temperature for a single scan for tropical daytime conditions. The test has been carried out for several atmospheric conditions and the outcome is very similar: negligible differences in the retrieved temperatures.

The OM-IAA is fully applied in the MIPAS *MA* observation mode, since its lowest tangent height is 18 km. On the other hand, *NLC* and *UA* observation modes scan down to 40 km, hence all the microwindows operating below this altitude are automatically excluded.

## 4.5. Temperature and nitric oxide retrieval scheme

The retrieval strategy is based on the retrieval scheme firstly developed by *Funke et al.* (2001) to jointly derive the nitric oxide volume mixing ratio (*vmr*) and the kinetic temperature in the thermosphere from

MIPAS measurements. The NO infrared emission at 5.3 $\mu$m is used for this purpose, where the rotational and spin structures of the fundamental band provide independent information on kinetic temperature. A comprehensive non-LTE model for NO ro-vibrational state populations needs to be included since, at thermospheric altitudes, not only the vibrational, but also the rotational and spin distributions depart from LTE. Further, the non-LTE state distributions depend on the retrieval parameters, NO *vmr* and $T_k$ (see Section 4.5.1). Hence, the NO distribution state populations are modelled in every iteration step (see Equation 4.2 and Figure 4.1).

The retrieval scheme of $T_k$ and NO *vmr* profiles (NO-$T_k$ retrieval scheme hereafter) is focused on the lower and mid-thermosphere and it is applied to MIPAS measurements on its upper atmospheric observation modes (40-170 km): the *UA4* mode during the full spectral resolution period (consisting of one single day, 14 June 2003) and the *UA* mode for the optimized spectral resolution since 2005. Retrieval of stratospheric and mesospheric NO *vmr* are not the subject of this but it has been treated in detail in *Funke et al.* (2005b).

By the time this thesis started, there existed already a preliminary version of the retrieval scheme for $T_k$ and NO *vmr* profiles which was applied to the *UA4* full spectral resolution MIPAS measurements. Since one of the main objectives of this work is to build an efficient, robust, stable and accurate NO-$T_k$ retrieval scheme, the efforts were put on the optimized resolution MIPAS measurements, for which there is much more available data, more than five years versus 1 single day. Thus, the NO-$T_k$ retrieval scheme developed in this work has been specifically tailored to retrieve the optimized resolution MIPAS spectra.

The vector of target retrieval parameters is composed of $T_k$ and the logarithm of the NO *vmr*. The use of $\ln[vmr]$ instead of *vmr* allows to better account for the pronounced temporal and spatial variability by reducing the dynamical range of the retrieval parameter vector. The vertical retrieval grid for $T_k$ and NO extends from 90 to 200 km with a variable altitude grid of 2.5 km from 90 to 115 km and 5 km above. Since the retrieval altitude grid is over-sampled compared to the tangent height spacing, the retrieval of NO and $T_k$ in the thermosphere needs to be stabilized with a numerical constraint. A Tikhonov-type first order regularization (*Steck*, 2002) is used. This does not constrain the column information but only the vertical distribution and, thus, opposite to the optimal estimation, provides a bias-free retrieval. The strength of the regularization is altitude dependent, with the aim of finding the best trade-off between the vertical resolution and the precision of the retrieved parameters. Similarly, it is also aimed to obtain a similar distribution of the degrees of freedom between NO and $T_k$, and the largest number of converged profiles.

The thermospheric NO distributions are characterized by a pronounced

spatial inhomogeneity, particularly near the auroral regions. Therefore, in addition to the target retrieval parameters, the horizontal NO *vmr* gradient along the latitudinal and longitudinal directions are retrieved from MIPAS single scans. These zonal and meridional gradients are defined as a relative *vmr* change per kilometer in easterly and southerly directions, respectively, at the center of scan location and a given altitude. NO abundances along the LOS are corrected accordingly to these gradients during the ray-tracing procedure performed within the forward calculation in each retrieval iteration. Further, a height-independent radiance offset is fitted jointly for each micro-window in order to compensate for offset calibration errors.

*A priori* information for temperature is provided by the NRLMSISE-00 empirical model (hereafter MSIS for short) (*Picone et al.*, 2002) and from the NOEM model (based on the SNOE climatology) for NO (*Marsh et al.*, 2004). Individual a priori profiles are extracted for each geo-location as a function of latitude, longitude, local time (only $T_k$), $A_p$ index and solar $F10.7$ flux. It has to be noted that the use of NOEM NO daytime climatology for both day and night conditions might induce some systematic errors in the retrieved $T_k$ and NO under low signal/noise conditions (see a detailed discussion in Section 6.5). Besides, stratospheric and mesospheric $T_k$ and pressure profiles, derived in a previous step (see Section 4.4), are used to build a consistent hydrostatic profile for thermospheric altitudes. The *a priori* information on NO gradients equals to zero profiles. MSIS also provides information on thermospheric atomic nitrogen and oxygen abundances, which are essential because they are involved in the chemical production and vibrational-thermal collisional processes of NO, respectively, and their uncertainties map into the systematic retrieval errors. This is analyzed in detail in Section 6.2. The partitioning of daytime $N(^4S)/N(^2D)$ is taken from model calculations as described in *Fesen et al.* (1989).

### 4.5.1. Non-LTE model for nitric oxide

The non-LTE model setup for the calculation of NO vibrational, rotational, and spin populations has been described in detail in *Funke and López-Puertas* (2000). It consists of 4 vibrational levels, each one containing 35 rotational levels, for both spin-folds, e.g., NO($v$ = 0-3, J = 0-35, S = 1/2, 3/2). Besides the principal isotope, two further isotopes ($^{15}N^{16}O$ and $^{14}N^{18}O$) are taken into account in order to avoid an overestimated thermospheric signal due to LTE assumption for these emitters.

The model includes the following production and loss processes of the thermospheric NO states: radiative processes, collisional relaxation within the same vibrational state (RT), collisional relaxation with a

change in the vibrational quantum number (VT), and chemical sources.

Absorption of tropospheric upwelling and solar radiation solar are the main radiative excitation processes. Since the spectral lines in the NO ro-vibrational bands are optically thin, the radiative transfer between atmospheric layers due to NO emission and absorption is rather small. However, particularly at polar winter conditions, the SEE cannot be solved locally due to high mesospheric NO concentrations. As a consequence, the radiative field at a given altitude depends on the NO($\nu$,J,S) state distribution at other altitudes. This is implemented in GRANADA code via the $\lambda$-iteration technique.

Collisions with atomic oxygen in the thermosphere represent the principal VT energy transfer mechanism, being further responsible for the sub-thermal part of the rotational-spin distribution. For these collisions, it is used an effective nascent rotational temperature of $T_{rot}$ = $0.74\,T_k + 0.24$ as determined by means of quasi-classical trajectory calculations (*Sharma and Duff*, 1997) and an effective spin nascent temperature[5] of $T_s$ = 200 K (*Lipson et al.*, 1994).

The NO chemical productions drive the super-thermal part of the rotational-spin distribution with $T_{rot}$ = 5000 K at daytime and $T_{rot}$ = 3000 K at nighttime and $T_s$ = 300 K. The RT processes are included with rates empirically fitted to an exponential power dependence on $E_{rot}$: $W_{\nu'',J'',S''\to\nu'',J',S'} = a_1\,(1-\beta|\Delta S|) \times \left(1+\gamma_{\Delta S}|\Delta J|(-1)^{|\Delta J|}\right) \times \left(\frac{|\Delta E_J|}{B_0}\right)^{a_2} \exp\left(-a_3\frac{|\Delta E_J|}{kT_k}\right)$. Here, $\Delta S$ and $\Delta J$ represent the change in the spin and rotational quantum number, respectively; $\beta$ is the spin propensity factor which accounts for the higher spin-conserving propensity ($\Delta S = 0$); and $\gamma_{\Delta S}$ is the rotational propensity factor which accounts for different probabilities of odd and even changes of $\Delta J$. $B_0$ is the rotational constant and $k$ is the Boltzmann constant; $a_i$ ($i = 1, 2, 3$) are the fitting parameters.

The atomic oxygen abundance, the atomic nitrogen concentration, and spin propensity factor are the major sources of uncertainty in the retrieved parameters. Their effect on the retrieved NO mixing ratio and temperature are discussed in Chapter 6.

Figure 4.8 shows non-LTE populations of NO for daytime mid-latitude conditions. Vibrational, spin and kinetic temperatures are shown in the left panel and LTE and non-LTE relative populations of the two spin states are shown in the right panel. The sub-LTE vibrational population of NO($\nu = 1$) above 110 km is explained by the dominance of the radiative losses over the collisional excitation by atomic oxygen and chemical production. Below 110 km, NO($\nu = 1$) is mainly affected by radiative processes (absorption of solar and tropospheric radiation), and the de-

[5] The spin temperature, $T_s$, is defined by the ratio of populations of the two spin-folds: $n_{S=3/2}/n_{S=1/2} = \exp(-\Delta E/kT_s)$, with $\Delta E \sim 120\,\mathrm{cm}^{-1}$.

excitation by collisional quenching with $O_2$ and O is much less important than spontaneous emission. This leads to NO($\nu = 1$) to have populations larger than in LTE.

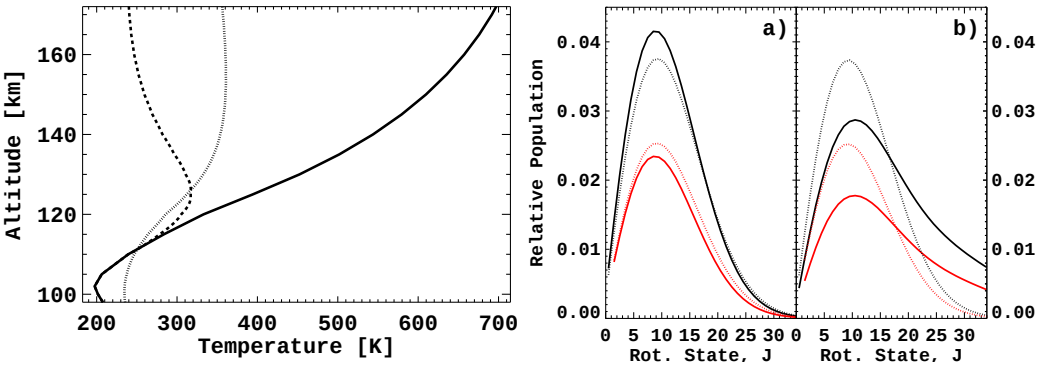


Figure 4.8: GRANADA calculations of NO($\nu$,J,S) populations for a daytime mid-latitude case. Left panel: NO($\nu = 1$) vibrational (dotted) and spin (dashed) temperatures; kinetic temperature is shown by a solid line. Right panel: relative rotational and spin state distributions for NO($\nu = 1$), panel a), and for NO($\nu = 2$), panel b), at 130 km. Spin-fold S=1/2 (3/2) is shown in black (red) and non-LTE (LTE) calculations are represented by solid (dotted) lines.

The spin temperature shows the influence of the NO production at 120--130 km and the NO + O collisions above. The right panel illustrates the non-LTE rotational and spin population distribution for NO($\nu = 1, 2$) at 130 km for the same atmospheric conditions. The rotational and spin state population distributions are relative to the corresponding vibrational state. For $\nu = 1$ (panel $a$)), the sub-thermal spin distribution is already visible, while the rotational distribution is only weakly affected by rotational non-LTE at this altitude. For $\nu = 2$ (panel $b$)), the rotational non-LTE is clearly distinguised at high $J$ for both spin folds.

### 4.5.2. Occupation matrix

MIPAS channel D (1820-2410 $cm^{-1}$) provides information on the NO fundamental band emission along more than 100 $cm^{-1}$. That is, ro-vibrational lines from the P and R branches and also from different NO spin-folds (S = 1/2, 3/2) are resolved, even for the MIPAS optimized spectral resolution of 0.0625 $cm^{-1}$. The optimizing tool KOMA was used to select a set of microwindows considering a trade-off between the number of spectral points and a tolerable random error. The result is a altitude-independent occupation matrix (OM) covering from 1835 to 1940 $cm^{-1}$. It contains 24 microwindows with typical widths narrower than 0.5 $cm^{-1}$, but wide enough to host one line or two close lines from different spin-folds (see Table 4.5).

Since the OM was initially created for the analysis of MIPAS full

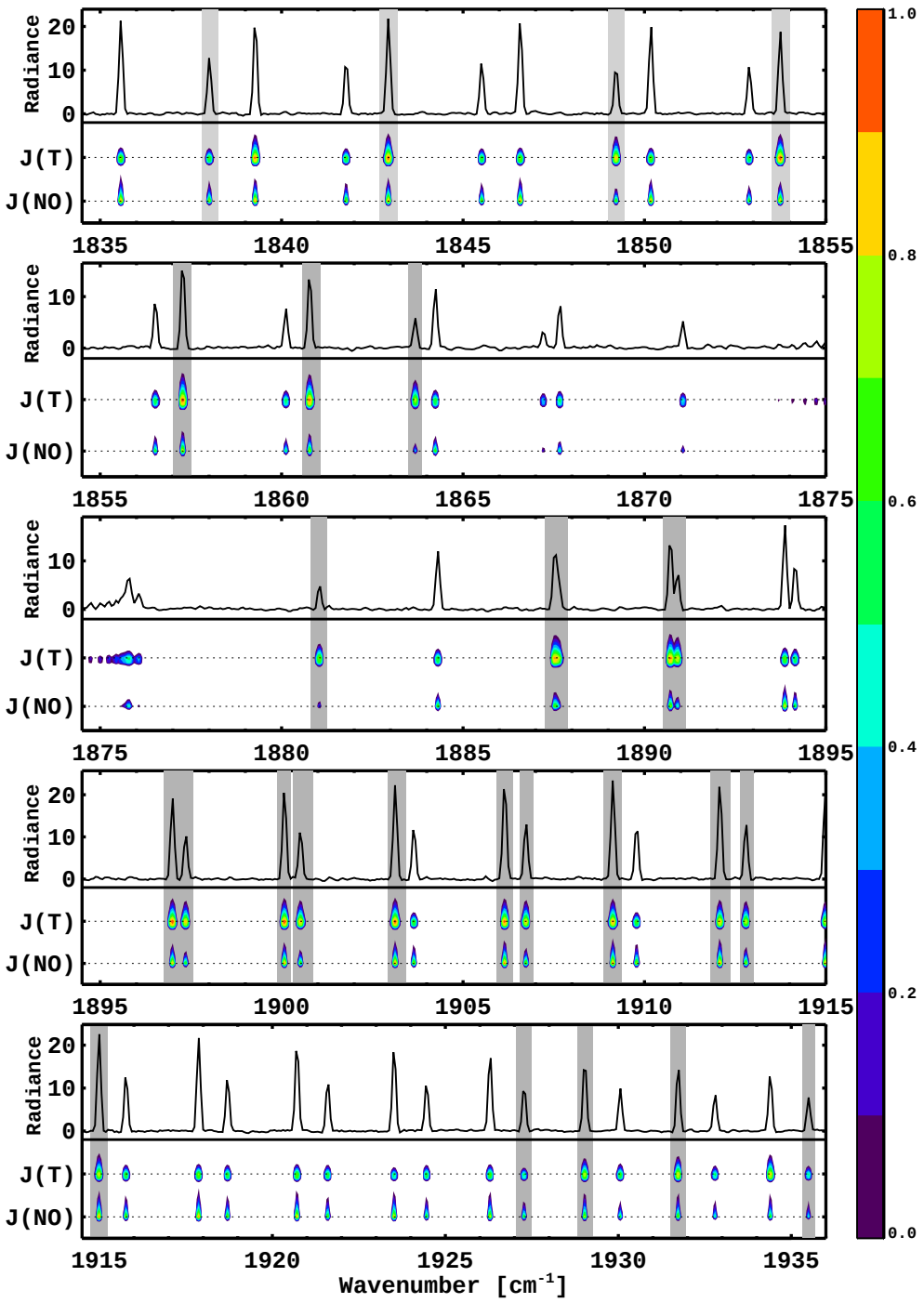


Figure 4.9: MIPAS co-added spectra at 120 km for polar summer conditions (21 January 2005, 70-90 S). The spectral radiance is in units of $\mathrm{nW/(cm^2\,sr\,cm^{-1})}$. Shaded regions represent the microwindows. Below the spectrum, the jacobians of kinetic temperature (top panel) and of NO *vmr* (bottom panel) at 120 km are also shown in a normalized scale from 0 to 1.

Table 4.5: Occupation matrix for the inversion of thermospheric temperature and NO *vmr*.

| Spectral range $[\mathrm{cm}^{-1}]$ | Most intense line(s) (Branch, $J$, $S$)$^{\dagger}$ |
|---|---|
| 1837.8125-1838.2500 | P, 10.5, 3/2 |
| 1842.8125-1843.1875 | P, 9.5, 1/2 |
| 1849.0625-1849.4375 | P, 7.5, 3/2 |
| 1853.4375-1853.9375 | P, 6.5, 1/2 |
| 1857.0000-1857.5000 | P, 5.5, 1/2; $^{\ddagger}$R, 3.5, 1/2 |
| 1860.6250-1861.1250 | P, 4.5, 1/2 |
| 1863.5000-1863.8750 | P, 3.5, 3/2; $^{\ddagger}$R, 5.5, 3/2 |
| 1880.7500-1881.2500 | R, 0.5, 1/2 |
| 1887.2500-1887.8750 | R, 2.5, 1/2; R, 2.5, 3/2 |
| 1890.5000-1891.1250 | R, 3.5, 1/2; R, 3.5, 3/2 |
| 1896.7500-1897.5000 | R, 5.5, 1/2; R, 5.5, 3/2 |
| 1899.9375-1900.2500 | R, 6.5, 1/2 |
| 1900.3750-1900.8750 | R, 6.5, 3/2 |
| 1902.9375-1903.3750 | R, 7.5, 1/2 |
| 1906.0000-1906.3125 | R, 8.5, 1/2 |
| 1906.5625-1906.8750 | R, 8.5, 3/2 |
| 1909.0000-1909.3125 | R, 9.5, 1/2 |
| 1911.9375-1912.2500 | R, 10.5, 1/2 |
| 1912.6250-1912.9375 | R, 10.5, 3/2 |
| 1914.8125-1915.1250 | R, 11.5, 1/2 |
| 1927.1250-1927.4375 | R, 15.5, 3/2 |
| 1928.8750-1929.1875 | R, 16.5, 1/2 |
| 1931.5625-1931.8750 | R, 17.5, 1/2 |
| 1935.3125-1935.6875 | R, 18.5, 3/2 |

$^{\dagger}$Most intense spectral lines ($S>10^{-22}\,\mathrm{cm}^{-1}/\mathrm{cm}^{-2}$) from vibrational level $\nu=1$ to $\nu=0$ of the main NO isotope with specified branch, $J$ and spin. $^{\ddagger}$Lines of the second most abundant NO isotope.

resolution data, it has been adapted for the MIPAS optimized resolution spectra, in order to cover the degraded spectral lines properly. The width of the adapted microwindows has been optimized by the inspections of the jacobians of temperature and NO *vmr*, in an analogous manner as it was performed for the OM of the TLOS retrieval scheme (see Figure 4.9).

It is worth mention that, in order to improve the temperature sensitivity, some relatively intense lines within the band are ruled out in favour of: *a)* a wider sampling of rotational lines belonging to P and R branches, from low to high rotational quantum numbers, and *b)* a sensitive coverage of rotational lines from both spin-folds.

# Chapter 5

# Temperature in the middle atmosphere

*Abstract*

The scheme presented in the previous chapter for the non-LTE retrieval of temperature and pointing in the middle atmosphere has been applied to MIPAS spectra at 15 $\mu$m in its *MA*, *NLC* and *UA* observation modes. Mean single profiles obtained for different atmospheric conditions are presented. The results are characterized by means of the random retrieval error and the vertical resolution of the retrieved profiles. The sources of systematic errors are characterized, being the uncertainties in the modelling of $CO_2$ vibrational populations the most important sources. The quality of the retrieved MIPAS $T_k$ in the middle atmosphere is assessed by comparisons with independent space-borne and ground instruments.

## 5.1. Characterization of retrieved $T_k$ and Line of Sight

The temperature and line of sight (TLOS) retrieval scheme described in Section 4.4 has been applied to MIPAS measurements from its observation modes: *MA* (v511), *NLC* (v711) and *UA* (v611) (see Section 2.7 and Tables 2.3-2.5) between 2005 and 2009. Before going into the characterization of the retrieved $T_k$ and LOS, we should remark on the very good efficiency of the retrieval scheme. Out of more than 250,000 inverted MIPAS profiles from these three observation modes, the overall convergence rate is larger than 95% (see Table 5.1). An inspection of the residual 5% of non-converged scans demonstrates that the proportion of converged scans generally declines at polar summer regions (see Figure 5.1). This is because the cold temperatures at the mesopause enhance the real non-linear dependence of the radiative transfer on the temperature, hence, the retrieval processor encounters more difficulty to reach

Table 5.1: Convergence rate (percentage) for TLOS retrievals performed on MIPAS measurements from *MA*, *NLC* and *UA* observation modes.

| | *MA* | *NLC* | *UA* |
|---|---|---|---|
| Convergence Rate [%] | 93.4 | 95.5 | 98.5 |

convergence for the linearized problem. Retrieval of measurements from *MA* mode have worse convergence rate than *NLC* and *UA*, specially at low daytime latitudes. This is mainly due to the additional retrieval of continuum for each microwindow, which is not always accurately fitted.

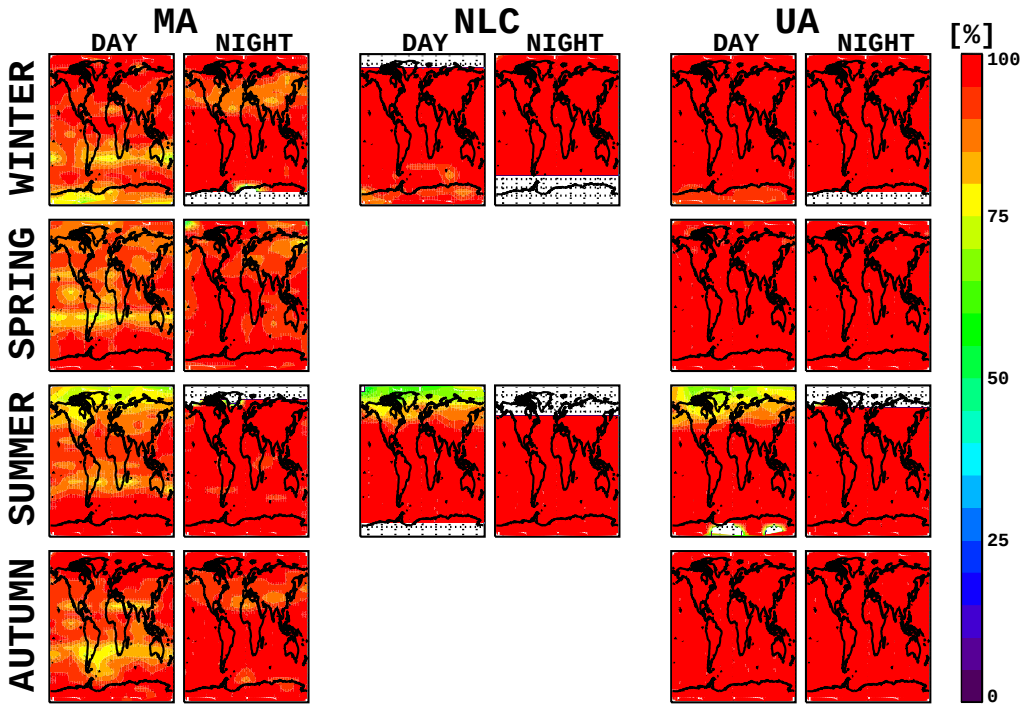


Figure 5.1: Convergence rate of TLOS retrievals from MIPAS measurements taken in *MA* (left column), *NLC* (central column) and *UA* (right column) modes seasonally averaged for the period 2005-2009. Daytime and nighttime convergence rates have been separated. White regions denote lack of MIPAS measurements.

The retrieval of MIPAS line of sight (LOS) represents a correction to the engineering pointing information provided by ESA. *Kiefer et al.* (2007) reported a systematic and orbit periodic pointing bias of ESA's L1b engineering information from the analysis of the retrieved LOS of nominal observations during the period 2002-2004. The mismatch between retrieved and engineering LOS shows an increase with latitude by 1.5-2 km from pole to pole. Figure 5.2 shows the average pointing mismatch from MIPAS *MA* observations in the periods December-February in 2007-2009 as a

function of altitude and latitude. The observed pattern is very similar to the results of *Kiefer et al.* (2007) for nominal (*NOM*) observations. The results found for the selected periods are representative for any other period and observation mode. In addition, the altitude-constant bias observed above around 65 km denotes the lack of independent spectral information on pressure and, hence, the retrieved relative tangent height spacing is taken directly from the ESA engineering information. The LOS random retrieval error, i.e., its precision, estimated individually for every profile, remains below 200 m for all tangent heights, as it was found by *von Clarmann et al.* (2003a) for nominal observations.

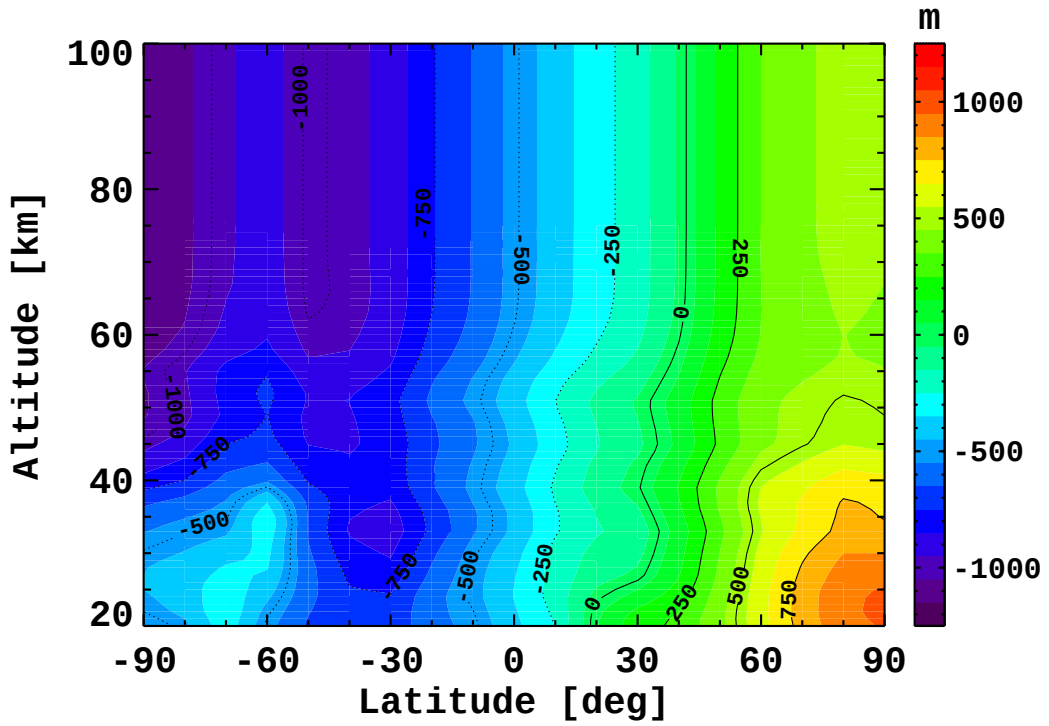


Figure 5.2: Average differences between retrieved and engineering tangent altitudes during December-February of 2007-2009.

The results of the temperature retrieval in the middle atmosphere from the three MIPAS observation modes, *MA*, *NLC* and *UA*, are now characterized. For such analysis, representative scenarios have been chosen, i.e., tropical and mid-latitudes, polar summer and polar winter. Left panels of Figures 5.3 and 5.4 show averaged retrieved temperature profiles for each scenario from MIPAS *MA* and *UA* measurements, respectively. Retrievals from MIPAS *NLC* measurements are not plotted to avoid redundancies. The mean temperatures show the typical structure of the middle atmosphere for solstice conditions. Further, the *MA* measurements that measures down to 18 km, shows the cold tropical tropopause (190 K), even

colder than the polar winter case (200 K) because of the upwards convection. The tropopause is also captured in the midlatitude case (210 K), but not for the polar summer, placed below the lowermost tangent height of the *MA* mode (18 km). In the middle atmosphere, the profiles from both *MA* and *UA* measurements show the general patterns of hemispheric asymmetry for solstices in: 1) the temperature of the stratopause (around 50 km for all latitudes), coldest in the polar winter pole (<250 K), being warmer towards the summer hemisphere (over 250 K in the winter midlatitudes and above 260 K at the tropics) and warmest in the polar summer (280 K); 2) the temperature and altitude of the mesopause, coldest (150 K) and lowest (∼87 km) in the polar summer, and higher (around 100 km, not always retrieved) and warmer (190-200 K) towards the winter hemisphere. It is interesting to point out the ability of the retrieval processor to retrieve vertical structure of the $T_k$ profile at a small scale, such as inversion layers ($T_k$ increasing with altitude) observed in the upper mesosphere, between 70 and 90 km, specially in mid and high latitudes in winter hemisphere. These inversion layers are thought to be produced by interaction between gravity waves and tides and by dissipation of planetary waves and, to a minor extent, by local gravity wave breaking and chemical heating, through the exothermic reaction between ozone and atomic hydrogen (*Meriwether and Gerrard*, 2004).

The random error of the retrieved temperature for a single scan, i.e., its precision, arises mainly from the propagation of the measurement noise through the retrieval. These are calculated by the retrieval algorithm using a wavelength dependent noise-equivalent-spectral-radiance that on MIPAS A band (685-970 $cm^{-1}$) is on average about 20 $nW/(cm^2\,sr\,cm^{-1})$. Despite the different atmospheric conditions displayed here, the random error for the retrieved temperature remains quite similar (see mid panels of Figures 5.3 and 5.4). Typical values are 0.2-0.5 K below 50 km, 0.5-2 K at 50-70 km, and 2-8 K above.

The average vertical resolution is shown in the right panels of Figures 5.3 and 5.4. Typical values are 4 km below 35 km, 3 km at 35-50 km, 4-6 km at 50-90 km, and 6-10 km above. Precision and vertical resolution vary only marginally with latitude and season despite of the pronounced variations in the retrieved temperature, except for the polar summer case, where the precision and vertical resolution worsen 1 K and 1 km, respectively, above 90 km.

The error budget includes not only the mapping of the measurement noise on the retrieved temperatures, but also the propagation of uncertainties of model parameters onto the result. This is discussed in the next section.

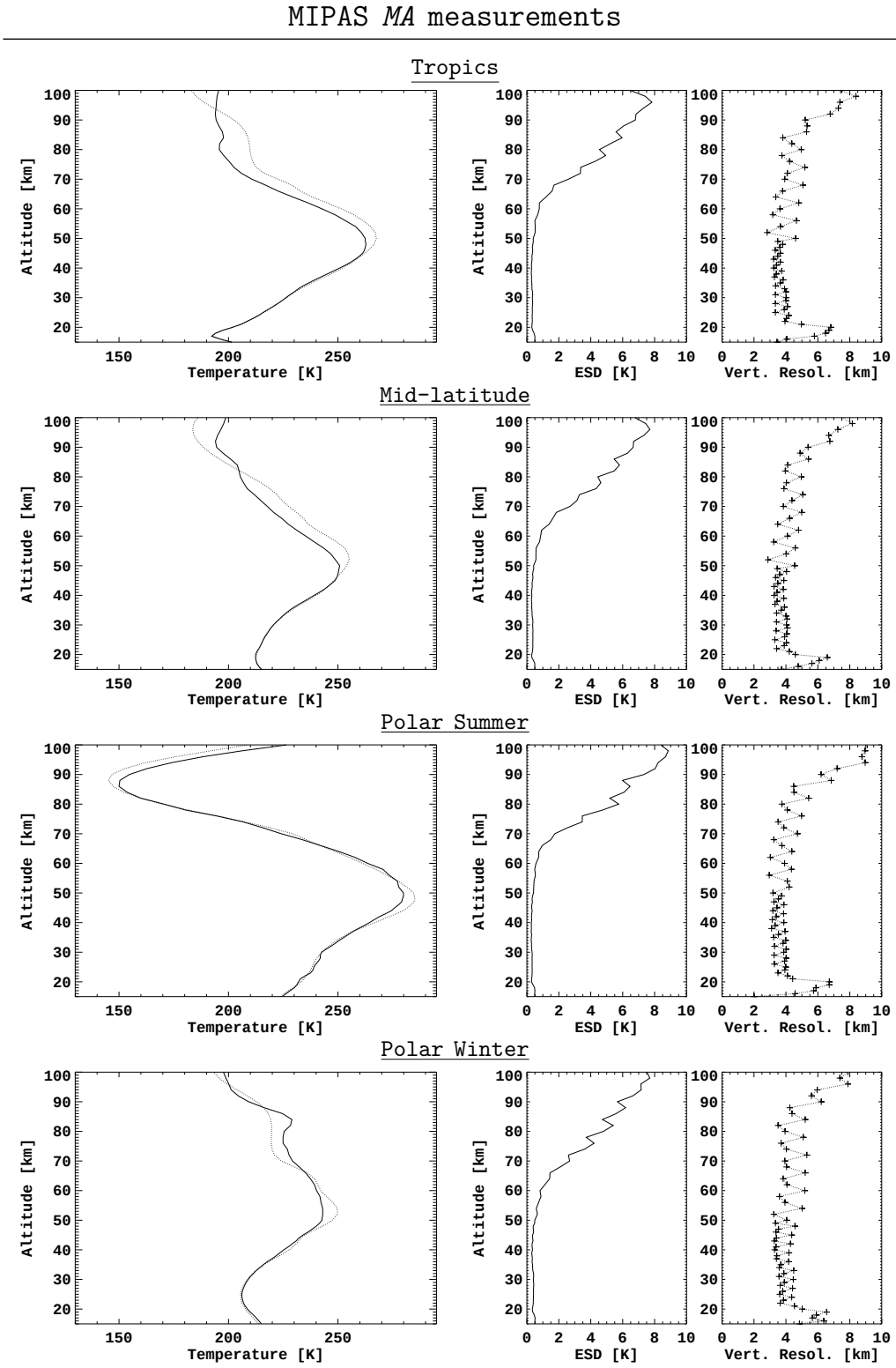


Figure 5.3: Left panels: mean retrieved $T_k$ from MIPAS *MA* measurements (solid) and respective *a priori* information (dotted). Mid and right panels: mean random error and mean vertical resolution, respectively. Measurements correspond to Winter 08/09 (8 days of MIPAS *MA* measurements). From top to bottom: tropics (25S, 25N), mid-latitude (30N, 60N), polar summer (90S, 70S) and polar winter (70N, 90N). Day and night measurements are merged.

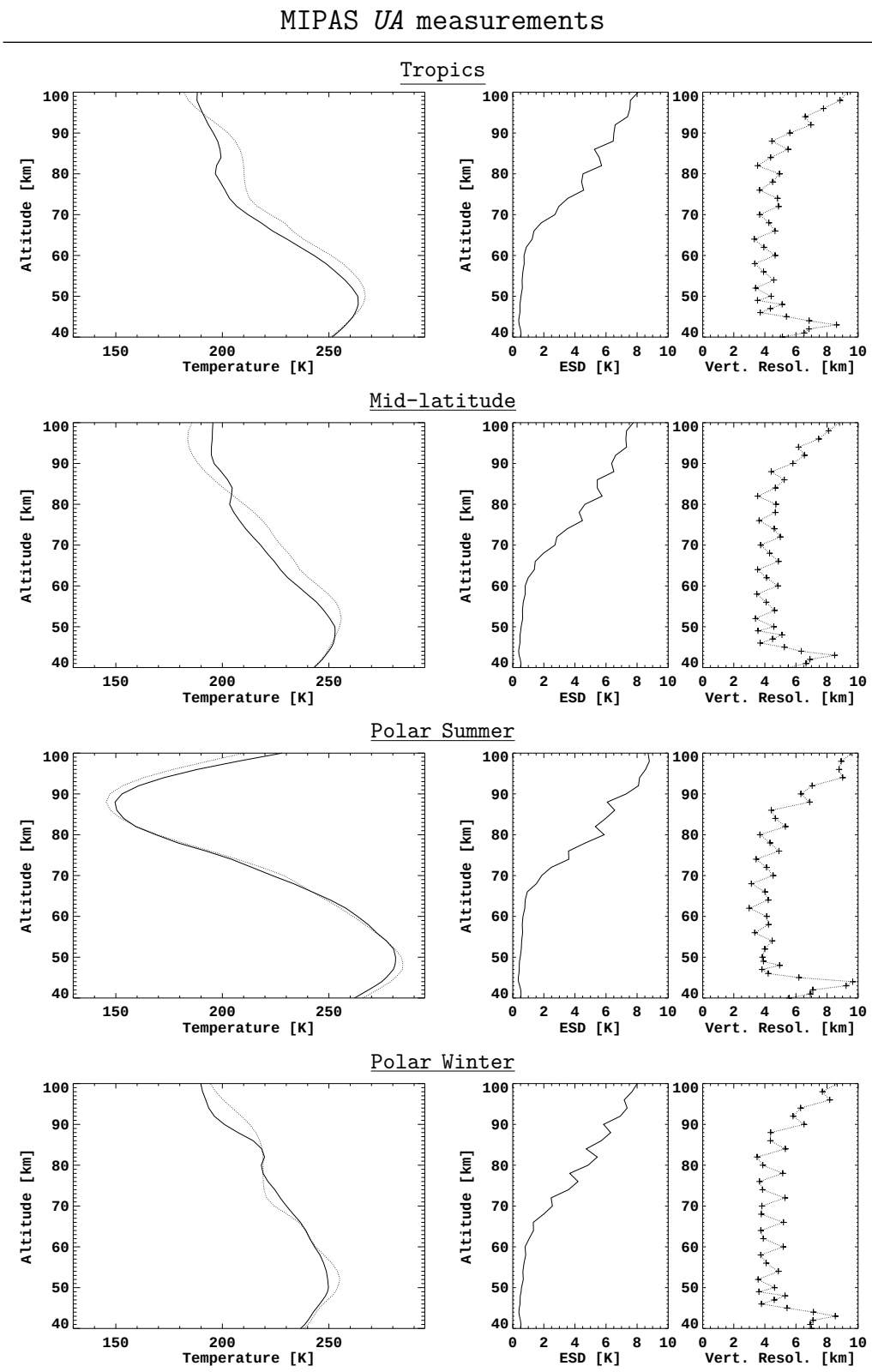


Figure 5.4: As in Figure 5.3 but for MIPAS *UA* measurements (10 days).

### 5.1.1. Systematic errors in the retrieved $T_k$

There are several sources of systematic errors affecting the non-LTE retrievals of kinetic temperature. The most important sources are due to the modeling of the non-LTE populations of $CO_2$ vibrational levels, which yield the largest uncertainties in the retrieved $T_k$ in the upper mesosphere and lower thermosphere. In particular, the collisional rates and the abundance of other species involved in the non-LTE reactions. The largest errors of this kind originate from uncertainties in the rate of $\upsilon_2$ vibrational exchange between $CO_2$ molecules ($k_{vv}$), the thermal quenching of $CO_2(\upsilon_2)$ by molecular nitrogen and molecular oxygen ($k_{air}$), the $CO_2(\upsilon_2)$ thermal quenching by atomic oxygen ($k_O$), and the abundance of the latter ([O]). The rates $k_{air}$ and $k_O$ used in the $T_k$ retrievals are taken from *Wintersteiner et al.* (1992) and *Sharma and Wintersteiner* (1990), respectively. For the non-LTE error estimation, an uncertainty of 30% and 50% have been assumed, respectively, based on the values reported in the literature for these two rates, as summarized in *García-Comas et al.* (2008). The atomic oxygen used in the retrievals is taken from 2D model calculations (*Garcia*, 1983) below 80 km and from MSIS above (*Picone et al.*, 2002), for which an uncertainty of 50% has been assumed, also based on considerations in *García-Comas et al.* (2008). The value for $k_{vv}$ is that measured by *Dang et al.* (1983) and its error measurement uncertainty, 20%, has been assumed. The contribution of each rate and [O] uncertainties to the $T_k$ systematic error has been estimated individually for different atmospheric conditions of mid-latitude, polar winter and polar summer. Such estimations have been performed by retrieving $T_k$ where the nominal values of the collisional rates and [O] abundance have been modified by a factor given by their respective uncertainties. The response of the retrieval of $T_k$ depends on the effect of such changes on the modeling of $T_v$ of the $CO_2$ vibrational levels responsible for the radiance measured by MIPAS. On the one hand, lowering (increasing) rate constants of thermal collisions, i.e., $k_{air}$ and $k_O$, leads to $CO_2(\upsilon_2)$ populations farther (closer) to LTE, that is, the respective $T_v$ are farther (closer) to $T_k$. On the other hand, lowering (increasing) the $k_{vv}$ rate leads to a weaker (stronger) vibrational energy exchange between the involved $CO_2{}^{i}(\upsilon_2)$ vibrational levels. That is, such vibrational levels are less (more) coupled and hence their respective $T_v$ are farther (closer) among themselves. In practice, the V-V exchange within the same $CO_2$ isotope consists of depopulate the higher $(\upsilon_2)$ levels, and in the case of V-V exchange between different isotopes, the minor isotopes are depopulated in favour of the $(01^10)$ level of the main isotope. The retrieval will respond by increasing (decreasing) the retrieved $T_k$ in order to compensate the decrease (increase) in the $T_v$ produced by the change in the collisional parameters, so that the measured radiance is matched. It is interesting to point out that the response of the retrieved $T_k$ to variations in the $T_v$'s is expected to be stronger (weaker) as long

as the $T_v$'s are farther (closer) to LTE, since the vibrational levels populated mainly by non-LTE processes depends weakly on the $T_k$. Also, the non-linear nature of the problem makes that symmetric changes in the collisional parameters yield no-symmetric responses in the retrieved $T_k$.

Tables 5.2, 5.3 and 5.4 show the retrieval response, i.e. the systematic error of the $T_k$, to the uncertainties in the collisional rates for mid-latitude, polar winter and polar summer conditions, respectively. Below 70 km, the effect of the rates' uncertainties on the retrieved $T_k$ is negligible. Above, the uncertainties in the rates of $CO_2(\upsilon_2)$ quenching with $N_2$ and $O_2$ and of $CO_2(\upsilon_2)$ vibrational exchange have small effects on the retrieved $T_k$, except for polar summer conditions. Collisions with atomic oxygen in the upper mesosphere, above 85 km, drive the non-LTE systematic error of the retrieved $T_k$ for all scenarios. Non-LTE systematic errors are largest (smallest) for polar summer (polar winter) conditions because the vibrational populations of involved $CO_2(\upsilon_2)$ levels are farthest (closest) to LTE values (see Figure 4.2). As expected, the sign of the changes in the retrieved $T_k$ agrees with the change in the $T_v$'s due to the effect of the modified rate. In the upper mesosphere and lower thermosphere, the $(\upsilon_2)$ main isotope fundamental band is the major contribution to the MIPAS microwindows in 15 $\mu$m, then it is useful to take $T_v$ of 626-(010) as a reference in order to understand such changes. For example, for polar winter conditions, $T_v$(626-010) is under LTE above 75 km. Then, variations in the collisional rates which leads this $T_v$ closer to $T_k$(increase of $k_{air}$, $k_O$ and $k_{vv}$) yield an increase in the level population (and hence in the radiance), which is compensated with a decrease in the retrieved $T_k$ (see Table 5.3). For polar summer conditions, $T_v$(626-010) is over LTE between 80 and 90 km, hence, the same variation in the rates leads to a decrease of the $T_v$, compensated by the retrieval with an increase in $T_k$ in the considered altitude range. Above 90 km, since the $T_v$ becomes under LTE the behaviour is the same as explained for polar winter (see Table 5.4).

For mid-latitude conditions, the typical non-LTE systematic error is smaller than $\pm$0.1 K below 70 km, $\pm$0.6 K at 85 km and $\pm$7.7 K at 100 km. For polar winter conditions, the errors are: $\pm$0.1 K at 70 km, $\pm$1.3 K at 85 km and $\pm$7 K at 100 km. The non-LTE errors are somewhat larger under polar summer conditions, where the $CO_2(\upsilon_2)$ levels are further away from LTE and hence, more sensitive to the uncertainties in the collisional rates. That scenario was also studied in *López-Puertas et al.* (2009b), who reported overall non-LTE errors of $\pm$0.1 K at 70 km, $\pm$5 K at 85 km and $\pm$30 K at 100 km. The non-LTE errors for these typical and extreme conditions are summarized in Table 5.5.

MIPAS kinetic temperature is retrieved from $CO_2$ emission and, hence, another source of systematic error is the assumed $CO_2$ abundance, since it can significantly depart from well-mixed values above around 70 km

Table 5.2: Estimated errors (K) in retrieved $T_k$ due to collisional rates uncertainties for mid-latitude conditions.

| z | $k_{air}$ | | $k_0$ / [O] | | $k_{vv}$ | | |
|---|---|---|---|---|---|---|---|
| (km) | -30% | +30% | -50% | +50% | -20% | 20% | Total † |
| 70 | -0.1 | 0.1 | 0.0 | 0.0 | -0.1 | 0.1 | ±0.1 |
| 85 | 0.2 | -0.1 | 0.5 | -0.2 | -0.2 | 0.1 | ±0.6 |
| 100 | -0.0 | 0.0 | 7.7 | -3.1 | -0.0 | 0.0 | ±7.7 |

†'Total' error is the quadratic average of the errors due to all collisional rates and [O] uncertainties: $\Delta T_k^{SysNLTE} = \sqrt{\left(\Delta T_k^{k(\mathrm{air})}\right)^2 + \left(\Delta T_k^{k(\mathrm{vv})}\right)^2 + \left(\Delta T_k^{k(\mathrm{O})}\right)^2 + \left(\Delta T_k^{[\mathrm{O}]}\right)^2}$, where the error due to each parameter is calculated as the linear average of the absolute values obtained for the error in each direction.

Table 5.3: Estimated errors in retrieved $T_k$ due to collisional rates uncertainties for polar winter conditions.

| z | $k_{air}$ | | $k_0$ / [O] | | $k_{vv}$ | | |
|---|---|---|---|---|---|---|---|
| (km) | -30% | +30% | -50% | +50% | -20% | 20% | Total † |
| 70 | -0.0 | 0.0 | -0.0 | 0.0 | 0.0 | -0.0 | ±0.0 |
| 85 | 0.5 | -0.4 | 1.1 | -0.6 | -0.1 | 0.1 | ±1.3 |
| 100 | -0.1 | 0.1 | 6.8 | -2.7 | -0.1 | 0.1 | ±6.7 |

Table 5.4: Estimated errors in retrieved $T_k$ due to collisional rates uncertainties for polar summer conditions.

| z | $k_{air}$ | | $k_0$ / [O] | | $k_{vv}$ | | |
|---|---|---|---|---|---|---|---|
| (km) | -30% | +30% | -50% | +50% | -20% | 20% | Total † |
| 70 | -0.1 | 0.1 | 0.0 | 0.0 | -0.1 | 0.1 | ±0.1 |
| 85 | -2.2 | 2.1 | -2.6 | 2.2 | -2.6 | 2.5 | ±4.7 |
| 100 | 3.0 | -2.4 | 27 | -15 | 3.3 | -2.7 | ±30 |

Table 5.5: Summary of non-LTE errors for MIPAS $T_k$ (in K).

| | Altitude [km] | | | | |
|---|---|---|---|---|---|
| Conditions | 60 | 75 | 85 | 95 | 100 |
| Mid-latitudes | 0.0 | 0.4 | 1.4 | 5.9 | 11 |
| Polar Winter | 0.0 | 0.3 | 1.3 | 1.8 | 6.7 |
| Polar Summer | 0.0 | 0.7 | 4.7 | 19 | 30 |

(*López-Puertas et al.*, 2000). The $CO_2$ abundance in $T_k$ retrievals is taken from the WACCM model (*Garcia et al.*, 2007). Assuming a 15% uncertainty (according to considerations in *Remsberg et al.* (2008)), the induced $T_k$

error is smaller than ±0.1 K below 70 km, ±2 K at 85 km, ±3 K at 90 km and ±2 K at 100 km.

A further systematic error source arises from horizontal temperature inhomogenities. Although horizontal gradients are retrieved simultaneously with temperature, they provide only a linear correction which might not be appropriate in all atmospheric situations, particularly in the presence of strong, located temperature anomalies, such as near polar vortex boundaries. *Kiefer et al.* (2010) investigated the impact of horizontal temperature inhomogenities in MIPAS retrievals from nominal observations by looking at differences between ascending and descending orbit branches (i.e., observations at local times of 10 p.m. and 10 a.m., respectively), assuming that the atmosphere does not change significantly within 12 hours. This assumption, however, does only hold at altitudes below approximately 60 km were tidal signatures are small. Figure 5.5 (left panel) shows the differences obtained from MIPAS *MA* temperature observations as seasonal zonal mean distributions. Except for the tropical atmosphere, differences are well below 2 K. In the tropics, differences are more pronounced (up to 4 K) and show a clear signature of the migrating diurnal tide. In order to assess the degree of tidal "contamination" in the differences between ascending and descending orbit measurements, these differences have been compared to similar differences obtained from ECMWF reanalysis data sampled on MIPAS locations and times (right panels of Figure 5.5). Since ECMWF temperatures include a tidal signature, this comparison allows to separate possible artifacts related to horizontal temperature inhomogenities from tides. The differences obtained from ECMWF data give a very similar picture as the observations, however, with a slightly smaller amplitude of the migrating diurnal tide. Since it is very unlikely that a stronger tidal amplitude in the observations is triggered by horizontal temperature inhomogenities it can be concluded that the smaller amplitude in ECMWF is a model-related feature. Apart of the tidal structures in the ascending-descending differences, MIPAS agrees very well with ECMWF (within 0.5 K), and therefore, no hint at relevant systematic errors related to horizontal temperature inhomogenities is found.

Other systematic errors arise from uncertainties in the radiometric gain (±1%), the instrumental line shape (ILS) (±3%) and the spectral shift previously retrieved. There are also errors coming from the $CO_2$ spectroscopic data used (*Flaud et al.*, 2006), mainly due to uncertainties in the strength, position and width of the emission lines (uncertainties assumed based on estimates supplied by J.M. Flaud, personal communication, 2008). The uncertainties in the abundances of interfering species in the microwindows used for the retrievals (mainly $O_3$ and $N_2O_5$, taken from climatology) are taken from estimates of *Remedios et al.* (2007). These errors are overall 0.5-1.2 K below 70 km and 1.2-3 K above.

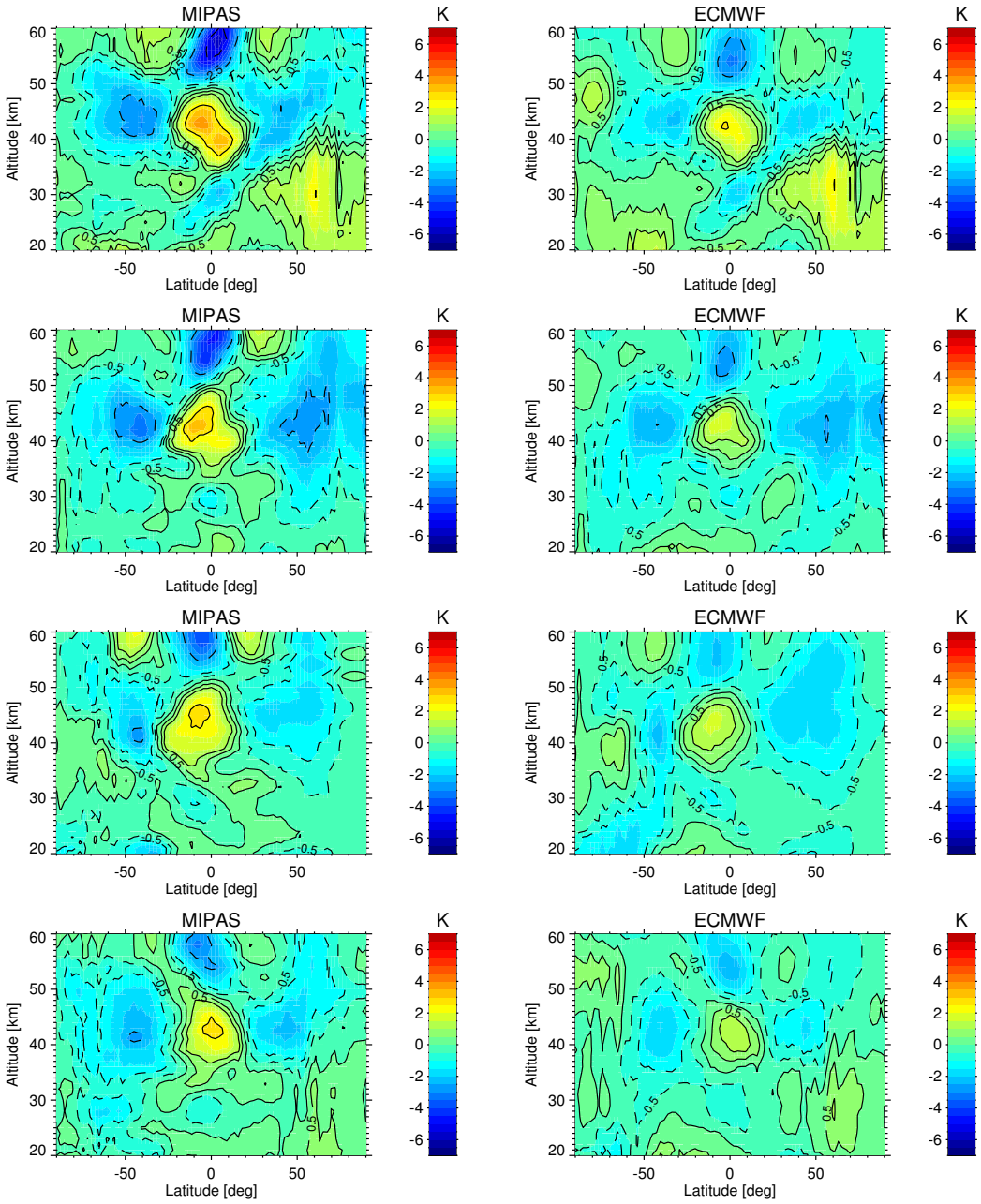


Figure 5.5: Seasonal averages of zonal mean temperature differences between descending (10 a.m.) and ascending (10 p.m.) MIPAS observations for 2008-2009 (left) and ECMWF (right) sampled at the corresponding MIPAS locations. Top to bottom: December-February, March-May, June-August, and September-November.

In Section 4.4 it was stated that in the TLOS retrieval the pressure profile is hydrostatically adjusted within each iteration by using the current guess of retrieved $T_k$ and a reference pressure and geometrical altitude taken from ECMWF. The altitude of this reference pressure point is selected near below the lowermost tangent altitude, that is, at around

20 km for MIPAS *MA* observation mode and near 40 km for *NLC* and *UA* modes. ECMWF data is known to be very accurate below 10 hPa (∼30 km), but above, ECMWF temperature data is affected by cold biases, around 3-4 K near 40 km, possibly due to problems in the treatment of radiation and dynamics and to the lack of radiosonde data at these altitudes (*Randel et al.*, 2004). This bias in ECMWF temperature turns into an uncertainty in the reference pressure of around 1.5%, derived from the equation of ideal gases. In order to assess a possible effect of this uncertainty on the retrieved parameters, an extreme situation has been proposed in which, the pressure at the reference point has been modified by ±15%. The retrieved atmosphere (pressure and temperature profiles) assuming the positive (negative) variation is expanded (contracted) with respect to the nominal values (see Figure 5.6) by ∼1 km. That is, the retrieved pressure profile and tangent altitudes are increased (decreased) by a 15% and 1 km, respectively, along the whole altitude range (40-100 km). This linear response of the retrieval to such a change in the reference pressure allows to extrapolate the result to the estimated uncertainty of 1.5%, yielding an uncertainty in the hydrostatic profile of 100 m, which is of minor importance for TLOS retrievals of MIPAS *NLC* and *UA* measurements.

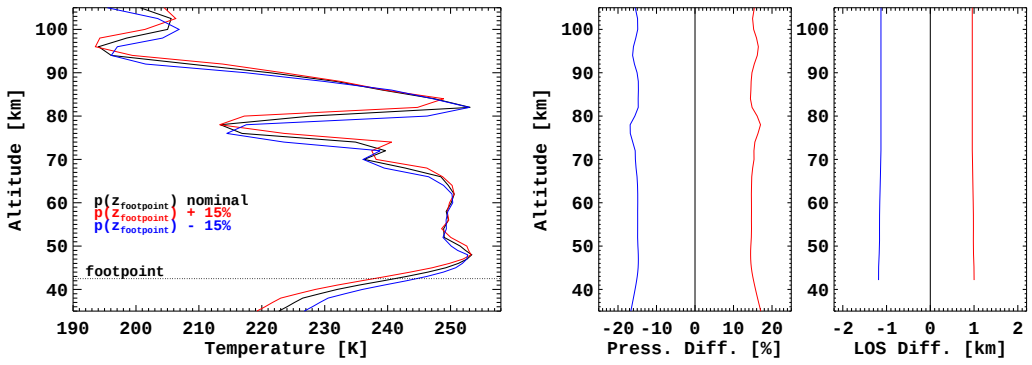


Figure 5.6: Effect of a change in the footprint pressure value on a TLOS retrieval of an *UA* scan (Polar Winter conditions, 21 January 2005). The left panel shows the retrieved temperature for three cases: nominal reference pressure (black), increased by 15% (red) and decreased by 15% (blue). The mid panel shows the difference in the retrieved pressure. The change in the retrieved pointing (LOS) is shown in the right panel.

A summary of typical estimated systematic errors in MIPAS v511 (*MA*), v611 (*UA*) and v711 (*NLC*) $T_k$ is given in Table 5.6. The overall systematic error is 0.5-1.2 K below 70 km, 1.2-3.7 K from 70 to 85 km and 3.7-12 K from 85 to 100 km. In the polar summer, where the non-LTE effect is larger, these values increase to 6 K at 85 km and 30 K at 100 km.

Table 5.6: Summary of main random and systematic errors in MIPAS $T_k$ (in K). Values in parenthesis are the errors for polar summer conditions

| | Altitude [km] | | | | |
|---|---|---|---|---|---|
| Source | 20 | 55 | 70 | 85 | 100 |
| *Systematic* | | | | | |
| Non-LTE | 0.0(0.0) | 0.0(0.0) | 0.1(0.1) | 1.4(4.7) | 11(30) |
| $[CO_2]$ | 0.06 | 0.03 | 0.12 | 2.3 | 1.6 |
| $[N_2O_5]$ | 0.05 | 0.1 | 0.3 | 0.14 | 0.03 |
| $[O_3]$ | 0.3 | 0.3 | 0.1 | 0.3 | 0.2 |
| Spectroscopic | 0.2* | 0.5* | 0.5# | 0.5# | 0.5# |
| Shift | 0.01 | 0.1 | 0.1 | 0.4 | 0.2 |
| Gain | 0.2 | 0.7 | 0.5 | 0.6 | 1.5 |
| ILS | 0.3 | 0.6 | 0.9 | 2.4 | 2.6 |
| Total Sys. | 0.5(0.5) | 1.1(1.1) | 1.2(1.2) | 3.7(5.8) | 12(30) |
| *Random* | | | | | |
| Noise (single scan) | 0.5 | 1.0 | 1.5 | 5.1 | 6.6 |

*From *von Clarmann et al.* (2009). #Extrapolated from *von Clarmann et al.* (2009).

## 5.2. Validation of MIPAS Temperature

In order to evaluate possible temperature biases, retrieved MIPAS kinetic temperatures (v511, v611, v711) from 2005 to 2009 have been compared with co-located measurements from other seven instruments and with a climatology at the northern high latitude summer from falling sphere measurements. The selection of instruments includes space-borne (SABER, ACE-FTS, MLS/Aura), ground-based (Mauna Loa and Table Mountain lidars, Davis and SATI spectrometers) and in-situ measurements (falling spheres). Out of them, only SABER measurements are affected by non-LTE effects[1], therefore, the set of instruments is well suited to validate MIPAS kinetic temperature in the mesosphere-lower thermosphere (MLT) region, for which the largest systematic errors come from non-LTE sources (see Table 5.6).

The coincident measurements (co-locations) have been chosen so that MIPAS observations were taken less than 1000 km and 2 hours apart from space-borne measurements. For ground-based measurements, this criterium is extended to 1500 km and 4 hours in order to increase the number of co-located measurements to have a meaningful statistical significance.

When a comparison between two instruments is addressed, it is nece-

[1]For each instrument, its measurement technique is briefly described in its corresponding section.

ssary to take into account the vertical resolutions of each instrument and the *a priori* information used in their respective retrievals. Let's see why. The relation between the retrieved atmospheric state parameter (the temperature profile in this case), the *a priori* information and the "true" value is given by (*Rodgers*, 2000):

$$\mathbf{T}_{ret} = \mathbf{T}_{ap} + \mathbf{A}\left(\mathbf{T}_{true} - \mathbf{T}_{ap}\right) + \epsilon, \tag{5.1}$$

where $\mathbf{A}$ is the *averaging kernel* matrix as defined in Section 3.4, and $\epsilon$ is the retrieval error. In practice, when comparing measurements from instruments with different vertical resolution, the influence of the *averaging kernel* matrix on the measurements taken with the instrument with better vertical resolution can be neglected and thus, these measurements can be considered the "truth" (*Rodgers and Connor*, 2003). Hence, the "true" temperature profile in Equation 5.1 can be replaced with the temperature profile retrieved using measurements from the instrument with better vertical resolution, $\mathbf{T}_R$:

$$\mathbf{T}_{smooth} = \mathbf{T}_a + \mathbf{A}\left(\mathbf{T}_R - \mathbf{T}_a\right), \tag{5.2}$$

where $\mathbf{T}_{smooth}$, is a smoothing of $\mathbf{T}_R$, and represents the profile that would be retrieved using measurements from the instrument with worse vertical resolution if the "true" temperature profile was equal to $\mathbf{T}_R$.

In case that MIPAS is the instrument with worse vertical resolution, the individual measurements from the other instrument are smoothed using the co-located MIPAS averaging kernel matrix and *a priori* profile. When the opposite occurs, the MIPAS measurements are smoothed accordingly, using averaging kernel matrix and *a priori* profile from the co-located measurement from the other instrument. No smoothing is applied when both instruments have similar vertical resolutions.

The comparisons are made in terms of the MIPAS bias profile, $\mathbf{b}$, which is estimated from the average difference of the coincident individual profiles:

$$\mathbf{b} = \frac{\sum_i (\mathbf{T}_{mipas,i} - \mathbf{T}_{instr,i})}{N}, \tag{5.3}$$

where $\mathbf{T}_{mipas,i}$ and $\mathbf{T}_{instr,i}$ are, respectively, the MIPAS and the other instrument coincident kinetic temperature profiles (smoothed or not according to the particular case), and $N$ is the number of coincidences. The bias error $\sigma_{\mathbf{b}}$ has been estimated with:

$$\sigma_{\mathbf{b}} = \sqrt{\frac{\sum_i (\mathbf{T}_{mipas,i} - \mathbf{T}_{instr,i} - \mathbf{b})^2}{N(N-1)}}. \tag{5.4}$$

The estimated bias is not considered significant while it stays smaller than the combination of the MIPAS systematic error, $\sigma_{sys,mipas}$

(see Section 5.1.1), and the instrument systematic error, $\sigma_{sys,instr}$, defined as:

$$\sigma_{comb,sys} = \sqrt{\sigma^2_{sys,mipas} + \sigma^2_{sys,instr}}\,. \tag{5.5}$$

Since it is expected a possible bias dependence on season and latitude, the comparisons have been split in subsets of three months for every year: two for solstices (December from the previous year, January and February, and June, July and August) and two for equinoxes (March, April and May, and September, October and November). For comparisons with satellite instruments, the comparisons have been grouped in 20°-wide latitude boxes. For each latitude band, season and year, zonal mean temperatures as well as average differences have been calculated for the coincident MIPAS and other instrument profiles.

The comparisons have been performed using MIPAS *MA* measurements since this observation mode covers a larger altitude range than *NLC* and *UA* (*MA* limb scanning extends down to 18 km, compared to 42 km for *NLC* and *UA*). Nevertheless, the quality of the results obtained from the comparisons with *MA* are absolutely valid for *NLC* and *UA* measurements.

### 5.2.1. SABER/TIMED

The Sounding of the Atmosphere using Broadband Emission Radiometry (SABER) orbits the Earth onboard the NASA's TIMED satellite since the end of 2001. It measures continuously and almost globally (52°S-82°N, alternating with 52°N-82°S every two months) the daytime and nighttime atmospheric infrared emission in ten broadband channels (*Russell III et al.*, 1999). The kinetic temperature is derived from about 20 km up to 110 km from measurements of the $CO_2$ emission at 15 $\mu$m using the onion-peeling technique and a Levenberg-Marquardt approach with a retrieval algorithm that considers non-LTE. More details on the $T_k$ retrieval can be found in *Remsberg et al.* (2008). The current SABER version, 1.07, has been used for the comparisons. SABER $T_k$ random errors are mainly due to noise (<0.6 K below 55 km, 1 K at 70 km, 2 K at 85 km and 7 K at 100 km) and the systematic errors are mainly due to uncertainties in the $CO_2$ abundance and the non-LTE parameters (<1.5 K below 55 km, 0.5 at 70 km, 4 K at 85 km and 5 K at 100 km) (see further details in *García-Comas et al.* (2008)).

The quality of SABER $T_k$ is assessed in *Remsberg et al.* (2008). The main conclusions are: i) SABER v1.07 temperatures are too high by 2-3 K in the lower stratosphere, and too low by 1 K in the upper stratosphere and by 2-3 K in the mid-mesosphere; ii) in the upper mesosphere and lower thermosphere, SABER comparisons with other instruments are more variable and show agreement within ±5 K at mid-latitudes.

Using the 2-hour and 1000 km coincidence criterium, there are a large

number of co-located measurements of MIPAS and SABER between 2005 and 2009. Their measurements have been compared in 20°-wide latitude boxes and for 3-month seasons of each year. For each of these, an average number of coincidences ranging from 800 at the tropics to 2800 at polar latitudes have been found. The total number of coincidences for all years is about 5000 at the tropics and 14000 at the poles. SABER vertical resolution is about about 2 km, slightly better than MIPAS', particularly above the stratopause, hence, SABER $T_k$'s have been smoothed to MIPAS' vertical resolution according to Equation 5.2.

Figure 5.7 shows comparisons for MIPAS and SABER co-locations for the summer (left column) and winter (right column) solstices at the tropics (10°-30°), mid-latitudes (30°-40°), high-latitudes (50°-70°) and the poles (70°-90°). The comparisons were done for coincidences during three-month long periods: December, January and February for the northern hemisphere (NH) winters and southern hemisphere (SH) summers, and June, July and August for the NH summers and SH winters.

The differences at all latitudes show 2-3 K colder MIPAS temperatures in the lower and mid-stratosphere, most likely due to the known SABER bias at those altitudes. That difference is not dependent on latitude, season nor year, although the yearly variability is slightly smaller at low latitudes. Altitudes from 40 to 60 km are generally about 1-3 K colder in MIPAS data during the summers, increasing with latitude until reaching a difference of -4 K at 50 km in the polar summers in both hemispheres. During the winters, this region shows similar temperatures, with MIPAS 0.5-1 K larger values, except for winters at high latitudes (50°-70°), where MIPAS is 3-4 K warmer. Half of these differences in the winters could be explained by the known SABER cold bias.

MIPAS and SABER comparisons in the mid and upper mesosphere are very good, generally within the estimated systematic error. The mid-mesosphere (up to 80-85 km) is slightly colder for MIPAS but the differences are usually smaller than 2 K. The worst case is at latitudes higher than 50°, where it goes up to 3-5 K, but still the behavior is excellent since the vertical gradient under those conditions is particularly large (see, for example, the typical polar summer $T_k$ profile in Figure 5.3). The differences in the NH polar winter of 2009 are significantly larger between 75 and 95 km than in other seasons and latitudes. That corresponds to altitudes where the high stratopause was located after the 2009 Stratospheric Sudden Warming (SSW), and MIPAS measures there temperatures 10-12 K larger than SABER.

In the upper mesosphere (up to 85-90 km), temperature differences lie below the combined errors, showing a systematic behaviour for all latitudes and seasons. It is noticeable that these differences are larger in polar summers, where it is known that the $CO_2$ vibrational levels which give rise to the band emission eventually measured by SABER and MIPAS

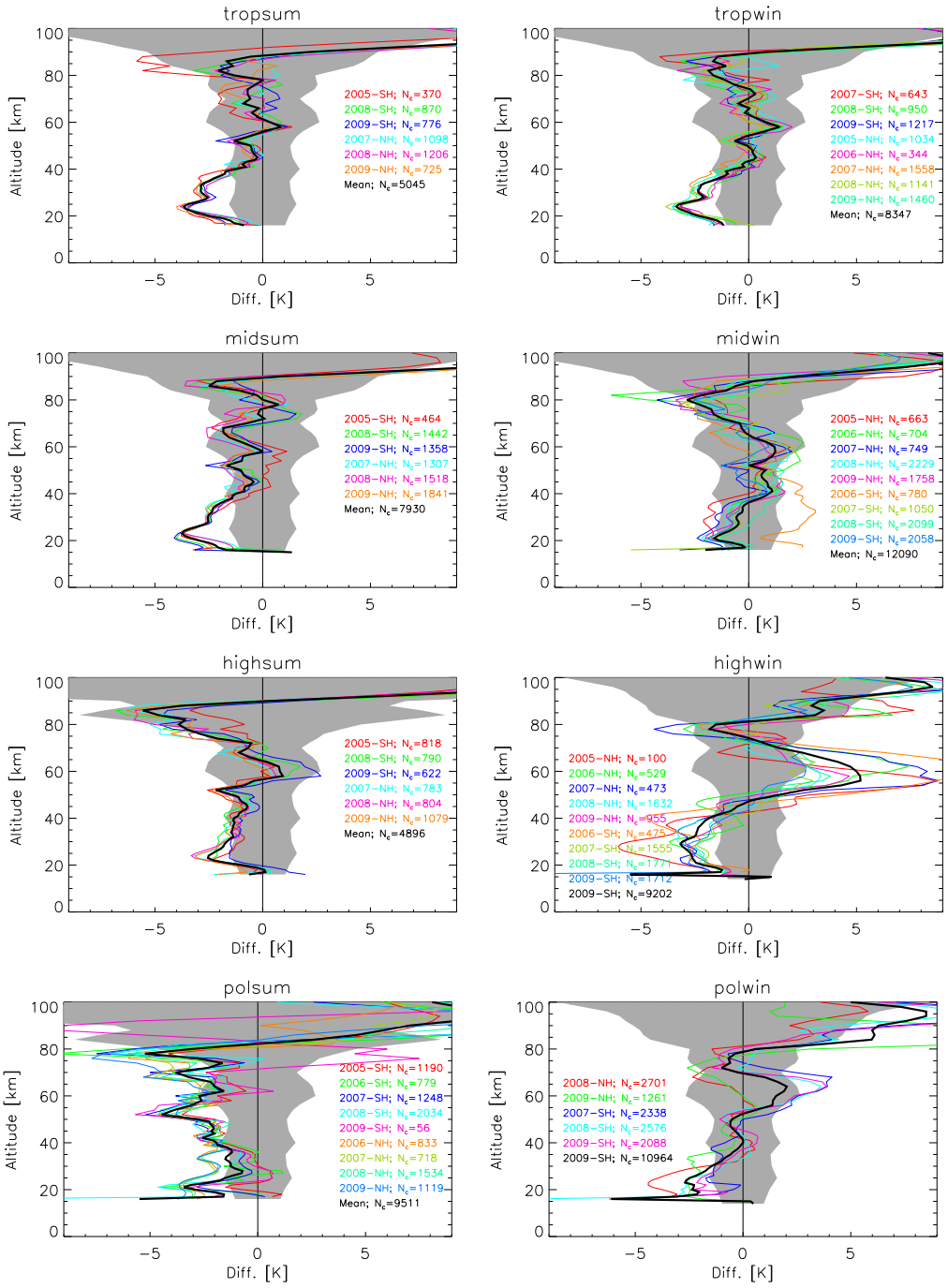


Figure 5.7: Mean temperature differences (MIPAS v511 minus SABER v1.07) for solstice conditions (left: summer; right: winter) and different latitudes: tropics (10°-30°;1$^{st}$ row), mid-latitudes (30°-50°; 2$^{nd}$ row), high latitudes (50°-70°; 3$^{rd}$ row), and the poles (70°-90°; 4$^{th}$ row). The differences averaged for the different years and hemispheres (for which the number of co-located measurements are also indicated) are shown in different colours (see legends). The average difference is shown in black. The shadowed area is the MIPAS and SABER combined systematic error.

have populations farther away from LTE. On the one hand, SABER is more sensitive to $CO_2$ hot bands, which are more affected by non-LTE than the $\upsilon_2$ fundamental band; on the other hand, MIPAS and SABER non-LTE parameterizations are not exactly the same.

The rate of $\upsilon_2$ V-V exchange ($k_{vv}$) is the same for both instruments for energy exchange involving the $\upsilon_2$ >1 states but the one involving the isotopes included in the MIPAS non-LTE scheme doubles that of SABER. According to *García-Comas et al.* (2008), equalling SABER v1.07 rates to the values used for MIPAS retrievals ($2.4\times10^{-11}\,cm^3s^{-1}$) would increase SABER mesopause temperatures in 3 K in the polar summer, reducing the SABER-MIPAS difference to 2 K. That would barely affect the temperature at mid-latitudes or polar winter. The rate of the $\upsilon_2$ states quenching by $N_2$ and $O_2$ ($k_{air}$) is also slightly different at very low $T_k$. Whereas both MIPAS and SABER retrievals use the same value for temperatures larger than 150 K, MIPAS' uses a threshold in this rate, keeping it constant for temperatures smaller than 150 K. Therefore, the value used in MIPAS retrievals is 15% larger at 125 K, which, if used in SABER retrievals would increase 1 K the retrieved temperature around the summer mesopause, reducing the difference with MIPAS at these latitudes.

The difference in the mesopause region could also be caused by the different atomic oxygen abundance used in the non-LTE models. During nighttime, both MIPAS and SABER [O] VMR are taken from the MSIS database at all altitudes but, during daytime, SABER uses the [O] derived from SABER $O_3$ retrieval of 1.27 $\mu$m measurements below 90 km. Typical MIPAS daytime [O] near the mesopause region is 50% smaller than SABER daytime [O], except for the polar summer, where it is 50-70% larger. If MIPAS mid-latitude [O] is used in SABER retrievals, the derived $T_k$ would be around 1.5 K larger at 90 km for mid-latitudes (*García-Comas et al.*, 2008), leading to a better agreement between MIPAS and SABER. The use of larger MIPAS polar summer [O] in SABER retrievals would lead to an increase in the retrieved $T_k$. Therefore, the different [O] used in MIPAS and SABER could explain half of the observed differences around the mesopause for all latitudes.

In summary, the difference of non-LTE collisional processes parameterization, in particular, $k_{vv}$ ,$k_{air}$ and the atomic oxygen abundance, in MIPAS and SABER retrievals, partially explains the temperature difference. Using the same values in both instruments retrievals would lead to an almost perfect agreement between the instruments at all latitudes, except in the polar winter, where the difference would be reduced to 3 K.

MIPAS temperatures in the lower thermosphere (above 85-90 km) are also warmer than SABER's (5-15 K, depending on the latitude band). A 50% larger SABER atomic oxygen in v1.07 could explain these differences. Alternatively, since both MIPAS and SABER show similar temperature gradients

at these altitudes and MIPAS lacks of information on absolute pointing at these altitudes, the differences could also be explained by a MIPAS negative (positive) altitude (pressure) shift.

### 5.2.2. ACE-FTS

The Fourier Transform Spectrometer (FTS), onboard SCISAT-1 (also known as Atmospheric Chemistry Experiment's or ACE), operates with a Michelson interferometer from 2.2 to 13.3 $\mu$m with a high spectral resolution (0.02 $cm^{-1}$). It is a solar occultation instrument which scans the atmosphere twice per orbit (sunrise and sunset). The sampled latitude and the latitude coverage depends on the season, covering all possible latitudes in about 2 months. This instrument is self-calibrating because the solar occultation spectra are divided by exoatmospheric solar spectra from the same occultation. The vertical sampling is variable but is usually done every 1-3 km in the troposphere and 5-6 km above. Its circular 1.25 mrad field of view provides a maximum vertical resolution of 3-4 km. Atmospheric temperature profiles are determined as a function of pressure (later converted into altitude) from measurements of the $CO_2$ atmospheric absorption of the sunlight using a global fit approach and the Levenberg-Marquardt non-linear least-squares method. Details on the retrieval algorithm are in *Boone et al.* (2005). Data version 2.2 is used here. The selected spectral microwindows above 70 km are restricted to absorption from lower-state vibrational bands in order to minimize non-LTE effects. The *a priori* profiles are taken from the MSIS atmospheric model combined with meteorological data from the Canadian Meteorological Centre. The $CO_2$ volume mixing ratio is assumed constant below a certain altitude (65-70 km, depending on latitude) and empirically determined above. The kinetic temperature is retrieved from the cloud top to about 100 km. ACE-FTS temperature precision, estimated from comparisons with lidars, provide is around 2 K (*Sica et al.*, 2008). They did not analyze, however, the systematic errors.

ACE-FTS temperatures have been compared with other instruments (*Sica et al.*, 2008), resulting in 2 K colder in the upper stratosphere and about 5 K warmer in the lower mesosphere. The latter statement was based on the comparison with SABER v1.06 but SABER is colder than other instruments by 2-3 K in that region (*Remsberg et al.*, 2008). Thus, ACE-FTS warm bias may be reduced to 2-3 K in the lower mesosphere. Although, due its moderate vertical resolution, the temperature structures in the upper mesosphere are significantly smoothed out, its magnitude generally agrees fairly well with lidars measurements. ACE-FTS temperatures at southern high latitudes at 87 km during the winter (compared to Davis OH spectrometer) are, however, 5-7 K too cold, and comparisons with HALOE show an ACE-FTS 5-6 K warmer upper mesosphere. Since there is no ACE-FTS systematic error estimation available, the comparisons presented in *Sica et al.*

(2008) have been used to compute the combined systematic error ($\sigma_{instr}$ in Equation 5.5).

The total number of ACE-FTS and MIPAS coincidences for the 2005-2009 period ranges from 60 (polar summer) to 500 (winter at 50°-70°). All coincidences are located at latitudes higher than 50°. Since ACE-FTS and MIPAS have similar vertical resolution in the upper mesosphere and lower thermosphere, no convolution was applied in this comparison.

Comparisons for spring and autumn for all latitudes, and for the winter and summer solstices divided in high (50°-70°) and polar (70°-90°) latitudes and years from 2005 to 2009 are shown in Figure 5.8. Differences up to 45 km are smaller than 1 K and within the systematic error in most cases, except for the lowest few kilometers of MIPAS measurements during the polar winters. Polar winters also show a larger variability with year than other seasons. MIPAS is generally colder than ACE-FTS in the stratosphere, except in the polar summer. The comparison there is particularly good. Differences at 50 km are slightly larger, and MIPAS is about 2 K colder, except in the polar summer.

MIPAS measurements are also colder than ACE-FTS' in the lower and middle mesosphere but the differences are somewhat larger. The differences there range from 2 K right above the stratopause to 3-4 K at 70-75 km. In polar summer, the difference is smaller. This result can be explained by the 2-3 K warm bias detected in ACE-FTS at those altitudes (*Sica et al.*, 2008).

Between 75-85 km, MIPAS is significantly colder, with maximum differences from 4 K to 12 K, the latter in the polar summer. That happens at all seasons except during the winter, where the maximum differences range from 5 K in the 50°-70° latitudinal band to 10 K around the pole (or to 6 K if the comparison for 2009 NH winter is removed, when the SSW occurred and MIPAS temperatures at 85 km are 30 K warmer). As in the comparisons in the lower mesosphere, these results are also consistent with the 5-6 K ACE-FTS warm bias found in comparisons with other instruments and the 5-7 K cold bias found in the night comparisons for the southern high latitudes. If the known biases found for ACE-FTS are subtracted, the remaining difference is small ($< 1$ K) in all seasons and latitudes, except for polar summer, where it is -6 K around the mesopause. This remaining negative difference could be reduced by using a more efficient $CO_2$ $\upsilon_2$ quenching or faster $CO_2$-$CO_2$ $\upsilon_2$ transfer rate in MIPAS non-LTE retrievals, which would lead to a 4-5 K increase in the MIPAS retrieved $T_k$ at 85 km. Still, the remaining difference could also be due to a further positive bias in ACE-FTS temperatures during this season.

In the lower thermosphere, above 85-90 km, MIPAS shows warmer temperatures. The difference between both instruments there are more pronounced during the spring and summer. In autumn and winter, the differences are significantly smaller (up to 7-10 K). Although these differences can be

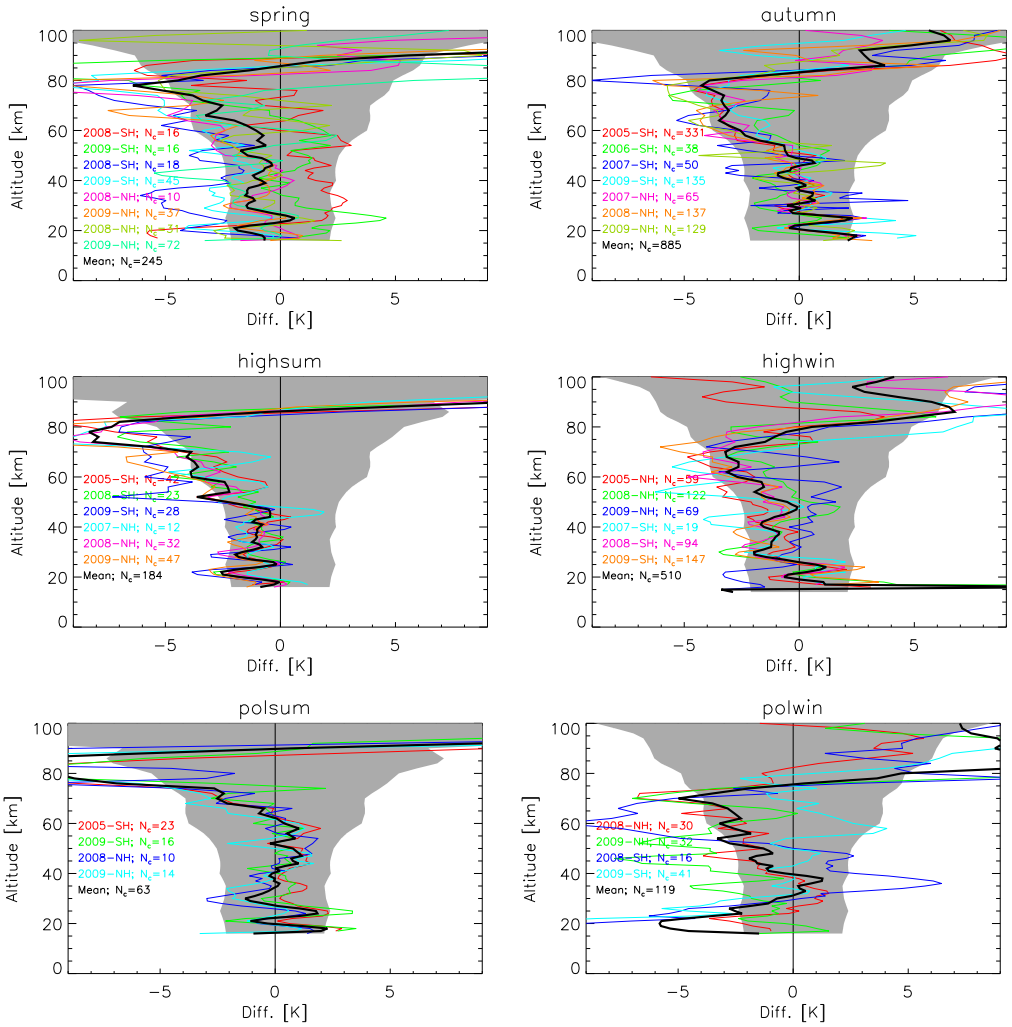


Figure 5.8: Average temperature differences (MIPAS v511 minus ACE-FTS) for spring and autumn (upper row), high latitudes (50°-70°) summer and winter (middle row), and polar (70°-90°) summer and winter (bottom row). The differences averaged for the different years and hemispheres (the number of co-located measurements are also indicated) are shown by different colours (see legends). Average difference for each period and latitude box is shown in black. The shadowed area is the MIPAS and ACE-FTS combined error.

partially explained with the negative bias found in the ACE-FTS, the use of larger [O] and $k_{air}$ would turn into smaller MIPAS $T_k$ and hence would reduce that differences at all latitudes and seasons.

### 5.2.3. MLS/Aura

The Microwave Limb Sounder (MLS) is a radiometer on board NASA's EOS Aura satellite, which flies in a sun-synchronous near-polar 705-

km-altitude orbit since its launch in mid 2004. MLS continuously observes the limb thermal microwave emission viewing forward along the Aura spacecraft flight direction, scanning its view from the ground to ∼90 km every ∼25 seconds, which provides profiles spaced about 165 km. It measures near-globally (82°S-82°N) both day and night and it completes about 14.5 orbits a day. MLS provides temperature of the atmosphere from 316 to 0.001 hPa from retrievals of the oxygen thermal emission at 118 and 190 GHz. These microwave measurements are not affected by the presence of ice clouds and aerosols nor non-LTE effects. The MLS data used here is version 2.2. As described in *Schwartz et al.* (2008), kinetic temperature is retrieved using the optimal estimation theory. The *a priori* is a merging of the GEOS-5 profiles below 1 hPa and the CIRA86 climatology above. MLS $T_k$ vertical resolution is 5 km from 316 to 100 hPa, 4 km from 31 to 3.16 hPa, 8 km from 1 to 0.316 hPa and 14 km at 0.1 hPa. The temperature random error, resulting mainly from radiometric noise, range from 0.6 K in the lower stratosphere to 2.5 K in the mesosphere. The systematic error, coming mainly from the radiometric and spectral calibration, is about 2 K at most altitudes, increasing to 3-4 K in the upper mesosphere.

A comprehensive study of the error budget and validation of MLS kinetic temperature is given in *Schwartz et al.* (2008). It yields a MLS cold bias in the lower stratosphere of 2 K. Differences with other instruments in the upper stratosphere and mesosphere are more variable but they point to a 2-3 K warm bias and a 0-7 K cold bias, respectively.

The coincidence criterium applied to MIPAS and MLS measurements from 2005 to 2009 provides a number of coincidences ranging from 400 at mid-latitudes to more than 70,000 at polar latitudes. Since MLS temperatures are provided as a function of pressure, the comparisons shown here were done on a pressure grid. MLS vertical resolution is worse than MIPAS', particularly, above the mid-mesosphere. Therefore MLS averaging kernels and *a priori* temperatures have been applied to MIPAS profiles (according to Equation 5.2).

The behaviour of the comparisons between MIPAS and MLS is very similar at all latitudes and all year round, both in the solstices (Figure 5.9) and the equinoxes (not shown), particularly below $10^{-3}$ mb. Temperatures measured by both instruments differ by less than 2 K below the 5 mb level (∼40 km) and is within the combined systematic error. The difference is slightly larger (being MIPAS 3 K warmer) at the winter tropopause (∼50 mb, ∼20 km), in agreement with the too cold MLS lower stratosphere reported in *Schwartz et al.* (2008). MIPAS temperature at 1 mb is colder at all seasons (MIPAS-MLS difference range from -2 K at mid-latitudes in the summer to -5 K in the polar summer). That could be partially explained by the 2-3 K warm bias in MLS upper stratosphere temperatures.

In the mesosphere (up to 0.005 mb in the polar summer and 0.001 mb in the polar winter), MIPAS temperatures are around 1-7 K warmer than MLS',

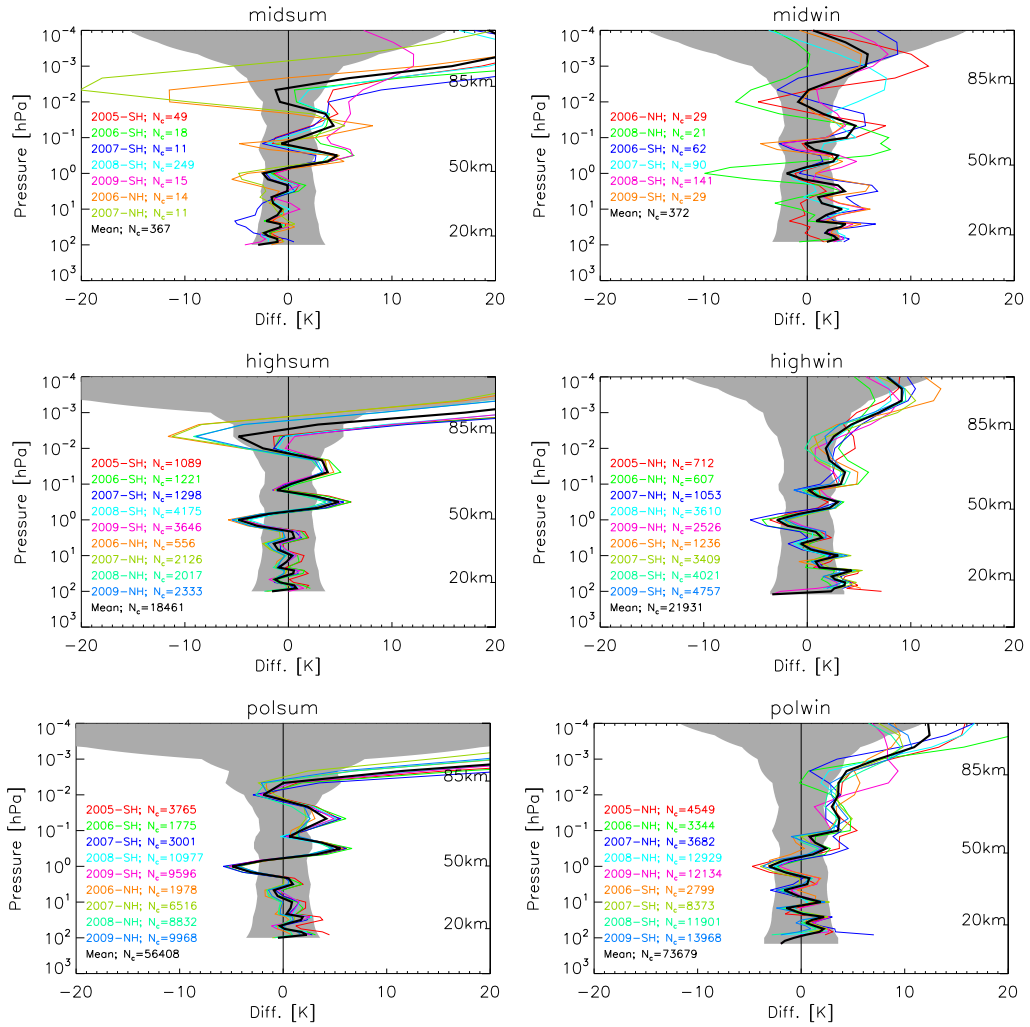


Figure 5.9: Average temperature differences (MIPAS v511 minus MLS v02) for solstice conditions (left: summer; right: winter) at different latitudes: mid-latitudes (30°-50°; upper row), high latitudes (50°-70°; middle row), and polar (70°-90°; bottom row). Differences averaged for the different years and hemispheres (the number of co-located measurements are indicated) are shown in different colours (see legends) and average difference for each period and latitude is shown in black. The shadowed area is the combined error. The corresponding mean MIPAS approximate altitude is also shown.

except for the MIPAS 1-4 K colder region at 0.01 mb in the summers. These differences are almost independent on latitude and season, and can be explained by the MLS 0-7 K cold bias detected by *Schwartz et al.* (2008).

The variability of the difference between hemispheres is small, except for the summer high latitude box around 0.01 mb, where averaged MIPAS $T_k$'s are colder than MLS' at 0.01 mb. This average negative difference mainly arises from a larger northern hemisphere negative difference. MLS

temperatures during the NH summers are too warm at those pressures and, contrary to MIPAS, show a very small variation with respect to the SH high latitude summer temperatures. Thus, while MIPAS temperatures at the polar summer mesopause is, on average, 8 K colder in the NH than in SH, in agreement with the well known inter-hemispheric difference in the polar summer mesopauses' temperatures (*Brasseur and Solomon*, 2005), MLS finds a polar summer mesopause in NH just 1.5 K warmer than in SH.

In the lower thermosphere (above 0.005 mb in the polar summer and 0.001 mb in the polar winter), MIPAS $T_k$'s are warmer than MLS', with differences more pronounced in the summers. As it has been discussed with SABER and ACE comparisons, considering larger [O] could reduce such difference.

### 5.2.4. Table Mountain and Mauna Loa lidars

The NASA Jet Propulsion Laboratory (JPL) runs two Differential Absorption Lidars (DIAL) in the Table Mountain Facility (TMF; 34°N, 118°W) and the Mauna Loa Observatory (MLO; 20°N, 156°W). The systems combine Rayleigh/Mie and nitrogen vibrational Raman scattering techniques, and includes 8 receiving channels (4 channels operating at the ozone-absorbed wavelengths of 308 nm and 332 nm, and 4 channels at the non-absorbed wavelengths of 355 nm and 387 nm). Besides ozone and aerosol backscatter ratio, the combination of its channels allows nighttime temperature retrievals between 12 km and 90-95 km with a vertical sampling of 300 m. Their typical temporal resolution ranges from 5 minutes to 2 hours and their measurement frequency from 3 to 5 times per week. Lidar temperature profiles have an effective vertical resolution of 1-2 km from 10 to 65 km, 2-4 km from 65 to 80 km and 7 km at 90 km. The precision (estimated from the statistics of the shot noise for the laser source) is smaller than $\pm$1K at 55 km and below $\pm$5 K at 80 km. More details on the instruments performance and algorithms used to derive temperature can be found in *McDermid et al.* (1995) and *Leblanc et al.* (1998). The dataset is publicly available through the Network for the Detection of the Atmospheric Composition Change (NDACC) Data Archive Center (http://www.ndsc.ncep.noaa.gov). Estimates of the errors can be found also in *Leblanc et al.* (1998), who determined errors of 4 K below 25 km, <1 K from 30 km to 60 km, 10 K at 80 km, and 15 K at 90 km.

The TMF lidar have been compared to the Goddard Space Flight Center (GSFC) mobile lidar, showing differences of 5 K at 30 km, 1 K at 40 km and 3 K at 50 km. However, the measurements were not made at the same time and some tidal effects might have been present. Comparisons with the Observatoire de Haute Provence and the GSFC lidars give differences of 1-2 K around the stratopause and 3-4 K at 80 km, although tidal effects were not removed (*Keckhut et al.*, 2004).

The coincidence criterium of 4-hour and 1500 km apart from the lidars provided 163 coincidences (103 during solstices and 60 during equinox) for Mauna Loa and 142 (74 in solstice and 68 in equinox) for Table Mountain. Due to the better vertical resolution of the lidars, their derived $T_k$'s have been degraded using MIPAS averaging kernel and *a priori* information.

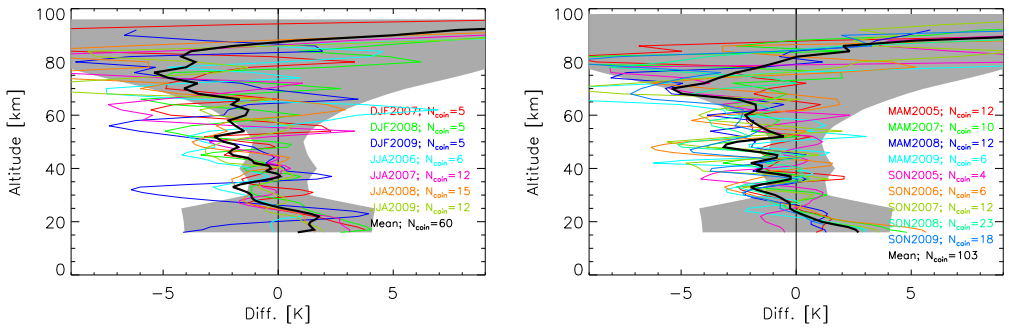


Figure 5.10: Mean temperature differences (MIPAS v511 minus Mauna Loa) for solstice (left) and equinox (right). The seasons, years and number of coincidences are indicated by different colours (see legends). The average difference is shown in black. The shadowed area is the combined systematic error.

The average differences between MIPAS and the lidar at MLO for the solstices and the equinoxes are shown in Figure 5.10. Both seasons exhibit similar values: MIPAS is 1-2 K warmer around 20 km and 1-2 K colder from 25 to 65 km. The difference increases to -5 K around 75 km in solstice and 70 km in equinox. The difference slightly exceeds the combined error between 40 km and the mid-mesosphere (70 km), where the non-LTE effects are not important. At 85 km, the difference rapidly becomes positive (MIPAS is warmer) and is +5 K in solstice and +10 K in equinox at 90 km. This change of sign around that altitude is related to the lower altitude of the mesopause in MIPAS profiles compared to the lidar, whose mesopause is generally located above 90 km or even does not show up. The average differences lie within the combined errors at those altitudes. The comparison does not change dramatically from year to year, although the variability for the solstices is larger than for the equinoxes.

The average differences between MIPAS and TMF lidar temperatures are shown in Figure 5.11 for all solstices (left panel) and equinoxes (right panel), respectively, from 2005 to 2009. As with the comparisons with the MLO lidar, MIPAS is also warmer (1-2 K) than the TMF lidar below 30 km. From 40 to 60 km in the solstice and from 40 to 70 km in the equinox, MIPAS is 1 K colder. Around 65 km in the solstice, it is about 1 K warmer. Differences at 75 km slightly increase in the solstice up to -3 K. The differences above 80 km also change in sign (although at a lower altitude than at MLO), become positive and reach 5-7 K at 90 km. All differences are

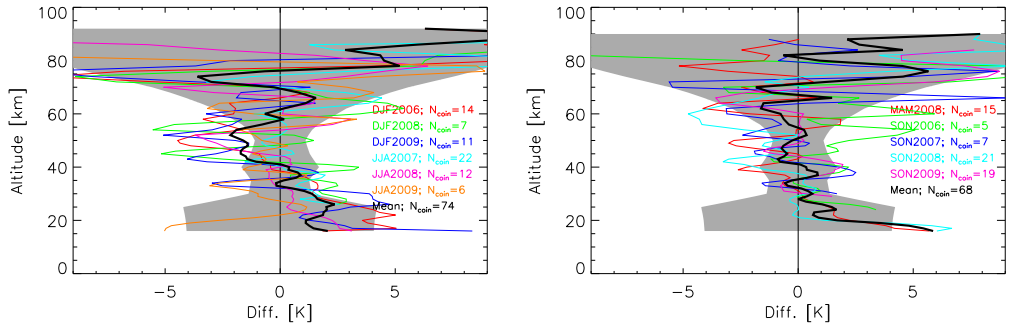


Figure 5.11: Mean temperature differences (MIPAS-Table Mountain lidar) for solstice (left) and equinox (right) . The seasons, years and number of coincidences are indicated by different colours (see legends). The average difference is shown in black. The shadowed area is the combined systematic error.

within the systematic errors at all altitudes, except at the stratopause during the equinox, where MIPAS is 1.5 K colder. In summary, comparisons with the TMF lidar show the same pattern as those with the MLO lidar, but with a better agreement, particularly in the middle mesosphere (70 km).

The positive bias found at 80-90 km for both lidars could be partially explained, as in the previous comparisons, by using a larger atomic oxygen abundance in MIPAS retrievals (midlatitude nighttime $T_v$-626-010 are under LTE and increasing [O] leads to a larger retrieved $T_k$). The considered uncertainty in [O] of 50% in MIPAS can account for an increase of 1-2 Kat these altitude range and mid-latitudes.

### 5.2.5. Sierra Nevada's SATI

The Spectral Airglow Temperature Imager (SATI) installed at the Sierra Nevada Observatory (37.06°N, 3.38°W), Granada, Spain, is a spatial and spectral imaging Fabry-Perot spectrometer in which the etalon is a narrow band interference filter and the detector is a CCD camera. The SATI instrumental concept and optical configuration is described in detail by *Sargoytchev et al.* (2004). The instrument uses two interference filters, one centered at 836.813 nm (in the spectral region of the OH Meinel (6-2) band) and another one centered at 867.689 nm (in the spectral region of the $O_2$ atmospheric (0-1) band). Since the peaks of maximum emission rate of $O_2$(0-1) and OH Meinel (6-2) are located at around 95 and 87 km, respectively, the derived nighttime $T_{OH}$ and $T_{O_2}$ rotational temperatures are a good indicator of kinetic temperature at such altitudes. The performance of the Sierra Nevada SATI is described in *López-González et al.* (2005). Since, up to date, there is not any study of SATI temperatures errors available, its precision is estimated from the standard deviation of temperatures measured during 1 hour, in about 5-10 minutes step. Such spread is assumed to be dominated by random errors more than

atmospheric variability. The values estimated in this way give a 5.5 K and and 3.5 K precisions for the OH and the $O_2$ temperatures, respectively. Regarding the systematic errors, there is no direct way to estimate them and, thus, they are not taken into account for the calculation of the combined systematic errors but only considered MIPAS systematic errors.

SATI temperatures have been validated by comparisons with SABER v1.06 for 2002-2006 period (*López-González et al.*, 2007), which show lower temperatures (6 K) for SATI at 87 km and 2.5 K higher temperatures at 95 km, and by comparisons with SABER v1.07 for 2002 (*Remsberg et al.*, 2008), which show 2 K larger temperatures for SATI at 87 km and 5 K at 95 km.

From the coincidence criterium of 4-hour and 1500 km away from SATI's measurements, a total of 19 nights from 2005 to 2009 have been compared, with a total of 173 MIPAS co-locations. SATI was out of order for more than a year (2008 and half 2009) and, thus, there is a lack of coincidences for that period. For the comparison, SATI measurements have been averaged for each night. In addition, since SATI averaging kernels are not known, it is assumed that $T_{OH}$ and $T_{O_2}$ are obtained for 87 km and 95 km, respectively, with a full width at half maximum (FWHM) of 10 km. The value chosen for FWHM is based on results from *Remsberg* (2008), where the estimation of the SATI $T_k$ kernel peak was derived from simultaneous SABER measurements of the OH emission. With these parameters, MIPAS $T_k$ profiles have been convolved and compared with SATI measurements.

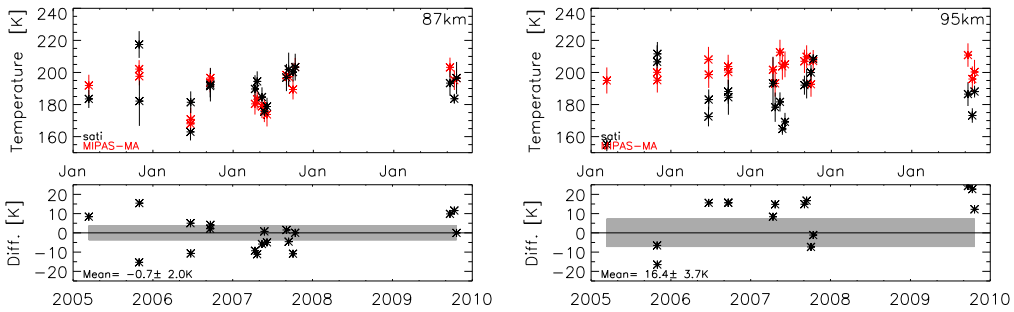


Figure 5.12: Nighttime MIPAS $T_k$ compared to SATI (37°N, 3°W) OH (left panels) and $O_2$ (right panels) rotational temperatures at 87 and 95 km, respectively, from 2005 to 2009. Top panels show absolute mean values (MIPAS, red; SATI, black), with their respective standard deviation (vertical bars). Bottom panels show the difference (MIPAS-SATI), the MIPAS systematic error (shadowed area) and the mean difference and its respective error.

MIPAS-SATI comparisons are shown in Figure 5.12. MIPAS $T_k$ at 87 km is in very good agreement with SATI OH temperature, both showing a similar seasonal pattern, with a colder mesopause during the summer. MIPAS $T_k$ is on average 0.7 K colder than SATI rotational temperatures, which is similar to the comparison with SABER v1.07. The average difference

in the whole period is within MIPAS estimated systematic error. The differences do not show any clear seasonal dependence. MIPAS temperatures in late 2009, when SATI was reinitialized after its failure, show a larger positive bias (+7 K), although the statistics, only three nights with coincidences, are poor to reach a clear conclusion.

Comparisons with SATI $O_2$ rotational temperatures reveal usually larger MIPAS temperatures at 95 km (16 K), although autumns of 2005 and 2007 show negative differences. The positive bias at these altitudes is present in the comparisons with all instruments. However the differences with SATI are larger for mid-latitude conditions (see e.g., lidars). The difference does not follow any clear seasonal pattern.

### 5.2.6. Davis station spectrometer

Hydroxyl rotational temperature over the Davis Station (DS; 69°S, 78°E), Antarctic, is derived from measurements with a Czerny-Turner scanning grating spectrometer. The temperature is derived from emissions OH in its (6-2) band (approximately at 87 km). A detailed description of the performance of the instrument and its temperature measurements is given in *French et al.* (2000) and *Burns et al.* (2002). The temperatures used here were determined from nighttime piece-wise scans collected in about 7.5 minutes. Temperature errors are usually less than 15 K and the vertical resolution is estimated to be about 8.7 km (*French and Mulligan*, 2010).

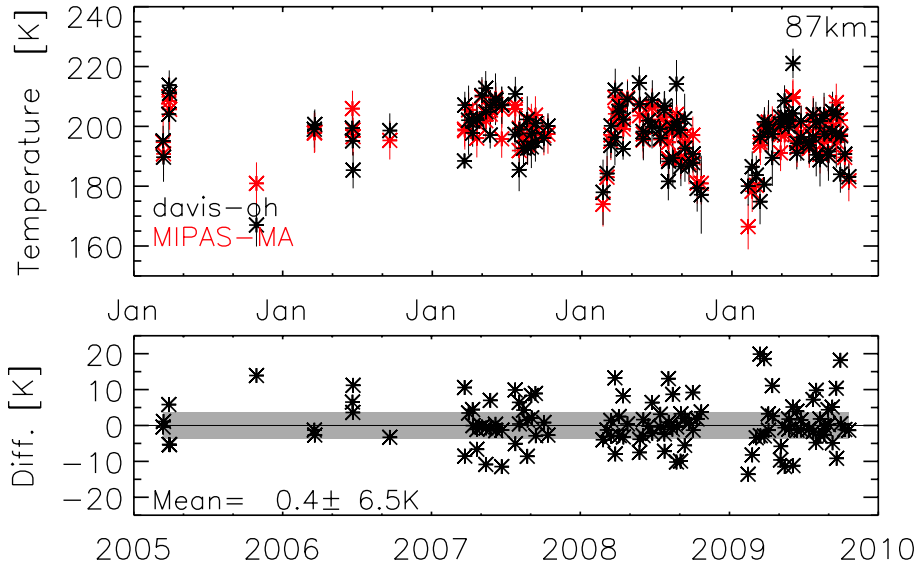


Figure 5.13: Nighttime MIPAS $T_k$ at 87 km (red) and Davis OH rotational temperatures (69°S, 78°E) (black) and their standard deviation (vertical bars) from 2005 to 2009 (top panel) and their difference (MIPAS-DS). The shadowed area is the combined error.

DS spectrometer OH temperatures have been compared with SABER and MLS (*French and Mulligan*, 2010). It was found a 2 K average bias with SABER over 8 year (2002-2009), being SABER warmer, and also a +0.7 K/yr trend in the SABER-DS bias. MLS measurements provided 10 K lower temperatures than the DS spectrometer but showed no trend along the period 2004-2009.

MIPAS temperatures at 87 km have been compared with DS OH temperatures as with SATI: MIPAS $T_k$'s have been vertically smoothed with a gaussian of 10 km FWHM centered at 87 km. The coincidence criterium applied for the period 2005-2008 yield 40 nights with coincidences. Since Davis station is placed at southern high latitudes, measurements are restricted to nights from March to November.

Figure 5.13 shows DS OH and MIPAS temperatures averaged for all coincidences found in each night. Both measurements show a similar seasonal pattern. The averaged difference between MIPAS and DS for all co-locations is -0.3 K, without any noticeable seasonal dependence. This value is well within the expected MIPAS systematic error, so the comparison can be considered as excellent.

A trend of $-1.2\pm0.8$ K/yr has been estimated for the MIPAS-DS difference along 4 years, which is of opposite sign to that found for the SABER-DS difference. Since MIPAS and SABER use a similar technique to derive kinetic temperature, and also their measurements are affected by similar uncertainties in $CO_2$ and O variability, it can be concluded that those trends cannot be due to natural variability. Nevertheless, an extension in time of MIPAS and DS comparisons would be very helpful to confirm or refute that statement.

### 5.2.7. Falling sphere climatology

*Lübken* (1999) reported a temperature climatology constructed by measurements taken from falling spheres (FS) from 1987 to 1997 in eight campaigns over Andoya (69°N) and Kiruna (68°N). The technique consists in the determination of atmospheric density by measuring the deceleration of the falling spheres. Then, assuming hydrostatic equilibrium, the temperature can be derived by integration of the density profile. The climatology ranges from 35 to 95 km, covering periods from April to September, with a 7 days temporal grid. As upper boundary, temperatures from CIRA-1986 climatology (COSPAR International Reference Atmosphere), or from rocket borne measurements when available, were used. Total errors estimated for temperature are 1.5, 3 and 7 K at 70, 80 and 90 km, respectively.

MIPAS v511 temperatures from 2008 to 2009 have been selected for the comparison, since this period has the best temporal coverage. MIPA $T_k$'s have been averaged taking weekly periods (centered at the FS date) and

within 10° in latitude centered at 68.5°N. For each FS date (April 22nd, May 16th, June 1st, June 22nd, July 16th, August 1st, August 16th and September 22nd) the number of MIPAS scans averaged ranges between 45 and 110.

In general, MIPAS and FS temperatures agree within 1-3 K in the upper stratosphere (up to 50 km), while in the lower mesosphere (up to 70 km), MIPAS temperatures are warmer between 5 and 15 K (largest differences for summer dates). In the upper mesospheres, the agreement is better (±5 K), and at the mesopause region, MIPAS $T_k$'s are usually larger within 2-10 K than FS, except for the FS date at the end of June, where MIPAS $T_k$ is around 3 K colder.

### 5.2.8. Summary of the comparisons

MIPAS temperatures from *MA* measurements (v511) have been compared with independent co-located measurements of nine instruments from 2005 to 2009. The results and conclusions for *MA* mode temperature measurements reported here can be extended to the *UA* and *NLC* modes. Figure 5.14 and Tables 5.7 and 5.8 summarize the comparisons between kinetic temperature measured by MIPAS and the space-borne instruments TIMED-SABER, Aura-MLS and ACE-FTS, and the ground-based instruments MLO lidar, TMF lidar, Sierra Nevada's SATI and the Davis spectrograph in mid-latitudes, polar summer and polar winter. The major conclusions are summarized below. More details can be found in *García-Comas et al.* (2011).

Table 5.7: Summary of comparisons with satellite measurements in solstice. Numbers shown are average temperature differences in K of MIPAS v511 minus the indicated instrument.

| Altitude* | Tropics | Mid-latitudes | | Polar Summer | | | Polar Winter | | |
|---|---|---|---|---|---|---|---|---|---|
| [km] | SABER | SABER | MLS | ACE | SABER | MLS | ACE | SABER | MLS |
| 20 | +2.5 | -2.0 | +0.2 | +0.0 | -2.8 | +0.2 | -5.0 | -2.3 | +1.1 |
| 30 | +2.4 | -1.4 | +0.8 | -1.2 | -1.2 | +0.9 | -0.5 | -1.5 | +0.5 |
| 50 | -0.1 | -0.1 | -2.5 | +0.7 | -2.7 | -5.4 | -1.7 | -0.6 | +1.9 |
| 70 | -0.7 | -0.6 | +4.7 | -2.9 | -3.7 | +2.7 | -4.0 | +0.1 | +3.6 |
| 80 | -1.6 | -1.7 | -0.2 | -9.4 | -4.6 | -1.0 | +4.7 | +0.8 | +3.2 |
| 90 | +1.8 | +1.6 | +9.3 | +0.7 | +6.2 | +19.7 | +8.7 | +3.9 | +8.3 |

*For MLS comparisons, altitude refers to corresponding MIPAS approximate altitude.

MIPAS v511 temperature compares very well with the other instruments measurements. Averaging over the period 2005-2009, MIPAS agrees with all instruments within 1-2 K from 20 to 70 km, within 4-10 K from 80 to 90 km and within 15-20 K above 95 km. The differences do not strongly depend on season, although they are larger in the high latitude summers,

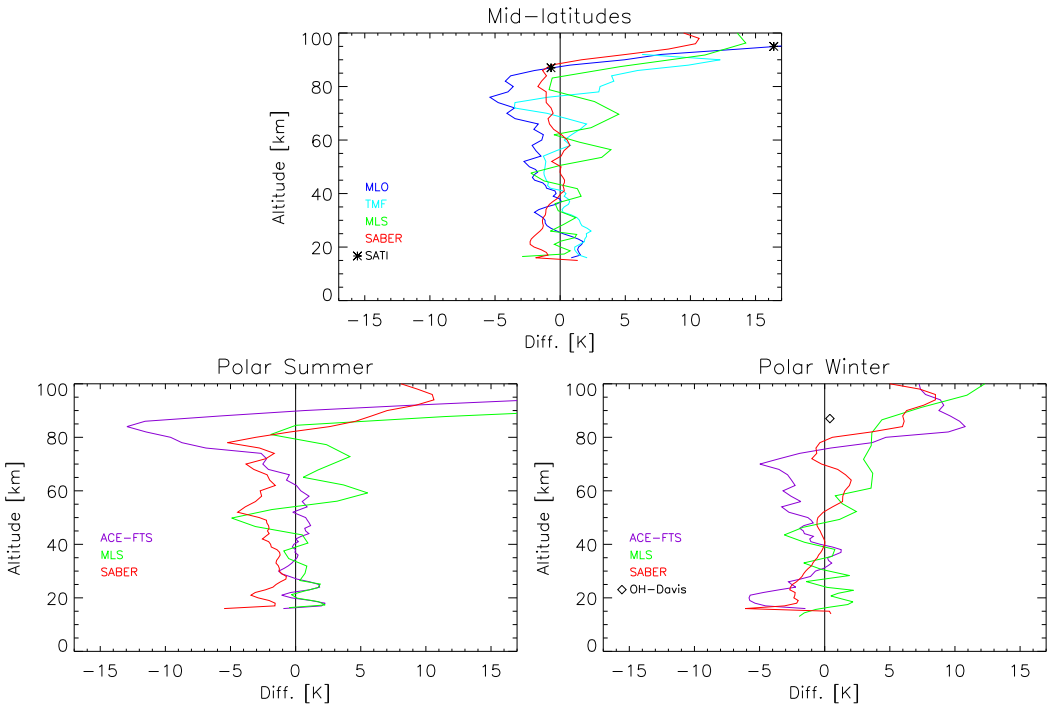


Figure 5.14: Mean temperature difference over 2005-2009 between MIPAS and SABER (red), ACE-FTS (purple), Aura-MLS (green), MLO lidar (dark blue), TMF lidar (light blue), SATI (asterisk), and the Davis Spectrograph (diamond) for mid-latitudes (top), polar summer (bottom left) and polar winter (bottom right).

Table 5.8: Summary of comparisons with ground-based measurements. Numbers shown are average temperature differences in K between MIPAS v511 and the indicated instrument.

| Altitude [km] | MLO (30°N) | TMF (34°N) | SATI (37°N) | Davis OH (69°S) |
|---|---|---|---|---|
| 20 | +1.4 | +1.1 | - | - |
| 30 | -1.2 | +1.5 | - | - |
| 50 | -2.4 | -1.1 | - | - |
| 70 | -4.0 | -1.0 | - | - |
| 80 | -3.6 | +3.0 | - | - |
| 87 | -0.6 | +7.9 | -0.7 | -0.3 |
| 95 | +16.6 | - | +16.4 | - |

particularly around the mesopause, which may point to a too low atomic oxygen used in MIPAS retrievals.

In the lower and mid-stratosphere (20-40 km), MIPAS agrees with other instruments at all seasons better than 1 K, except with SABER. In this case, MIPAS is 2-3 K colder than SABER in this altitude region. Nevertheless, it is known the warm bias of SABER of similar magnitude (*Remsberg*

*et al.*, 2008), which may explains the found disagreement.

In the high stratopause (45-50 km), MIPAS temperatures are generally 1-2 K colder, although it agrees very well with SABER in mid-latitudes and polar winter (not in polar summer, where the general bias is found). However, SABER has a cold bias of 1-2 K around the stratopause (*Remsberg et al.*, 2008). In the same way, the comparisons at 50 km in polar summer with ACE-FTS also show better agreement but ACE-FTS might also have a 2 K negative bias in the upper stratosphere.

MIPAS temperatures are generally less than 3 K colder in the lower mesosphere (up to 70 km), except for MLS that shows a positive bias, although MLS comparisons with other instruments showed a negative MLS bias in the mesosphere (0-7 K). The agreement at those altitudes with SABER and the TMF lidar in mid-latitudes is particularly good (<1 K).

Above the mid-mesosphere (70-85 km), the comparisons slightly worsen in some cases. Except for the polar winter, (and also comparisons with the TMF lidar and Aura-MLS), MIPAS temperatures from 75 to 85 km show colder values. The negative bias ranges from -1 to -2 K (-4 K for the MLO lidar) in mid-latitudes and from 1 to 10 K in polar summer. Polar winter MIPAS temperatures are 3 K warmer at those altitudes. The differences with ACE-FTS between 75 and 85 km of -10 K and +10 K found in polar summer and polar winter, respectively, are consistent with differences found in previous ACE-FTS comparisons with other instruments (*Sica et al.*, 2008).

Around the mesopause and above (85-100 km), MIPAS temperatures are generally warmer in mid-latitudes and in polar winter above 88 and 80 km, repectively. Comparisons with SATI (mid-latitudes) and Davis spectrograph (high latitudes) show excellent agreement (within 1 K at 87 km). In the polar summer, MIPAS is up to 10 K colder than ACE-FTS between 85 and 90 km (around the mesopause) and warmer above. Compared to MLS, MIPAS has a large positive bias at 85-90 km, due to the higher altitude and too low temperatures of the mesopause measured by MLS. The difference between MIPAS and SABER in the polar summer mesopause would be reduced if both MIPAS and SABER used the same $CO_2(\upsilon_2)$ V-V exchange, the $CO_2$ quenching with $N_2$ and $O_2$ and the same atomic oxygen concentration.

The negative difference between MIPAS and ACE-FTS around the polar summer mesopause could be partially explained by the known ACE-FTS positive bias (*Sica et al.*, 2008) at these altitudes. The remaining MIPAS-ACE difference suggests a too small collisional rate or [O] used in MIPAS retrievals. However, the good agreement between MIPAS and FS climatology in this region may hint a further bias in ACE temperatures rather than higher collisional rates or [O].

It is very interesting to point out that the generally warmer MIPAS temperatures at the mesopause (except for the polar summer) and above support the argument that the [O] used in MIPAS retrievals is too low,

i.e., a larger [O] would lead to colder temperatures and hence better agreement. The same conclusion is drawn for the polar summer mesopause, but for different reasons. There, the effect of [O] on the retrieved $T_k$ is of opposite sign, but MIPAS measurements are generally colder than other instruments'. Hence, a larger [O] would lead to warmer MIPAS $T_k$ and then to a better agreement with SABER and the FS climatology. A similar effect would be achieved in the polar summer mesopause by using smaller rates for the $CO_2(\upsilon_2)$ V-V exchange and for the $CO_2$ quenching with $N_2$ and $O_2$, which would barely affect the MIPAS temperatures at other latitudes and seasons.

# Chapter 6

# Temperature and nitric oxide in the thermosphere

*Abstract*

The scheme presented in Chapter 4 for the retrieval of thermospheric kinetic temperature and NO *vmr* profiles has been applied to MIPAS spectra at 5.3 $\mu$m in its *UA* observation mode. The result have been characterized by mean single profiles for typical atmospheric conditions: low and polar latitudes and low and high geomagnetic activity. The quality of the results is analyzed by means of the retrieval random error, the vertical resolution and the averaging kernels. The most important sources of systematic errors are characterized: atomic oxygen and atomic nitrogen abundances, the spin propensity factor and the nascent rotational and spin distributions of NO($v$,$J$,$S$). Temperature and NO profiles observed under auroral conditions are rather insensitive to smoothing errors related to the mapping of *a priori* profile shapes. However, for extra-polar and low $A_p$ conditions, a potential systematic bias in the retrieved nighttime temperature and NO profiles related to smoothing errors has been identified from a comparison to Thermosphere Ionosphere Mesosphere Electrodynamics General Circulation Model (TIME-GCM) simulations. Finally, the MIPAS measurements taken during the Delta-2 Campaign in January 2009 offers an unique opportunity to validate the retrieved $T_k$.

## 6.1. NO-$T_k$ retrievals

The NO-$T_k$ retrieval scheme introduced in Section 4.5 has been applied to MIPAS *UA* measurements (Table 2.5 in Section 2.7) between 2005 and 2009. Along this period, different auroral conditions and atmospheric conditions have taken place, and this is reflected in the quality of the retrievals. Figure 6.1 (left panels) shows the retrieved $T_k$ and NO *vmr* average profiles for high/low geomagnetic activity ($A_p$ greater/smaller than 15), as well as polar ($>45^\circ$) and extra-polar ($<45^\circ$) locations. The criterium followed in the grouping of MIPAS mean single retrievals allows to illustrate the correlation between the geomagnetic activity

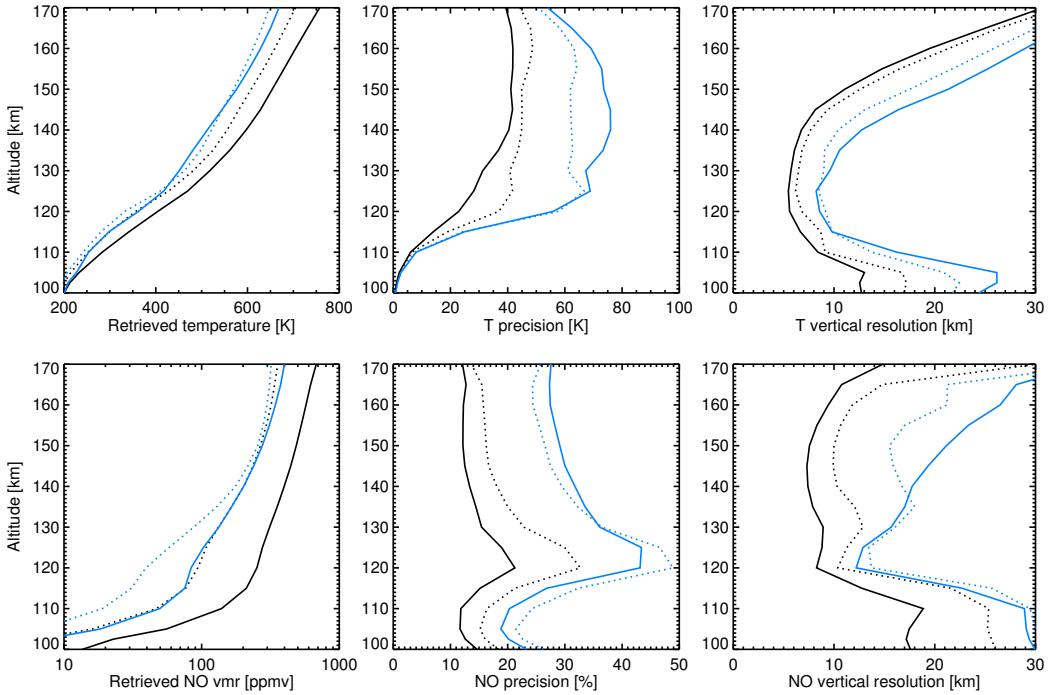


Figure 6.1: Averages of retrieved kinetic temperatures (top left) and NO *vmr* profiles (bottom left), corresponding single measurement precisions (middle), and vertical resolutions (right) for high (black) and low (blue) geomagnetic activity conditions (mean $A_p$ index of 24 and 3, respectively), as well as polar (latitudes $> 45°$, solid) and extrapolar (latitudes $< 45°$, dotted) locations.

and the higher values of retrieved kinetic temperature and NO *vmr* as well as the typically higher values of NO *vmr* at polar regions than that at mid-latitudes due to auroral activity (*Barth*, 1992).

The single measurement precision (Figure 6.1, middle panels) is estimated by means of linear theory as suggested by *Rodgers* (2000). For a joint NO and $T_k$ retrieval, the precision depends on the signal to noise ratio of the measured 5.3 $\mu$m spectra, which in turn is driven by kinetic temperature and NO abundance itself. Thus, the best precision is achieved for high $A_p$ in the polar regions (highest temperature and NO *vmr*): of around 5-30 K for $T_k$ and less than 20% for NO *vmr* in the 100--170 km altitude range. In contrast, the poorest precision corresponds to low $A_p$ cases in the extra-polar regions with 30-80 K for $T_k$ and 20-50% for NO *vmr*.

The vertical resolution has been expressed as the full width at half maximum of the rows of the averaging kernel matrix (*Rodgers*, 2000). It can be seen in Figure 6.1 (right panels) that the best vertical resolution is always achieved in the same altitude region (120-140 km), though the absolute values change with the atmospheric situation. Again, the best vertical resolution for both $T_k$ and NO *vmr* is found in the polar regions under high $A_p$, which are 5-7 km for $T_k$ and 7-8 km for NO at the mentioned

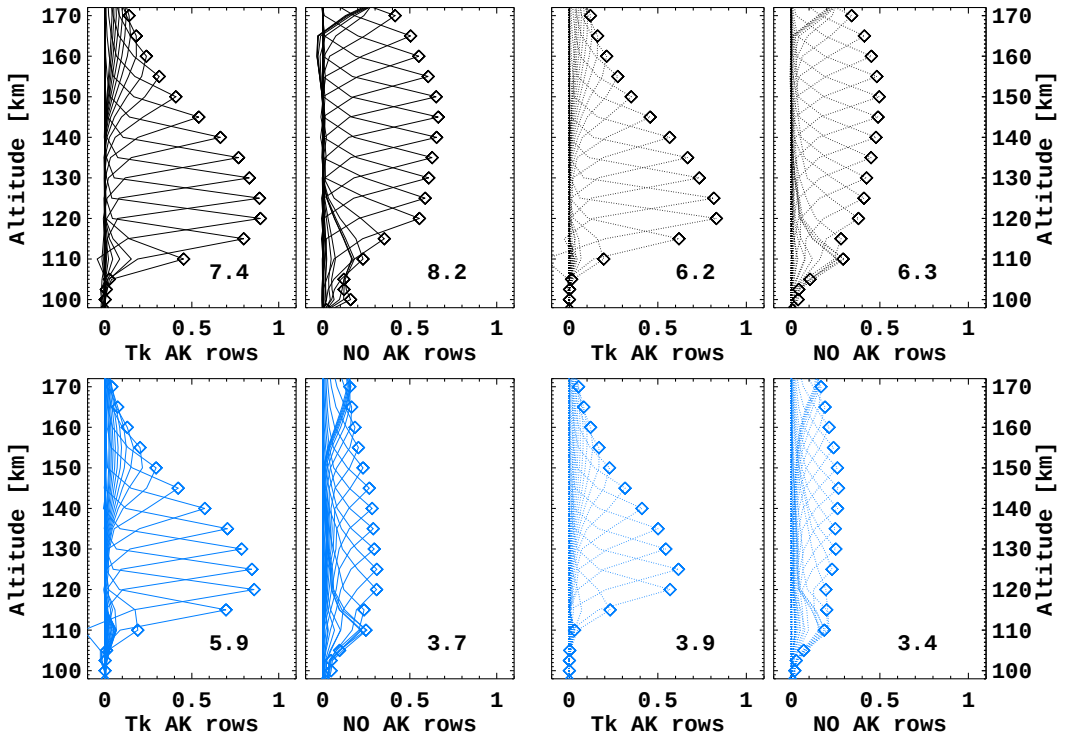


Figure 6.2: AK rows for retrieved $T_k$ and NO profiles shown in Figure 6.1. Left (Right) panels are for Polar (Extra-Polar) regions; Top (Bottom) panels are for High (Low) $A_p$ conditions. Numbers on the low right corner denote the averaged independent pieces of information (degrees of freedom).

optimal altitude range of 120-140 km. Vertical resolutions of kinetic temperature and NO *vmr* under low $A_p$ extra-polar conditions are considerably broader and range between 10 and 15 km, respectively, in this vertical region. By inspection of the averaging kernels (see Figure 6.2), the retrievals manage to extract independent pieces of information of $T_k$ from MIPAS spectra more efficiently at 120-140 km, whereas the behaviour for NO *vmr* is quite constant from 120 to 160 km. In short, MIPAS retrievals are in fact meaningful in the range between 110 and 160 km.

In a totally analogous manner, the NO-$T_k$ retrieval scheme has been applied to MIPAS full spectral resolution measurements (*UA4* observation mode, 14 June 2003). Both retrieval schemes, TLOS and NO-$T_k$, have been adapted to full resolution spectra. Recall that the only difference between full and reduced spectral resolution schemes lies on the occupation matrix, which microwindows have suffered marginal changes in their borders. The quality of the retrieved profiles, i.e., precision and vertical resolution, is quite similar with respect to those obtained for the reduced resolution retrievals, particularly compared to the results for the high $A_p$ conditions, since 14 June 2003 is considered high $A_p$ ($\sim$28).

### 6.1.1. Retrieval convergence

The NO-$T_k$ retrieval scheme yields a very high convergence rate. Taking into account all the processed MIPAS measurements in the 2005-2009 period, it is higher than 92%. But, as shown in the case of TLOS retrievals, this coefficient does not distribute homogeneously. Figure 6.3 shows the geographical distribution of the convergence rate for different seasons and illumination conditions. Except for local features, the behaviour of the convergence rate is quite similar along the seasons. Just the polar summer case shows a convergence rate sistematically lower than the rest of latitudes and seasons.

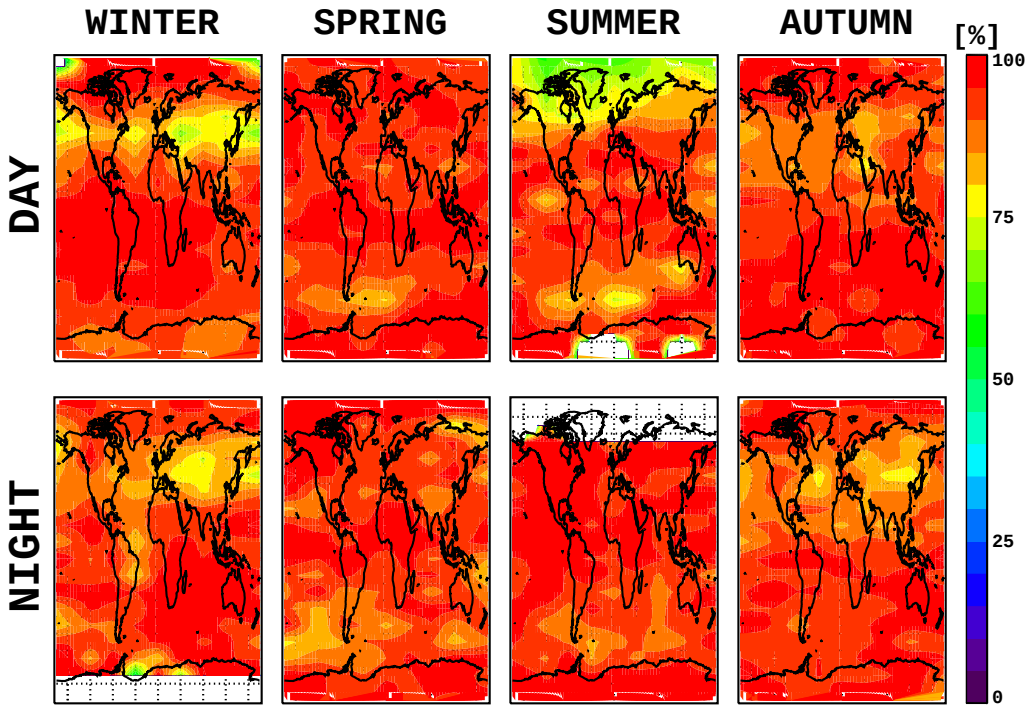


Figure 6.3: MIPAS NO-$T_k$ retrievals convergence rate. Measurements from 2005 to 2009 have been seasonally averaged (from left to right). Convergence rates have been separated in daytime (top) and nighttime (bottom). White gaps mean no MIPAS measurements.

An inspection of the non-converged retrievals suggests that the retrieved low temperatures at the mesopause has an effect on the temperature profile slope right above and, indirectly, on the NO *vmr* profile, which is not properly treated by the retrieval processor (see Figure 6.4 as an example of this effect). Generally, the no convergence on the retrieval process comes in situations with low signal, which enhance the non-linear dependence of the emission on $T_k$ and NO.

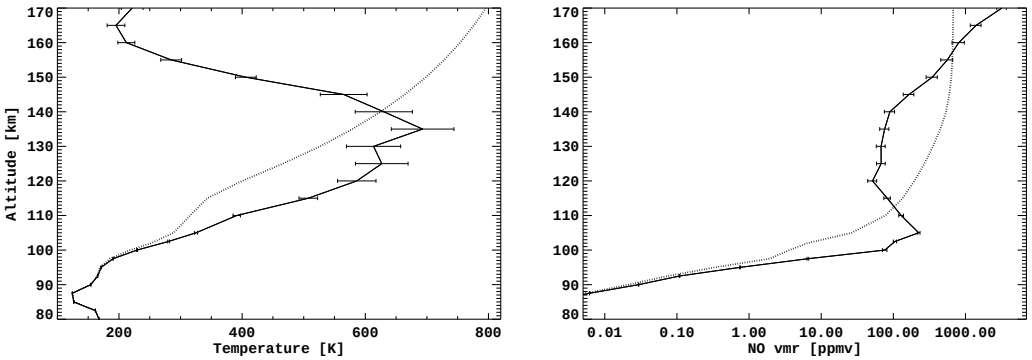


Figure 6.4: Non converged retrieval of a MIPAS single measurement at polar summer conditions. $T_k$ (left) and NO *vmr* (right) profiles are shown in solid lines, with their respective random retrieval errors as horizontal bars. A priori profiles are shown in dotted lines.

## 6.2. Systematic errors assessment

This section addresses the systematic errors related to uncertainties in atmospheric parameters that have a significant impact on the NO 5.3 $\mu$m emission and, subsequently, in the retrieval parameters. In particular, uncertainties in the atomic oxygen, atomic nitrogen, and spin propensity factor. Their influence on the retrieval results is analyzed separately.

### 6.2.1. Atomic oxygen

In the thermosphere, above 100 km, VT collisions with atomic oxygen become as fast as the spontaneous emission and they affect the population of NO($\upsilon = 1$), and hence the retrieved NO. In fact, VT collisions with atomic oxygen are responsible for most of the NO 5.3 $\mu$m emission (*Sharma et al.*, 1996a) for quiet atmospheric conditions.

Under quiescent conditions, other excitation and de-excitation processes (i.e., collisions with $N_2$ and $O_2$, the chemical production ($N+O_2$) and absorption of solar and tropospheric radiation) play a minor role at these altitudes. Therefore, the population of NO(1) can then be approximated by

$$[\mathrm{NO}(1)] = [\mathrm{NO}]\,\frac{k_O\,[\mathrm{O}]}{A + k_O\,[\mathrm{O}]}\,\exp(-h\nu_0/kT), \tag{6.1}$$

where $k_O$ is the rate coefficient of NO($\upsilon = 1$) in collisions with atomic oxygen, O; $A$ is the spontaneous Einstein coefficient for the NO 1→0 band; $T$ is temperature; $\nu_0$ is the central wavenumber of the band; and $h$ and $k$ are the Planck and Boltzmann constants, respectively. The brackets indicate number densities.The radiance under optically thin conditions can be approximated by $R \approx A\,[\mathrm{NO}(1)]$. Hence, at the lower altitudes studied here, below approximately 120 km, $k_O\,[\mathrm{O}] \gg A$, and the radiance

can be approximated by $R \approx A\,[\mathrm{NO}]\,\exp(-h\nu_0/kT)$, which is independent of the atomic oxygen concentration. At higher altitudes, $k_O\,[\mathrm{O}] \ll A$ and then $R \approx k_O\,[\mathrm{NO}]\,[\mathrm{O}]\,\exp(-\mathrm{h}\nu_0/\mathrm{kT})$, and the radiance is proportional to [O].

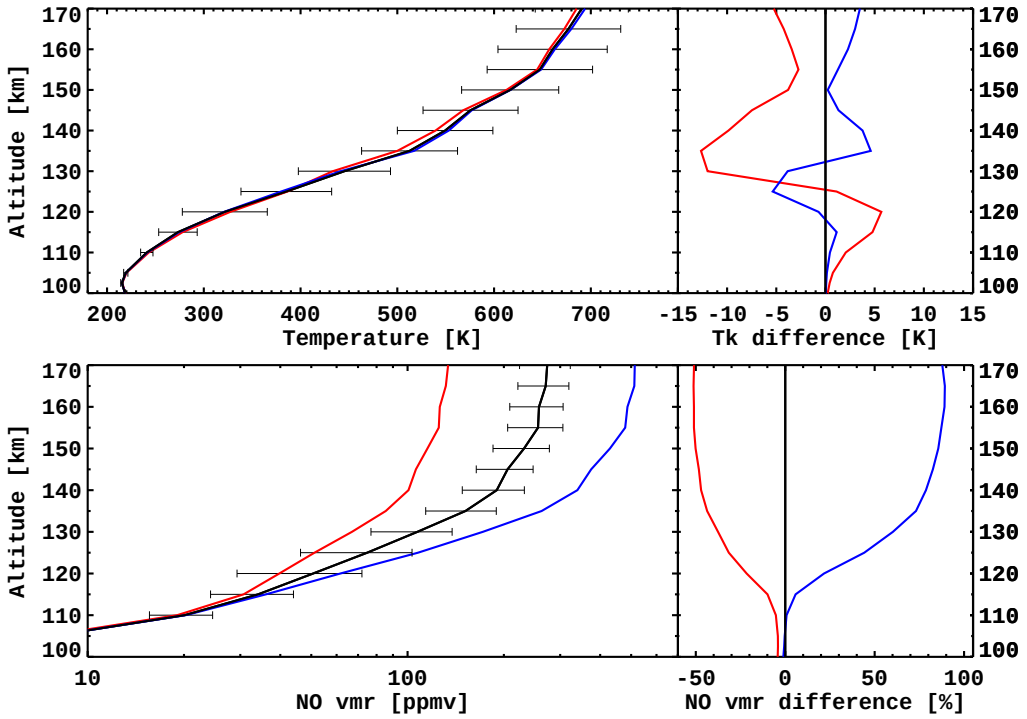


Figure 6.5: Retrieval response to a change in atomic oxygen by a factor 2. Black solid lines represent nominal retrievals; blue (red) lines represent the retrieved $T_k$ (upper panel) and NO *vmr* (lower panel) profiles when atomic oxygen abundance is halved (doubled). Mean single measurement errors are plotted as horizontal bars.

A sensitivity study where the atomic oxygen abundance used in the retrieval was increased and decreased by a factor 2 has been performed on MIPAS measurements for different atmospheric and auroral conditions. For all cases, the change in the retrieved NO *vmr* was, as expected, of similar magnitude and opposite sign than the variation in the atomic oxygen above 120 km and much smaller below. In contrast, the $T_k$ hardly changed, because information on $T_k$ is essentially contained in the ratio of radiances through the rotational temperature of the nascent distribution from VT collisions with atomic oxygen, rather than the absolute radiances. Figure 6.5 illustrates the sensitivity study for extra-polar and moderate auroral conditions (averaged profiles) on 4 September 2008. The result of this study is consistent with the approximations made above that the NO($\upsilon = 1$) *vmr* depends almost linearly on [O] above 120 km while this dependence vanishes below 120 km (lower panel).

The dependence of MIPAS NO results on *a priori* assumptions on atomic oxygen can cause artefacts when MIPAS data are compared to other data sets which go along with different atomic oxygen concentrations. If, for example, MIPAS NO results are to be compared to a model whose atomic oxygen concentration is $[O_{model}]$, MIPAS NO number densities should be multiplied by the factor

$$f = \frac{1 + A/(k_O\,[O_{model}])}{1 + A/(k_O\,[O_{MSIS}])},$$

where $A$=12.54 $s^{-1}$, $k_O$=2.8×$10^{-11}$ cm, and $[O_{MSIS}]$ are the MSIS atomic oxygen concentrations, in order to remove related explained differences from the intercomparison.

### 6.2.2. Atomic nitrogen

The atomic nitrogen influences both the population of NO vibrational levels and the super-thermal part of the rotational distribution. Regarding the latter, it is expected that an increase of atomic nitrogen concentration will enhance the population of the higher rotational levels which will be compensated in the retrieval by a lower kinetic temperature and a subsequent but slightly increase in the NO *vmr*. Contrary to higher vibrational levels, the population of NO($\upsilon = 1$) depends only weakly on the N abundance, since the super-thermal contribution to the rotational and spin distribution produced by the N+$O_2$ reactions are more pronounced for $\upsilon > 1$ than for $\upsilon = 1$ (*Funke and López-Puertas*, 2000; *Armstrong et al.*, 1994).

Test retrievals for all auroral and atmospheric conditions have been performed by doubling and halving the nominal MSIS atomic nitrogen. The effects on the retrieved $T_k$ and NO *vmr* are of minor importance for all cases. Figure 6.6 shows the results for the polar summer conditions and high auroral conditions (averaged profiles) on 21 January 2005. Changes are less than 30 K in temperature and than 10% in the NO *vmr*, both remaining under mean single measurement errors. The systematic error induces by this uncertainty is then rather small.

### 6.2.3. Spin propensity factor

The spin propensity factor ($\beta$) accounts for the spin conservation in rotational-translational (RT) collisions. Its nominal value is set to 0.9 as the best agreement between calculations and CIRRIS-1A observations (*Funke and López-Puertas*, 2000). This value is assumed to be constant for all rotational levels for collisions of NO with $N_2$, $O_2$, and with atomic oxygen. This assumption suppose an uncertainty of $\pm 0.1$ in the $\beta$ factor. A test has been performed by varying $\beta$ in those values.

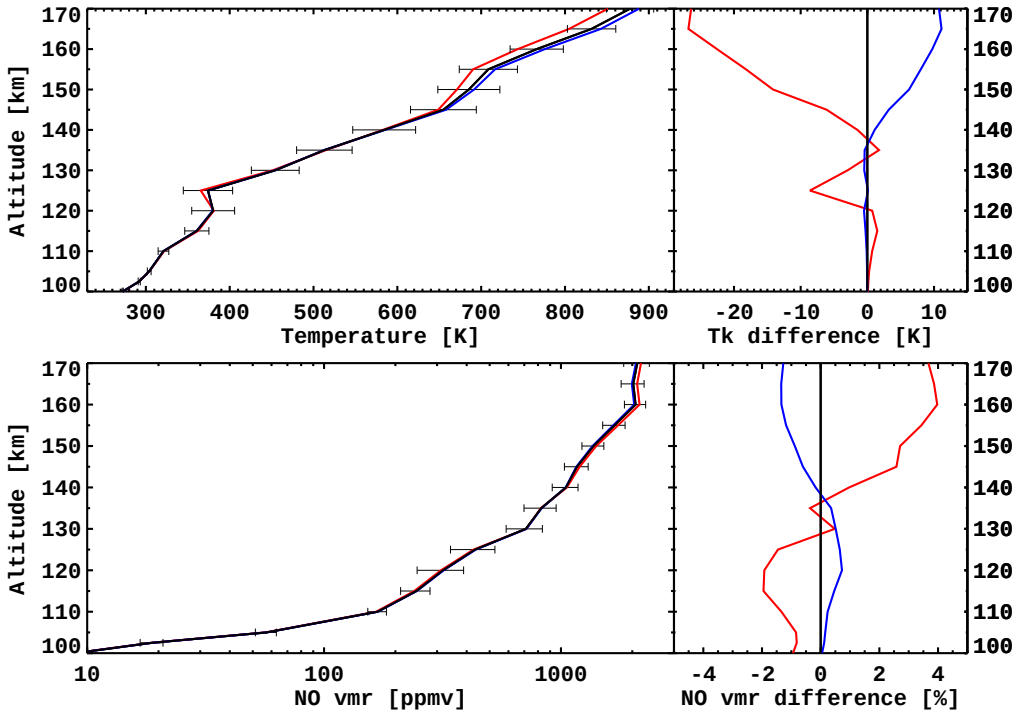


Figure 6.6: Retrieval response to a change in atomic nitrogen by a factor 2. Black solid lines represent nominal retrievals; blue (red) lines represent the retrieved $T_k$ (upper panel) and NO *vmr* (lower panel) profiles when atomic nitrogen abundance is halved (doubled). Mean single measurement errors are plotted as horizontal bars.

The retrieval response to changes in $\beta$ is indistinguishable from the noise (Figure 6.7). However, an inspection of the residuals shows that the smallest $\chi^2$ is obtained for $\beta$=0.9, in agreement with the previous results.

### 6.2.4. Nascent rotational and spin distributions

Further potential systematic error sources, particularly for temperature, are the nascent rotational and spin orbit distributions produced in collisions with atomic oxygen. They are responsible for the sub-thermal rotational-spin populations of NO($\upsilon = 1$), which are dominant at lower and middle thermospheric altitudes. These distributions have not been measured in the laboratory. However, the rotational and spin non-LTE populations has been validated with the CIRRIS-1A and MIPAS measurements (*Funke and López-Puertas*, 2000; *Gardner et al.*, 2007), and good agreement of modelled and observed spin temperatures as function of rotational temperatures has been found. Comparisons with MSIS temperatures have indicated that observed rotational temperatures are slightly lower than MSIS kinetic temperatures, in agreement with the model predictions. Thus

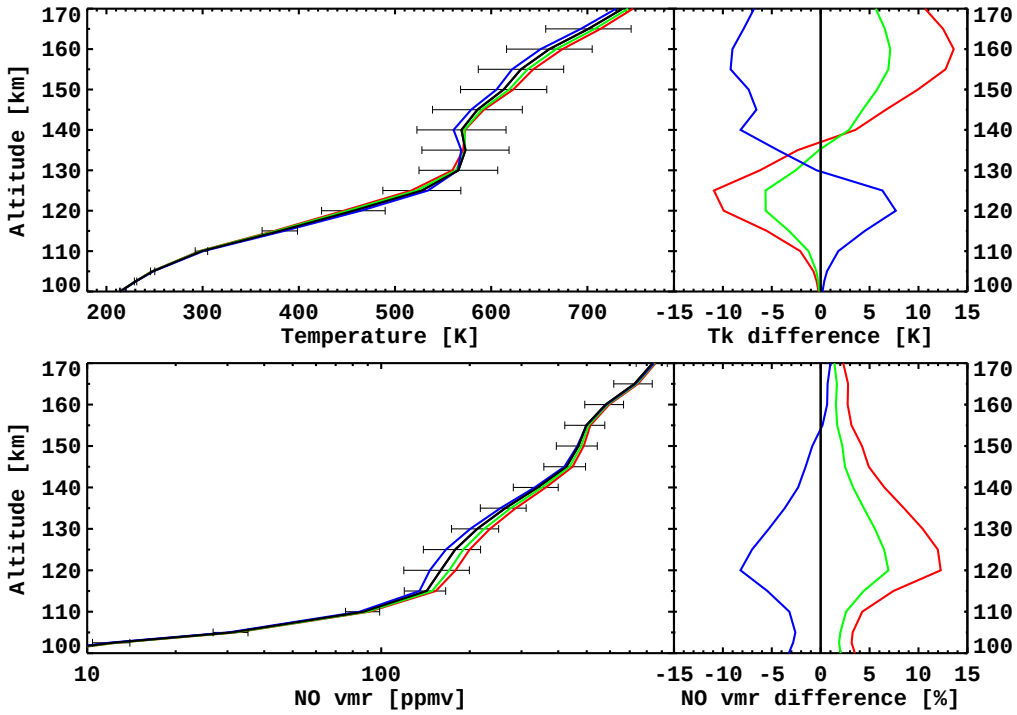


Figure 6.7: Retrieval response to a change in the spin propensity factor. Moderate $A_p$ polar summer conditions has been selected as representative. Black, nominal ($\beta = 0.9$); red, $\beta = 0.8$; green, $\beta = 0.85$; blue, $\beta = 0.95$. Average profiles have been plotted. The error bars represent the mean single precision for the nominal case.

there is full confidence in the applied nascent rotational temperatures of NO-O collisions and only small systematic errors are expected.

## 6.3. Retrieval response to different spectral resolutions

In Chapter 4, it was stated that the retrieval scheme for $T_k$ and NO *vmr* profiles in the thermosphere was initially developed for MIPAS full spectral resolution measurements in its upper atmosphere observation mode. This scheme needed to be adapted in order to process MIPAS data in its reduced spectral resolution *UA* observation mode, specially focusing on the adaptation of the spectral microwindows.

Once the retrieval scheme is fixed, it is necessary to validate it. The purpose of the validation is to assess the retrieval scheme response when it is applied to spectra of different resolutions, that is, the viability of the retrieval scheme for future instruments is tested.

The validation consists of comparing the results obtained when the re-

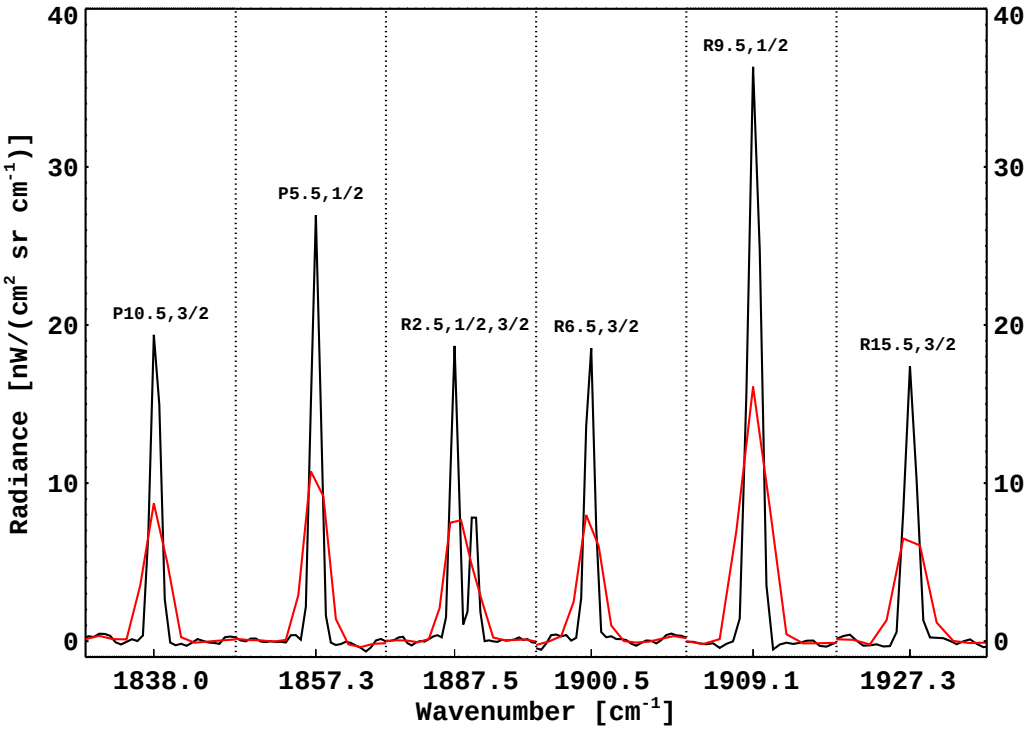


Figure 6.8: Six regions of MIPAS spectrum at ∼125 km from its upper atmosphere observation mode. Black colour denotes full resolution (0.025 $cm^{-1}$) measured and apodized lines; red colour corresponds to the same lines but degraded to the reduced resolution (0.0625 $cm^{-1}$).

trieval scheme has been applied to the same full-resolution measurements but with original and artificially degraded spectral resolution. Hence, on the one hand, MIPAS full resolution spectra were inverted by using the full-spectral-resolution occupation matrix. On the other hand, the spectra were artificially degraded to the reduced resolution (see Figure 6.8), by applying the appropriate apodization[1]. Then, they were inverted by using the reduced-spectral-resolution occupation matrix. It is noticeable the broader and the less intense spectral lines for the coarser spectral resolution.

Three standard conditions, extra-polar, polar summer and polar winter, have been chosen to perform the validation. Figures 6.9, 6.10 and 6.11 show their respective results. In general, the quality of the retrievals, represented by the noise errors, the vertical resolutions and the averaging kernels are very similar for both spectral resolutions. Therefore, the worst spectral resolution does not mean a loss in the retrievals quality, i.e., a worse retrieval error and a worse vertical resolution. It is more complex, however, to analyze the differences observed in the retrieved profiles. In the same way as the distribution

[1] see Section 2.3 for details on the apodization.

of the retrieved information is preserved with a change in the spectral resolution (see averaging kernels), the profiles' structures, i.e., the profile shapes, are also equally retrieved from both spectral resolutions, although the absolute values may show differences.

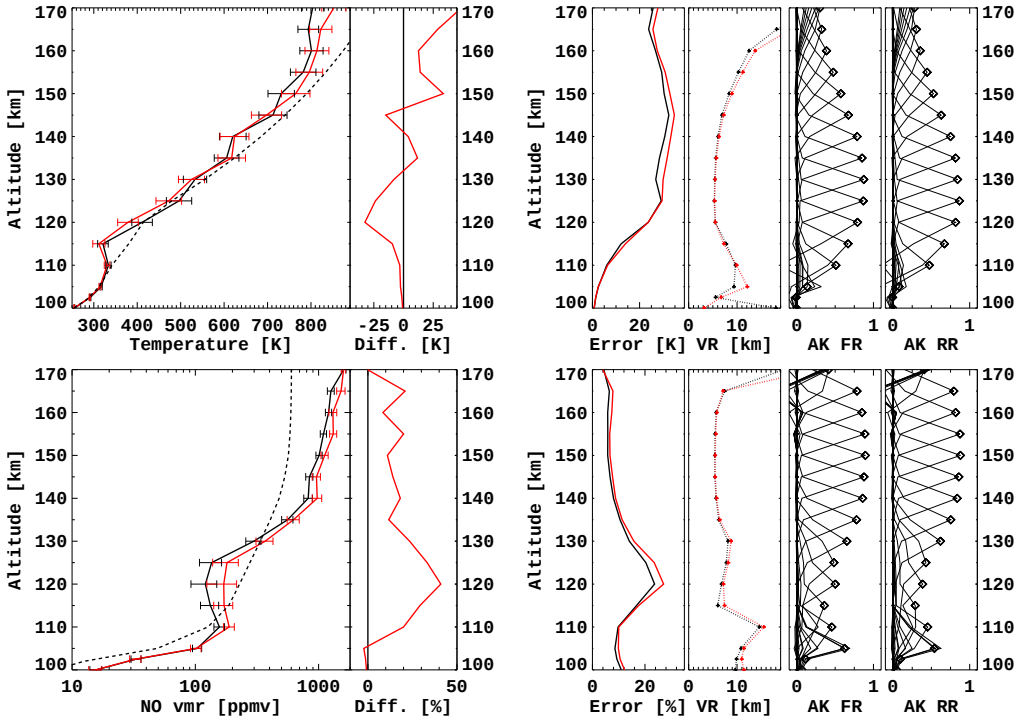


Figure 6.9: Comparison between FR (black colour) inversion and RR (red colour) inversion of single scans: Extra-Polar case. Left panels show the $T_k$ (top) and NO *vmr* (bottom) retrievals and the differences RR - FR obtained, in Kelvin for temperature, and relative to FR inversion for NO *vmr*. A priori profiles are also plotted with dashed lines. Right panels show a comparison between the quality of the retrievals (top for $T_k$ and bottom for NO *vmr*): Noise retrieval error (absolute for $T_k$ and relative for NO *vmr*), vertical resolutions and the averaging kernel rows for FR and RR are plotted.

With respect to the differences found between retrieved profiles from high and degraded spectral resolutions, these tend to be larger at regions where the signal to noise ratio worsens. For example, the NO at 110-130 km in the extra-polar case (differences up to 50 %), the temperature above 150 km in the polar summer case (differences larger than 50 K) or NO at 110-130 km (differences up to 50 %) and temperature at 120 km and above 130 km (differences up to 50 K) in the polar winter case. In these mentioned examples, it is observed an apparent anti-correlation between the retrieved $T_k$ and NO profiles. The origin of this anti-correlation lies in the fact that the intensity of the spectral lines depends on both temperature and NO abundance in a non-linear manner. The possi-

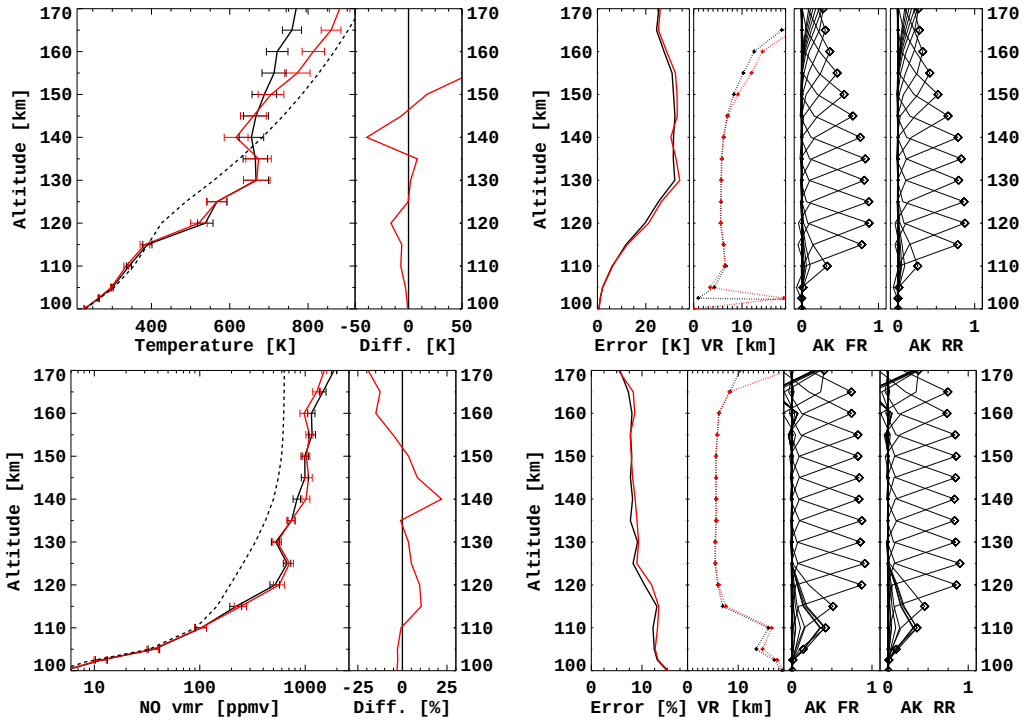


Figure 6.10: Comparison between FR (black colour) inversion and RR (red colour) inversion of single scans: Polar Summer case.

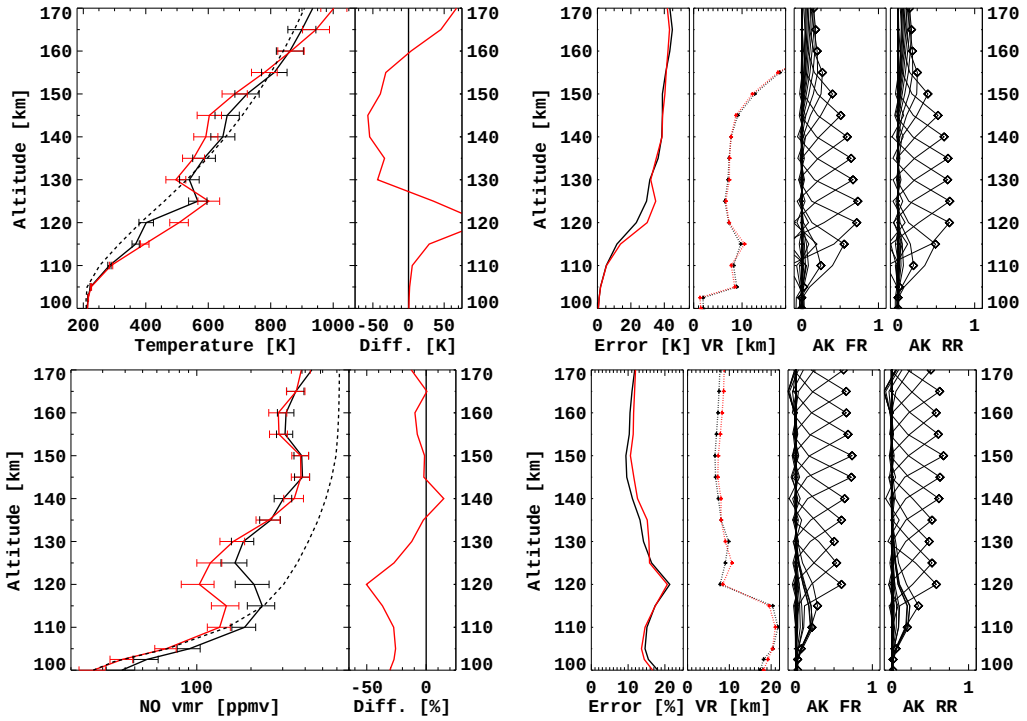


Figure 6.11: Comparison between FR (black colour) inversion and RR (red colour) inversion of single scans: Polar Winter case.

ble effects that these actual non-linearity may have on the retrieved profiles is analyzed deeply in the next two sections.

## 6.4. Statistical robustness of the retrieval method

The analysis of the retrieved temperatures and NO abundances often requires averaging in order to reduce the noise error. In principle, this approach is valid only if the single measurement noise errors in the temperature and concentration space depend linearly on the errors in the measurement space. This, however, is not strictly true in the joint retrieval of the two parameters from the same 5.3 $\mu$m emission lines, since their intensity depends on both parameters in a non-linear manner.

In order to assess a possible bias in averages of retrieved NO *vmr*'s and temperatures related to a non-Gaussian and correlated mapping of random errors, an ensemble of retrieval simulations including synthetic spectral noise (corresponding to the NESR of MIPAS Channel D, around $2\,\mathrm{nW/(cm^2\,sr\,cm^{-1})}$) has been computed. Five scenarios have been chosen in order to cover all possible retrieval solutions: *1)* large values for both NO *vmr* and $T_k$; *2)* high NO *vmr* and low $T_k$; *3)* low NO *vmr* and high $T_k$; *4)* both low NO *vmr* and $T_k$; *5)* medium values for NO *vmr* and $T_k$.

Figure 6.12 shows the results of the ensemble simulations and the "true"[2] solution for the five scenarios in the NO-temperature space at 130 km, the altitude where the amount of information gained from the spectra is typically the largest. While a circular surface centered at the "true" ($T_k$-NO *vmr*) pair, with a Gaussian density distribution would be expected in the linear approximation, a general anti-correlation in the scatter of solution pair ($T_k$, NO *vmr*) is clearly visible instead. The anti-correlation is very weak for case *1)* but increases as the $T_k$ and NO *vmr* values get lower. From the comparison of the ensemble averages (squares) with the "true" solutions (circles) it is found that temperature averages are only weakly biased, less than 12 K for all the cases, except the case *4)*, that deviates 30 K. The bias in the average NO is very small (only a few percent) for the scenarios with medium and high NO *vmr*. For low NO *vmr* values, however, the NO *vmr* averages present a positive bias which can be as large as a factor 2, e.g., scenario 4 (see in more details in Table 6.1). In any case, however, this bias remains below the standard error of the average (i.e., the precision of the average) indicated in Figure 6.12 by the colored error bars.

In summary, the biasing effect assessed, which is caused by averaging non-linear retrievals, does happen but the bias was always found to be smaller than the standard error of the menan, indicating that averaging

[2] The "true" solution is just the $T_k$ and NO *vmr* profiles used to simulate the synthetic spectra subsequently retrieved.

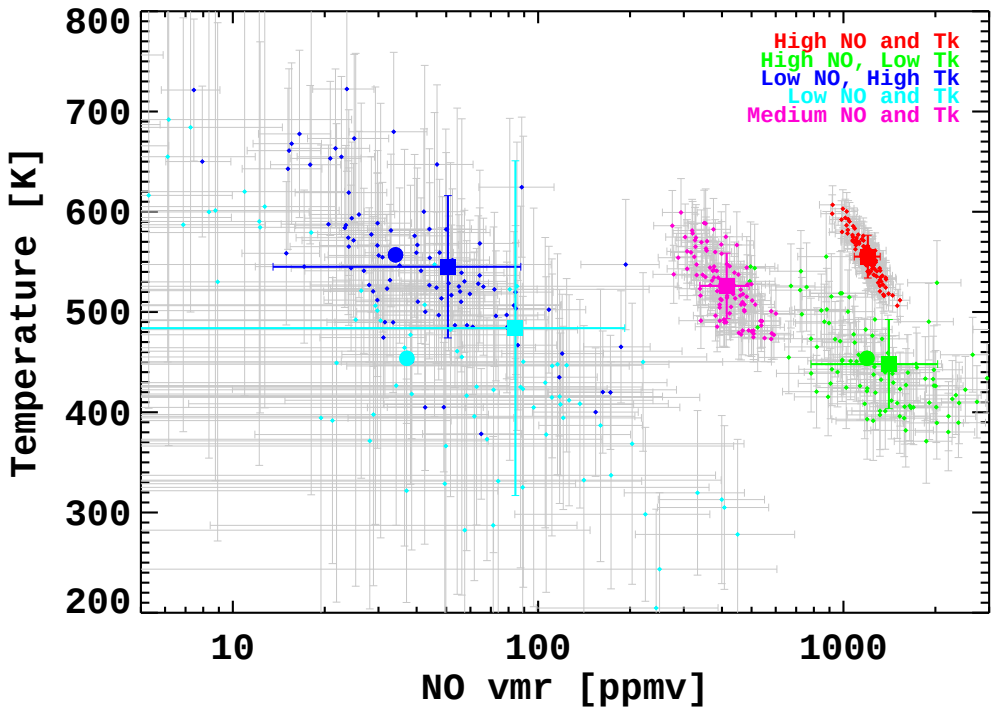


Figure 6.12: $T_k$ and NO *vmr* obtained in retrievals of synthetic spectra for five different scenarios at 130 km. The small coloured diamonds represent single retrievals; the squares are the average of the solutions for each scenario and the circles stands for "true" values. The grey horizontal and vertical lines represent the retrieved noise in each single retrieval. The coloured horizontal and vertical lines are the standard deviation of the retrieved values for each scenario. Note that the solution (squares) and the "true" values (circles) are overlaid for scenarios 1) and 5) (red and pink, respectively).

Table 6.1: Noise-dependent Bias (Mean Value minus True Value) for five considered atmospheric conditions obtained at 130 km. The temperature bias is in Kelvin and the NO *vmr* bias is calculated relative to the true value.

| Case | | Bias $T_k$ [K] | Bias NO *vmr* [%] |
|---|---|---|---|
| NO High | $T_k$ High | -1.8 | 0.7 |
| NO High | $T_k$ Low | -5.8 | 18.0 |
| NO Low | $T_k$ High | -11.9 | 48.5 |
| NO Low | $T_k$ Low | 30.0 | 126.7 |
| NO Medium | $T_k$ Medium | 0.3 | 0.6 |

is still meaningful.

## 6.5. Effect of *a priori* information on retrieved $T_k$ and NO *vmr*

In Section 3.4 has been pointed out the importance of the inclusion of *a priori* information; at those altitudes where real information from the spectrum is scarce, the weight of the a priori information on the retrieved targets may become significant. As a result, the random errors decrease and the averaging kernels values get lower, giving poorer vertical resolutions (see Figure 6.1). In addition, the theory of inversion states that choosing an inappropriate *a priori* maps onto the retrieval smoothing error.

In Section 6.4, it was found that the noise errors of $T_k$ and NO *vmr* profiles, simultaneously retrieved from the same 5.3 $\mu$m emission lines, are somewhat anti-correlated. Hence, mapping of the smoothing errors of one parameter space to the other might also occur. That is, deviations of the *a priori* temperature profile shape from the "true" profile shape can lead to significant distortions of the retrieved NO *vmr* profile and vice versa. This smoothing error crosstalk between state subspaces is described by the non-diagonal parts of the full averaging kernel:

$$\mathbf{A} = \begin{pmatrix} \mathbf{A}_{T,T} & \mathbf{A}_{T,NO} \\ \mathbf{A}_{NO,T} & \mathbf{A}_{NO,NO} \end{pmatrix} \tag{6.2}$$

with:

$$\mathbf{A}_{T,T} = \frac{\partial \widehat{T_k}}{\partial T_k}, \qquad \mathbf{A}_{T,NO} = \frac{\partial \widehat{T_k}}{\partial \ln(\mathrm{NO})}$$

$$\mathbf{A}_{NO,T} = \frac{\partial \ln \widehat{(\mathrm{NO})}}{\partial T_k}, \qquad \mathbf{A}_{NO,NO} = \frac{\partial \ln \widehat{(\mathrm{NO})}}{\partial \ln(\mathrm{NO})}$$

The full averaging kernel spans over the complete target parameter space given by the $\widehat{T_k}$ and $\ln \widehat{(\mathrm{NO})}$ profiles.

Following *Rodgers* (2000), the retrieval solution for $T_k$ and $\ln(\mathrm{NO}\ vmr)$ can be constructed from the "true" profiles, in linear approximation, by

$$\widehat{\begin{bmatrix} T_k \\ \ln(\mathrm{NO}) \end{bmatrix}} = \mathbf{A} \begin{bmatrix} T_k \\ \ln(\mathrm{NO}) \end{bmatrix}_{\mathrm{t}} + (\mathbf{I} - \mathbf{A}) \begin{bmatrix} T_k \\ \ln(\mathrm{NO}) \end{bmatrix}_{\mathrm{a}}, \tag{6.3}$$

where "^", "t", and "a" stand for "retrieved", "true", and "a priori", respectively. This equation is particularly useful when comparing MIPAS $T_k$ and NO *vmr* profiles to model simulations. By application of this transformation to the simulated profiles instead of the (usually unknown) "true" profiles, the retrieval response to the model atmosphere can be estimated, which is then directly comparable to the observed profiles.

Table 6.2: Atmospheric conditions of "true" and *a priori* profiles used in the retrieval simulations.

| Simulation | Latitude | "True" | $T_k$ *a priori* | NO *vmr a priori* |
|---|---|---|---|---|
| SA1 | polar | high-$A_p$ | high-$A_p$ | low-$A_p$ |
| SA2 | polar | high-$A_p$ | low-$A_p$ | high-$A_p$ |
| SB1 | extra-polar | low-$A_p$ | high-$A_p$ | low-$A_p$ |
| SB2 | extra-polar | low-$A_p$ | low-$A_p$ | high-$A_p$ |

In order to assess the impact of imperfect $T_k$ and NO *vmr a priori* profile shapes on the inverted profiles, retrieval simulations have been performed using synthetic spectra, computed with the $T_k$ and NO *vmr* profiles shown in Figure 6.1 for polar high-$A_p$ and extra-polar low-$A_p$ conditions. These conditions represent typical cases of high and low signal-to-noise ratios, respectively. In order to not mask the smoothing error cross talk, no artificial noise has been added to the spectra. The MIPAS measurement noise covariance matrix, however, has been considered in the retrievals in order to maintain the weighting between the *a priori* and the measurement information. Two retrieval simulations have been performed for each of the generated synthetic spectra, combining the a priori profiles such that one, either $T_k$ or NO *vmr*, was equal to the "true" profile while the other corresponded to a different atmospheric condition (i.e., high-$A_p$ conditions for low-$A_p$ simulations and vice versa). A summary of the performed retrieval simulations is given in Table 6.2.

For polar high-$A_p$ simulations (SA1 and SA2 of Table 6.2, see Figure 6.13), deviations between the retrieved and the "true" $T_k$ and NO profiles are very small when using the inappropriate a priori profile, being less than 20 K and 15%, respectively, except for simulation SA1, where retrieved NO *vmr*'s below 120 km deviate from the truth by 30-50%. Here, stronger deviations are expected due to the very pronounced differences of the true and a priori NO profile shapes. It should be noted that, in spite of these deviations, the smoothing error cross talk (i.e., deviations of the retrieved $T_k$ profile from the truth) is very small.

In the extra-polar low-$A_p$ simulations (SB1 and SB2 of Table 6.2, see Figure 6.14), more pronounced deviations occur. Particularly the application of the inappropriate *a priori* NO profile then results in deviations of the retrieved $T_k$ and NO *vmr* profiles from the "true" profiles in the order of 70 K and 50%, respectively. Deviations of up to 40 K and 10% in the NO *vmr* were found when using the inappropriate $T_k$ *a priori* profile.

The retrieval simulations yield that smoothing error cross talk may occur in the retrievals corresponding to extra-polar and/or weak geomagnetic activity conditions, if the *a priori* profile shape (particularly that of NO) deviates significantly from the true profile, while

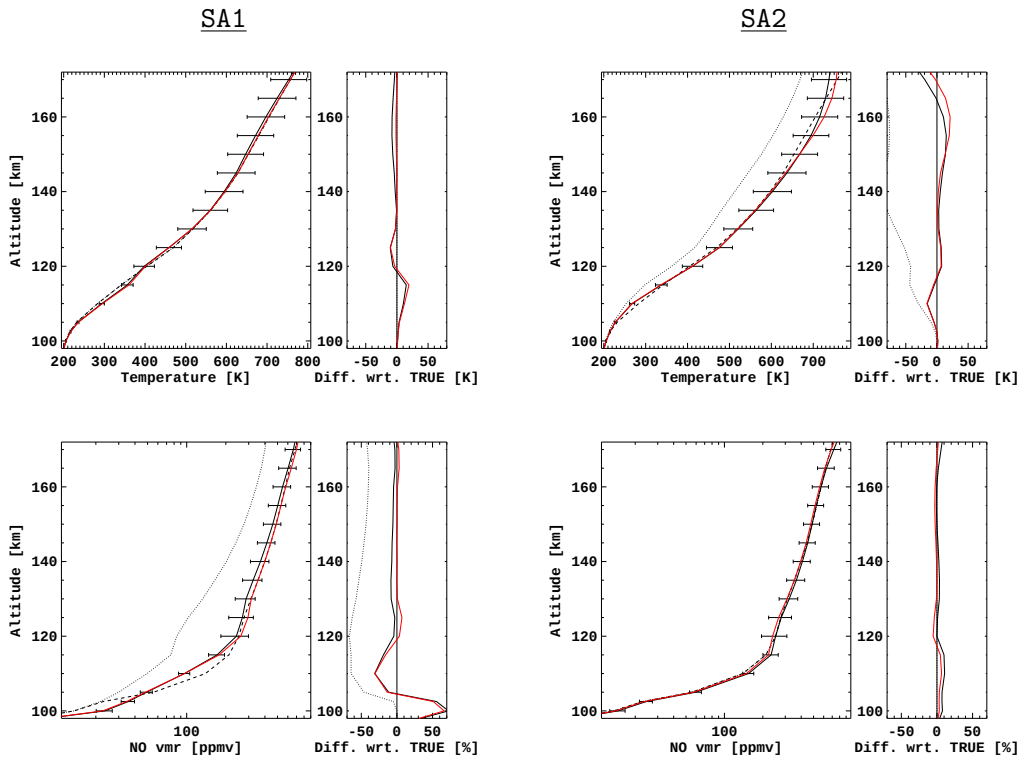


Figure 6.13: Retrieved $T_k$'s (top) and NO *vmr*'s (bottom) from simulated spectra for polar high-$A_p$ conditions and the following deviations of the *a priori* profile from the "truth". Left: NO *a priori* profile corresponding to low-$A_p$ conditions and $T_k$ *a priori* identical to "truth" (SA1), right: $T_k$ *a priori* profile corresponding to low-$A_p$ conditions and NO *a priori* identical to "truth" (SA2). Solid: retrieval results, dashed: "true" profile, dotted: *a priori* profile, red: linear retrieval response (application of the AK to the "true'' profile). Error bars reflect the noise error.

these errors are of minor importance for polar and high geomagnetic activity conditions. On the other hand, the generally good agreement of the retrieved profiles with the linear retrieval response calculated by means of Equation 6.3 (red lines in Figures 6.13 and 6.14) indicates that comparisons of MIPAS observations and model simulations are meaningful whenever the MIPAS averaging kernels are applied to the model profiles, and provided that both $T_k$ and NO profiles are available from the simulations. Significant deviations of the retrieved NO profile with the linear retrieval response are only found in the simulation SB1. In this particular case, the mismatch can be explained to a major part by atomic oxygen number density differences between the true and retrieved atmospheric state, related to the pronounced deviations of the retrieved $T_k$ (and hence total density) profile. In a comparison of MIPAS and model NO data, this apparent mismatch can be avoided by adjusting the MIPAS NO profiles to model atomic oxygen densities as described in Section 6.2.

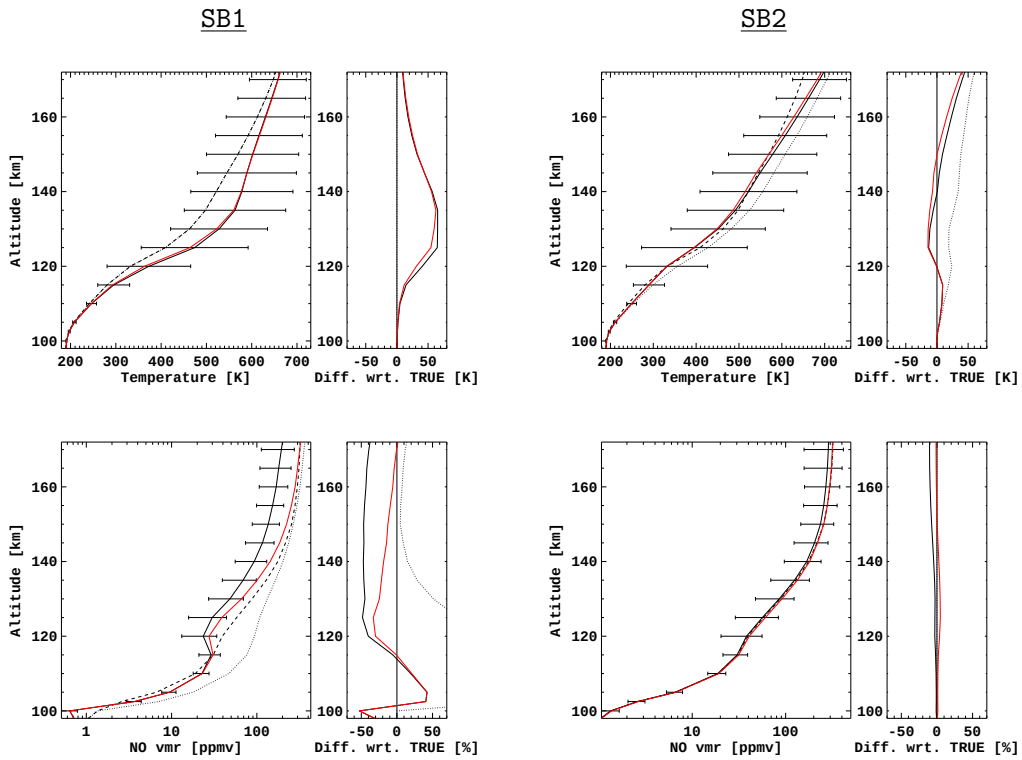


Figure 6.14: Retrieved $T_k$'s (top) and NO *vmr*'s (bottom) from simulated spectra for extra-polar low-$A_p$ conditions and the following deviations of the *a priori* profile from the "truth". Left: NO *a priori* profile corresponding to high-$A_p$ conditions and $T_k$ *a priori* identical to "truth" (SB1), right: $T_k$ *a priori* profile corresponding to high-$A_p$ conditions and NO *a priori* identical to "truth" (SB2). Solid: retrieval results, dashed: "true" profile, dotted: *a priori* profile, red: linear retrieval response (application of the AK to the "true" profile). Error bars reflect the noise error.

## 6.6. Validation of MIPAS $T_k$ and NO *vmr* in the upper atmosphere

In the previous sections, the retrieved profiles of NO *vmr* and $T_k$ have been characterized comprehensively. The influence of the spectral noise and the a priori information via averaging kernels (AK) on the retrieved parameters was pointed out using retrieval simulations. Now, a further validation is carried out. On the one hand, it will be shown the result of appying full AK on data from models when comparing to MIPAS data; on the other hand, ionic temperatures measured with the EISCAT UHF radar during the Delta-2 Campaign will allow to compare MIPAS temperatures with nearly simultaneous measurements.

### 6.6.1. Comparison with TIME-GCM model simulations

In order to better understand the characteristics of MIPAS $T_k$ and NO observations, comparisons to TIME-GCM simulations have been carried out. The purpose of this comparison is not to learn about the physical and chemical processes occurring in the thermosphere, which will be pursued in the future, but to find out potential shortcomings related to a priori effects in this data version and to stress the importance of applying MIPAS averaging kernel to model data when performing model/measurements comparisons.

As an example, both datasets for 22 July 2005 have been compared. The geomagnetic conditions were quiet ($A_p = 15$), though on 20-21 July, a high speed coronal hole wind stream caused the geomagnetic field to respond with mostly unsettled to minor storm conditions with major storm periods at high latitudes (maximum $A_p$ of 48). Therefore, rather high thermospheric NO abundances are expected at polar latitudes.

The Thermosphere Ionosphere Mesosphere Electrodynamics General Circulation Model (TIME-GCM) is a time-dependent 3D model that predicts global 3-D temperature, density, composition and wind fields for the neutral gas, as well as ionospheric electron density and ion distributions from 30 km to about 500 km altitude (*Roble*, 1995). The model is an extension, down to 10 mb (∼30 km), of that described by *Roble et al.* (1987) for the global mean structure of the thermosphere and ionosphere above 97 km, and the model described by *Roble and Dickinson* (1989) that included both a portion of the thermosphere and ionosphere and a portion of the mesosphere down to 60 km. The extension of the physics, chemistry, radiation and transport to that described in *Roble et al.* (1987) is reported in *Roble* (1995). The standard horizontal resolution is 5° in longitude by 5° in latitude, with a vertical resolution ranging from -17 to 5 by 0.5 in $-\ln(p/p_0)$, with $p_0 = 50\mu Pa$. The inputs to the TIME-GCM include specifications of the solar flux, the high latitude convection and the particle precipitation, as well as the tides propagating up from the lower atmosphere. The model is forced at its lower and upper boundaries. At the lower boundary, the tide and planetary waves are specified either using the GSWM (*Hagan and Forbes*, 2002). At the upper boundary, auroral precipitation and plasma convection are imposed from empirical models driven by $K_p$. In this particular model simulation, input from empirical models was used.

In order to reduce errors related to the different sampling of the MIPAS observations and gridded model data, the model results have been interpolated to the MIPAS measurement locations and times, as well as to the retrieved altitudes of the $T_k$ and NO profiles. This approach has the further advantage that diurnal variations are implicitly taken into account. MIPAS averaging kernel have been applied to the TIME-GCM $T_k$ and

NO profiles as described in Section 6.5. For the comparisons, MIPAS and resampled TIME-GCM data have then been treated in an identical manner.

Figure 6.15 shows the effect of the application of MIPAS averaging kernels to the TIME-GCM simulations separately for day and night conditions. Differences between convolved and not-convolved model results are rather small at daytime above 120 km, not exceeding 10 K and 15% for $T_k$ and NO, respectively. In contrast, substantial differences are encountered during night at the tropics and mid-latitudes. There, convolved temperatures are up to 50 K colder above 140 km and approximately 20 K warmer around 125 km. The opposite behavior shows up in the modeled NO distributions with the convolved model abundances being 20-40% higher than in the un-convolved results above 140 km.

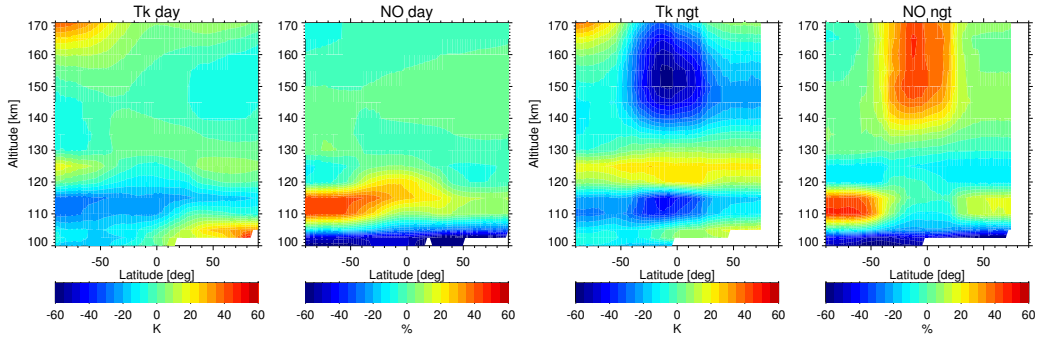


Figure 6.15: Effect of the application of MIPAS averaging kernels to TIME-GCM $T_k$ and NO *vmr* zonal mean distributions on 22 July 2005 separately for daytime (left) and nighttime (right). Differences "with minus without" AK application are shown.

These nighttime effects are related to the NO *a priori* information used in the MIPAS retrievals, which is taken from the NOEM model based on the SNOE. Since SNOE measured NO at a fixed local time of 10:45 a.m. ($\pm$ 30 min.), i.e., very similar to the MIPAS daytime observations, diurnal variations of NO are not considered in the NOEM empiric model. The TIME-GCM simulations, however, show a generally lower nighttime NO than at daytime, particularly in the tropics, with an increasing diurnal amplitude towards the middle thermosphere. In consequence, important differences between the TIME-GCM and MIPAS *a priori* profile shapes of NO are expected during nighttime, particularly in the extra-polar regions, right where the biggest differences between convolved and un-convolved simulations show up.

The encountered differences hence indicate a potential systematic smoothing error in the MIPAS $T_k$ and NO nighttime retrievals in the middle thermosphere, with a magnitude in the order of the differences between the convolved and not-convolved simulations, provided that the model diurnal amplitude for this particular day can be considered as repre-

sentative for any atmospheric conditions. Future data versions of MIPAS $T_k$ and NO will therefore be retrieved under consideration of a diurnal correction of the NO a priori information for nighttime measurements.

For the analysis of nighttime $T_k$ and NO at extra-polar latitudes, a systematic bias related to smoothing errors should then be considered. This, however, does not affect the comparison of MIPAS data with model simulations, even for nighttime and extra-polar latitude conditions, provided that MIPAS averaging kernels are taken into account.

At lower altitudes, around 115 km, convolved model temperatures are 10-30 K colder, particularly in the SH, while model NO *vmr*'s are up to 40% higher when MIPAS averaging kernels are applied. Contrary to the behavior at higher altitudes, this occurs at both day and night conditions, thus excluding the neglect of NO diurnal variations in the a priori as possible reason. It might be possible that these differences around 115 km are related to deficiencies in the MSIS a priori temperature profile shape. As discussed in Section 7.3, there is evidence for a possible low-bias of MSIS temperatures in this altitude range. More detailed studies, however, are required in order to investigate if the differences between convolved and un-convolved model temperatures in this region are related to systematic deficiencies of the a priori profile shapes or to other effects.

After application of MIPAS averaging kernel to the TIME-GCM simulations, a comparison of both observed and simulated data sets can be performed. Figure 6.16 shows observed and modeled zonal mean distributions of temperature. In general, MIPAS and TIME-GCM temperature distributions are in good agreement, both showing a warm polar summer thermosphere related to enhanced EUV heating, with maximum temperatures around 700 K at 150 km. Differences are found in the polar winter region above 130 km (MIPAS up to 70 K warmer) and in the tropical and NH midlatitude lower thermosphere around 120 km (MIPAS up to 60 K colder).

For comparison of NO distributions, MIPAS data has to be adjusted to TIME-GCM atomic oxygen concentrations as described in Section 6.2. Adjusted MIPAS NO distributions show considerably lower NO amounts in the polar regions while tropical NO is increased with respect to the original data, particularly in the lower thermosphere (compare Figure 6.17, left panels). This behavior is related to differences between TIME-GCM and MSIS atomic oxygen concentration of opposite sign (i.e., lower/higher TIME-GCM O concentrations in the polar/tropical regions). It is evident from Figure 6.17 that the the adjustment of observed NO distributions to modelled O concentrations results in a noticeably better agreement of MIPAS and TIME-GCM. However, adjusted MIPAS observations and modeled NO distributions after application of averaging kernels still exhibit significant differences in absolute terms, though latitudinal and vertical variations are in reasonable qualitative agreement. In the extra-polar

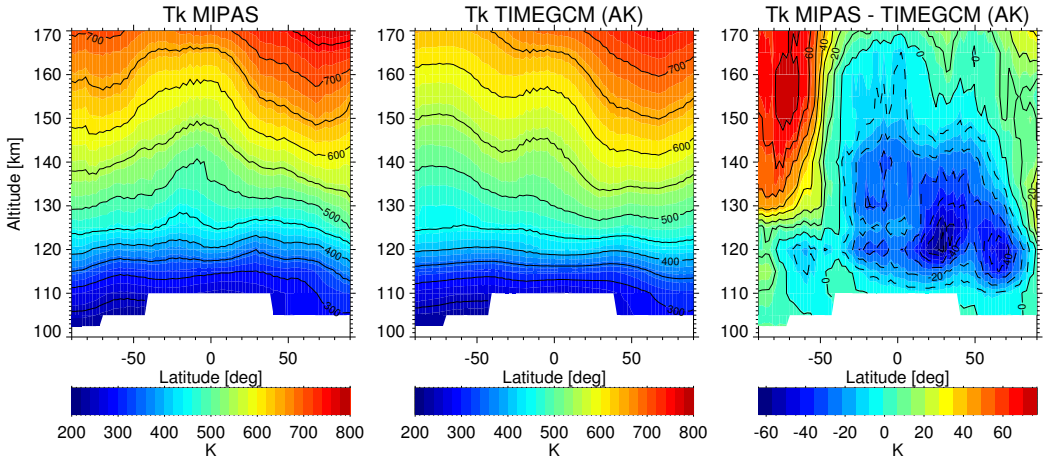


Figure 6.16: Temperature zonal mean distributions for 22 July 2005. From left to right: MIPAS observations, TIME-GCM simulations (AK applied), differences between MIPAS observations and TIME-GCM simulations.

regions, MIPAS tends to exhibit lower NO abundances than in the simulations, most pronounced around 120 km with differences around 10-20%. In the polar middle thermosphere, adjusted MIPAS NO *vmr*'s are still considerably higher than in the simulations. A possible reason for this difference could be the use of an empirical model instead of assimilated particle fluxes in this TIME-GCM simulation. Nevertheless, both observed and simulated distributions show important similarities with respect to the hemispheric asymmetry of extra-polar NO related to solar inclination with larger values in the summer hemisphere (*Marsh et al.*, 2004). Also, observations and simulations show the auroral NO maximum over the winter pole (SH) at lower altitudes (i.e., around 110 km) than over the summer pole (NH).

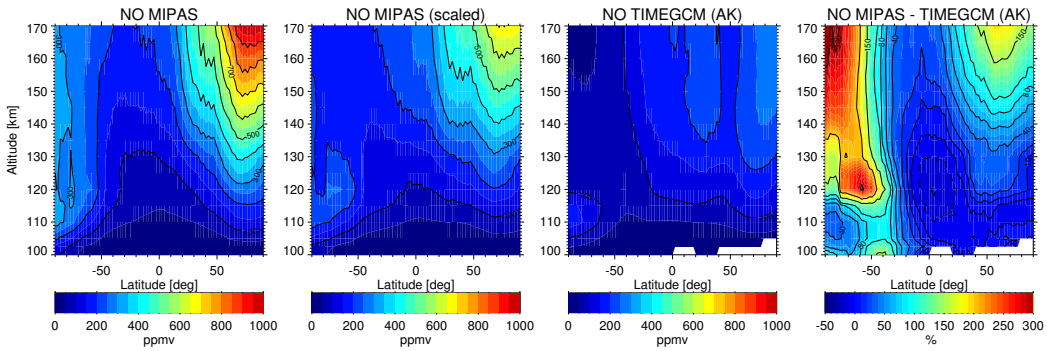


Figure 6.17: NO *vmr* zonal mean distributions for 22 July 2005. From left to right: MIPAS observations, MIPAS observations adjusted to TIME-GCM atomic oxygen concentrations, TIME-GCM simulations (AK applied), differences between the adjusted MIPAS observations and TIME-GCM simulations.

### 6.6.2. Comparison with EISCAT measurements

The Delta-2 Campaign offers an unique opportunity to compare MIPAS thermospheric $T_k$ with nearly simultaneous measurements. The Delta-2 Campaign coordinates sounding rocket observations with the European Incoherent Scatter (EISCAT) radar and ground-based Fabry-Perot Interferometers (FPIs). It aims to study the dynamics and energetics in the polar lower thermosphere. The rocket provides in situ measurements of neutral temperature and density; the EISCAT radar measures ion drift, ion temperature and electron temperature and density; FPIs measures neutral wind and neutral temperature. The campaign was carried out during the second half of January 2009, and the MIPAS *UA* observation mode schedule was coordinated with it. The last 3 orbits of MIPAS for every day (between 18:30 and 24:00 UT, approximately) were dedicated to the *UA* mode. Ion temperatures ($T_i$) measured by EISCAT UHF radar (*Folkestad et al.*, 1983) at Tromsø(Norway) are available to compare with MIPAS $T_k$. EISCAT observations during the DELTA campaign (December 2004) showed a good agreement between ion and neutral temperatures below 110 km, while $T_i$ increases by 200 K above, possibly due to Joule heating, although the shape of the altitude profiles are similar (*Nozawa et al.*, 2006).

Since the primary purpose of the campaign is to investigate the lower thermospheric response to an auroral energy input, the EISCAT radar observations are concentrated after the sunset between $14^{th}$ and $26^{th}$ January 2009. The derived $T_i$ profiles typically range between 75 and 600 km, with a variable spacing increasing with altitude (from 4 km at 105 km to 12 km at 160 km). They are geolocated in a closed region centered near (69.5° N, 19.2° E, reference point) and spread 0.25° in latitude and 1.5° in longitude. A group of coincidences (in time and geolocation) between MIPAS and EISCAT has been determined. The criterium is to find MIPAS measurements within a geographical box of ±5° in latitude and ±14 in longitude away the reference point (± ∼550 km) taken during a time interval of ±1 h of the EISCAT measurement. The MIPAS observations taken along one orbit (typically 2) were averaged and considered as a single measurement. The radar measurements are rather noisy and hence those taken during a lapse of ±1 h were averaged together in a single profile. In total, 10 coincidences have been found. The number of MIPAS and EISCAT measurements for each coincidence is shown in Table 6.3.

Figure 6.18 shows MIPAS and EISCAT mean profiles and their differences, averaged over the resulting 10 coincidences. MIPAS temperature is colder than EISCAT ion temperature in the whole altitude range (110-170 km), being the differences within a range of -15 K between 125 and 135 km, and colder below (up to 50 K) and above (up to 140 K), which goes in the direction of the results found in *Nozawa et al.* (2006). Further, combined errors of both instruments are approximately several times smaller than the standard deviation of the differences, suggesting

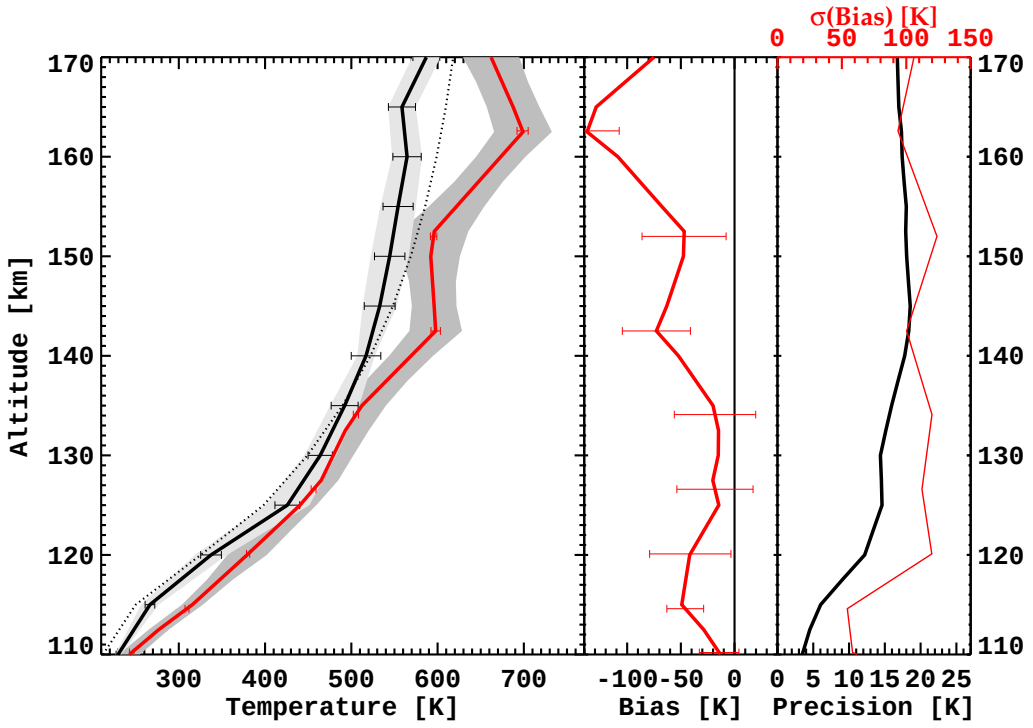


Figure 6.18: Left panel: Mean profiles of MIPAS (black) and EISCAT (red) temperatures. Shaded regions stand for the standard error of the mean of MIPAS (faint) and EISCAT (dark) observations corresponding to the 10 coincidences (see Table 6.3). Horizontal bars represent the respective precisions of the averages. Corresponding MSIS temperatures are also shown for comparison (dotted). Mid panel: bias (MIPAS - EISCAT, red); the horizontal bars reflect the standard error of the bias. Right Panel: standard deviation of the differences (red) and combined noise error (quadratic sum of mean noise errors of MIPAS and EISCAT) (black).

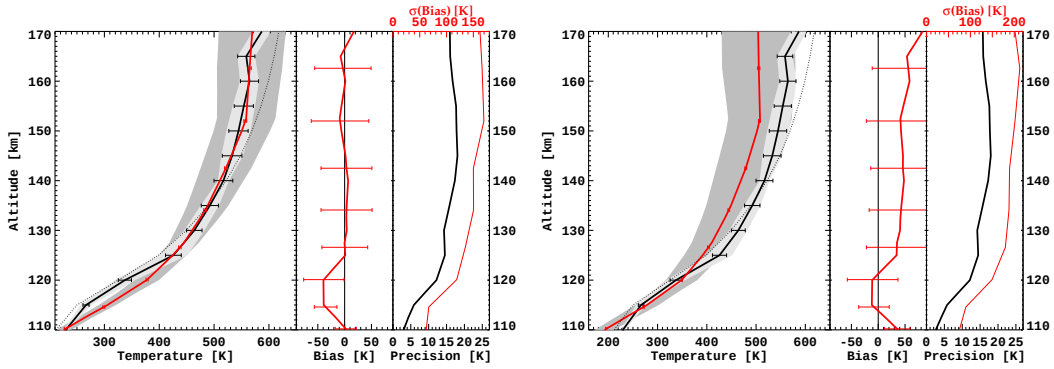


Figure 6.19: MIPAS-EISCAT comparisons analogous to comparison in Figure 6.18 with a threshold in EISCAT error of 400 K (left panel) and of 100 K (right panel).

that dispersion is dominated by natural variability. For comparison, the

Table 6.3: MIPAS and EISCAT number of measurements for each coincidence

| MIPAS | EISCAT | Date , Time Lapse (UT) |
|---|---|---|
| 2 | 19 | 15 Jan , 20:30-22:30 |
| 2 | 81 | 16 Jan , 20-22 |
| 1 | 80 | 17 Jan , 19:30-21:30 |
| 2 | 80 | 18 Jan , 19-21 |
| 1 | 60 | 18 Jan , 20:30-22:30 |
| 2 | 58 | 19 Jan , 20-22 |
| 2 | 80 | 20 Jan , 19:30-21:30 |
| 2 | 80 | 21 Jan , 19-21 |
| 2 | 40 | 23 Jan , 19:30-21:30 |
| 2 | 39 | 24 Jan , 19-21 |

corresponding MSIS temperature profile is also shown. MIPAS (EISCAT) observations are colder (warmer) than MSIS above 135 km, up to 50 K ($\sim$100 K) at 165 km. On the other hand, below 135 km, both instruments obtained warmer temperatures than MSIS, between 20 and 30 K for MIPAS and higher differences for EISCAT, which is in consonance with previous studies (*Gardner et al.*, 2005, 2007).

However, it has been found that there are EISCAT $T_i$ profiles which have quite large noise error values. For this reason, the MIPAS-EISCAT differences have been recalculated, removing those EISCAT measurements which errors are higher than a reasonable threshold. Figure 6.19 shows the new comparisons using a threshold of 400 K (left panel) and 100 K (right panel). A clear dependence of the mean $T_i$ on its noise error is observed: the $T_i$ profile gets smaller as the threshold value decreases. In conclusion, a deeper analysis of EISCAT errors is required in order to make a reliable selection of EISCAT measurements before undertaking a more meaningful comparison with MIPAS $T_k$.

# Chapter 7

# MIPAS climatology

*Abstract*

The retrieval methods described in Chapter 4 and validated in Chapters 5 and 6 have been applied to all MIPAS data taken in reduced spectral resolution in the middle and upper atmosphere, from January 2005 to December 2009. Thus, a climatology for kinetic temperature in the middle and upper atmosphere and for NO *vmr* in the upper atmosphere has been built. MIPAS thermospheric $T_k$ has been compared to MSIS model, and MIPAS NO with NOEM model and the NO climatology based on HALOE+SME data. Day−night differences in MIPAS NO have been analyzed. The evolution of MIPAS thermospheric $T_k$ and NO abundance along the period 2005-2009 as well as their correlations with geomagnetic and solar activities are also discussed. Most of the results presented here for the thermosphere has been published in *Bermejo-Pantaleón et al.* (2011).

## 7.1. Introduction

The MIPAS instrument offers the opportunity to measure the infrared emission from the atmosphere with global coverage, geographically and independently on the illumination conditions. Along its duty cycle, MIPAS is able to observe at different altitude ranges, depending on the programmed observation mode (see Section 2.6), from the middle troposphere (6 km) to the middle thermosphere (170 km). Thanks to the instrument's wide spectral range (4.15 to 14.6 $\mu$m), profiles of temperature and abundance of key gases can be retrieved by applying inversion schemes on the measured spectra. In addition, MIPAS has been measuring almost continuously since 2002 (except the period from March to December 2004), turning into a vast database available to perform scientific analysis.

In the context of this work, the retrieval schemes described in Chapter 4 and validated in Chapters 5 and 6 have been applied to specific MIPAS measurements in its reduced spectral resolution, i.e., its middle and upper atmosphere observation modes since January 2005. As a result, it has been built a climatology composed of two databases, separating the

Table 7.1: Days of the year during the 2005-2009 period of MIPAS duty cycle in which the instrument has measured in any of the observation modes of interest: *MA* (red), *NLC* (blue) and *UA* (green). Most of remaining days in white belong the *Nominal* mode.

**2005**

| | 1 | 2 | 3 | 4 | 5 | 6 | 7 | 8 | 9 | 10 | 11 | 12 | 13 | 14 | 15 | 16 | 17 | 18 | 19 | 20 | 21 | 22 | 23 | 24 | 25 | 26 | 27 | 28 | 29 | 30 | 31 |
|---|---|---|---|---|---|---|---|---|---|---|---|---|---|---|---|---|---|---|---|---|---|---|---|---|---|---|---|---|---|---|---|
| Jan | | | | | | | | | | | | | | | | | | | | | | | | | | | | | | | |
| Feb | | | | | | | | | | | | | | | | | | | | | | | | | | | | | | | |
| Mar | | | | | | | | | | | | | | | | | | | | | | | | | | | | | | | |
| Apr | | | | | | | | | | | | | | | | | | | | | | | | | | | | | | | |
| May | | | | | | | | | | | | | | | | | | | | | | | | | | | | | | | |
| Jun | | | | | | | | | | | | | | | | | | | | | | | | | | | | | | | |
| Jul | | | | | | | | | | | | | | | | | | | | | | | | | | | | | | | |
| Aug | | | | | | | | | | | | | | | | | | | | | | | | | | | | | | | |
| Sep | | | | | | | | | | | | | | | | | | | | | | | | | | | | | | | |
| Oct | | | | | | | | | | | | | | | | | | | | | | | | | | | | | | | |
| Nov | | | | | | | | | | | | | | | | | | | | | | | | | | | | | | | |
| Dec | | | | | | | | | | | | | | | | | | | | | | | | | | | | | | | |

**2006**

| | 1 | 2 | 3 | 4 | 5 | 6 | 7 | 8 | 9 | 10 | 11 | 12 | 13 | 14 | 15 | 16 | 17 | 18 | 19 | 20 | 21 | 22 | 23 | 24 | 25 | 26 | 27 | 28 | 29 | 30 | 31 |
|---|---|---|---|---|---|---|---|---|---|---|---|---|---|---|---|---|---|---|---|---|---|---|---|---|---|---|---|---|---|---|---|
| Jan | | | | | | | | | | | | | | | | | | | | | | | | | | | | | | | |
| Feb | | | | | | | | | | | | | | | | | | | | | | | | | | | | | | | |
| Mar | | | | | | | | | | | | | | | | | | | | | | | | | | | | | | | |
| Apr | | | | | | | | | | | | | | | | | | | | | | | | | | | | | | | |
| May | | | | | | | | | | | | | | | | | | | | | | | | | | | | | | | |
| Jun | | | | | | | | | | | | | | | | | | | | | | | | | | | | | | | |
| Jul | | | | | | | | | | | | | | | | | | | | | | | | | | | | | | | |
| Aug | | | | | | | | | | | | | | | | | | | | | | | | | | | | | | | |
| Sep | | | | | | | | | | | | | | | | | | | | | | | | | | | | | | | |
| Oct | | | | | | | | | | | | | | | | | | | | | | | | | | | | | | | |
| Nov | | | | | | | | | | | | | | | | | | | | | | | | | | | | | | | |
| Dec | | | | | | | | | | | | | | | | | | | | | | | | | | | | | | | |

**2007**

| | 1 | 2 | 3 | 4 | 5 | 6 | 7 | 8 | 9 | 10 | 11 | 12 | 13 | 14 | 15 | 16 | 17 | 18 | 19 | 20 | 21 | 22 | 23 | 24 | 25 | 26 | 27 | 28 | 29 | 30 | 31 |
|---|---|---|---|---|---|---|---|---|---|---|---|---|---|---|---|---|---|---|---|---|---|---|---|---|---|---|---|---|---|---|---|
| Jan | | | | | | | | | | | | | | | | | | | | | | | | | | | | | | | |
| Feb | | | | | | | | | | | | | | | | | | | | | | | | | | | | | | | |
| Mar | | | | | | | | | | | | | | | | | | | | | | | | | | | | | | | |
| Apr | | | | | | | | | | | | | | | | | | | | | | | | | | | | | | | |
| May | | | | | | | | | | | | | | | | | | | | | | | | | | | | | | | |
| Jun | | | | | | | | | | | | | | | | | | | | | | | | | | | | | | | |
| Jul | | | | | | | | | | | | | | | | | | | | | | | | | | | | | | | |
| Aug | | | | | | | | | | | | | | | | | | | | | | | | | | | | | | | |
| Sep | | | | | | | | | | | | | | | | | | | | | | | | | | | | | | | |
| Oct | | | | | | | | | | | | | | | | | | | | | | | | | | | | | | | |
| Nov | | | | | | | | | | | | | | | | | | | | | | | | | | | | | | | |
| Dec | | | | | | | | | | | | | | | | | | | | | | | | | | | | | | | |

**2008**

| | 1 | 2 | 3 | 4 | 5 | 6 | 7 | 8 | 9 | 10 | 11 | 12 | 13 | 14 | 15 | 16 | 17 | 18 | 19 | 20 | 21 | 22 | 23 | 24 | 25 | 26 | 27 | 28 | 29 | 30 | 31 |
|---|---|---|---|---|---|---|---|---|---|---|---|---|---|---|---|---|---|---|---|---|---|---|---|---|---|---|---|---|---|---|---|
| Jan | | | | | | | | | | | | | | | | | | | | | | | | | | | | | | | |
| Feb | | | | | | | | | | | | | | | | | | | | | | | | | | | | | | | |
| Mar | | | | | | | | | | | | | | | | | | | | | | | | | | | | | | | |
| Apr | | | | | | | | | | | | | | | | | | | | | | | | | | | | | | | |
| May | | | | | | | | | | | | | | | | | | | | | | | | | | | | | | | |
| Jun | | | | | | | | | | | | | | | | | | | | | | | | | | | | | | | |
| Jul | | | | | | | | | | | | | | | | | | | | | | | | | | | | | | | |
| Aug | | | | | | | | | | | | | | | | | | | | | | | | | | | | | | | |
| Sep | | | | | | | | | | | | | | | | | | | | | | | | | | | | | | | |
| Oct | | | | | | | | | | | | | | | | | | | | | | | | | | | | | | | |
| Nov | | | | | | | | | | | | | | | | | | | | | | | | | | | | | | | |
| Dec | | | | | | | | | | | | | | | | | | | | | | | | | | | | | | | |

**2009**

| | 1 | 2 | 3 | 4 | 5 | 6 | 7 | 8 | 9 | 10 | 11 | 12 | 13 | 14 | 15 | 16 | 17 | 18 | 19 | 20 | 21 | 22 | 23 | 24 | 25 | 26 | 27 | 28 | 29 | 30 | 31 |
|---|---|---|---|---|---|---|---|---|---|---|---|---|---|---|---|---|---|---|---|---|---|---|---|---|---|---|---|---|---|---|---|
| Jan | | | | | | | | | | | | | | | | | | | | | | | | | | | | | | | |
| Feb | | | | | | | | | | | | | | | | | | | | | | | | | | | | | | | |
| Mar | | | | | | | | | | | | | | | | | | | | | | | | | | | | | | | |
| Apr | | | | | | | | | | | | | | | | | | | | | | | | | | | | | | | |
| May | | | | | | | | | | | | | | | | | | | | | | | | | | | | | | | |
| Jun | | | | | | | | | | | | | | | | | | | | | | | | | | | | | | | |
| Jul | | | | | | | | | | | | | | | | | | | | | | | | | | | | | | | |
| Aug | | | | | | | | | | | | | | | | | | | | | | | | | | | | | | | |
| Sep | | | | | | | | | | | | | | | | | | | | | | | | | | | | | | | |
| Oct | | | | | | | | | | | | | | | | | | | | | | | | | | | | | | | |
| Nov | | | | | | | | | | | | | | | | | | | | | | | | | | | | | | | |
| Dec | | | | | | | | | | | | | | | | | | | | | | | | | | | | | | | |

31st October 2005 is half *MA* and half *UA*.

MIPAS data into middle and upper atmosphere regions. On the one hand, a database of kinetic temperature in the middle atmosphere corresponding to the days which MIPAS measured in its *MA*, *NLC* and *UA* observation modes, giving the respective data versions: V4O_T_511, V4O_T_711 and V4O_T_-611. The $T_k$ profiles range up to 100 km, starting from 20 km in the case of *MA* mode, and from 40 km for *NLC* and *UA* modes. On the other hand, the *UA* mode provides a database of thermospheric $T_k$ and NO *vmr*, V4O_T_611 and V4O_NO_611 respectively, ranging from 100 to 170 km.

Table 7.1 shows the days in which MIPAS has operated in any of the observation modes relevant to this work since 2005. The increase of the *MA* and *UA* modes' frequency in the MIPAS duty cycle since mid-2007 is evident. From January 2005 until November 2007, both modes are represented in each season by one, two or three days. Since November 2007, about 1 day out of 10 is dedicated to each mode. As an exception, *UA* observations have been performed on a daily basis (however, restricted to 3 orbits per day) during the Delta-2 campaign during 14-27 January 2009 (see Section 6.6.2). Since noctilucent clouds occur during polar summer, the *NLC* mode is concentrated on July, and since 2009, also on January.

## 7.2. $T_k$ in the Middle Atmosphere

The large database obtained for $T_k$ in the middle atmosphere is illustrated as zonal mean distributions in Figure 7.1. Seasonal averages for solstice conditions have been chosen along the five years of measurements from *MA*, *NLC* and *UA* observation modes. A latitude binning of 10 degrees have been chosen.

The temperature structure for solstices, with the inter-hemispheric asymmetry dominated by the solar irradiance, the absorption of solar UV by $O_3$ in the stratosphere, the radiative cooling at winter polar vortex in the lower stratosphere and the adiabatic heating/cooling in polar summer/winter caused by the meridional circulation, is well reproduced by MIPAS. The troposphere is not captured by this climatology. At polar regions, winter stratopauses and mesopauses are situated at higher altitudes than summer's. Polar summer stratopause is placed at a quite stable altitude of 50 km for both hemispheres and all years, while at winter its altitude is only slightly higher, 2-3 km. In contrast, the polar summer mesopause is placed at around 87 km, while at winter it reaches up to 100 km. Further, it is interesting to observe the contrast between the stability of the stratopause along the latitude around 50 km and the mesopause. The altitude of the latter shows an clear steep transition from winter to summer hemispheres at tropical latitudes and it is much more irregular shaped along the latitude.

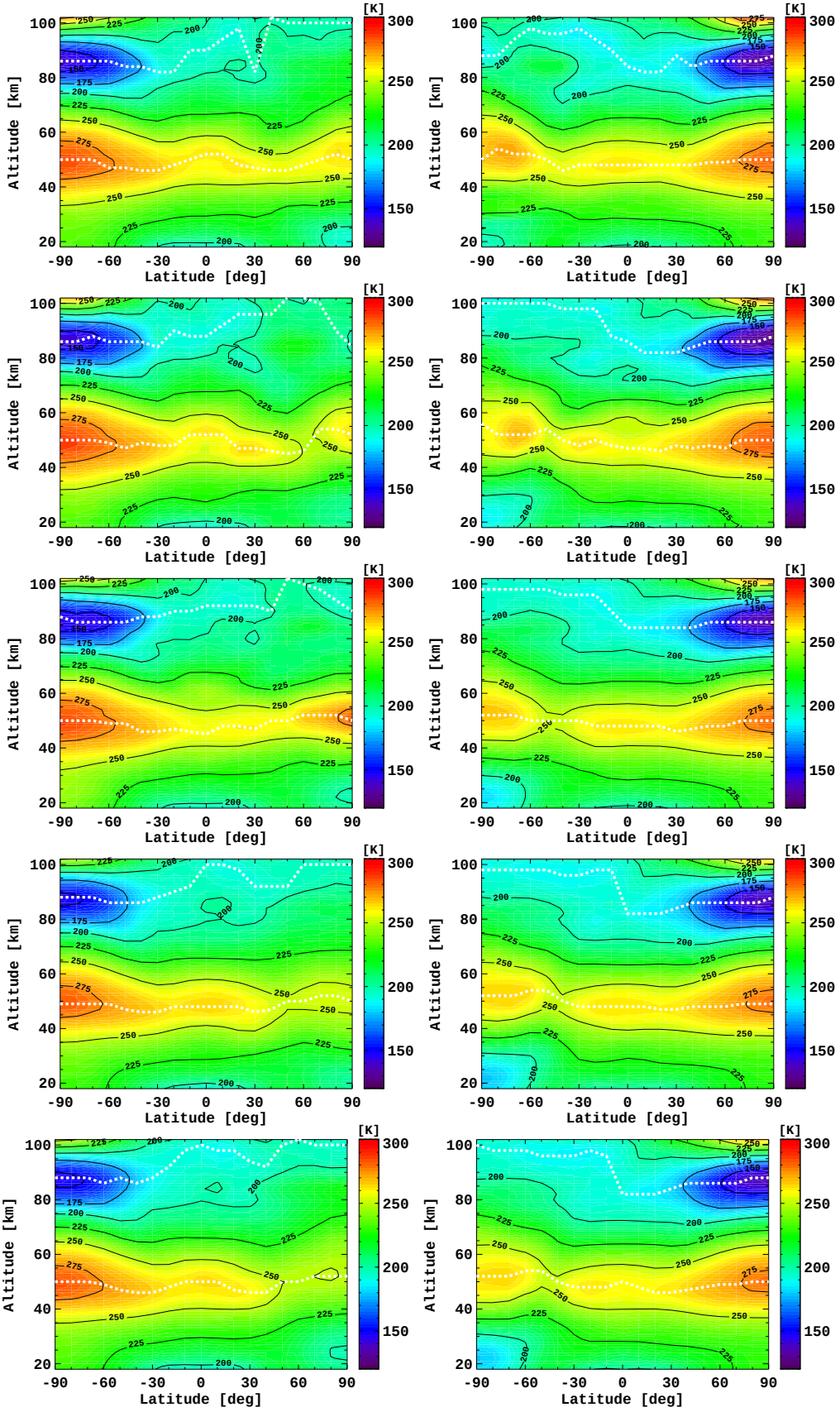


Figure 7.1: Zonal means of middle atmosphere $T_k$ for solstice conditions: northern winter (left) and summer (right). From top to bottom, years 2005 to 2009. Strato- and mesopauses are indicated with white dashed lines.

The stratopause is warmer at polar regions, being warmest in the summer pole, with values close to 285 K, while in winter pole it gets values around 10-30 K colder. These winter-summer differences are due to longer solar illumination and absorption of solar radiation by ozone. In contrast, the mesopause is coldest in the summer pole, below 150 K, caused by the meridional circulation. It progresses from the summer to the winter hemisphere, producing upwelling motion and subsequent nearly adiabatic expansion and a net cooling over the summer pole, while the opposite occurs in the polar winter (*Andrews et al.*, 1987). The polar winter mesopause is 45-60 K warmer than summer's. The cold summer mesopause shows an inter-hemispheric asymmetry, i.e., 130 K at northern pole and 140 K at southern, due to a stronger ascent at the north pole (*Vincent*, 1994; *Brasseur and Solomon*, 2005), thought to be caused by a stronger gravity wave activity in the northern summer than in the southern (*Siskind et al.*, 2003; *Xu et al.*, 2007).

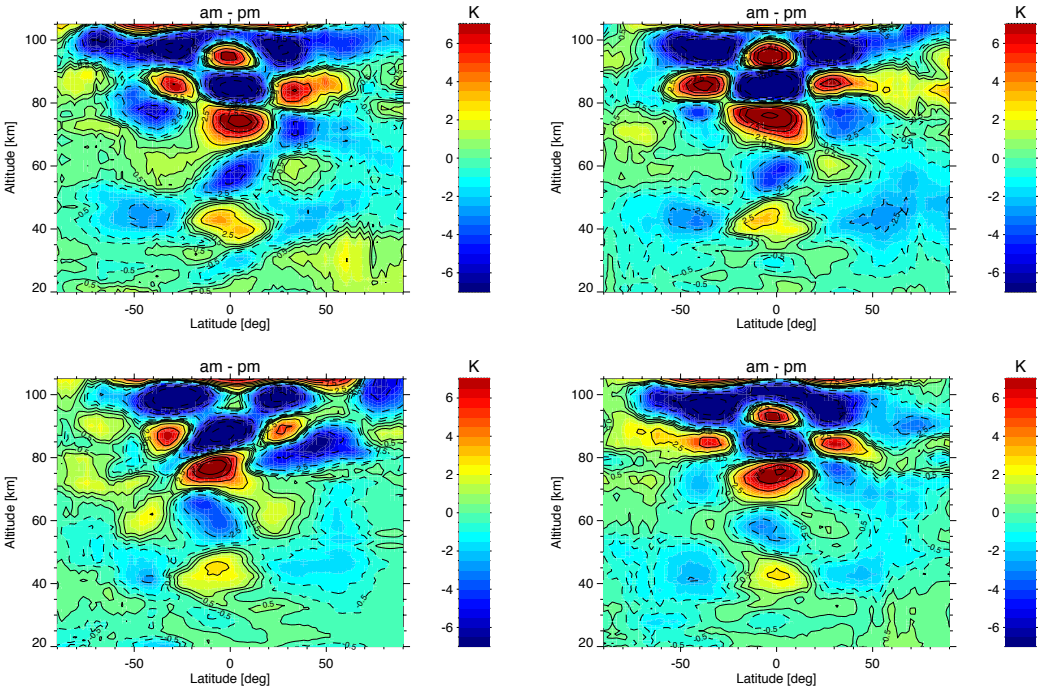


Figure 7.2: Seasonal averages of zonal mean temperature differences between descending (10 a.m.) and ascending (10 p.m.) orbit branch observations of MIPAS. Years 2008 and 2009 are merged. Top left: DJF; top right: MAM; bottom left: JJA; bottom right: SON.

As it was found in the study of horizontal temperature inhomogeneities (Section 5.1.1), MIPAS is able to detect signatures of migrating diurnal tides. The differences between descending (10 a.m. local time) and ascending (10 p.m. local time) orbit branches have been calculated as seasonal zonal means merging MIPAS data from 2008 and 2009 (Figure 7.2).

The tidal structure is clearly visible at the equator, and tropical and mid- latitudes from the lower stratosphere to the lower thermosphere at all seasons, reaching amplitudes of up to 10 K. The amplitude of the tides decreases towards increasing latitudes, and above $\pm 50^{\circ}$ the differences are below 2 K.

## 7.3. MIPAS NO and $T_k$ monthly climatology for solar minimum (2008-2009)

The relatively high and homogeneous data availability during 2008-2009, around 3 days per month (green days in Table 7.1), has allowed to construct a monthly zonal mean climatology for this particular time period belonging to solar minimum conditions.

In this section, zonal mean distributions for temperature and NO abundance are discussed and compared to the corresponding distributions (sampled on MIPAS locations and times) of MSIS (temperature) and NOEM (NO) climatologies. For the comparisons, figures are shown only for seasonal periods, December-February (DJF), March-May (MAM), June-August (JJA), and September-November (SON), which are very representative for the encountered differences.

In addition, due to the potential bias of MIPAS nighttime observations related to smoothing errors (see Section 6.6.1), the analysis of this data version is focused on daytime conditions. Nevertheless, since diurnal variations of thermospheric NO have not been measured prior to MIPAS, the observed day-night differences of NO are discussed at the end of this section.

Figure 7.3 shows the monthly averages of zonal mean daytime temperatures retrieved from MIPAS. Temperatures vary from around 250 K in the lower thermosphere to 600-700 K around 170 km. As a result of particle-induced ionization and Joule heating in the auroral regions, highest temperatures are observed in the polar thermosphere. A warmer summer middle thermosphere compared to the winter hemisphere is an expected result which can be explained by the magnitude of EUV heating in dependence on solar inclination. Surprisingly, a hemispheric asymmetry is also found during the equinoxes (e.g. compare April and May with June and July; and October and November with December), suggesting a seasonal phase shift of the polar summer maximum towards the preceding equinox. During the solstices, a pronounced latitudinal temperature gradient can also be observed in the lower thermosphere (around 115 km) with higher temperatures at the summer pole. It is not clear, if this asymmetry is only caused by illumination differences or if there is also a dynamical contribution related to a winter to summer residual thermospheric circulation and, consequently, adiabatic heating (cooling) over the summer

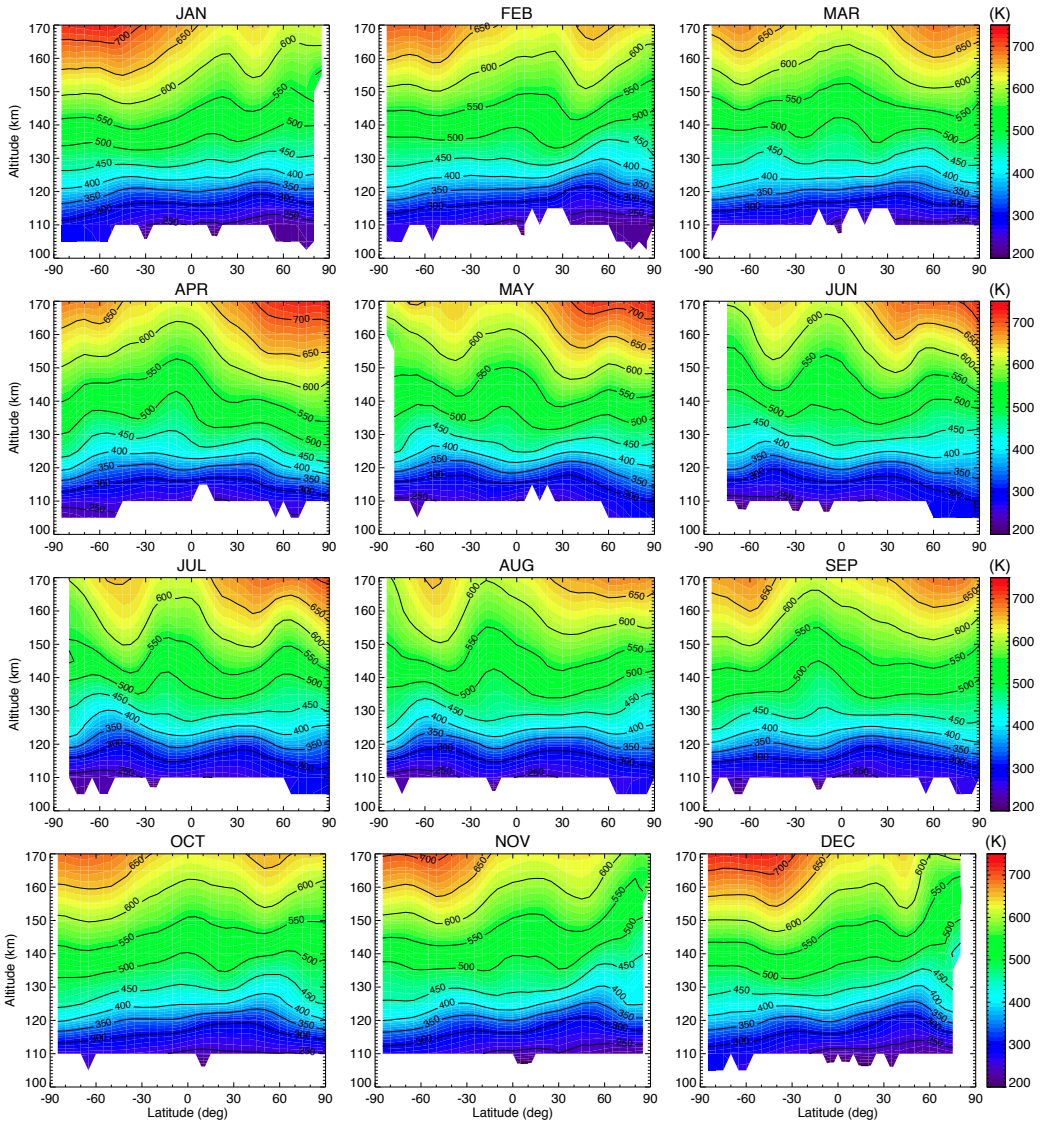


Figure 7.3: Monthly zonal mean of thermospheric daytime temperatures measured by MIPAS during the 2008-2009 period.

(winter) pole.

Figure 7.4 shows the differences of the seasonal temperature averages between MIPAS and MSIS. In general, there is good agreement within 25 K, except for the polar middle thermosphere around 150 km (mainly in the summer) and for the tropics and polar regions at around 120-125 km, where differences can exceed 40 K. MIPAS is generally colder than MSIS in the polar middle thermosphere. At equinox conditions, this behaviour is less pronounced over the preceding summer pole, indicating that the observed seasonal phase shift does not exist or, is strongly damped, in the MSIS climatology. In agreement with previous studies (*Gardner et al.*, 2005, 2007), warmer temperatures than in MSIS are observed in the lower thermo-

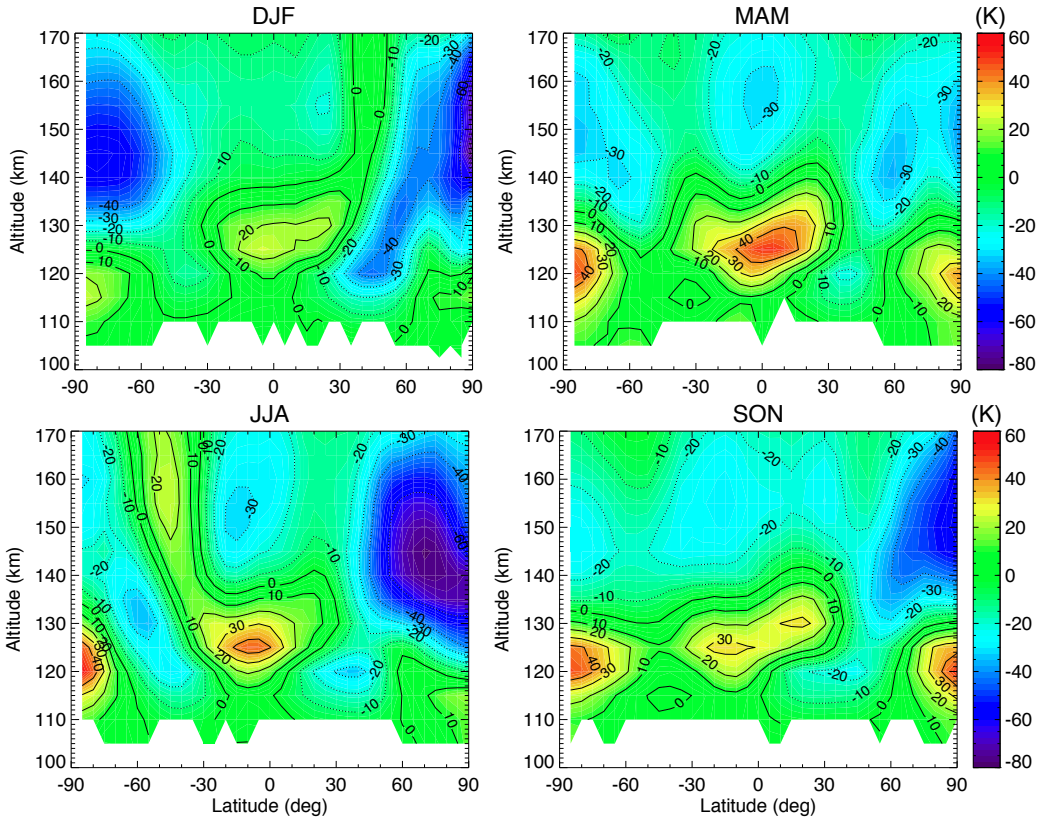


Figure 7.4: Zonal mean MIPAS-MSIS temperatures differences for daytime. From left to right and top to bottom: DJF, MAM, JJA, SON.

sphere around 120-125 km. These differences are most pronounced over the tropics and over the poles. The latitudinal temperature variability at these altitudes is then much smaller in MSIS than in MIPAS observations.

The thermospheric observations of MIPAS provide the second global data set of nitric oxide using limb-scanning technique after the SNOE mission which operated during 1998-2000. Previous non-global thermospheric measurements of NO were taken by the SME instrument, and also by HALOE although limited to the lower thermosphere (*Siskind et al.*, 1998). MIPAS NO observations thus allow for an extension of the available climatological record from solar maximum to solar minimum conditions.

Figure 7.5 shows the monthly averages of zonal mean NO *vmr* for daytime conditions retrieved from MIPAS data. The figure shows clearly the seasonal evolution along the year. It also shows the typical behaviour of the NO concentration following its two major sources. On the one hand, its production by solar X-rays, more important in the middle thermosphere (above about 130 km), which is reflected in a summer (larger NO) to winter (smaller NO) latitudinal gradient under solstices conditions. On the other hand, higher NO abundances are observed at the auroral regions (60°-80°) in the lower thermosphere (around 110-115 km) due to energetic

electron precipitation (the electron precipitations occur at auroral regions at geomagnetic latitudes: 65°-75° (*Newell et al.*, 1996)), particularly at winter hemisphere, where smaller photochemical losses occur compared to the summer hemisphere. This produces the typical latitudinal shape of NO at about 110-130 km, with a steady decrease with latitude from the summer pole towards the winter hemisphere and then an abrupt increase at about 50-60° in the winter hemisphere. Complementary to the photochemistry, the summer-winter asymmetry in the distribution of polar NO is suggested to be driven by a seasonal dependendence of auroral electron precipitation, stronger during winter than during summer (*Newell et al.*, 2001; *Barth et al.*, 2004).

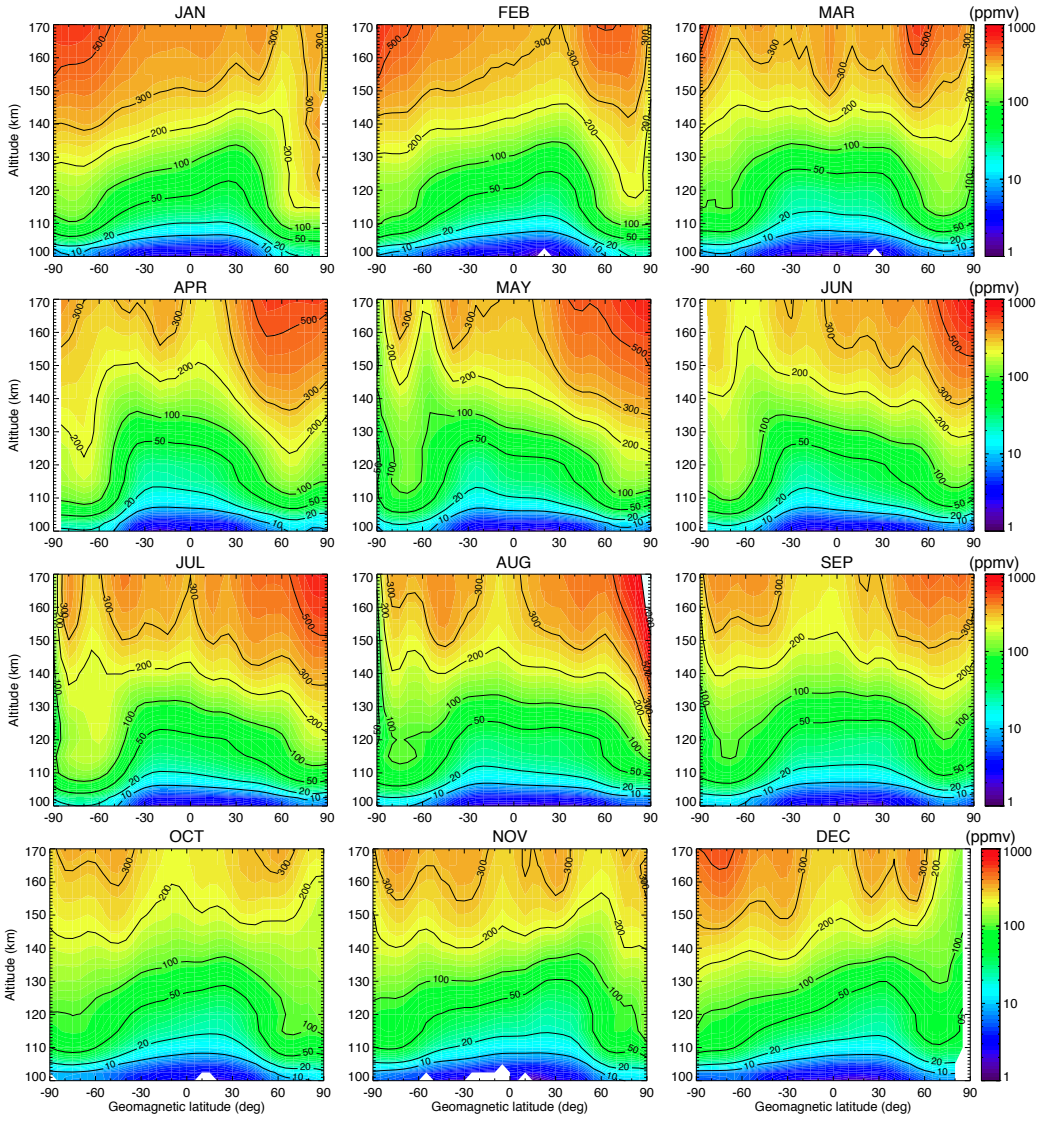


Figure 7.5: Monthly zonal mean daytime NO *vmr* measured by MIPAS during the 2008-2009 period.

As happens to the temperature, the winter-summer seasonal transition seems to take place rather early in the middle thermosphere, with an apparent shift towards the preceding equinox. Thus, as early as April a typical summer distribution of NO in the NH middle thermosphere is observed.

In order to compare MIPAS data to SNOE measurements and NOEM predictions of NO densities, the MIPAS NO *vmr* profiles have been converted into number density using the simultaneously retrieved kinetic temperatures. MIPAS seasonal averages of daytime NO density zonal mean distributions on geomagnetic latitudes are shown in Figure 7.6 (left). These figures very clearly show the features described above for the NO *vmr*. Maximum densities are found around 110 km during all seasons with pronounced peaks of 1-2.5$\times 10^8$ cm$^{-3}$ in the auroral regions caused by low energy electrons precipitating into the thermosphere. These peak values are slightly smaller than the average auroral densities observed by SNOE during 1998-2000, ranging from 1.7 to 3.8$\times 10^8$,cm$^{-3}$ depending on geomagnetic activity (*Barth et al.*, 2003). In the extra-polar regions, MIPAS observed maximum densities in the order of 2-5$\times 10^7$ cm$^{-3}$, considerably smaller than those observed by SNOE (8-13$\times 10^7$ cm$^{-3}$). In these regions, NO is predominantly generated by solar X-rays. Hence, the encountered difference is expected, given the solar cycle variations that have occurred since the SNOE operations. The decrease of NO towards higher altitudes is more pronounced in the winter hemisphere, related to the latitudinal dependence of solar inclination. The fact that this behavior is visible at altitudes above 150 km even over the auroral regions, clearly demonstrates that X-ray-related NO production is the dominating process in the middle thermosphere compared to particle precipitation. Typical NO concentrations around 170 km vary between 3-8$\times 10^6$ cm$^{-3}$.

Results of the NOEM empirical model (Figure 7.6, right), sampled on the MIPAS locations and times, represent an extrapolation of the SNOE climatology to the atmospheric conditions of the MIPAS observations, hence enabling a direct comparison of both data sets in the 100-150 km range. Further, since SNOE and MIPAS daytime observations have been taken at nearly the same local time, no bias related to diurnal variations is expected. The agreement of MIPAS and NOEM is very good, particularly with respect to the seasonal, latitudinal and vertical variabilities. NOEM densities tend to be slightly higher in the polar regions. There, differences between MIPAS and NOEM are in the order of 10-60 % (see Figure 7.7), being more pronounced above around 120 km than at the peak height itself (i.e., 115 km). In the extra-polar regions, differences do not exceed 20 % in the whole altitude range, and there is no indication for a systematic bias between both data sets.

In addition, MIPAS NO number density has been compared to the climatology composed by *Siskind et al.* (1998) based on HALOE and SME data

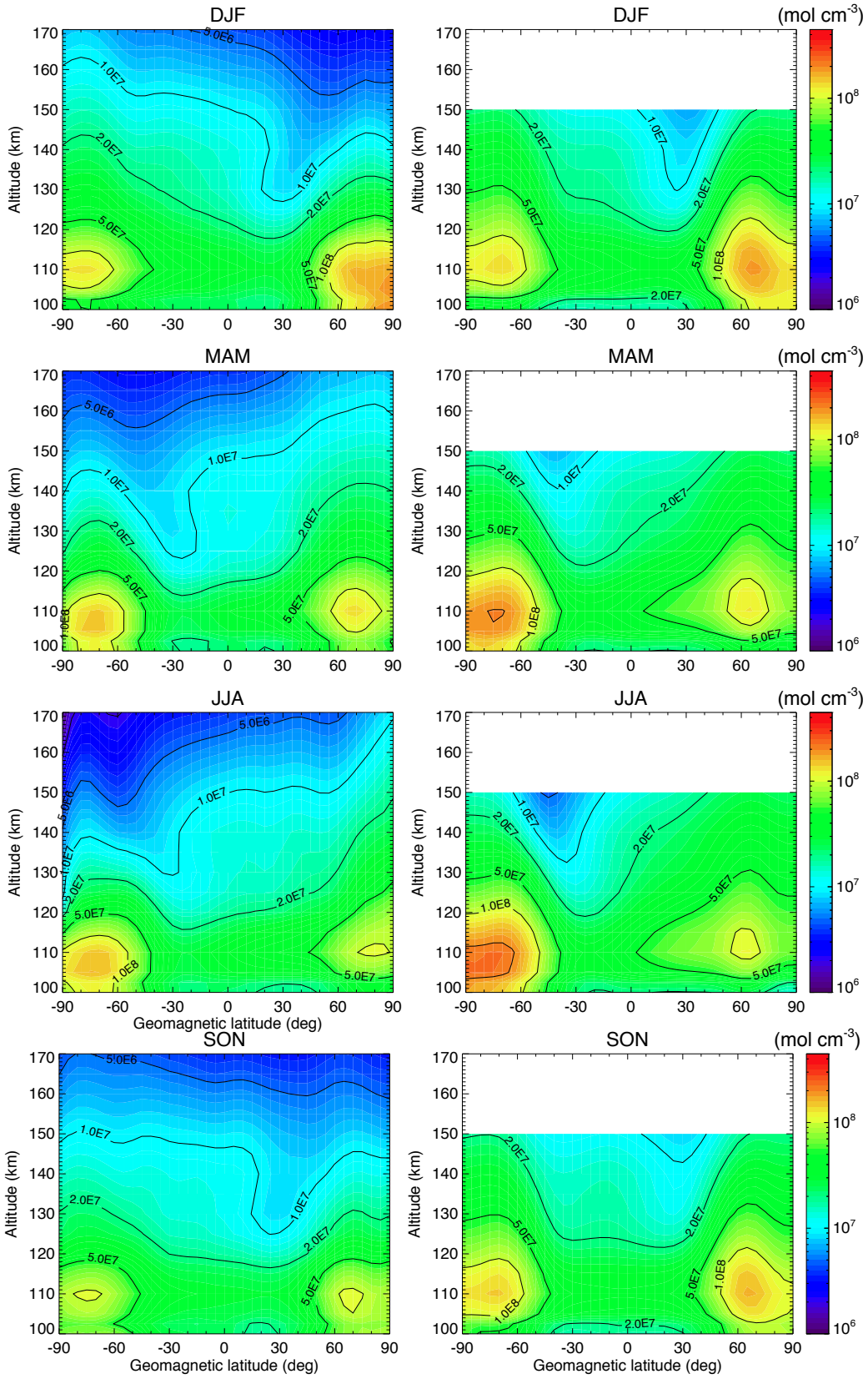


Figure 7.6: Zonal mean NO daytime number densities as measured by MIPAS (left panels) and NOEM model results (right panels). From top to bottom: DJF, MAM, JJA, SON.

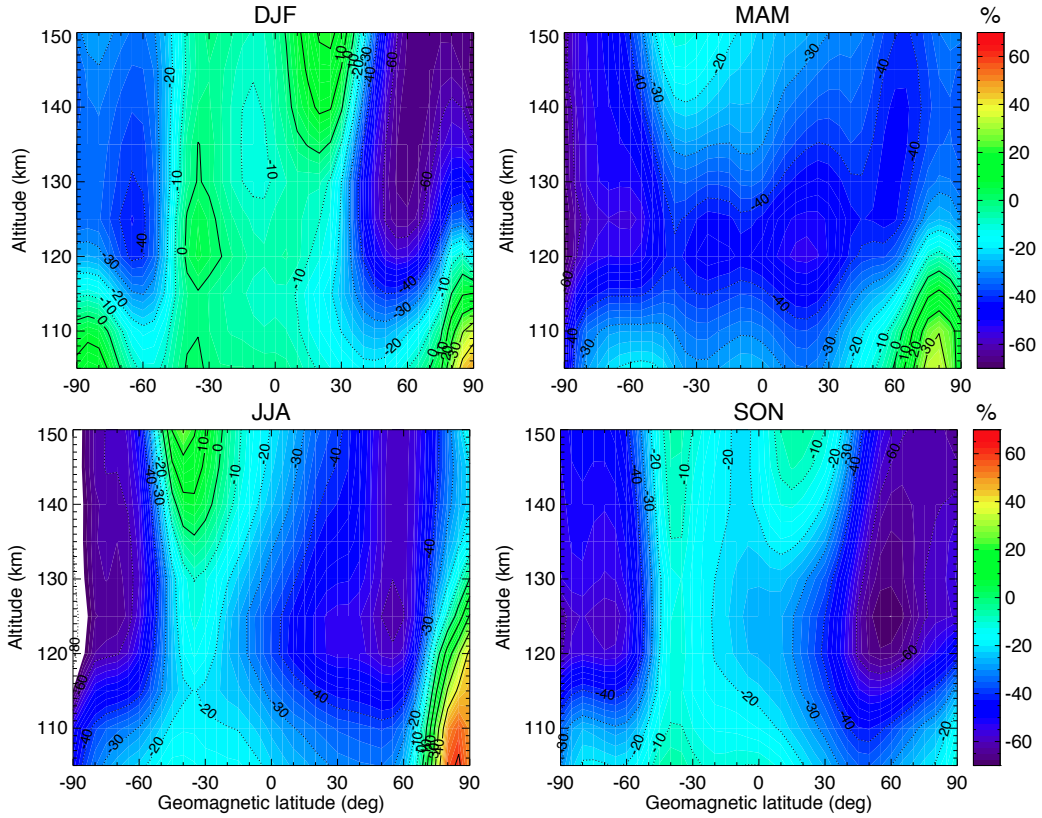


Figure 7.7: Zonal mean MIPAS-NOEM daytime NO number density relative differences. Top, left: DJF; top, right: MAM; bottom left: JJA; and bottom, right: SON.

which also were taken in declining phases of the solar cycle. Due to the restriction of MIPAS data to a period of low Sun activity, the comparison with SME+HALOE data is limited to this condition ($F_{10.7}$ index below 75). The comparison has been carried out for three periods: equinox (including MIPAS data for the months of March, April, May, September, October and November for 2008 and 2009) for low $A_p$ ($<$15), and for high $A_p$ ($>$15); and for the Northern hemisphere winter for low $A_p$ ($<$15). In all cases only MIPAS daytime data were taken into account.

For equinox conditions and high $A_p$, the distribution of MIPAS NO number density is very similar to that of HALOE+SME, except that the "valley" at tropical latitudes is less pronounced in MIPAS observations (see Figure 7.8). Taking the ratio of the two distributions at common latitudes and altitudes, MIPAS observations are generally larger, by factors of 1 to about 2.5. The differences are more pronounced between 50°S and 50°N above around 130 km, where the ratio brackets from 1.4 and 2.5, and at auroral latitudes in the 110–120 km region where the ratio is between 1 and 1.5. There are little differences between high and low $A_p$ conditions. The maximum of the NO density seems to be a few ($\sim$2) kilometers higher in MIPAS data.

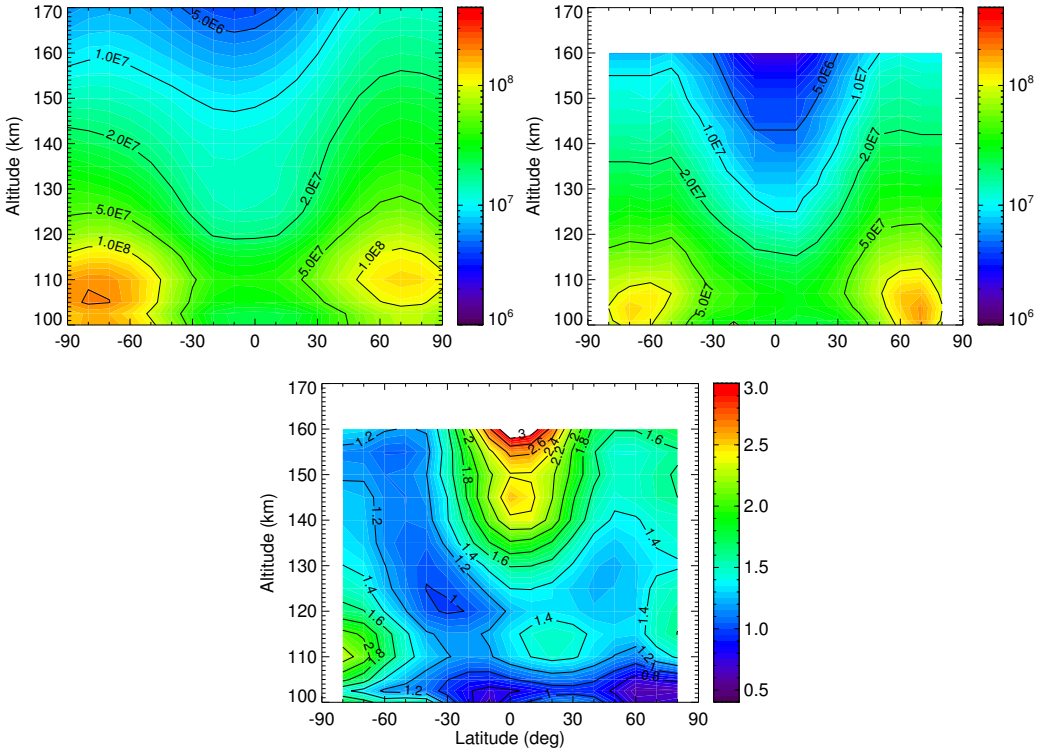


Figure 7.8: Comparison of NO number density (molecules/cm$^3$) for daytime, equinox, low solar activity and high $A_p$ from MIPAS observations (top) with the HALOE and SME climatology *Siskind et al.* (1998) (middle). The bottom panel shows the ratio of MIPAS to HALOE/SME climatology.

For winter conditions in the Northern hemisphere (not shown), the NO density distribution in both data sets show similar features as for equinox. MIPAS NO density is also larger with similar ratios to those for equinox.

Note that the climatology of *Siskind et al.* (1998) was composed from HALOE data that measured in occultation (i.e. sunrise and sunset), and from SME data, that were taken in the late afternoon. In this comparison it is included only daytime data for MIPAS, taken at 10 am (local time). HALOE measurements were taken only up to 125 km. Above that altitude only SME data were included but a large fraction of SME data were limited to 140 km and the values above until 160 km were extrapolated assuming diffusive equilibrium (*Siskind et al.*, 1998). Hence, the large discrepancies between MIPAS and HALOE/SME, obtained above around 130 km (see Figure 7.8), might be due to that assumption.

The second largest difference between MIPAS and HALOE+SME is found in the polar regions in the 100-120 km altitude range. The HALOE mixing ratios were limited to 70°S to 70°N and therefore the HALOE+SME climatology in the polar regions is composed of SME data only. HALOE data are higher by about 20-60% than SME at auroral latitudes (50-70°) in this altitude

region (*Siskind et al.*, 1998). Hence the MIPAS-HALOE/SME differences are in agreement with the previous HALOE-SME differences.

At auroral latitudes (80°S-50°S, 50°N-80°N), comparison of MIPAS with HALOE and SME NO for similar conditions as in *Siskind et al.* (1998) reveals that MIPAS is larger by a factor of 1.4 than HALOE at the peak. This factor reduces to 1.25 if both daytime and night-time MIPAS data are included. The altitude of the peak in MIPAS is located at 110 km, a few kilometers higher than in HALOE. Since HALOE measured larger values than SME (*Siskind et al.*, 1998), MIPAS NO density is also significantly larger than SME.

The MIPAS measurements of thermospheric NO represent the first observational data set for both day and night conditions. This allows to extract unique information about NO diurnal variations and provide important observational constraints onto the involved photochemistry. Figure 7.9 shows the observed seasonal day-night differences of thermospheric NO, corresponding to the observations taken at 10 am and 10 pm local times. NO concentrations are up to 140 % higher at daytime in the middle thermosphere above approximately 120-130 km, most pronounced at tropical and mid-latitudes regions. An opposite behavior is observed in the lower thermosphere, particularly in the polar regions. There, daytime NO concentrations are about 10-50 % smaller than during night.

The diurnal cycle of thermospheric NO is mainly controlled by the competition of production via the highly temperature-dependent reaction pathway $N(^4S)+O_2$ (Reaction 1.2) and losses by photolysis and the cannibalistic reaction $NO+N(^4S)$ (Reaction 1.4). Both production and losses are much faster during daytime. During night, chemistry is rather slow, and vertical redistribution gets more important. Increasing daytime NO enhancements with altitude in the extra-polar regions are related to increasing temperatures, favoring NO buildup via R2, hence resulting in a net NO production. In the lower thermosphere, where temperatures are lower, $N(^4S)$-related NO production (R2) is less efficient and losses start to dominate. Higher nighttime concentrations are often found in the lower thermosphere around 110-120 km, most pronounced in the auroral regions, i.e., where NO production is highest. Cannibalistic destruction of NO with N (R4), being more pronounced at daytime, is also stronger in the auroral regions due to the increased availability of odd nitrogen. The smaller diurnal amplitude in the extra-polar lower thermosphere indicates that there the odd nitrogen partitioning is closer to equilibrium. The observed behavior of diurnal variations in the extra-polar and auroral lower thermosphere are in good agreement with model simulations (*Bailey et al.*, 2002).

As discussed in Section 6.6.1, the observed diurnal amplitude in the tropical and mid-latitudes middle thermosphere might be underestimated due to smoothing errors related to the use of NOEM daytime NO as a priori

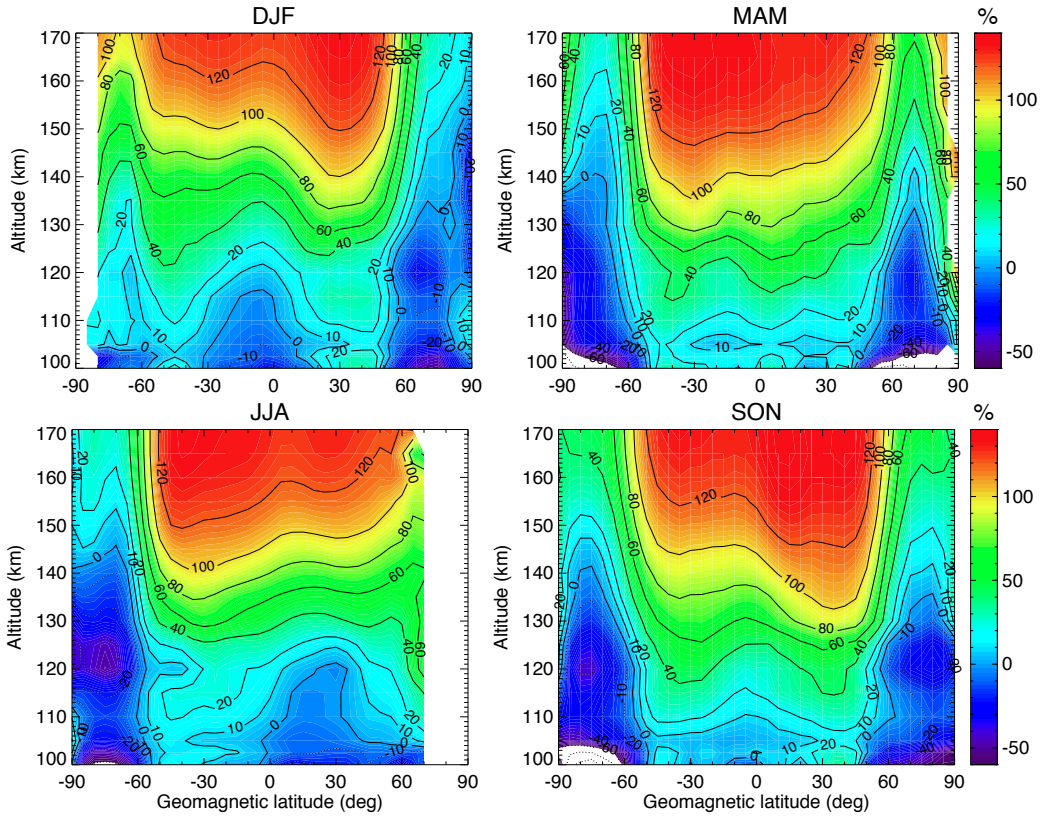


Figure 7.9: Zonal mean MIPAS day-night NO number density differences (referred to the mean day+night). Top left: DJF; top right: MAM; bottom, left: JJA, bottom right: SON.

information for nighttime conditions. However, this does not disable a future quantitative analysis of the observed diurnal variations by means of model-data comparisons if MIPAS averaging kernels are considered. Though beyond the scope of this study, such comparisons on an extended time period (i.e., covering seasonal variability) will provide an opportunity to test thermospheric odd nitrogen photochemistry in detail. The outcome of such study will also be very useful to improve the a priori knowledge of nighttime NO to be included in future versions of the data.

## 7.4. Inter-annual variability

The period 2005-2009, for which MIPAS *UA* measurements in the thermosphere have been analyzed, corresponds to the descending phase of the solar cycle 23, as reflected by the temporal evolution of the $F_{10.7}$ index (see Fig. 7.10, left panel). The monitoring of EUV solar flux by the CELIAS/SEM spectrometer on board spacecraft SOHO establish that the

minimum of the solar cycles 23/24 was reached in November 2008 and lasted until end of 2009 (*Didkovsky et al.*, 2010). It further shows that the solar flux in this spectral band is reduced up to a 15 % with respect to the previous minimum in 1996. Since EUV solar photons are the main heat source of the thermosphere (*Roble*, 1995), during a solar minimum it is expected a colder and a less dense thermosphere (contracted atmosphere), and the opposite occurs during solar maximum. The analysis of atmospheric drag on satellite orbits indicates that the thermospheric density at ∼400 km reached the lowest values during the 2007-2009 period since the beginning of the space age (*Emmert et al.*, 2010). Simulations made with the NCAR TIME-GCM supports the descent in EUV solar flux as the main cause of the observed decrease in density (*Solomon et al.*, 2010). In addition to the low solar activity, the period 2007-2009 is characterized by a very low geomagnetic activity, as shown by the temporal evolution of the $A_p$ index (see Figure 7.10, right panel). MIPAS *UA* measurements analyzed in this work can provide unique information on the effects of this quiescent period over temperature and nitric oxide in the low and mid-thermosphere.

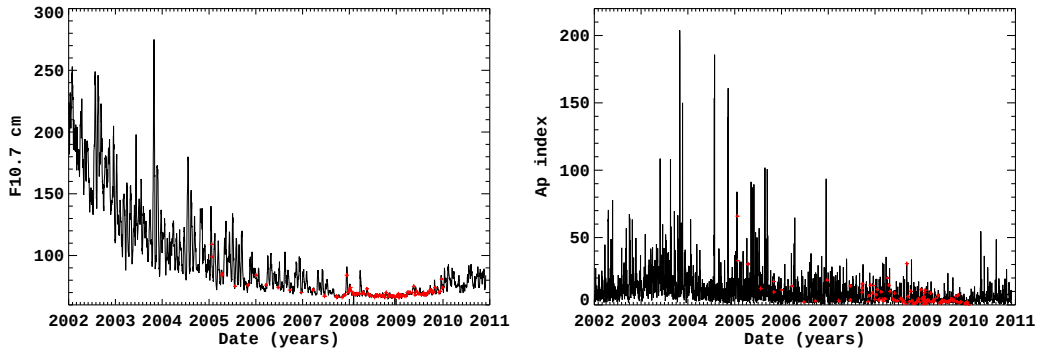


Figure 7.10: 10.7 cm radio flux in *SFU* (left) and geomagnetic index $A_p$ (right) temporal evolution from 2002 to 2011. MIPAS *UA* days are marked with red crosses.

Although the available MIPAS data between November 2007 and 2009 allows to construct a monthly climatology for a solar minimum conditions, the available MIPAS data between 2005 and 2007 are not sufficient to construct such a climatology, since there are only 1 to 3 days per season available. These days, however, are very useful to address particular case studies, e.g. the solar storm in January 2005 (see Chapter 8), or to study correlations of thermospheric NO and $T_k$ with solar and geomagnetic activities (see next Section). Thus, to study the temporal evolution of thermospheric NO and $T_k$ along the descending phase of the solar cycle 23, MIPAS days available earlier than November 2007 have been seasonally averaged.

Figure 7.11 shows the temporal evolution of MIPAS daytime NO and $T_k$

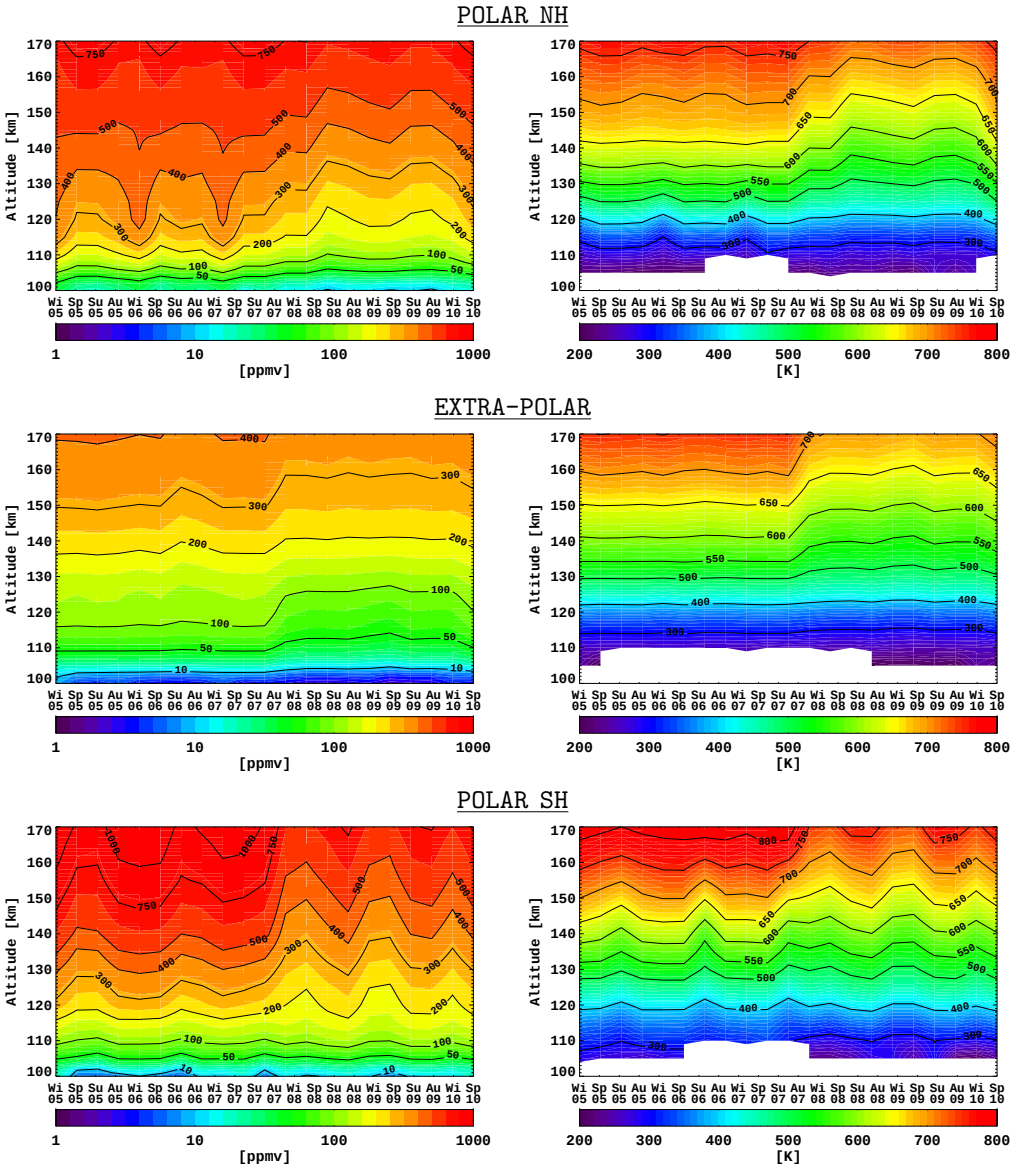


Figure 7.11: Time series from 2005 to 2009 for MIPAS daytime NO *vmr* (left panels) and $T_k$ (right panels) for NH polar latitudes (45°N-90°N), top panels; extra-polar (45°S-45°N) latitudes, mid panels; and SH polar latitudes (90°S-45°S), bottom panels. The seasons in the x-axis correspond to the NH.

from 2005 to 2009 inclusive for polar ($|\text{latitude}| > 45°$) and extra-polar ($|\text{latitude}| < 45°$) regions. From NH winter 2005 until spring 2007, the temporal evolution of NO *vmr* and $T_k$ is relatively flat for all latitude bands, with the exception of the captured seasonal NO variability in the polar region of both hemispheres (see Figure 7.5) and the highest temperatures typical of summer poles but observed in the preceding equinox (see Figure 7.3). Then, on NH summer 2007 a steep descent in NO *vmr* is observed. Above 130 km, a descent of up to 40 % is observed in the SH polar

region, being more moderate, between 10 and 20 %, in the extra-polar and NH polar regions. Below 130 km, the largest decrease is observed in the extra-polar and SH polar regions (up to 40 %), while it is below 20 % for NH polar region.

For temperature, the decrease is also observed at all latitudes and altitudes, being more pronounced above 130 km (up to 70 K). The maxima of NO *vmr* and $T_k$ at polar regions during winter and summer, respectively, are also present and reach smaller values than before summer 2007. Taking the summer 2007 as a reference, average differences for NO *vmr* and $T_k$ before and after that date have been calculated at several altitudes in order to estimate the observed descent (see Table 7.2). Furthermore, on winter 2010 (December 2009), it is observed a general increase in NO and $T_k$ at all latitudes, more pronounced above 120 km, probably caused by the onset of the ascending phase of the solar cycle 24. In the next section, the causes for such variability are analyzed in detail.

Table 7.2: Average change in NO *vmr* and in $T_k$ observed by MIPAS: after summer 2007 minus before summer 2007 at several altitudes.

| | Polar NH | | Extra-Polar | | Polar SH | |
|---|---|---|---|---|---|---|
| Altitude (km) | ΔNO (%) | $\Delta T_k$ (K) | ΔNO (%) | $\Delta T_k$ (K) | ΔNO (%) | $\Delta T_k$ (K) |
| 170 | -10 | -31 | -15 | -51 | -39 | -68 |
| 150 | -14 | -52 | -13 | -43 | -37 | -38 |
| 130 | -31 | -48 | -18 | -25 | -29 | -15 |
| 110 | -40 | -2 | -34 | -5 | 8 | -26 |

## 7.5. Correlations with solar and geomagnetic activities

It is well known that the geomagnetic activity (particle precipitation) has its major influence on the production of NO at auroral regions, and also contributes to increase temperature in those latitudes by particle and Joule heating. The solar activity (soft X-rays and EUV flux), however, influences the production of NO and the heating of the thermosphere globally, i.e., at all illuminated latitudes.

The typical indicators of the solar and geomagnetic activities are the $F_{10.7}$ and $A_p$ indices. Their values for the MIPAS days of measurements have been smoothed with a 30-days and 3-days running means, respectively. The top panels of Figure 7.12 show the distributions of the 89 days of MIPAS *UA* measurements with those indices. The days corresponding to the Solar Storm in January 2005, 21$^{st}$ and 22$^{nd}$, were excluded in this study since they are an extreme case and $A_p$ was very variable during MIPAS

measurements in those days. Also, days 14th to 18th and 21nd to 27th in January 2009, corresponding to the Delta-2 Campaign, were removed since they only provide 3 orbits of measurements. The figure clearly shows that most of MIPAS measurements were taken at low values of $F_{10.7}$ and $A_p$, i.e., during the declining phase of solar cycle 23; 95% of the days have values of $F_{10.7}$ and $A_p$ indices below 80 and 15, respectively. The bottom panel of Figure 7.12 shows the relation between $F_{10.7}$ and $A_p$ indices. Here it is clearly observed the large number of days with both low geomagnetic ($A_p < 15$) and low solar ($F_{10.7} < 80$) activities, and that days with relatively high solar activity ($F_{10.7} < 80$) have also moderate to high ($A_p < 10$) geomagnetic activity.

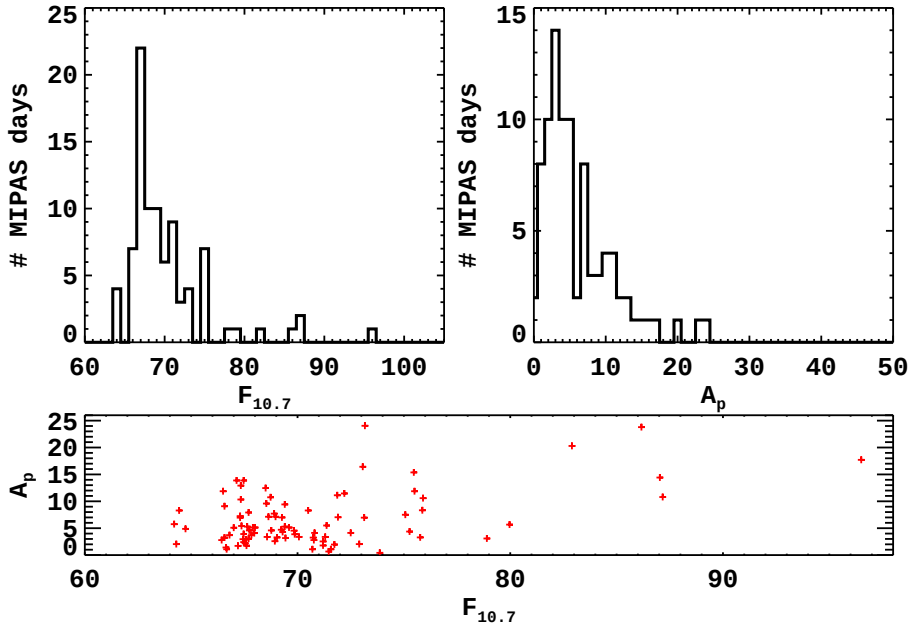


Figure 7.12: Distribution of MIPAS *UA* days with respect to the $F_{10.7}$ (top, left) and the $A_p$ (top, right) indices. Bottom panel shows the correlation between $F_{10.7}$ and $A_p$ for the MIPAS days of measurements.

Figure 7.13 shows the dependences of MIPAS thermospheric temperature and NO with the solar and geomagnetic activities (the $F_{10.7}$ and $A_p$ indices). Anomaly values, e.g. the difference (absolute for $T_k$ and relative for NO) with respect to the mean values, have been plotted. In order to differentiate the auroral and equatorial sources of heating and NO production, two latitudinal regions have been chosen: equatorial ($|\text{latitude}| < 25°$) in the case of the $F_{10.7}$ index, and the polar (or auroral) (50°-80°, geomagnetic latitudes) in the case of $A_p$. The positive correlation of NO and $T_k$ with $F_{10.7}$ at the equatorial region is clear (top panels), being more pronounced for NO below 120 km and for $T_k$ above 150 km. *Barth et al.* (2003) found a linear correlation, with a

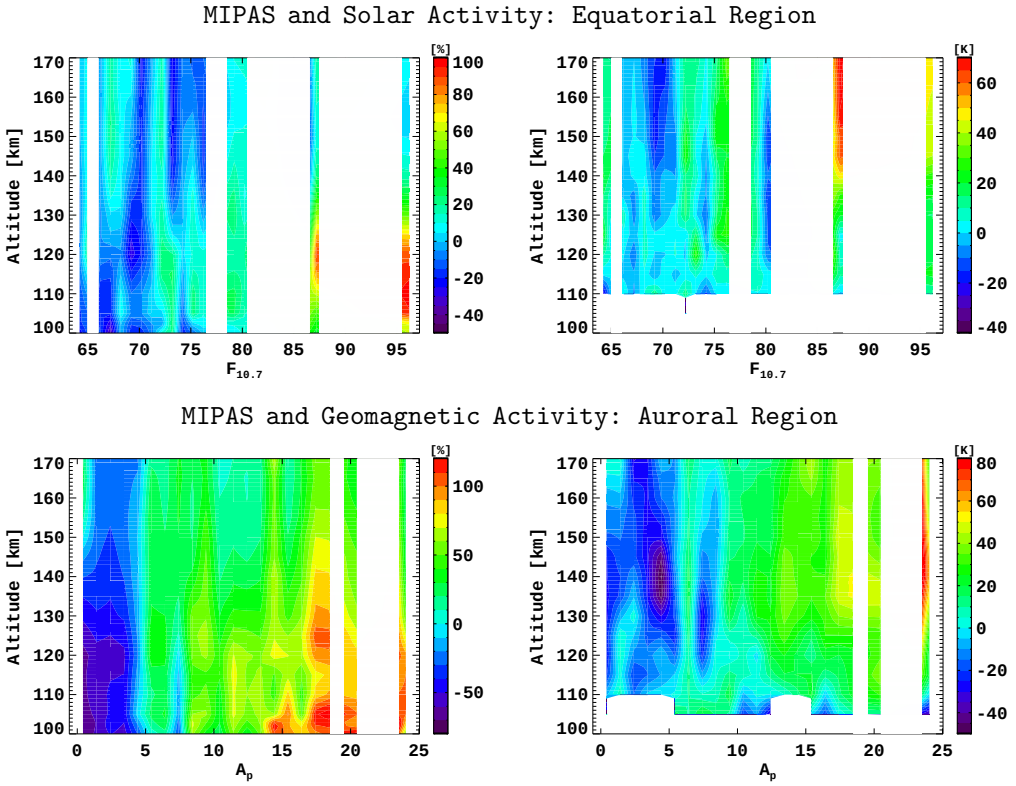


Figure 7.13: MIPAS daytime NO *vmr* (left panels) and $T_k$ (right panels) anomalies as a function of $F_{10.7}$ at equatorial ($|\text{latitude}| < 25°$) (top panels) and as function of $A_p$ at auroral (50°-80°) latitudes (bottom panels).

correlation coefficient larger than 0.75, between NO measured by SNOE and solar X-rays at 100-120 km, where their effect on the NO production is most efficient. MIPAS NO shows also a similar correlation, peaking at 110 km with a correlation coefficient of 0.71 (see Figure 7.14, top left panel). For temperature, the correlation coefficient is not as good as for NO, reaching values of 0.55-0.67 above 150 km (see Figure 7.14, top right panel).

The correlation of NO and $T_k$ with $A_p$ index in the auroral region can be also appreciated for the whole altitude range, more pronounced below 120 km for NO. The correlation coefficient calculated for auroral NO is larger than 0.85 below 130 km, reaching maximum value of 0.90 at 105 and 110 km (see Figure 7.14, bottom left panel). For temperature, the correlation coefficient is over 0.7 between 130 and 160 km, peaking at 140 km with a value of 0.75 (see Figure 7.14, bottom right panel).

As expected, no significant correlations of NO and $T_k$ with $A_p$ index were found at equatorial region (not shown here), and the moderate correlation with $F_{10.7}$ at auroral regions (not shown here) is completely masked by the auroral activity. In order to separate both contributions (solar and geomagnetic) on the retrieved NO and $T_k$, MIPAS data have been av-

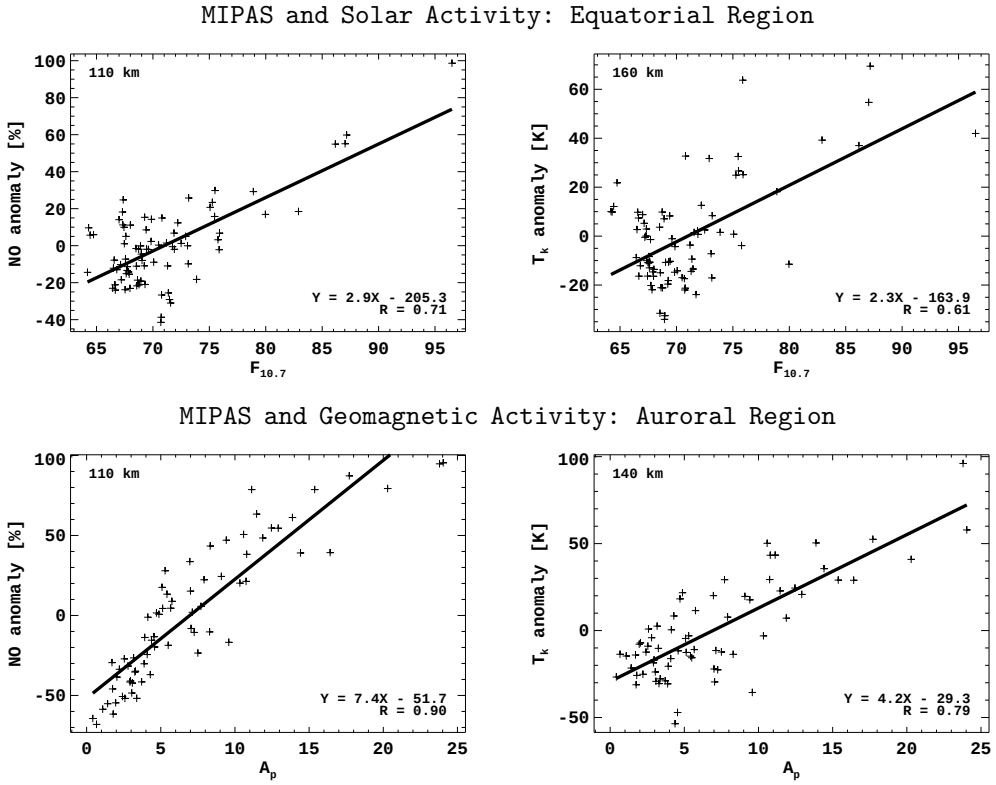


Figure 7.14: NO (left panels) and $T_k$ (right panels) anomalies against $F_{10.7}$ at equatorial regions (top) and against $A_p$ at auroral regions (bottom) at fixed altitudes.

eraged by considering different combinations of the $F_{10.7}$ and $A_p$ indices (see next Sections).

### 7.5.1. Variability with the solar activity

The scenarios of different solar activity (see Table 7.3) have been defined by minimizing the geomagnetic contribution. To achieve it, and considering the poor statistics of MIPAS days with high solar activity and the positive correlation of high $F_{10.7}$ and $A_p$ indices (see Figure 7.12), days with $A_p$ values lower than 15 have been taken. The threshold of $F_{10.7}$ that indicates "low" or "high" solar activity has been set to 75. This is high enough to give significant differences in thermospheric NO and $T_k$ between "high" and "low" solar activities, and it is low enough to provide at least 3 days for every season. The drawback is that the average $A_p$ values for each data subsets are not similar and this can yield possible geomagnetic contributions in the auroral regions.

Figure 7.15 shows zonal means of MIPAS NO number density and $T_k$ for "low" and "high" solar activity and the "high"-"low" differences for equinox conditions, i.e., both hemispheres are equally illuminated. The

Table 7.3: Scenarios of various auroral/solar activity. Numbers in parenthesis represent averaged values of $F_{10.7}$ and $A_p$.

| | | $F_{10.7}$ | $A_p$ | # days |
|---|---|---|---|---|
| | Solar | | | |
| 1 | Low $F_{10.7}$ | $<75$ (69.1) | $<15$ (5.5) | 39 |
| 2 | High $F_{10.7}$ | $>75$ (79.7) | $<15$ (9.8) | 4 |
| | Auroral | | | |
| 3 | Low $A_p$ | $<100$ (69.5) | $<6$ (3.2) | 27 |
| 4 | Moderate $A_p$ | $<100$ (70.5) | 6-12 (9.0) | 11 |
| 5 | High $A_p$ | $<100$ (73.5) | $>12$ (16.5) | 8 |

Table 7.4: Scenarios used in the study of variability in the Equatorial region.

| Scenarios | # days | # scans | $\overline{A_p}$ | $\overline{F_{10.7}}$ |
|---|---|---|---|---|
| $F_{10.7}$ < 75, $A_p$ < 15 | 39 | 5103 | 5.5 | 69.1 |
| $F_{10.7}$ > 75, $A_p$ < 15 | 4 | 313 | 9.8 | 79.7 |
| $F_{10.7}$ < 75, $A_p$ > 15 | 2 | 266 | 20.2 | 73.1 |
| $F_{10.7}$ > 75, $A_p$ > 15 | 1 | 63 | 23.8 | 86.2 |

results obtained for solstices are totally analogue and are not shown. Increases of NO and $T_k$ at high latitudes due to geomagnetic activity are clearly seen. At low latitudes, the variability of NO and $T_k$ is not as strong as in the $A_p$-driven auroral regions, and it is mainly due to solar activity. NO above 130 km at mid-latitudes and in the whole altitude range in the tropics show increases of up to 50%, while $T_k$ has more moderate increases, less than 50 K.

In order to show that the variability of NO and $T_k$ at low latitudes is mainly controlled by the solar activity rather than by the geomagnetic activity, we additionally distinguish the MIPAS data between high ($A_p$>15) and low ($A_p$<15) values for both solar activity conditions (see Table 7.4).

NO and $T_k$ profiles in the latitudinal range 25°S-25°N have been averaged and plotted in Figure 7.16. Despite the poor statistics, it can be seen that the influence of the solar activity on NO and $T_k$ at low latitudes is stronger than the influence of the geomagnetic activity. that is, the high-low solar activity (solid-dashed in the figure) differences are larger than the high-low geomagnetic activity ones (red-blue in the figure), particularly for the NO density peak, at 110 km, and above 140 km, and for temperature above 130 km.

*Siskind et al.* (1998) also showed for the NO climatology based on HALOE+SME data that the sensitivity of equatorial NO density to variations with solar cycle is larger than to variations with geomagnetic activity. Comparing the variability found here to that in the HALOE/SME

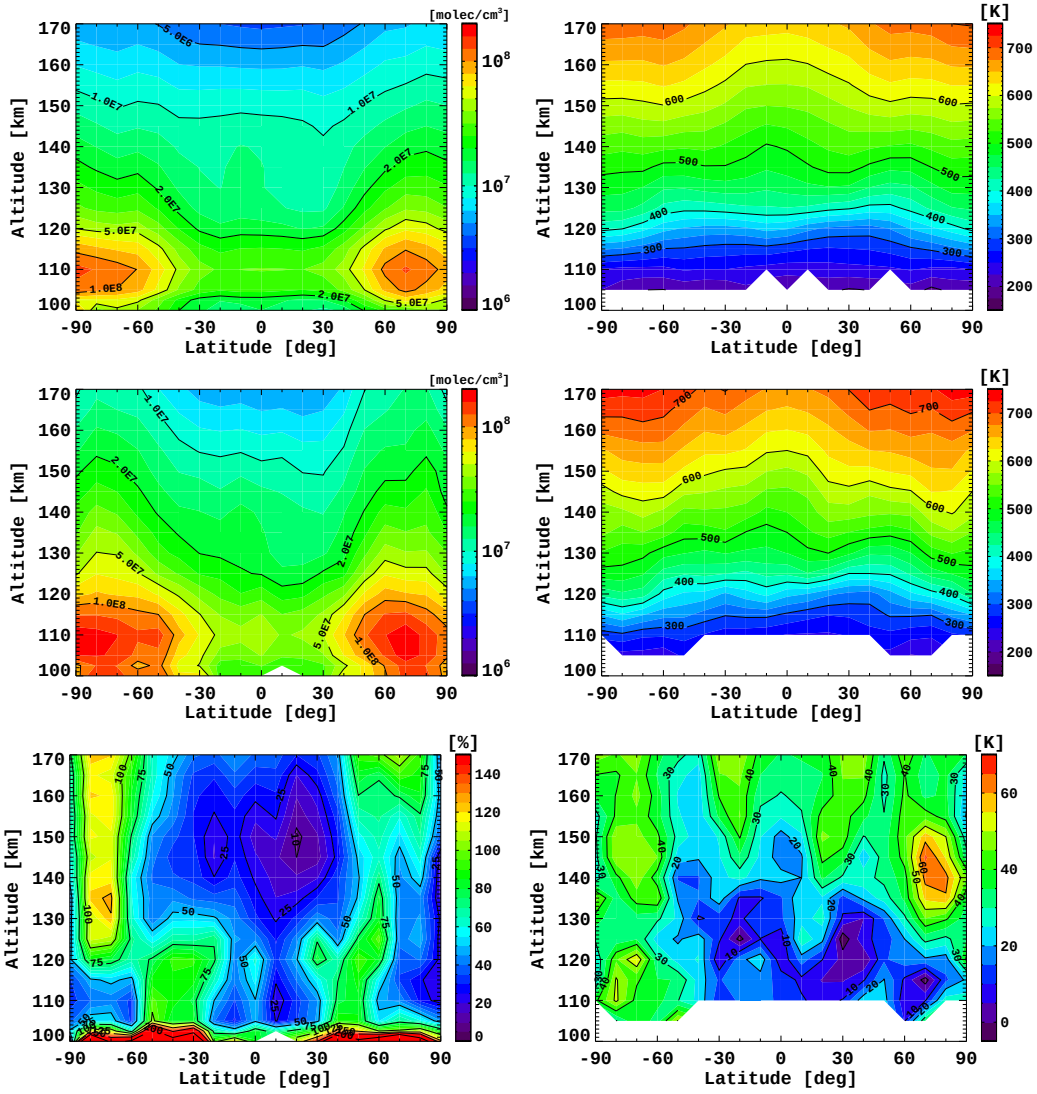


Figure 7.15: Zonal means of MIPAS thermospheric daytime NO number density (left) and $T_k$ (right) for "low" (top) and "high" (middle) solar activity. The bottom panels show the "high"-"low" difference.

climatology (see Figure 1 in *Siskind et al.* (1998)), it can be seen that the variability found with MIPAS data is closer to that found for HALOE measurements than for SME data.

### 7.5.2. Variability with the geomagnetic activity

To analyze the variability of NO and $T_k$ with the geomagnetic activity MIPAS days of measurements have been grouped into: low ($A_p < 6$), moderate ($6 < A_p < 12$), and high ($A_p > 12$) $A_p$ indices. Figure 7.17 show zonal means of NO density and temperature for those cases for equinox conditions, as well as the difference between high and low auroral activity. The

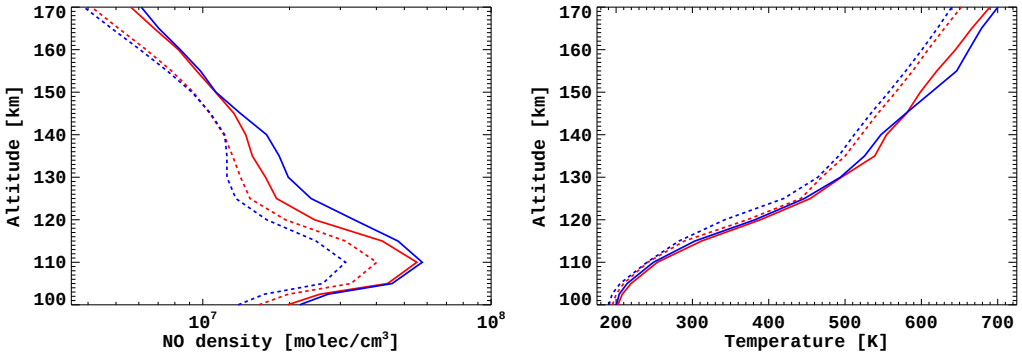


Figure 7.16: Mean single profiles of MIPAS daytime NO number density (left) and $T_k$ (right) at low latitudes (25°S, 25°N) for equinox conditions. Solid lines, $F_{10.7} > 75$; dashed lines, $F_{10.7} < 75$; red lines, $A_p > 15$; blue lines, $A_p < 15$.

dependence of auroral NO with the geomagnetic activity is clear, showing increases of up to 200% at the peak altitude, near 110 km, from low to high $A_p$'s. Temperature increases at auroral regions are also observed, increasing with altitude up to 75 K. These enhancements are larger for stronger auroral activity, as can be drawn when comparing the high-low $A_p$ differences with moderate-low $A_p$ ones (see Figure 7.17).

At low latitudes, NO and $T_k$ for high $A_p$ conditions have slight increases with respect to low $A_p$. This is thought to be caused by the larger solar activity, which is correlated with $A_p$ as shown in Fig. 7.12. This argument is further supported by the very small changes observed in the NO and $T_k$ at low latitudes for moderate and low $A_p$ values (bottom panels in Figure 7.17), both of which cases have very similar $F_{10.7}$ values. The same pattern of differences at auroral and low-latitude regions have been found for the solstices periods and hence are not shown.

In fact, the response of NO and $T_k$ to the intensity of the geomagnetic activity is quasi-linear. When averaging the NO density and $T_k$ profiles in the auroral region (50°N-80°N) (see Figure 7.18 for equinox conditions), the resulting NO density profiles for high and moderate $A_p$'s are around 2.0-2.5 and 1.6-1.75 times larger than the NO profile for low $A_p$, respectively. The mean temperature profiles for high and moderate $A_p$'s have a nearly constant difference with respect to that for low $A_p$ of 55-65 K and 30-38 K, respectively. Comparing the averaged profiles for the auroral regions (Figure 7.18) to those obtained for low latitudes (Figure 7.16), it can be seen that, whereas the overall change in temperature is small, less than 50 K (warmer in the auroral regions), the auroral NO is larger by up to a factor 2-4 at the peak's altitude (110 km).

The HALOE/SME climatology shows an auroral variation for NO of a factor of 2 between low ($A_p < 10$) and high ($A_p > 20$) geomagnetic activity scenarios (*Siskind et al.*, 1998). If the same scenarios are taken for

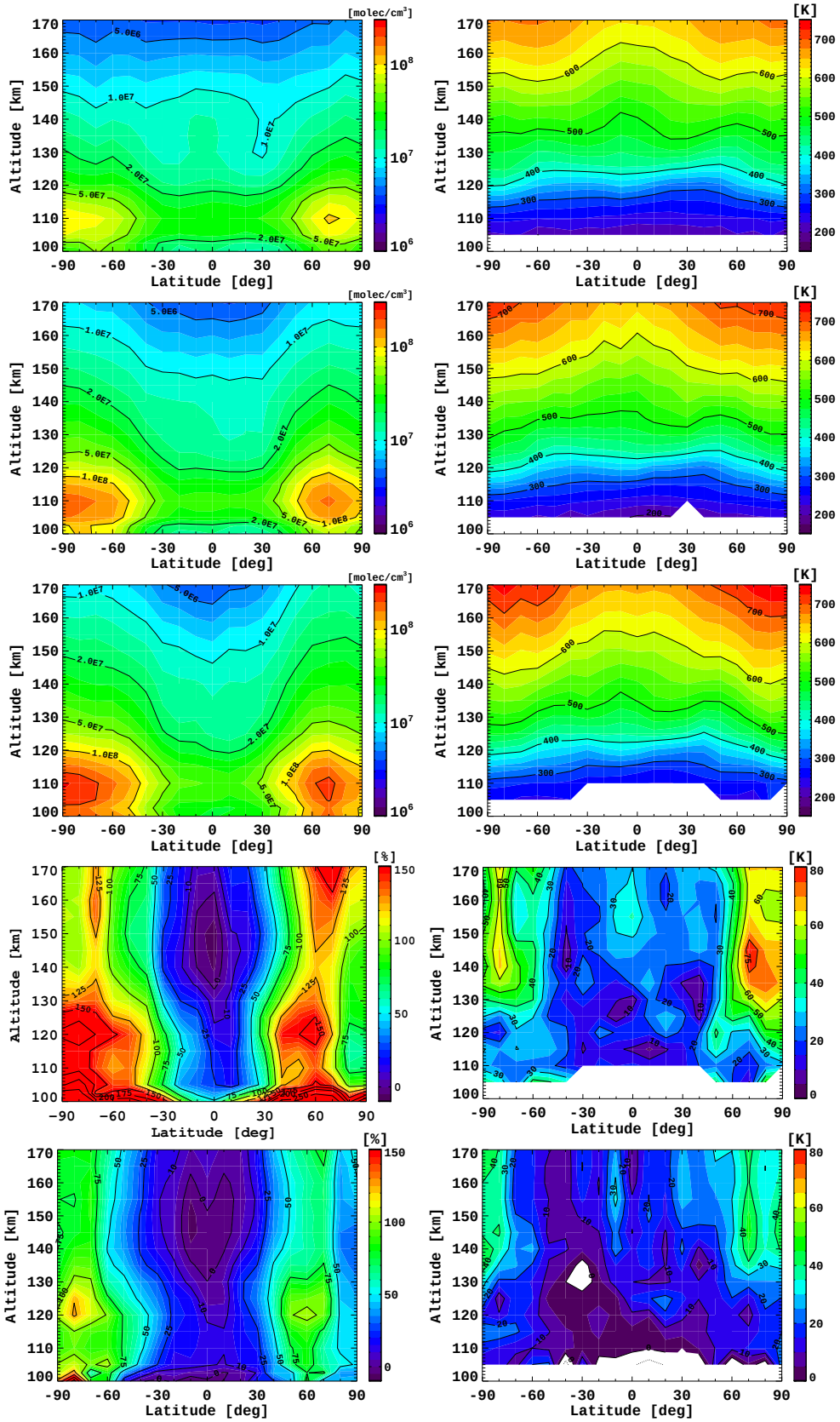


Figure 7.17: Zonal means of MIPAS daytime NO number density (left) and temperature (right) for low ($A_p < 6$, top), moderate ($6 < A_p < 12$, 2$^{nd}$ row), and high ($A_p > 12$, 3$^{rd}$ row) geomagnetic activity for equinox. The 4$^{th}$ and bottom panels show the high-low and moderate-low $A_p$ differences, respectively.

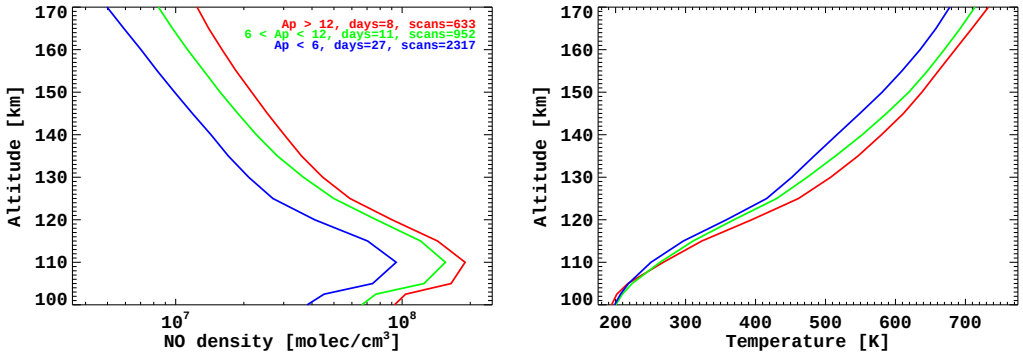


Figure 7.18: Mean single profiles of MIPAS daytime NO number density (left) and $T_k$ (right) at auroral region (50°N, 80°N) for equinox conditions and three different geomagnetic scenarios: $A_p < 6$ (blue), $6 < A_p < 12$ (green), $A_p > 12$ (red).

MIPAS NO, a variation of a factor of 2-2.5 is found, which is in good agreement with the HALOE/SME NO climatology, even though MIPAS NO is larger than HALOE/SME NO by around a factor of 1.4.

# Chapter 8

# Case Studies

*Abstract*

The MIPAS thermospheric NO and temperature climatology are used to analyze particular case studies: the major stratospheric warming occurred in January 2009 and the solar storm in January 2005. In addition, MIPAS thermospheric NO and $T_k$ are compared to simulations performed by the 3D model TIME-GCM for atmospheric quiet conditions.

## 8.1. Dynamical coupling during a major stratospheric warming

### 8.1.1. Introduction

The stratospheric sudden warmings (SSW) are dramatic disturbances which occur in the polar winter atmosphere in a wide altitude range. The interaction of upward propagating planetary waves from the troposphere with the mean flow is the responsible mechanism for this event. It decelerates (or reverses) the eastward winter stratospheric jet, yielding an acceleration of the downward meridional circulation which produces an adiabatic heating in the stratosphere. The SSW induces a deceleration of the downward mesospheric descent producing a cooling in this region (*Matsuno*, 1971). Besides, simulations with the 3D model TIME-GCM (*Liu and Roble*, 2002) predicts the existence of a lower thermospheric warming caused by a secondary downward flow induced by an equator-ward mesospheric circulation, which is driven by the eastward forcing due to gravity wave breaking.

Measurements of temperature by SABER instrument (*Siskind et al.*, 2005) have confirmed the mesospheric cooling associated to SSWs, and also have found possible positive correlations of temperatures at $10^{-3}$-$10^{-4}$ hPa (90-110 km) with temperatures at 10 hPa (30 km) during SSWs, in line with the TIME-GCM simulations. However, information from measure-

ments is scarce above 110 km. Measurements from incoherent scatter radar (*Goncharenko and Zhang*, 2008) showed alternating cooling regions between 150 and 300 km, and a warming band at 120-140 km during minor SSWs in January 2008.

In January 2009 occurred the strongest and most prolonged SSW so far recorded. The temperature at 10 hPa at the North Pole increased by 70 K within a week. Temperature profiles from 40 to 170 km derived from MIPAS *UA* measurements taken during January 2009 (see Table 8.1) are used to analyzed this SSW.

Table 8.1: Measurements taken by MIPAS in the *UA* mode during January 2009.

| | Days | Orbits/day | Spatial coverage |
|---|---|---|---|
| Routine *UA* | 2, 12, 19, 20 Jan<br>6 Feb | 14 | global |
| Non-routine *UA*† | 14-18, 21-27 Jan | 3 | 20°W-70°E, 160°E-110°W |

†MIPAS measurement taken as support for the Dynamics and Energetics of the Lower Thermosphere in Aurora 2 (DELTA-2) campaign.

### 8.1.2. Analysis of MIPAS measurements

In the analysis of MIPAS temperatures during the SSW of January 2009, two important issues have been taken into account. First, since the altitude range of the *UA* observations is 40-170 km, complementary data below 40 km have been considered from the *a priori* information used in the temperature retrievals, i.e., ECMWF temperature. Second, the short-term response of thermospheric temperature to geomagnetic activity (chemical and Joule heating and radiative cooling by NO 5.3 $\mu$m emission) must be taken into account. MIPAS temperatures within 70-90°N at 120 and 140 km show similar temporal behavior as geomagnetic activity represented by the daily $A_p$ index (see Figure 8.1 black and red lines, respectively). This dependence of temperature on geomagnetic activity is also observed in the temperature from the climatological model MSIS (blue dotted lines in the figure), which includes geomagnetic response but no dynamical forcing due to SSW. Hence, the response to the geomagnetic activity is subtracted by means of a linear $A_p$ term obtained by a regression fit.

With these two considerations, the temporal evolution of the temperature anomaly has been constructed from 20 to 170 km in the 70-90°N region (Figure 8.2). The SSW produces a maximum temperature increase of 50 K around 22 January. At the same time, temperatures in the upper mesosphere (80-90 km) decrease by the same amount, in agreement with previous observations and simulations. At the beginning of February, a strong reestablished polar vortex produces an increase in mesospheric tempera-

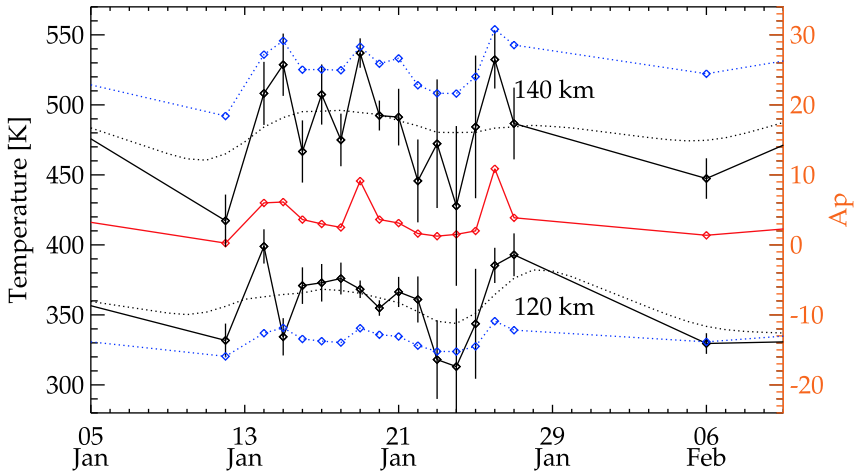


Figure 8.1: Temporal evolution of average kinetic temperatures within 70--90°N at 120 and 140 km from 5 January 2009 to 10 February 2009 (black solid: MIPAS observations, blue dotted: NRLMSISE00 at MIPAS locations, black dotted: smoothed MIPAS observations corrected for geomagnetic variability). The daily $A_p$ index is shown (red solid line). Error bars represent precision of the MIPAS temperature averages. Days with available MIPAS data are indicated by symbols.

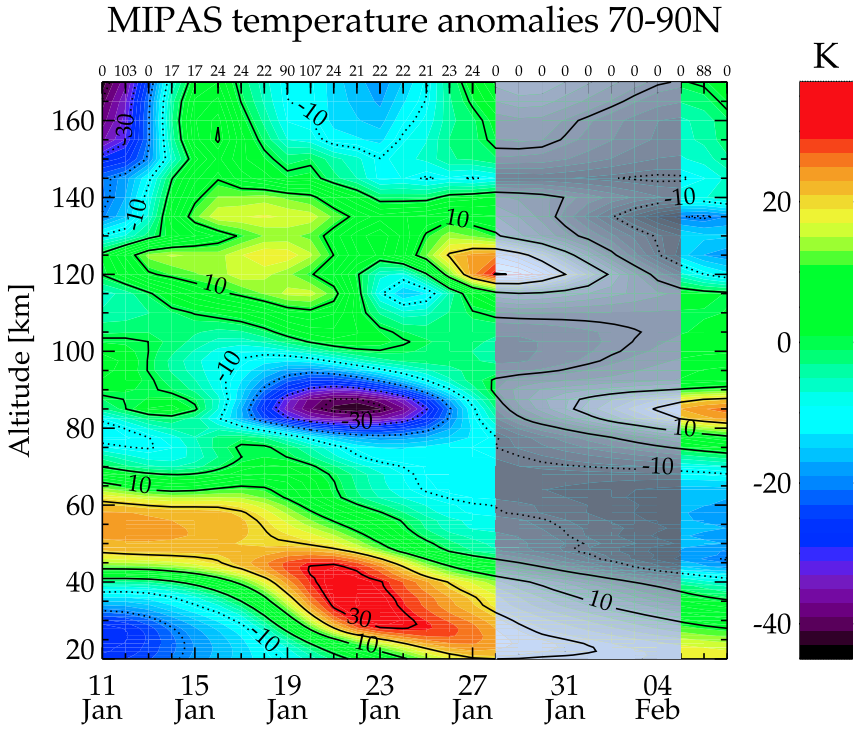


Figure 8.2: Temporal evolution of zonally averaged MIPAS temperature anomalies (with respect to the temporal average) within 70-90°N. During the MIPAS data gap between 28 January and 5 February (grey-shaded) temperature anomalies are interpolated. Numbers at the top x-axis reflect the number of averaged observations.

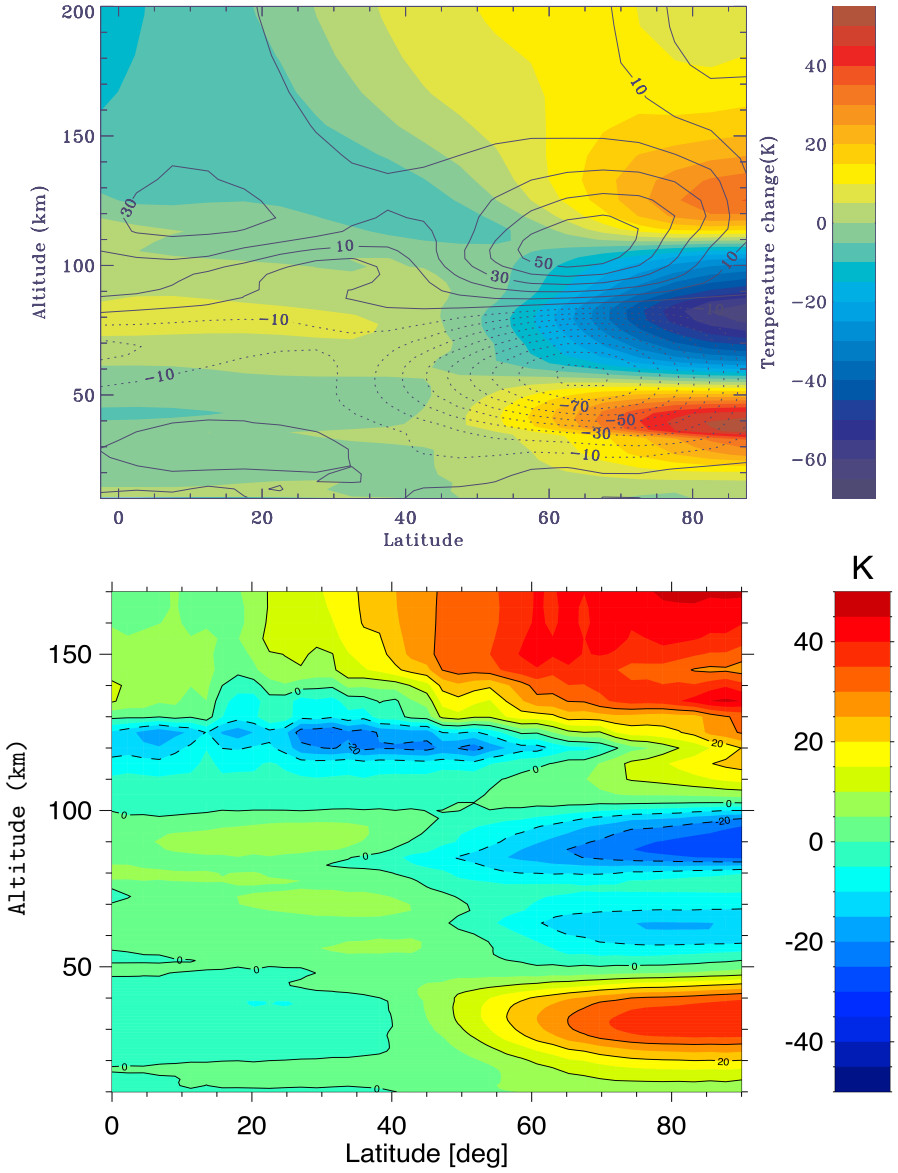


Figure 8.3: Zonal mean temperature anomalies simulated by TIME-GCM during a SSW (top) (after *Liu and Roble* (2002)), and measured by MIPAS during the Jan 2009 major strat-warm (bottom).

ture, giving raise to a very high stratopause (∼80 km).

Above 100 km, a 15-20 K increase with a double-peak structure was found at 120-130 km, with maximum values around 18 K (prior to the SSW pulse) and 26 K (after the SSW pulse) January. These observed thermospheric temperature variations are in good agreement with the TIME-GCM simulations (*Liu and Roble*, 2002), suggesting that they are linked to the SSW. Another observational evidence of vertical coupling is given by the ion temperatures measured by the EISCAT UHF radar in this period, which show an anti-correlation between 100 and 120-140 km (*Kurihara et al.*, 2010).

The temperature slightly decreases at 130 km at the beginning of February, at the time the polar vortex is restored. Above 150 km, a cooling is observed at the time of maximum stratospheric temperature, although it is not clear if it is related with the thermospheric cooling layer observed during the minor SSW in January 2008 at lower latitudes (*Goncharenko and Zhang*, 2008).

Figure 8.3 shows the zonal mean temperature anomaly (difference between day of warming peak and 15 days before the warming starts) simulated by a free-running version of the TIME-GCM model (top panel) compared to the that observed by MIPAS (difference between the mean of 15 to 27 January and the mean of 12 January) (bottom panel). The comparison between both data is remarkably similar, despite the fact that the meteorological conditions during the simulated and the observed warming are completely independent. The stratospheric warming ($\sim$50 K) and the related mesospheric cooling ($\sim -50$ K) observed by MIPAS have the same magnitude and the same altitude range than those predicted. Both measurements and simulations also extend equator-wards up to 50°N with very similar distributions. The thermospheric warming predicted by the simulations is also observed by MIPAS temperatures, but MIPAS shows larger values (20 K warmer), and it extends up to higher altitudes and lower latitudes than model results. These observations represent the first experimental evidence of a dynamical coupling of the lower atmosphere and the thermosphere in the 120-150 km range by means of satellite data. More details can be found in *Funke et al.* (2010).

## 8.2. Changes in temperature and NO during a solar storm.

### 8.2.1. Introduction

Solar storms are transient events that occur at the Sun surface. They consist of solar flares and coronal mass ejections (CME) that emit charged energetic particles into space. The particle flux is dominated by protons, accompanied by electrons and heavier ions. Therefore, this event is also called Solar Proton Event (SPE). Guided by the interplanetary and Earth's magnetic fields, this particle flux eventually precipitate its energy in the middle and upper atmosphere in the polar cap and the auroral zone. SPE's typically last for a few days and the energy that they deposit in the middle and upper atmosphere from particle precipitation and Joule heating (*Banks*, 1977, 1979; *Rees et al.*, 1983) causes changes in temperature, density and composition. The particle precipitation is responsible for the enhancement of the nitric oxide production in the thermosphere, mainly at auroral latitudes but also at mid and even low latitudes, as it has been previously studied from SME (*Siskind*

Table 8.2: *UA* MIPAS measurements during the solar storm of January 2005.

| Period | # Orbits | Orbits | TIME (UT) | Date |
|---|---|---|---|---|
| Pre-Storm | 4 | 15135-15138 | 10:15-16:32 | 21 Jan |
| During Storm | 5 | 15139-15143 | 16:34-24:00 | 21 Jan |
| Post-Storm | 7 | 15144-15147, 15150-15152 | 00:00-14:40 | 22 Jan |

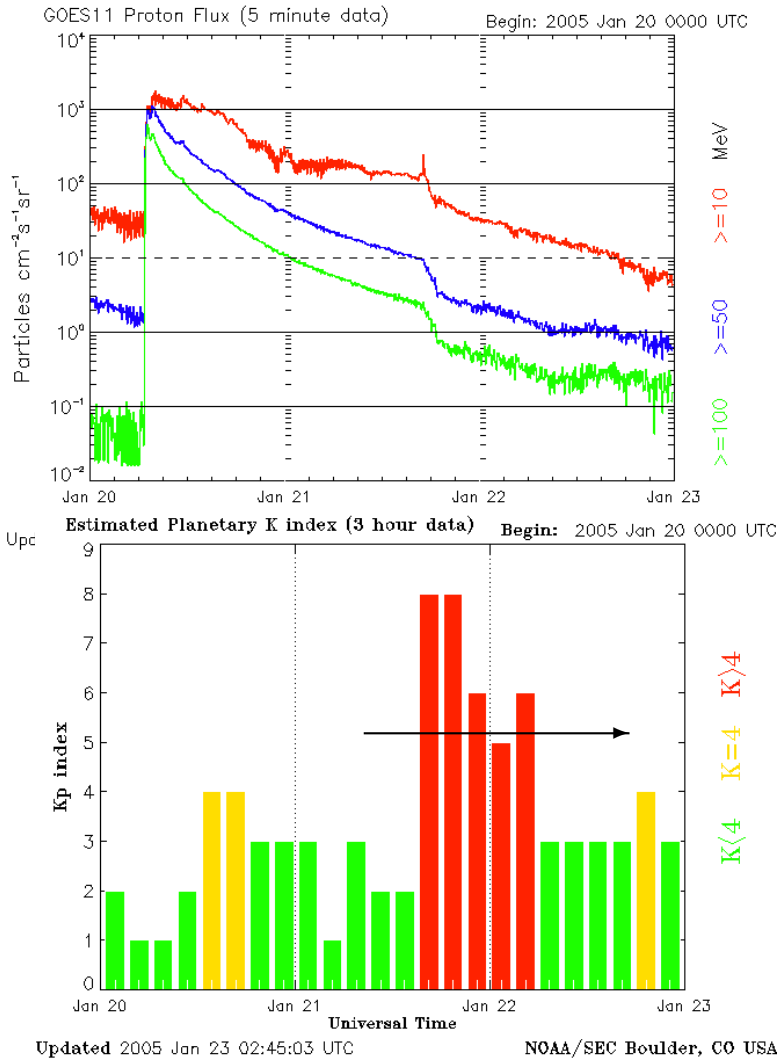


Figure 8.4: GOES11 proton fluxes (top) and estimated planetary $K_p$ index (bottom) during 20-22 of January 2005 when occurring the second phase of the solar storm. Data taken from NOAA/SEC. The period of MIPAS measurements in the *UA* mode is marked with the black arrow (bottom panel), covering periods of low $K_p$ (pre-storm), during the storm (high $K_p$) and post-storm (low $K_p$ again).

*et al.*, 1989a,b) and SNOE (*Barth et al.*, 2003) measurements and by 3D modelling (CMAT) (*Dobbin and Aylward*, 2008).

The solar flares and CME's that occurred during 16-21 January 2005 marked the hardest and most energetic SPE of solar cycle 23. The $>10$ MeV proton flux peaked on 20$^{th}$January and showed an enhanced level until about 18:00 UT 22$^{nd}$ January. Additionally, the declining phase of the SPE (21-22 January) is accompanied by an intense geomagnetic storm activity.

MIPAS thermospheric NO and temperature have been obtained from 21$^{st}$ January at 10:15 UT, to 22$^{nd}$ January at 14:40, covering conditions of pre-storm, during the storm and post-storm (see Fig. 8.4 and Table 8.2). The analysis of the MIPAS measurements is presented here and compared to the temperature and NO simulated by the 3D model TIME-GCM (*Roble*, 1995). The TIME-GCM model was already described in Sec. 6.6.1. An important difference in these simulations, however, with respect to those used in Secs. 6.6.1 and 8.3, is that the imposed auroral precipitation and plasma convection at the upper boundary of the model were not taken from empirical models driven by $K_p$, as usual, but from the AMIE model data assimilation results (*Richmond*, 1992). This takes into account more realistically the geomagnetic conditions, which is very important under such highly perturbed conditions.

### 8.2.2. MIPAS vs TIME-GCM

For the comparison between MIPAS and TIME-GCM, the model results have been interpolated to the MIPAS measurement locations and times, as well as to the retrieved altitudes of the Tk and NO profiles, with the aim of reducing possible biases due to the different sampling of MIPAS observations and the model grid. In addition, MIPAS averaging kernels have been applied to the TIME-GCM Tk and NO profiles as described in Section 6.5, and the MIPAS NO was scaled with the atomic oxygen predicted by TIME-GCM by using Eq. 6.1 (see Sec. 6.2.1). MIPAS and TIME-GCM data were treated in the same way for performing zonal mean and post/pre-storm differences.

Figure 8.5 shows the comparison of MIPAS zonal mean temperature with TIME-GCM predictions for pre-storm (left panels) and post-storm (right panels) conditions. The vertical structure of the temperature as well as the latitudinal distribution before the solar storm are very similar in both MIPAS and TIME-GCM datasets. Clear differences between MIPAS and TIME-GCM, however, exist (see Figure 8.6, left panel). For pre-storm conditions, MIPAS temperatures are generally colder (10-20 K) between 110 and 120 km for almost all latitudes, while they are warmer (20-60 K) above 120 km with more pronounced values in the Southern (summer) hemisphere at higher altitudes.

Right panels of Figure 8.5 show the temperature fields after the solar storm occurred. Under these conditions the altitude/latitude distribution of temperature is also similar in both MIPAS and TIME-GCM datasets, showing an increase in the polar regions. The difference between MIPAS

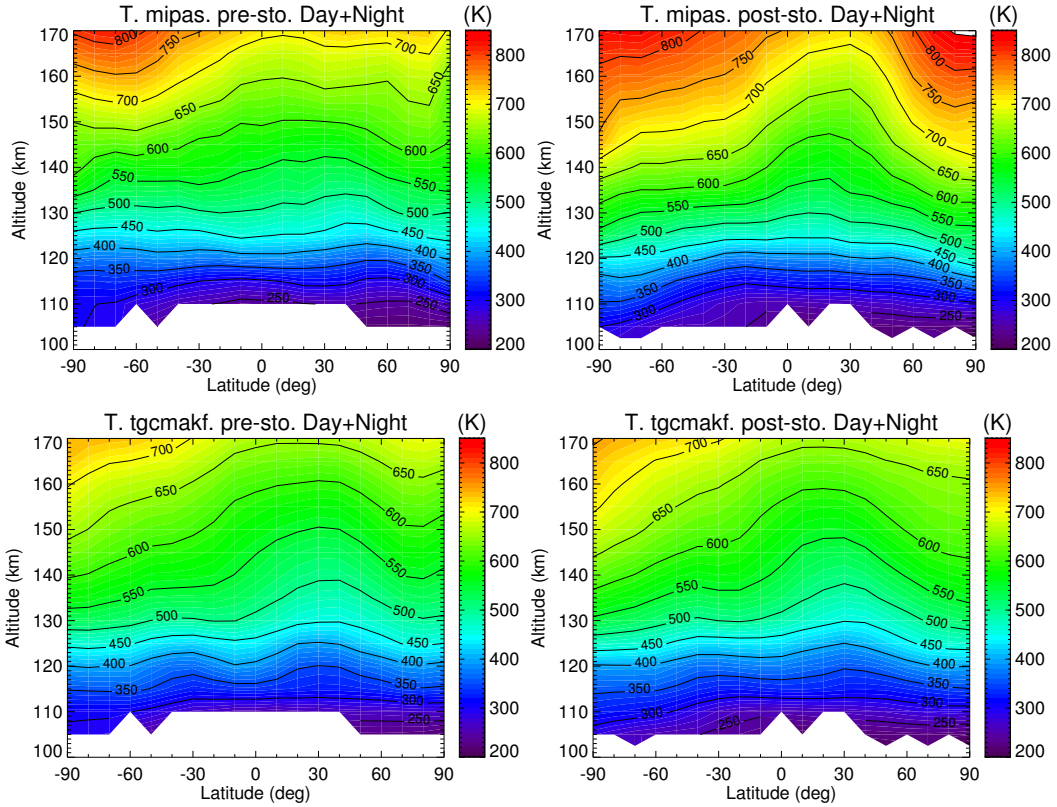


Figure 8.5: Temperature comparison of MIPAS (top row) vs TIME-GCM (bottom row) for pre-storm (left panels) and post-storm (right panels) (see Table 8.2). Both, day- and night-time data were included.

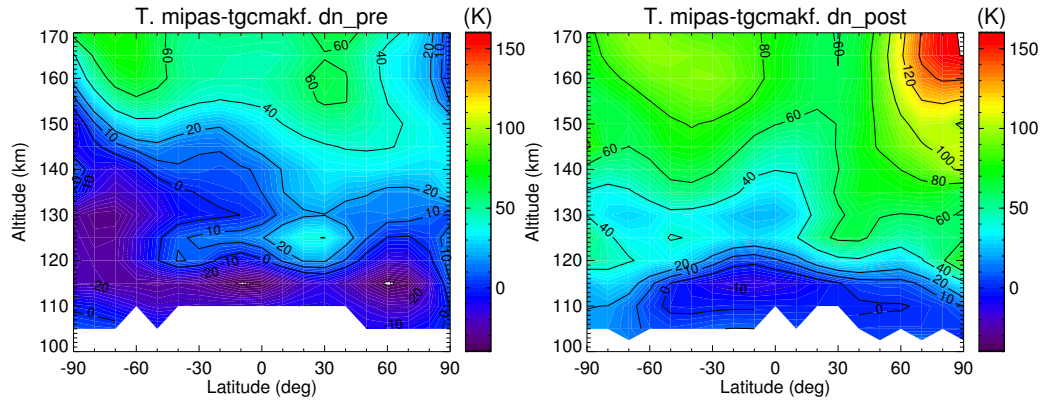


Figure 8.6: Differences between MIPAS and TIME-GCM kinetic temperature for pre-storm (left panel) and post-storm (right panel). Both, day- and night-time data were included.

and TIME-GCM for post-storm conditions (see Figure 8.6, right panel) is rather similar than for pre-storm conditions, although, in general, the differences are larger. That is, the enhancement in the temperature field observed by MIPAS is overall larger than that predicted by TIME-

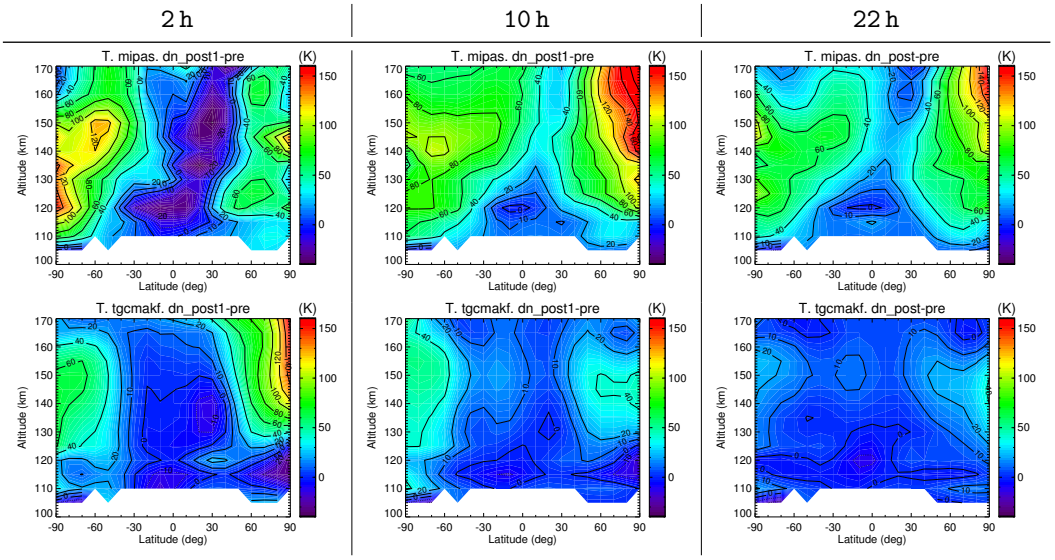


Figure 8.7: Effect of the solar storm on temperature 2, 10 and 22 hours after the storm. Top panels: MIPAS; bottom panels: TIME-GCM.

GCM. Other significant features are that the colder MIPAS temperatures in the 120-140 km region in the Southern polar region (50-90°S) have nearly disappeared, and the differences above 140 km in the Northern polar region are more pronounced in MIPAS data.

Since MIPAS was measuring along the occurrence of the solar storm, the data have been also compared to model predictions at intermediate stages, e.g. during the early phase of the storm (approximately 2 hours after it began), a few hours later (10 hours later), and at the final phase of the measurements (post-storm) (see Table 8.2 and Figure 8.7). MIPAS observations of temperature (top panels) show an initial enhancement at polar latitudes and all altitudes, that progressively extends to equatorial latitudes but essentially remain with very similar perturbations. This enhancement is more important above 120 km and at latitudes poleward of 60°, particularly in the Northern (winter) hemisphere. Here, the enhancement exceeds 100 K even 1 day after the storm. At tropical latitudes the enhancement is small, generally below 10-20 K. TIME-GCM temperature enhancements (bottom panels) agree quite well with those of MIPAS 2 hours after the storm, with the largest enhancements taking place in the polar regions and at altitudes between 130 and 160 km. They suffer, however, a faster relaxation than that observed in MIPAS data, in such a way that 1 day after the storm the effects on temperature are underestimated by about a factor of 2. This then suggests that the initial perturbations are well captured by the model but, for some reasons, possibly because of an over-estimated NO enhancement which very quickly radiatively cools the atmosphere (see below), it underestimate the warming of the atmosphere at about one day after the storm began.

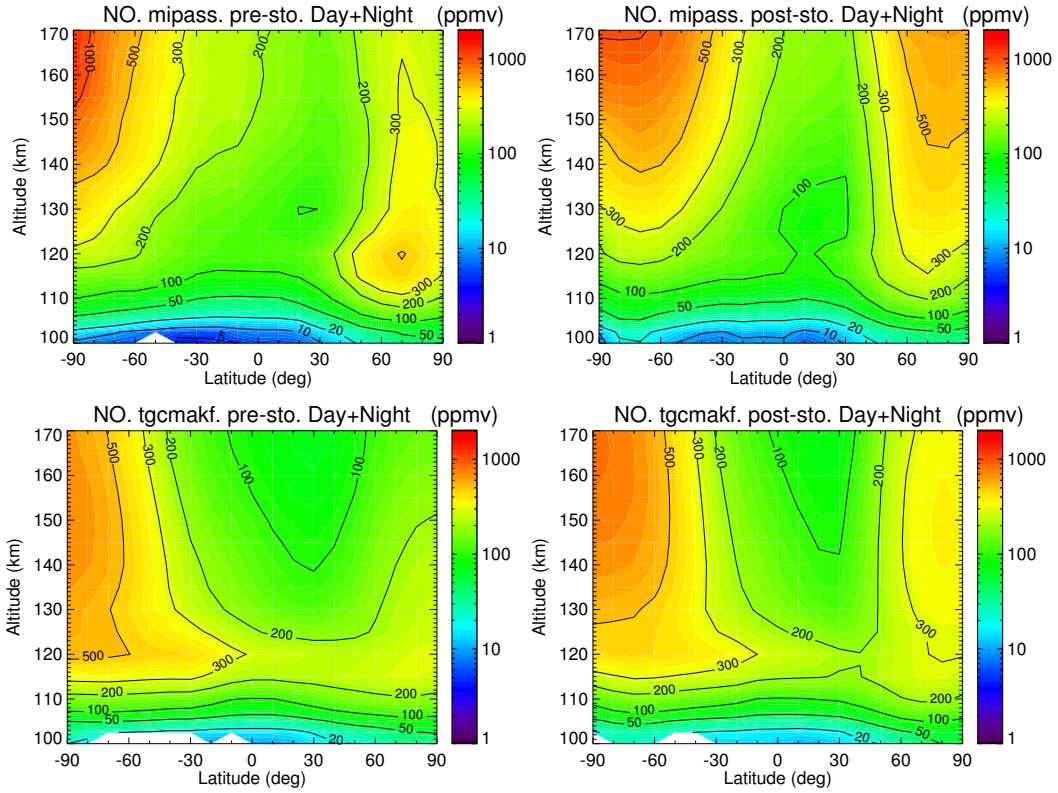


Figure 8.8: Nitric oxide comparison of MIPAS (top panels) vs TIME-GCM predictions (lower panels) for pre-storm (left panels) and post-storm (right panels) (see Table 8.2). Both, day- and night-time data were included.

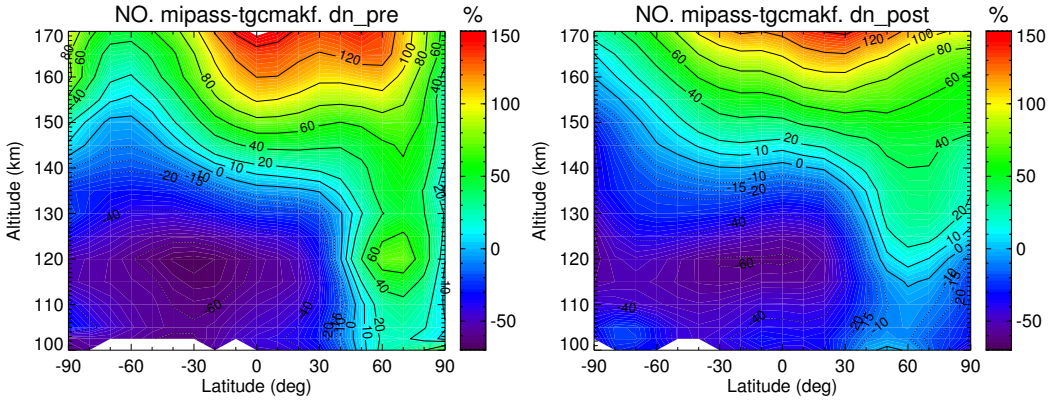


Figure 8.9: Differences between MIPAS and TIME-GCM NO densities for pre-storm (left panel) and post-storm (right panel). Both, day- and night-time data were included.

Figure 8.8 shows a comparison of MIPAS zonal mean NO *vmr* with TIME-GCM predictions for the pre-storm and post-storm conditions. MIPAS NO has also been corrected by using the atomic oxygen of TIME-GCM as suggested in Section 6.2.1. Comparing the data for pre-storm conditions, there are many common features among the MIPAS and TIME-GCM NO zonal mean fields.

The two distributions show large NO over the polar regions with minimum values in the tropical latitudes. Both also show larger NO *vmr*'s in the Southern (summer) pole than in the Northern (winter). The maximum in NO in the Northern hemisphere is about 120 km, in rather good agreement between model and measurements. In the Southern hemisphere they both show the maximum at higher altitudes with a rather broad peak. The maximum of NO in the Southern polar region is located at higher altitudes in MIPAS than in TIME-GCM. This might be caused by the coarse vertical resolution of MIPAS in the uppermost altitude region of MIPAS retrieval (160-180 km) (see Figure 6.1).

There are however significant differences between MIPAS and TIME-GCM for both before and after the storm as can be appreciated in Figure 8.9. MIPAS has measured significantly lower values (up to 60-70%) below about 130 km, at most latitudes except in the Northern polar region ($>50^{\circ}$N). However, in the mid-thermosphere (between 140 and 170 km), MIPAS NO is significantly larger than predicted by TIME-GCM, up to 100-120%, with larger values in the Northern (winter) hemisphere. These features in the MIPAS/TIME-GCM differences are very similar before and after the storm.

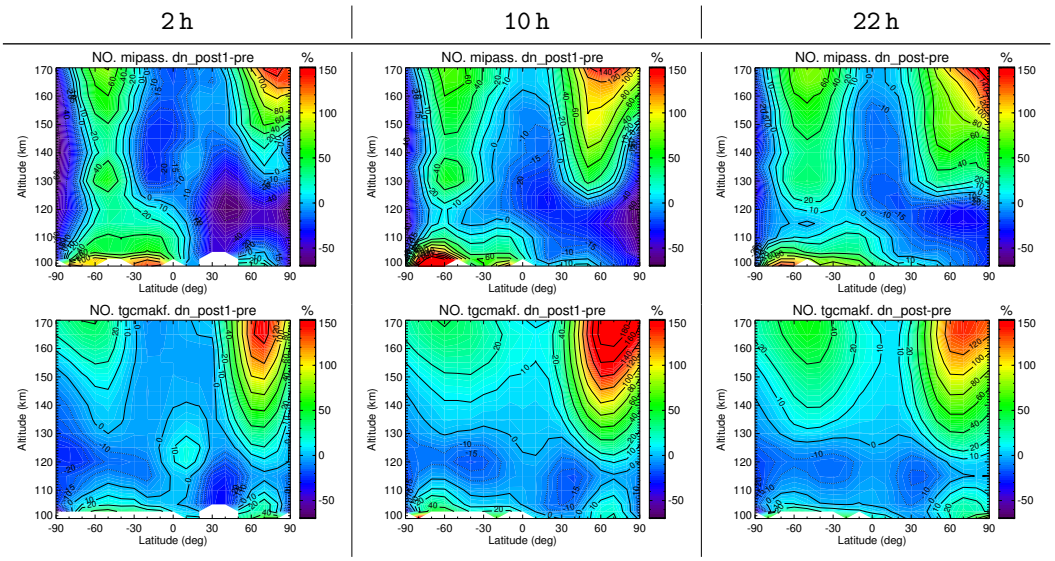


Figure 8.10: Effect of solar storm on nitric oxide 2, 10 and 22 hours after the storm. Top panels: MIPAS; bottom panels: TIME-GCM.

It is interesting to note, however, that, despite the absolute values of MIPAS and TIME-GCM are rather different, the predicted enhancement in NO by the TIME-GCM model is in very good agreement with MIPAS measurements (see Figure 8.10). Both show an enhancement in the polar regions, around $50^{\circ}$S in the Southern (summer) hemisphere and at latitudes polewards of $60^{\circ}$N in the Northern hemisphere. The latter reach values over 100 %. The enhancement is somewhat larger in TIME-GCM than in MIPAS, particu-

larly in the Northern hemisphere (see middle panels at 10 hours after the storm in the NH). This is contrary to the perturbations in temperature discussed above, where MIPAS temperature enhancements are significantly larger. One plausible explanation is that TIME-GCM over-predicts the NO enhancement which, because of it fast radiative cooling at 5.3 $\mu$m, lead to a large cooling and hence to faster temperature relaxation.

The temporal evolution of the TIME-GCM predicted NO shows a slight enhancement towards mid- and low latitudes above 140 km, which is also observed in MIPAS NO, although less pronounced. It is noticeable also how the enhancement around 120 km is small in both datasets but increases also below this altitude, where the NO production is very efficient, being slightly larger in MIPAS.

## 8.3. Quiet conditions: MIPAS vs TIME-GCM

### 8.3.1. Introduction

The comparison between measurements and models has a double motivation. On one hand, the model output can be useful for checking potential systematic errors in the measured atmospheric parameters. A good example is that described in Section 6.5, where comparison between MIPAS and TIME-GCM model concluded that nighttime MIPAS NO and $T_k$ are affected by significant systematic smoothing errors related to the use of a daytime climatology (NOEM) as *a priori* information for retrieval of nighttime NO. On the other hand, and most important, they can be compared to models in order to improve the knowledge on the physical (dynamical, radiative) and chemical processes that govern the properties of the atmosphere.

The daytime climatology of thermospheric NO and $T_k$ obtained from MIPAS measurements falls in a period (2005-2009) of low solar and geomagnetic activity (descent phase of solar cycle 23). That is, most of the observed days have a quiescent thermosphere, with the exception of the solar storm occurred in January 2005 during which MIPAS has provided 2 days of measurements. The NO and temperature obtained from MIPAS measurements at representative days of equinox and solstice conditions for this quiescent period have been compared to simulations by TIME-GCM.

### 8.3.2. MIPAS vs TIME-GCM

Thermospheric NO and temperature have been simulated with the TIME-GCM 3D model (*Roble*, 1995), described in Section 6.5, in order to compare with MIPAS thermospheric quiet climatology. For such simulation, single days representative for equinox and solstice conditions have been chosen: 21 March 2006 and 23 June 2006. As described in previous sections,

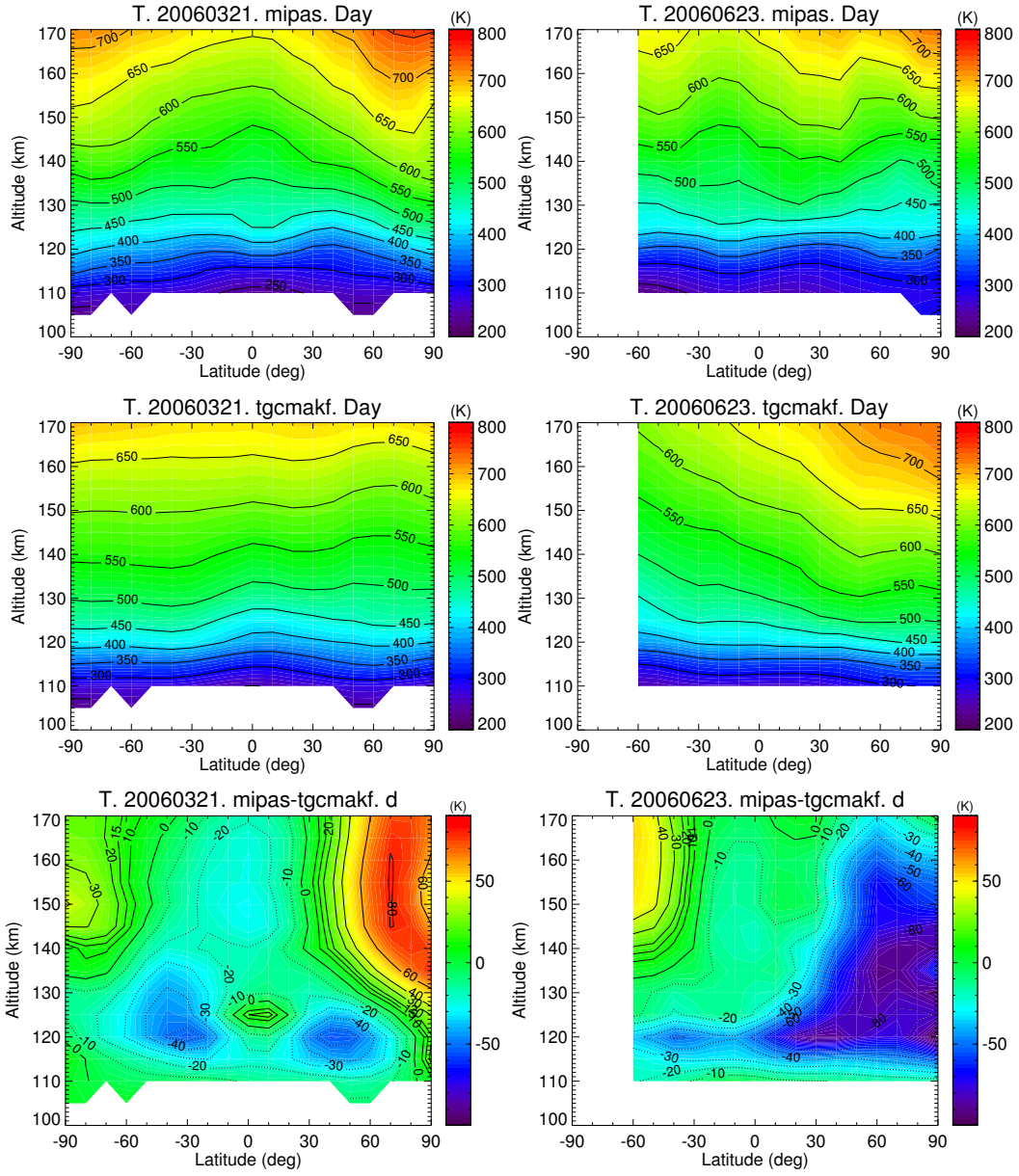


Figure 8.11: Comparison of daytime temperature of MIPAS (top) vs TIME-GCM (middle) for 21 March 2006 (left) and for 23 June 2006 (right). MIPAS-TIME-GCM differences are shown in bottom panels.

the model results have been interpolated to the MIPAS measurement locations and times, as well as to the retrieved altitudes of the Tk and NO profiles. Additionally, MIPAS averaging kernel have been applied to the TIME-GCM Tk and the MIPAS NO profiles have been scaled with the TIME-GCM atomic oxygen concentration as described in Section 6.5.

Figure 8.11 shows the comparison of MIPAS zonal mean daytime temperatures with TIME-GCM predictions for 21 March 2006 and 23 June 2006

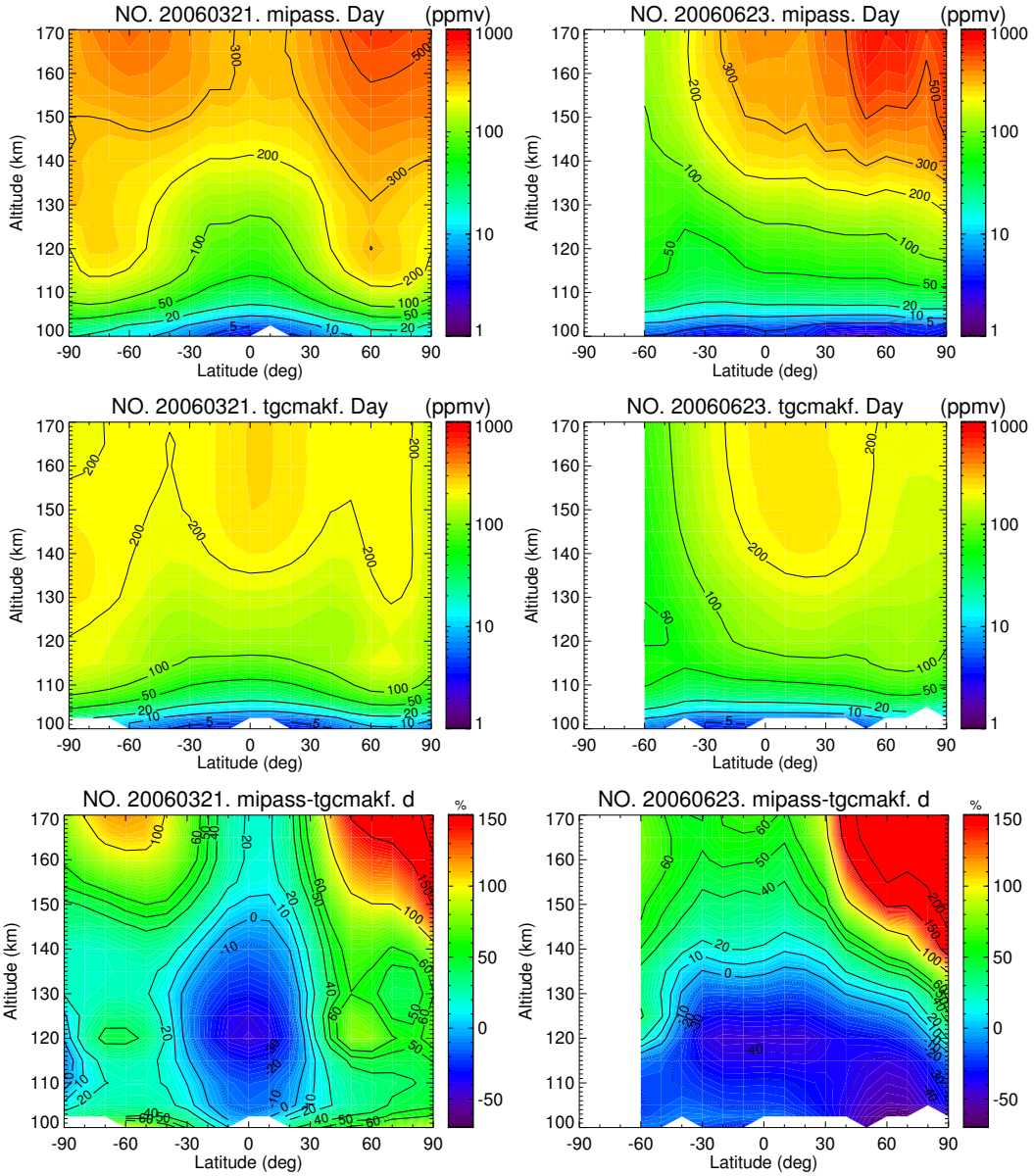


Figure 8.12: Comparison of daytime NO *vmr* of MIPAS (top) vs TIME-GCM (middle) for 21 March 2006 (left) and for 23 June 2006 (right). MIPAS-TIME-GCM differences are shown in bottom panels.

(equinox and solstice conditions, respectively). In the upper thermosphere (above around 130 km) MIPAS shows a good agreement with TIME-GCM at the tropical latitudes but the model clearly underestimates the temperatures in the polar regions, by values in the range of 30-80 K, in both hemispheres for equinox conditions and in the polar winter hemisphere. However, in the polar summer, the situation is reversed being TIME-GCM overestimating MIPAS temperatures.

In the lower thermosphere (110-130 km), the agreement is better and

differences hardly reach 30 K. It is noticeable, however, that the polar summer temperatures are also overestimated by TIME-GCM, as well as for equinox conditions at mid-latitudes in both hemispheres around 120 km.

Note that the MIPAS temperature fields for these two days of March and June in 2006 are very consistent with the monthly mean for March and June shown in Fig. 7.3 for 2008-2009 climatology. In the same line, the comparison shown in Fig. 6.16 for 22 July 2005 shows also very similar features as those shown here for solstice conditions, 23 June 2006 (right panels of Fig. 8.11). Hence, the discrepancies found here seem to be systematic and not just attributable to these two particular days in 2006. It it not clear what are the reasons for that. There are very few measurements of this atmospheric regions and models have not been sufficiently verified yet. Work is currently in progress, in collaboration with Gang Lu from NCAR (USA) (nowadays responsible for the TIME-GCM model), to understand these differences.

Figure 8.12 shows the corresponding MIPAS and TIME-GCM comparison for the daytime NO *vmr* for the same days. The NO observed by MIPAS above about 130 km is systematically larger at all latitudes but particularly at high latitudes, where the differences exceeds 100 %. At tropical latitudes. MIPAS NO is also larger than the model prediction (up to a 20 %).

Below about 130 km, MIPAS NO for equinox conditions is also larger at auroral and mid-latitudes but smaller at lower altitudes up to a 40 % at 120 km. For solstice, MIPAS NO are also smaller but in this case for almost all latitudes.

As discussed above for temperature, the MIPAS NO *vmr* monthly fields for March and June for the 2008-2009 climatology shown in Fig. 7.5, are very similar to those shown here for 21 March 2006 and 23 June 2006 (Fig. 8.12). Also, the differences found for 22 July 2005 in Sec. 6.6.1, exhibit similar features (though with significantly different values) to those shown here. Hence this suggests that the differences found are systematic. As in the case of temperature, these differences are not still fully understood. In the case of the underestimation of NO in the auroral regions (high latitudes below about 130 km) for equinox, it could be due to an inadequate input of the auroral precipitation (in this case it was included using empirical models driven by $K_p$ rather than assimilated measurements). However, the underestimation above 130 km for all latitudes should be due to another reason. As mentioned above for temperature, work is also in progress, in collaboration with Gang Lu from NCAR (USA), responsible of TIME-GCM, to understand these differences.

# Chapter 9

# Conclusions and Future Work

*Abstract*

MIPAS (Michelson Interferometer for Passive Atmospheric Sounding) is a high spectral resolution emission spectrometer successfully launched on 1$^{st}$ March 2002 as part of the core payload of the ENVISAT mission by ESA dedicated to study and monitor the Earth's environment. The main characteristics of MIPAS are: 1) wide spectral coverage (4.15-14.6 $\mu$m) and high spectral resolution (0.0625 $cm^{-1}$ in its optimized resolution); 2) high sensitivity (i.e., NESR of 3-50 $nW/(cm^2\,sr\,cm^{-1})$) and a wide field of view; 3) wide spatial (pole to pole) and temporal (day and nighttime) coverage. These make MIPAS and ideal instrument to study the middle and upper atmosphere. The spectra recorded by MIPAS are used to derive atmospheric parameters such as temperature and abundances of key constituents. For that purpose, inversion codes have been developed in the frame of this work. The emission spectra measured in the middle and upper atmosphere are affected by non-LTE, that is, the populations of the energy states responsible for the emissions are governed by non-LTE processes. Hence, the inversion codes must include these processes in order to retrieve accurately the atmospheric parameters in the mentioned regions.

In this work, MIPAS measurements in the middle and upper atmosphere from 2005 to 2009 have been inverted to derive: 1) temperature profiles from 20 to 100 km from $CO_2$ emissions at 15 $\mu$m; 2) temperature and nitric oxide (NO) volume mixing ratio profiles from 100 to 170 km from NO emissions at 5.3 $\mu$m. The main conclusions are now exposed. The chapter ends with a brief summary of the work which is still ongoing and with some suggestions to continue this study, and further applications of the results obtained in this work.

## 9.1. Retrieval of temperature from the stratosphere to the lower thermosphere

Temperature profiles have been retrieved from $CO_2$ 15 $\mu$m emission recorded by MIPAS in its special observation modes dedicated to the middle and upper atmosphere from 2005 to 2009: *MA* (20-100 km), *NLC* (40-100 km) and *UA* (40-100 km). Together with the temperature, the line of

sight of the instrument (i.e., the tangent altitudes of each limb scan) and horizontal temperature gradients have also been retrieved. The retrieval setup has been adapted from that developed for nominal retrievals (6-70 km), but taking into account the extended altitude range of *MA*, *NLC* and *UA* MIPAS observations. On the one hand, since the $CO_2$ emission at 15 $\mu$m above 70 km is affected by non-LTE, an updated non-LTE model for $CO_2$ populations emitting at this spectral range has been included. On the other hand, the spectral regions (microwindows) used in the retrieval have been extended by adding microwindows that include strong emission features, and hence large signal/noise ratio, in the upper mesosphere and lower thermosphere. These additional microwindows include fundamental band ($01^10$-$00^00$) R-branch lines and hot band ($10^00$-$01^10$) Q-branch lines. The characterization of the retrieved temperature from the stratosphere to the lower thermosphere is summarized below:

- Temperature random errors arising from the propagation of measurement noise are typically of 0.2-0.5 K below 50 km, 0.5-2 K at 50-70 km, and 2-8 K above.
- The vertical resolution for the obtained temperature profiles are 4 km below 35 km, 3 km at 35-50 km, 4-6 km at 50-90 km, and 6-10 km above. Neither the random errors nor the vertical resolution vary significantly with latitude and season.
- Systematic errors in temperature mainly arise from uncertainties in the non-LTE parameters, which become important in the mesosphere and lower thermosphere. Other sources of systematic errors are uncertainties in the spectroscopy, gain calibration, instrument line shape and interfering species. The overall systematic errors are 0.5-1.2 K below 70 km, 1.2-3.7 K at 70-85 km, and 3.7-12 K at 85-100 km. In the polar summer, the larger non-LTE effects increase the systematic errors up to 6 K at 85 km and up to 30 K at 100 km.

## 9.2. Validation of MIPAS $T_k$ in the middle atmosphere

The MIPAS temperatures retrieved from the $CO_2$ emission at 15 $\mu$m have been compared with independent co-located measurements of several instruments, including space-borne instruments: SABER on board TIMED, ACE-FTS on board SCISAT-1 and MLS on board EOS Aura satellite; ground-based: Mauna Loa (MLO) and Table Mountain (TMF) lidars and Davis and SATI spectrometers; in-situ measurements: falling spheres climatology (FS). MIPAS temperatures compares well in general with other instruments, within 1-2 K at 20-70 km, within 4-10 K at 80-90 km and within 15-20 K above 95 km. The differences do not show strong variability with latitude and season, except in the high latitude summers, particularly

around the mesopause. The most important biases found in MIPAS temperatures are summarized:

- In the lower and mid-stratosphere, MIPAS agrees with other instruments at all seasons better than 1 K, except with SABER, which is 2-3 K warmer than MIPAS, although SABER has a well known warm bias of this magnitude.

- MIPAS temperatures are generally 1-2 K colder at 45-50 km.

- In the lower mesosphere (below 70 km), MIPAS temperatures are generally colder within 2 K. The agreement at these altitudes is particularly good with SABER and the TMF lidar.

- At 75-85 km, MIPAS temperatures are generally colder (1-2 K at mid-latitudes and 1-10 K at polar summer), except for polar winter (and also comparisons with the TMF lidar and MLS), for which MIPAS is 3 K warmer.

- Around the mesopause and above, MIPAS temperatures are generally warmer in mid-latitudes and in the polar winter (above 88 km and 80 km, respectively). The comparison with the ground-based spectrometers SATI and Davis is excellent (within 1 K at 87 km). In the polar summer, MIPAS is colder than ACE (10 K) near the mesopause and warmer everywhere else; MIPAS is warmer than MLS at 85-90 km (associated to mesopause altitude mismatch); MIPAS is warmer than SABER near the mesopause, although this difference would decrease if the same atomic oxygen abundance and the same rates for $CO_2$ $\upsilon_2$ exchange and for $CO_2$-$N_2$ and $CO_2$-$O_2$ quenching were used.

The comparisons around the mesopause (except for polar summer conditions) suggest that perhaps the atomic oxygen abundance used in MIPAS non-LTE retrievals is too low. The MIPAS warmer temperatures in the lower thermosphere supports this argument. In contrast, comparison of MIPAS with SABER and with FS climatology in the polar summer mesopause would improve if lower atomic oxygen were used. On the other hand, a reduction in the rates for $CO_2$ $\upsilon_2$ exchange and for $CO_2$-$N_2$ and $CO_2$-$O_2$ quenching would act in the same direction, with negligible effect on temperatures at other latitudes and seasons.

In summary, given the excellent performance and quality, and the wide spatial and temporal coverage of the MIPAS observations, MIPAS temperature of *MA*, *UA* and *NLC* modes embody a suitable dataset for studies aiming at the understanding of the physics of the atmosphere, particularly, the mesosphere and lower thermosphere region, and for the retrieval of atmospheric species abundances from emission measurements at IR wavelengths.

## 9.3. Retrieval of temperature and nitric oxide in the thermosphere

Temperature and nitric oxide mixing ratio profiles have been retrieved jointly from the NO fundamental band emission at 5.3 $\mu$m recorded by MIPAS in its upper atmosphere observation mode (100-170 km) from 2005 to 2009. Since the distribution of NO in the thermosphere shows a pronounced spatial inhomogeneity, particularly close to the auroral regions, horizontal NO *vmr* gradients are also retrieved, and to cope with the high spatial and temporal variability, the $ln$(NO) parameter space has been used. The retrieval setup includes a non-LTE model for the populations of NO vibrational levels, since the observed emission is affected by vibrational, rotational and spin non-LTE. The regularization strength used in the retrieval setup is altitude dependent, aiming the best trade-off between the vertical resolution and the precision of the retrieved parameters, as well as a similar distribution of the degrees of freedom between NO and $T_k$ and the largest number of converged profiles. In summary, the joint NO-$T_k$ retrieval is characterized in the following way:

- The quality of the retrieval, i.e., the random errors and the vertical resolution obtained for temperature and NO, shows a clear dependence on the signal to noise ratio. For auroral conditions (auroral region and high $A_p$ conditions), the precisions of $T_k$ and NO are better than 40 K and of 10-20 %, respectively, obtaining a vertical resolution of 5-10 km at 115-150 km, getting coarser below and above. For low $A_p$ conditions in general, and in the tropical and mid-latitude regions, where the signal to noise ratio is generally smaller, the precisions of $T_k$ and NO are better than 70 K and of 20-40 %, respectively. In these conditions, vertical resolutions range between 10 and 20 km.

- The precisions obtained for thermospheric $T_k$ and NO can be improved by averaging of profiles without introducing significant statistical biases related to the non-linear dependences on the retrieval parameters.

- The retrieved NO abundances have a strong dependence on the assumptions made on thermospheric atomic oxygen above 120 km (taken from NRL-MSISE-00 model). Hence, in order to make consistent comparisons between the retrieved NO and model results, a correction based on the ratios of model and NRL-MSISE-00 atomic oxygen must be applied. In contrast, the retrieved $T_k$ depends only weakly on the atomic oxygen, yielding systematic errors below 15 K.

- Other sources of systematic error sources are: atomic nitrogen uncertainties and the propensity for spin-conserving collisions,

which largely control thermospheric spin non-LTE distributions. These parameters lead to minor systematic errors of 10-20 K for temperature and 5-10 % for NO.

- Smoothing errors of the retrieved $T_k$ and NO related to the mapping of *a priori* profile shapes have been analyzed by means of retrievals performed on synthetic spectra. Under auroral conditions, the retrieved $T_k$ and NO are rather insensitive to the smoothing errors. However, for extra-polar and low $A_p$ conditions, smoothing errors can be significant. It has been found that, if the *a priori* profile shape, particularly that of NO, deviates significantly from the true profile, a cross talk between the retrieved $T_k$ and NO may occur. On the other hand, retrieval simulations have shown that the retrieval response, i.e., the averaging kernels applied to the true profiles, shows a good agreement with the retrieved profiles. This indicates that a comparison between MIPAS observations and a model simulation is meaningful even at low $A_p$ conditions if the MIPAS averaging kernels are applied to the model profiles. Comparisons between MIPAS and TIME-GCM reveal a potential systematic smoothing error in the retrieved nighttime Tk and NO profiles. This smoothing error is related to the NO *a priori*, which is taken from a daytime climatology (NOEM based on SNOE data). Future work will address the improvement on the knowledge of *a priori* nighttime NO.

## 9.4. MIPAS NO and $T_k$ thermospheric climatology

The relatively high and homogeneous data availability during 2008-2009, around 3 days per month has allowed to construct a monthly zonal mean climatology for this particular time period belonging to solar minimum conditions. Due to the potential bias found in the MIPAS nighttime observations the climatology presented here is based on daytime observations only. The main features of the climatology are summarized as follows:

- The temperature distributions show good agreement with the existing climatologies, i.e., NRL-MSISE-00, although some differences exist. MIPAS $T_k$ is generally colder than MSIS in the polar middle thermosphere (mainly in the summer polar region) by up to 40 K, and is generally warmer than MSIS in the lower thermosphere around 120-125 km by 10-40 K.

- MIPAS temperatures show a seasonal phase shift of the polar summer temperature maximum towards the preceding equinox, which is not present in MSIS data. The nature of this phase shift is not clear and dedicated studies are required to analyze this feature in detail.

- Around 120 km, MIPAS temperatures tend to be warmer than MSIS. This result is in agreement with previous studies which describe a possible cold bias of MSIS (*Gardner et al.*, 2005, 2007).
- The NO distributions have been compared to the NOEM empirical model based on SNOE measurements taken during the period 1998-2000, corresponding to a period of solar maximum. In general, the agreement is good, except in the polar regions above 120 km, where NOEM NO abundances are 20-60 % larger.
- MIPAS NO has been also compared to a climatology for the declining phase of the solar cycle based on HALOE and SME data. MIPAS NO is generally larger about 10-40 %. In the auroral region and at equatorial latitudes above 130 km, MIPAS NO is even larger, by a factor 1.6-2.
- MIPAS has provided the first observations of thermospheric nighttime NO. Although they have not been included in the climatology due to the found bias, the observed day/night differences have been analyzed since they provide knowledge on the photochemical processes involved in the diurnal variations. In the tropical and midlatitude regions of the middle thermosphere, a diurnal enhancement of up to 140 % is observed. In the polar regions, below 140 km, daytime concentrations are about 10-50 % smaller than during night. This behavior observed in MIPAS measurements are in good qualitative and quantitative agreement with model simulations (*Bailey et al.*, 2002).
- The MIPAS observations analyzed in this work fall in a period of quiescent atmosphere, within the descending phase of the solar cycle 23. Nevertheless, it was possible to perform a study of the variability of thermospheric NO and $T_k$ with the solar and geomagnetic activities. NO and temperature at auroral regions show a clear correlation with the geomagnetic activity, represented by the $A_p$ index. Likewise, NO and temperature at low latitudes are correlated with the solar flux, represented by the $F_{10.7}$ index.
- The MIPAS climatology has allowed to find the first experimental evidence of a dynamical coupling of the lower atmosphere and the thermosphere at 120-150 km during the major stratospheric warming (SSW) of January 2009. The observed warming (cooling) in the stratosphere (mesosphere) agrees very well with the predictions from the TIME-GCM model. The predicted thermospheric warming associated to the SSW is also observed by MIPAS measurements, being MIPAS temperatures warmer by around 20 K.
- MIPAS thermospheric NO and $T_k$ has allowed to study in detail the effects of a solar proton event (January 2005) in the upper atmosphere. MIPAS observes an increase in temperature and NO in the

auroral regions of 20-100 K and of 20-120 %, respectively, above 120 km. Simulations from TIME-GCM model predicts a smaller enhancement and a faster relaxation for the temperature than that observed by MIPAS. Concerning NO, both MIPAS observations and simulations show a very good agreement in the evolution of NO after the storm, although MIPAS abundances are smaller at the early stage.

- Currently, the large MIPAS thermospheric NO and $T_k$ database is being compared to 3D simulations from TIME-GCM model. So far, preliminary comparison for quiet conditions (quiescent atmosphere) for equinox and solstice conditions (1 day each) yield systematic differences between observations and predictions that are still not fully understood and hence this work is still in progress, in collaboration with Gang Lu from NCAR (Boulder, USA), responsible of TIME-GCM.

## 9.5. Future work

There are several issues that deserve dedication in future works:

- First, the nighttime retrievals of thermospheric NO and $T_k$ must be improved with dedicated studies about a more appropriate *a priori* information for nighttime NO. In this direction, model-data comparisons of NO diurnal variations will shed light on thermospheric odd nitrogen photochemistry and, indirectly, on a better knowledge of nighttime NO to be included as *a priori* information in future versions of the data.

- The large database of thermospheric NO and $T_k$ obtained from MIPAS is planned to be compared to 3D model simulations as the TIME-GCM (*Roble*, 1995; *Liu and Roble*, 2002) and WACCM (*Garcia et al.*, 2007). This work is currently in progress.

- MIPAS is still measuring routinely in the upper atmospheric (*UA*) mode with the current baseline of 1/10 days and the Envisat mission has been extended until the end of 2013. It is planned to apply the retrieval scheme developed in this Thesis to those data. Thus, the NO and $T_k$ database will cover a nearly complete solar cycle.

# Bibliography


Akmaev, R. (2002), Modeling the cooling due to CO2 increases in the mesosphere and lower thermosphere, *Physics and Chemistry of the Earth*, *27*, 521-528, doi:10.1016/S1474-7065(02)00033-5.

Akmaev, R. A., and V. I. Fomichev (1998), Cooling of the mesosphere and lower thermosphere due to doubling of CO 2, *Annales Geophysicae*, *16*, 1501-1512, doi:10.1007/s00585-998-1501-z.

Akmaev, R. A., V. I. Fomichev, and X. Zhu (2006), Impact of middle-atmospheric composition changes on greenhouse cooling in the upper atmosphere, *Journal of Atmospheric and Solar-Terrestrial Physics*, *68*, 1879-1889, doi:10.1016/j.jastp.2006.03.008.

Andrews, D. G., J. R. Holton, and C. B. Leovy (1987), *Middle Atmosphere Dynamics*, *International Geophysics Series, R. Dmowska and J. R. Holton, eds.*, vol. 40, Academic Press.

Armstrong, P. S., S. J. Lipson, J. A. Dodd, J. R. Lowell, and A. M. Blumberg (1994), Highly rotationally excited NO($\nu, J$) in the thermosphere from CIRRIS 1A limb radiance measurements, *Geophys. Res. Lett.*, *21*(22), 2425-2428.

Bailey, S. M., T. N. Woods, C. A. Barth, S. C. Solomon, L. R. Canfield, and R. Korde (2000), Measurements of the solar soft x-ray irradiance by the student nitric oxide explorer: First analysis and underflight calibrations, *J. Geophys. Res.*, *105*, 27,179-27,194, doi:10.1029/2000JA000188.

Bailey, S. M., C. A. Barth, and S. C. Solomon (2002), A model of nitric oxide in the lower thermosphere, *J. Geop*, *107*(A8), 1205, doi:10.1029/2001JA000258.

Banks, P. M. (1977), Observations of joule and particle heating in the auroral zone, *Journal of Atmospheric and Terrestrial Physics*, *39*, 179-193.

Banks, P. M. (1979), Joule heating in the high-latitude mesosphere, *J. Geophys. Res.*, *84*, 6709-6712, doi:10.1029/JA084iA11p06709.

Bartels, J. (1949), The standardized Index Ks and the planetary index Kp, in *IATME Bull 126*, vol. 97, edited by IUGG Publ., Office, Paris.

Barth, C., and F. Eparvier (1993), A method of measuring the temperature of the lower thermosphere, *J. Geophys. Res.*, *98*(A6), 9437-9441.

Barth, C. A. (1964), Rocket measurement of the nitric oxide dayglow, *J. Geophys. Res.*, *69*, 3301-3303, doi:10.1029/JZ069i015p03301.

Barth, C. A. (1992), Nitric oxide in the lower thermosphere, *Planet. Space Sci.*, *40*, 315-336, doi:10.1016/0032-0633(92)90067-X.

Barth, C. A., D. W. Rusch, and A. I. Stewart (1973), The uv nitric-oxide experiment for atmosphere explorer, *Radio Science*, *8*, 379.

Barth, C. A., W. K. Tobiska, D. E. Siskind, and D. D. Cleary (1988), Solar-terrestrial coupling: Low-latitude thermospheric nitric oxide, *Geophys. Res. Lett.*, *15*, 92-94.

Barth, C. A., D. N. Baker, K. D. Mankoff, and S. M. Bailey (2001), The northern auroral region as observed in nitric oxide, *Geophys. Res. Lett.*, *28*, 1463.

Barth, C. A., K. Mankoff, S. M. Bailey, and S. Solomon (2003), Global observations of nitric oxide in the thermosphere, *J. Geophys. Res.*

Barth, C. A., D. N. Baker, and S. M. Bailey (2004), Seasonal variation of auroral electron precipitation, *Geophys. Res. Lett.*, *31*, L04,809, doi:10.1029/2003GL018892.

Barth, C. A., G. Lu, and R. Roble (2009), Joule heating and nitric oxide in the thermosphere, *J. Geophys. Res.*, *114*(A13), 05,301, doi:doi:10.1029/2008JA013765.

Beig, G., et al. (2003), Review of mesospheric temperature trends, *Reviews of Geophysics*, *41*, 1015, doi:10.1029/2002RG000121.

Bermejo-Pantaleón, D., et al. (2011), Global observations of thermospheric temperature and nitric oxide from mipas spectra at 5.3 $\mu$m, *J. Geophys. Res.*, *in press*.

BOMEM (1992a), MIPAS in-flight spectral calibration and instrument line shape retrieval, pO-TN-BOM-GS-0006.

BOMEM (1992b), MIPAS Michelson Interferometer for Passive Atmospheric Sounding, POEM phase B, determination of instrument line shape and spectral characteristics in the performance model, mIP-BM-TN-62120-0005.

BOMEM (1996), Non-Linearity Characterization and Correction, issue 1A, PO-TN-BOM-MP-0019.

Boone, C. D., R. Nassar, K. A. Walker, Y. Rochon, S. D. McLeod, C. P. Rinsland, and P. F. Bernath (2005), Retrievals for the atmospheric chemistry experiment Fourier- transform spectrometer, *Appl. Opt.*, *44*(33), 7218-7231.

Brasseur, G., and S. Solomon (2005), *Aeronomy of the Middle Atmosphere-Chemistry and Physics of the Stratosphere and Mesosphere*, Atmospheric and Oceanographic Sciences Library 32, third ed., Springer, P. O. Box 17, 3300 AA Dordrecht, The Netherlands.

Bremer, J. (2001), Trends in the thermosphere derived from global ionosonde observations, *Advances in Space Research*, *28*, 997-1006, doi: 10.1016/S0273-1177(01)80029-6.

Bremer, J. (2005), Detection of long-term trends in the mesosphere/lower thermosphere from ground-based radio propagation measurements, *Advances in Space Research*, *35*, 1398-1404, doi:10.1016/j.asr.2005.01.021.

Budzien, S., R. Bishop, A. Stephan, A. B. Christensen, and D. McMullin (2010), Atmospheric remote sensing on the international space station, *EOS*, *91*(42), 381-382.

Burns, G. B., W. J. R. French, P. A. Greet, F. A. Phillips, P. F. B. Williams, K. Finlayson, and G. Klich (2002), Seasonal variations and inter-year trends in 7 years of hydroxyl airglow rotational temperatures at Davis station (69°S,78°E), Antarctica, *Journal of Atmospheric and Solar-Terrestrial Physics*, *64*, 1167-1174, doi:10.1016/S1364-6826(02)00066-4.

Carlotti, M., G. Brizzi, E. Papandrea, M. Prevedelli, M. Ridolfi, B. M. Dinelli, and L. Magnani (2006), GMTR: Two-dimensional geo-fit multitarget retrieval model for Michelson Interferometer for Passive Atmospheric Sounding/Environmental Satellite observations, *Applied Optics*, *45*, 716-727, doi:10.1364/AO.45.000716.

Chauhan, S., et al. (2009), MIPAS reduced spectral resolution UTLS-1 mode measurements of temperature, $O_3$, $HNO_3$, $N_2O$, $H_2O$ and relative humidity over ice: retrievals and comparison to MLS, *Atmos. Meas. Tech.*, *2*, 337-353.

Clilverd, M., T. Clark, E. Clarke, and H. Rishbeth (1998), Increased magnetic storm activity from 1868 to 1995, *Journal of Atmospheric and Solar-Terrestrial Physics*, *60*(10), 1047 - 1056, doi:DOI:10.1016/S1364-6826(98)00049-2.

Cnossen, I., and A. D. Richmond (2008), Modelling the effects of changes in the Earth's magnetic field from 1957 to 1997 on the ionospheric hmF2 and foF2 parameters, *Journal of Atmospheric and Solar-Terrestrial Physics*, *70*, 1512-1524, doi:10.1016/j.jastp.2008.05.003.

Curtis, A. R. (1956), The computation of radiative heating rates in the atmosphere, *Proc. R. Soc. London, Ser. A*, *236*, 156-159.

Dang, C., J. Reld, and B. Garside (1983), Dynamics of the $CO_2$ lower laser levels as measured with a tunable diode laser, *Applied Physics B: Lasers and Optics*, *31*, 163-172, doi:10.1007/BF00688838.

Didkovsky, L. V., D. L. Judge, S. R. Wieman, and D. McMullin (2010), Minima of Solar Cycles 22/23 and 23/24 as Seen in SOHO/CELIAS/SEM Absolute Solar EUV Flux, in *SOHO-23: Understanding a Peculiar Solar Minimum*, *Astronomical Society of the Pacific Conference Series*, vol. 428, edited by S. R. Cranmer, J. T. Hoeksema, & J. L. Kohl, pp. 73-+.

Dobbin, A., and A. Aylward (2008), A three-dimensional modelling study of the processes leading to mid latitude nitric oxide increases in the lower thermosphere following periods of high geomagnetic activity, *Adv. Space Res.*, *42*, 1576-1585, doi:doi:10.1016/j.asr.2008.03.004.

Duff, J. W., F. Bien, and D. E. Paulsen (1994), Classical dynamics of $N(^4S)+O_2(X^3\Sigma_g^-) \rightarrow NO(X^2\Pi)+O(^3P)$ reaction, *Geophys. Res. Lett.*, *21*(18), 2043-2046.

Echle, G., et al. (2000), Optimized spectral microwindows for data analysis of the Michelson Interferometer for Passive Atmospheric Sounding on the Environmental Satellite, *Appl. Opt.*, *39*(30), 5531-5540.

Emmert, J. T., J. M. Picone, J. L. Lean, and S. H. Knowles (2004), Global change in the thermosphere: Compelling evidence of a secular decrease in density, *Journal of Geophysical Research (Space Physics)*, *109*, A02,301, doi:10.1029/2003JA010176.

Emmert, J. T., J. L. Lean, and J. M. Picone (2010), Record-low thermospheric density during the 2008 solar minimum, *Geophys. Res. Lett.*, *37*, L12,102, doi:10.1029/2010GL043671.

Eparvier, F., and C. Barth (1992), Self-absorption theory applied to rocket measurements of the nitric oxide (1, 0) γ band in the daytime thermosphere, *J. Geophys. Res.*, *97*(A9), 13,723-13,731.

Fesen, C. G., J.-C. Gérard, and D. W. Rusch (1989), Rapid deactivation of $N(^2D)$ by O: Impact on thermospheric and mesospheric odd nitrogen, *J. Geophys. Res.*, *94*, 5419-5426.

Fischer, H., and H. Oelhaf (1996), Remote sensing of vertical profiles of atmospheric trace constituents with MIPAS limb-emission spectrometers, *Appl. Opt.*, *35*(16), 2787-2796.

Fischer, H., et al. (2008), MIPAS: an instrument for atmospheric and climate research, *Atmos. Chem. Phys.*, *8*, 2151-2188.

Flaud, J.-M., G. Brizzi, M. Carlotti, A. Perrin, and M. Ridolfi (2006), MIPAS database: Validation of $HNO_3$ line parameters using MIPAS satellite measurements, *Atmos. Chem. Phys.*, *6*, 5037-5048.

Folkestad, K., T. Hagfors, and S. Westerlund (1983), EISCAT - An updated description of technical characteristics and operational capabilities, *Radio Science*, *18*, 867-879, doi:10.1029/RS018i006p00867.

French, W. J. R., and F. J. Mulligan (2010), Stability of temperatures from TIMED/SABER v1.07 (2002-2009) and Aura/MLS v2.2 (2004-2009) compared with OH(6-2) temperatures observed at Davis Station, Antarctica, *Atmospheric Chemistry & Physics*, *10*, 11,439-11,446, doi: 10.5194/acp-10-11439-2010.

French, W. J. R., G. B. Burns, K. Finlayson, P. A. Greet, R. P. Lowe, and P. F. B. Williams (2000), Hydroxyl (6-2) airglow emission intensity ratios for rotational temperature determination, *Ann. Geophys.*, *18*(10), 1293-1303.

Fuller-Rowell, T. J. (1995), *The Dynamics of the Lower Thermosphere*, pp. 23-+.

Funke, B. (2000), Line mixing, in *The Karlsruhe Optimized and Precise Radiative transfer Algorithm (KOPRA)*, edited by G. P. Stiller, Wissenschaftliche Berichte FZKA 6487, pp. 69-75, Forschungszentrum Karlsruhe.

Funke, B., and M. López-Puertas (2000), Nonlocal thermodynamic equilibrium vibrational, rotational, and spin state distribution of NO($\nu$= 0,1,2) under quiescent atmospheric conditions, *J. Geophys. Res.*, *105*(D4), 4409-4426.

Funke, B., M. López-Puertas, G. P. Stiller, T. von Clarmann, and M. Höpfner (2001), A new non-LTE retrieval method for atmospheric parameters from MIPAS-ENVISAT emission spectra, *Adv. Space Res.*, *27*(6-7), 1099-1104.

Funke, B., M. López-Puertas, S. Gil-López, T. von Clarmann, G. P. Stiller, H. Fischer, and S. Kellmann (2005a), Downward transport of upper atmospheric $NO_x$ into the polar stratosphere and lower mesosphere during the Antarctic 2003 and Arctic 2002/2003 winters, *J. Geophys. Res.*, *110*, D24308, doi:10.1029/2005JD006463.

Funke, B., et al. (2005b), Retrieval of stratospheric $NO_x$ from 5.3 and 6.2 $\mu$m nonlocal thermodynamic equilibrium emissions measured by Michelson Interferometer for Passive Atmospheric Sounding (MIPAS) on Envisat, *J. Geophys. Res.*, *110*(D9), D09302, doi:10.1029/2004JD005225.

Funke, B., M. López-Puertas, , D. Bermejo-Pantaleón, T. von Clarmann, G. P. Stiller, M. Höpfner, U. Grabowski, and M. Kaufmann (2007), Analysis of nonlocal thermodynamic equilibrium CO 4.7 $\mu$m fundamental, isotopic and hot band emissions measured by the Michelson Interferometer for Passive Atmospheric Sounding on Envisat, *J. Geophys. Res.*, *112*(D11), D11305, doi:10.1029/2006JD007933.

Funke, B., M. García-Comas, M. López-Puertas, N. Glatthor, G. P. Stiller, T. von Clarmann, K. Semeniuk, and J. C. McConnell (2008a), Enhancement of $N_2O$ during the October-November 2003 solar proton events, *Atmos. Chem. Phys.*, *8*, 3805-3815.

Funke, B., M. López-Puertas, M. García-Comas, G. P. Stiller, T. von Clarmann, and N. Glatthor (2008b), Mesospheric $N_2O$ enhancements as observed by MIPAS on Envisat during the polar winters in 2002-2004, *Atmos. Chem. Phys.*, *8*, 5787 - 5800.

Funke, B., et al. (2009), Carbon monoxide distributions from the upper troposphere to the mesosphere inferred from 4.7 $\mu$m non-local thermal equilibrium emissions measured by MIPAS on Envisat, *Atmos. Chem. Phys.*, *9*(7), 2387-2411.

Funke, B., M. López-Puertas, D. Bermejo-Pantaleón, M. García-Comas, G. P. Stiller, T. von Clarmann, M. Kiefer, and A. Linden (2010), Evidence for dynamical coupling from the lower atmosphere to the thermosphere during a major stratospheric warming, *Geophys. Res. Lett.*, *37*, 13,803-+, doi:10.1029/2010GL043619.

Funke, B., et al. (2011), Composition changes after the "Halloween" solar proton event: the High-Energy Particle Precipitation in the Atmosphere (HEPPA) model versus MIPAS data intercomparison study, *Atmos. Chem. Phys. Discuss.*, *11*(3), 9407-9514, doi:10.5194/acpd-11-9407-2011.

Garcia, R. R. (1983), A numerical model of the zonally averaged dynamical and chemical structure of the middle atmosphere, *J. Geophys. Res.*, *88*(C2), 1379-1400.

Garcia, R. R., D. R. Marsh, D. E. Kinnison, B. A. Boville, and F. Sassi (2007), Simulation of secular trends in the middle atmosphere, *J. Geophys. Res.*, *112*, D09301, doi:10.1029/2006JD007485.

García-Comas, M., et al. (2008), Errors in SABER kinetic temperature caused by non-LTE model parameters, *J. Geophys. Res.*, *113*, D24106, doi:10.1029/2008JD010105.

García-Comas, M., M. Lopez-Puertas, B. Funke, D. Bermejo-Pantaleón, G. Stiller, U. Grabowski, and T. von Clarmann (2010), MIPAS middle atmosphere water vapor distributions, in *38th COSPAR Scientific Assembly*, *COSPAR, Plenary Meeting*, vol. 38, pp. 88-+.

García-Comas, M., et al. (2011), On the Quality of MIPAS Kinetic Temperature in the Middle Atmosphere, *Atmos. Chem. Phys. Discuss.*, *11*, 24,233-24,312, doi:10.5194/acpd-11-24233-2011.

Gardner, J. L., M. López-Puertas, B. Funke, S. M. Miller, S. J. Lipson, and R. D. Sharma (2005), Rotational and spin-orbit distributions of NO observed by MIPAS/ENVISAT during the solar storm of October/November 2003, *J. Geophys. Res.*, *110*, A09S34, doi:10.1029/2004JA010937.

Gardner, J. L., B. Funke, M. G. Mlynczak, M. López-Puertas, F. J. Martin-Torres, J. M. R. III, S. M. Miller, R. D. Sharma, and J. R. Winick (2007), Comparison of nighttime nitric oxide 5.3 $\mu$m emissions in the thermosphere measured by MIPAS and SABER, *J. Geophys. Res.*, *112*, A10301, doi:10.1029/2006JA011984.

Gerard, J.-C., and C. A. Barth (1977), High-latitude nitric oxide in the lower thermosphere, *J. Geophys. Res.*, *82*, 674-680, doi:10.1029/JA082i004p00674.

Gérard, J.-C., V. I. Shematovich, and J. W. Duff (1997), An updated model of the hot nitrogen atom kinetics and thermospheric nitric oxide, *J. Geophys. Res.*, *102*, 285-294.

Gil-López, S., et al. (2005), Retrieval of stratospheric and mesospheric $O_3$ from high resolution MIPAS spectra at 15 and 10 $\mu$m, *Adv. Space Res.*, *36*(5), 943-951, doi:10.1016/j.asr.2005.05.123.

Glatthor, N., et al. (2004), Spaceborne ClO observations by the Michelson Interferometer for Passive Atmospheric Sounding (MIPAS) before and during the Antarctic major warming in September/October 2002, *J. Geophys. Res.*, *109*, D11307, doi:10.1029/2003JD004440.

Glatthor, N., et al. (2005), Mixing processes during the Antarctic vortex split in September/October 2002 as inferred from source gas and ozone distributions from ENVISAT-MIPAS, *J. Atmos. Sci.*, *62*(3), 787-800.

Glatthor, N., et al. (2007), Global peroxyacetyl nitrate (PAN) retrieval in the upper troposphere from limb emission spectra of the Michelson Interferometer for Passive Atmospheric Sounding MIPAS, *Atmos. Chem. Phys.*, *7*, 2775-2787.

Glatthor, N., et al. (2009), Large-scale upper tropospheric pollution observed by mipas hcn and $c_2h_6$ global distributions, *Atmospheric Chemistry and Physics*, *9*(24), 9619-9634.

Godson, W. L. (1953), The evaluation of infra-red radiative fluxes due to atmospheric water vapour, *Q. J. R. Meteorol. Soc.*, *79*, 367-379.

Goncharenko, L., and S.-R. Zhang (2008), Ionospheric signatures of sudden stratospheric warming: Ion temperature at middle latitude, *Geophys. Res. Lett.*, *35*, L21103, doi:10.1029/2008GL035684.

Griffin, E. M., A. L. Aruliah, I. McWhirter, H. Yiu, A. Charalambous, and I. McCrea (2008), Upper thermospheric neutral wind and temperature measurements from an extended spatial field, *Annales Geophysicae*, *26*, 2649-2655.

Hagan, M., and J. Forbes (2002), Migrating and nonmigrating diurnal tides in the middle and upper atmosphere excited by tropospheric latent heat release, *J. Geophys. Res.*, *107*(D24), 4754.

Hase, F., P. Demoulin, A. J. Sauval, G. C. Toon, P. F. Bernath, A. Goldman, J. W. Hannigan, and C. P. Rinsland (2006), An empirical line-by-line model for the infrared solar transmittance spectrum from 700 to 5000 $cm^{-1}$, *J. Quant. Spectrosc. Radiat. Transfer*, *102*(3), 450-463, doi:10.1016/j.jqsrt.2006.02.026.

Hervig, M., M. McHugh, and M. E. Summers (2003), Water vapor enhancement in the polar summer mesosphere and its relationship to polar mesospheric clouds, *Geophys. Res. Lett.*, *30*(20), 2041, doi:10.1029/2003GL018089.

Holt, J. M., and S. R. Zhang (2008), Long-term temperature trends in the ionosphere above Millstone Hill, *Geophys. Res. Lett.*, *35*, L05,813, doi:10.1029/2007GL031148.

Höpfner, M., et al. (2004), First spaceborne observations of Antarctic stratospheric $ClONO_2$ recovery: Austral spring 2002, *J. Geophys. Res.*, *109*(D11), D11308, doi:10.1029/2004JD004609.

Höpfner, M., et al. (2006a), MIPAS detects Antarctic stratospheric belt of NAT PSC's caused by mountain waves, *Atmos. Chem. Phys.*, *6*, 1221-1230.

Höpfner, M., et al. (2006b), Spectroscopic evidence for $\beta$-NAT, STS, and ice in MIPAS infrared limb emission measurements of polar stratospheric clouds, *Atmos. Chem. Phys.*, *6*, 1201-1219.

Höpfner, M., J. Orphal, T. von Clarmann, G. Stiller, and H. Fischer (2009a), Stratospheric $BrONO_2$ observed by MIPAS, *Atmos. Chem. Phys.*, *9*, 1735-1746.

Höpfner, M., M. C. Pitts, and L. R. Poole (2009b), Comparison between CALIPSO and MIPAS observations of polar stratospheric clouds, *J. Geophys. Res.*, *114*, D00H05, doi:10.1029/2009JD012114.

Houghton, J. T. (1986), *The Physics of Atmospheres*, second ed., Cambridge University Press, Cambridge.

Kaye, J. A., and J. B. Kumer (1987), Nonlocal thermodynamic equilibrium effects in stratospheric NO and implications for infrared remote sensing, *Appl. Opt.*, *26*(22), 4747-4754.

Keckhut, P., et al. (2004), Review of ozone and temperature lidar validations performed within the framework of the Network for the Detection of Stratospheric Change, *J. Environ. Monit.*, *6*(9), 721-733, doi:{10.1039/b404256e}.

Kiefer, M., T. von Clarmann, U. Grabowski, M. De Laurentis, R. Mantovani, M. Milz, and M. Ridolfi (2007), Characterization of MIPAS elevation pointing, *Atmos. Chem. Phys.*, *7*, 1615-1628.

Kiefer, M., et al. (2010), Impact of temperature field inhomogeneities on the retrieval of atmospheric species from mipas ir limb emission spectra, *Atmos. Meas. Tech.*, *3*(5), 1487-1507, doi:10.5194/amt-3-1487-2010.

Kleinert, A., G. Aubertin, G. Perron, M. Birk, G. Wagner, F. Hase, H. Nett, and R. Poulin (2007), MIPAS Level 1B algorithms overview: operational processing and characterization, *Atmos. Chem. Phys.*, *7*, 1395-1406.

Kockarts, G. (1980), Nitric oxide cooling in the terrestrial thermosphere, *Geophys. Res. Lett.*, *7*(2), 137-140.

Kurihara, J., et al. (2006), Observations of the lower thermospheric neutral temperature and density in the DELTA campaign, *Earth Planets Space*, *58*, 1123-1130.

Kurihara, J., Y. Ogawa, S. Oyama, S. Nozawa, M. Tsutsumi, Y. Tomikawa, and R. Fujii (2010), Links between a stratospheric sudden warming and thermal structures and dynamics in the high-latitude mesosphere, lower thermosphere, and ionosphere, *Geophys. Res. Lett.*, *37*, L13806, doi:10.1029/2010GL043643.

Kutepov, A. A., D. Kunze, D. G. Hummer, and G. B. Rybicki (1991), The solution of radiative transfer problems in molecular bands without the LTE assumption by accelerated lambda iteration methods, *J. Quant. Spectrosc. Radiat. Transfer*, *46*(5), 347-366.

Kutepov, A. A., A. G. Feofilov, B. T. Marshall, L. L. Gordley, W. D. Pesnell, R. A. Goldberg, and J. M. Russell III (2006), SABER temperature observations in the summer polar mesosphere and lower thermosphere: Importance of accounting for the $CO_2$ $\nu_2$ quanta V-V exchange, *Geophys. Res. Lett.*, *33*, L21809, doi:10.1029/2006GL026591.

Laštovička, J. (2005), On the role of solar and geomagnetic activity in long-term trends in the atmosphere ionosphere system, *Journal of Atmospheric and Solar-Terrestrial Physics*, *67*, 83-92, doi:10.1016/j.jastp.2004.07.019.

Laštovička, J., and J. Bremer (2004), An Overview of Long-Term Trends in the Lower Ionosphere Below 120 km, *Surveys in Geophysics*, *25*, 69-99, doi:10.1023/B:GEOP.0000015388.75164.e2.

Laštovička, J., R. A. Akmaev, G. Beig, J. Bremer, and J. T. Emmert (2006), Global change in the upper atmosphere, *Science*, *314*(5803), 1253-1254, doi:10.1126/science.1135134.

Leblanc, T., I. S. McDermid, P. Keckhut, A. Hauchecorne, C. Y. She, and D. A. Krueger (1998), Temperature climatology of the middle atmosphere from long-term lidar measurements at middle and low latitudes, *J. Geophys. Res.*, *103*(D14), 17,191-17,204.

Levenberg, K. (1944), A method for the solution of certain non-linear problems in least squares, *Quart. Appl. Math.*, *2*, 164-168.

Lipson, S. J., P. S. Armstrong, J. A. Dodd, J. R. Lowell, and A. M. Blumberg (1994), Subthermal nitric oxide spin-orbit distributions in the thermosphere, *Geophys. Res. Lett.*, *21*(22), 2421-2424.

Liu, H.-L., and R. G. Roble (2002), A study of a self-generated stratospheric sudden warming and its mesospheric-lower thermospheric impacts using the coupled TIME-GCM/CCM3, *J. Geophys. Res.*, *107*(D23), 4695, doi:10.1029/2001JD001533.

López-González, M. J., E. Rodríguez, G. G. Shepherd, S. Sargoytchev, M. G. Shepherd, V. M. Aushev, S. Brown, M. García-Comas, and R. H. Wiens (2005), Tidal variations of $O_2$ Atmospheric and OH(6-2) airglow and temperature at mid-latitudes from SATI observations, *Annales Geophysicae*, *23*, 3579-3590, doi:10.5194/angeo-23-3579-2005.

López-González, M. J., et al. (2007), Ground-based mesospheric temperatures at mid-latitude derived from $o_2$ and oh airglow sati data: Comparison with saber measurements, *Journal of Atmospheric and Solar-Terrestrial Physics*, *69*, 2379-2390, doi:10.1016/j.jastp.2007.07.004.

López-Puertas, M., and F. W. Taylor (2001), *Non-LTE radiative transfer in the Atmosphere*, World Scientific Pub., Singapore.

López-Puertas, M., R. Rodrigo, J. J. López-Moreno, and F. W. Taylor (1986a), A non-LTE radiative transfer model for infrared bands in the middle atmosphere. II. $CO_2$ (2.7 and 4.3 $\mu$m) and water vapour (6.3 $\mu$m) bands and $N_2(1)$ and $O_2(1)$ vibrational levels, *J. Atmos. Terr. Phys.*, *48*(8), 749-764.

López-Puertas, M., R. Rodrigo, A. Molina, and F. W. Taylor (1986b), A non-LTE radiative transfer model for infrared bands in the middle atmosphere. I. Theoretical basis and application to $CO_2$ 15 $\mu$m bands, *J. Atmos. Terr. Phys.*, *48*(8), 729-748.

López-Puertas, M., G. Zaragoza, M. Á. López-Valverde, and F. W. Taylor (1998a), Non local thermodynamic equilibrium (LTE) atmospheric limb emission at 4.6 $\mu$m 1. An update of the $CO_2$ non-LTE radiative transfer model, *J. Geophys. Res.*, *103*(D7), 8499-8513.

López-Puertas, M., G. Zaragoza, M. Á. López-Valverde, and F. W. Taylor (1998b), Non local thermodynamic equilibrium (LTE) atmospheric limb emission at 4.6 $\mu$m 2. An analysis of the daytime wideband radiances as measured by UARS improved stratospheric and mesospheric sounder, *J. Geophys. Res.*, *103*(D7), 8515-8530.

López-Puertas, M., M. Á. López-Valverde, R. R. Garcia, and R. G. Roble (2000), A review of $CO_2$ and CO abundances in the middle atmosphere, in *Atmospheric Science Across the Stratopause*, *Geophysical Monograph Series*, vol. 123, edited by D. E. Siskind, S. D. Eckermann, and M. E. Summers, p. 83, American Geophysical Union.

López-Puertas, M., et al. (2004), Evidence for an OH($\upsilon$) excitation mechanism of $CO_2$ 4.3 $\mu$m nighttime emission from SABER/TIMED measurements, *J. Geophys. Res.*, *109*, D09307, doi:10.1029/2003JD004383.

López-Puertas, M., B. Funke, S. Gil-López, T. von Clarmann, G. P. Stiller, M. Höpfner, S. Kellmann, H. Fischer, and C. H. Jackman (2005a), Observation of $NO_x$ enhancement and ozone depletion in the northern and southern hemispheres after the October-November 2003 solar proton events, *J. Geophys. Res.*, *110*(A9), A09S43, doi:10.1029/2005JA011050.

López-Puertas, M., et al. (2005b), $HNO_3$, $N_2O_5$ and $ClONO_2$ enhancements after the October-November 2003 solar proton events, *J. Geophys. Res.*, *110*(A9), A09S44, doi:10.1029/2005JA011051.

López-Puertas, M., et al. (2005c), Atmospheric non-local thermodynamic equilibrium emissions as observed by the Michelson Interferometer for Passive Atmospheric Sounding (MIPAS), *Comptes Rendus Physique*, *6*(8), 848-863, doi:10.1016/j.crhy.2005.07.012.

López-Puertas, M., M. E. Koukouli, B. Funke, S. Gil-López, N. Glatthor, U. Grabowski, T. von Clarmann, and G. P. Stiller (2005d), Evidence for $CH_4$ 7.6 $\mu$m non-local thermodynamic equilibrium emission in the mesosphere, *Geophys. Res. Lett.*, *32*, L04805, doi:10.1029/2004GL021641.

López-Puertas, M., B. Funke, T. von Clarmann, H. Fischer, and G. P. Stiller (2007a), The stratospheric and mesospheric $NO_y$ in the 2002-2004 polar winters as measured by MIPAS/ENVISAT, *Space Sci. Rev.*, *125*, 403-416, doi:10.1007/s11214-006-9073-2.

López-Puertas, M., B. Funke, D. Bermejo-Pantaleón, T. von Clarmann, G. P. Stiller, U. Grabowski, and M. Höpfner (2007b), Evidence for $N_2O$ $\nu_3$ 4.5 $\mu$m non-local thermodynamic equilibrium emission in the atmosphere, *Geophys. Res. Lett.*, *34*(2), L02825, doi:10.1029/2006GL028539.

López-Puertas, M., B. Funke, García-Comas, D. Bermejo-Pantaleón, M. Kaufmann, and A. Dudhia (2009a), Extension of the Reference atmospheres and Vibrational Temperatures (WP9220). Support to MIPAS

Level 2 product validation (MIPAS L2), *Report ESA ESRIN contract no 21719/08/i-ol*, European Space Agency.

López-Puertas, M., M. García-Comas, B. Funke, D. Bermejo-Pantaleón, M. Höpfner, U. Grabowski, G. P. Stiller, T. von Clarmann, and C. von Savigny (2009b), Measurements of polar mesospheric clouds in infrared emission by MIPAS/ENVISAT, *J. Geophys. Res.*, *114*, D00I07, doi: 10.1029/2009JD012548.

López-Valverde, M. Á., M. López-Puertas, J. J. Remedios, C. D. Rodgers, F. W. Taylor, E. C. Zipf, and P. W. Erdman (1996), Validation of measurements of carbon monoxide from the improved stratospheric and mesospheric sounder, *J. Geophys. Res.*, *101*(D6), 9929-9955, doi: 10.1029/95JD01715.

Lübken, F.-J. (1999), Thermal structure of the arctic summer mesosphere, *J. Geophys. Res.*, *104*, 9135-9150, doi:10.1029/1999JD900076.

Maeda, S., S. Nozawa, M. Sugino, H. Fujiwara, and M. Suzuki (2002), Ion and neutral temperature distributions in the E-region observed by the EISCAT Tromsøand Svalbard radars, *Annales Geophysicae*, *20*, 1415-1427.

Marcos, F. A., J. O. Wise, M. J. Kendra, N. J. Grossbard, and B. R. Bowman (2005), Detection of a long-term decrease in thermospheric neutral density, *Geophys. Res. Lett.*, *32*, L04,103, doi:10.1029/2004GL021269.

Marquardt, D. W. (1963), An algorithm for least-squares estimation of nonlinear parameters, *J. Soc. Indust. Appl. Math.*, *11*(2), 431-441.

Marsh, D. R., S. C. Solomon, and A. E. Reynolds (2004), Empirical model of nitric oxide in the lower thermosphere, *Journal of Geophysical Research (Space Physics)*, *109*, 7301-+, doi:10.1029/2003JA010199.

Matsuno, T. (1971), A Dynamical Model of the Stratospheric Sudden Warming., *Journal of Atmospheric Sciences*, *28*, 1479-1494, doi:10.1175/1520-0469(1971)028<1479:ADMOTS>2.0.CO;2.

McDermid, I. S., T. D. Walsh, A. Deslis, and M. L. White (1995), Optical systems design for a stratospheric Lidar, *Appl. Opt.*, *34*, 6201-6210.

Mengistu Tsidu, G., et al. (2004), Stratospheric $N_2O_5$ in the austral spring 2002 as retrieved from limb emission spectra recorded by the Michelson Interferometer for Passive Atmospheric Sounding (MIPAS), *J. Geophys. Res.*, *109*, D18301, doi:10.1029/2004JD004856.

Mengistu Tsidu, G., et al. (2005), $NO_y$ from Michelson Interferometer for Passive Atmospheric Sounding on Environmental Satellite during the southern hemisphere polar vortex split in September/October 2002, *J. Geophys. Res.*, *110*(D11), D11301, doi:10.1029/2004JD005322.

Meriwether, J. W., and A. J. Gerrard (2004), Mesosphere inversion layers and stratosphere temperature enhancements, *Reviews of Geophysics*, *42*, RG3003, doi:10.1029/2003RG000133.

Milz, M., et al. (2005), Water vapor distributions measured with the Michelson Interferometer for Passive Atmospheric Sounding on board Envisat (MIPAS/Envisat), *J. Geophys. Res.*, *110*, D24307, doi:10.1029/2005JD005973.

Mlynczak, M., et al. (2010), Observations of infrared radiative cooling in the thermosphere on daily to multiyear timescales from the TIMED/SABER instrument, *J. Geophys. Res.*, *115*(A3), A03309, doi:10.1029/2009JA014713.

Moore, D. P., J. J. Remedios, and A. M. Waterfall (2010), Global distributions of acetone in the upper troposphere from MIPAS-E spectra, *Atmospheric Chemistry & Physics Discussions*, *10*, 23,539-23,557, doi:10.5194/acpd-10-23539-2010.

Müller-Wodarg, I. C. F., A. D. Aylward, and T. J. Fuller-Rowell (2001), Tidal oscillations in the thermosphere: a theoretical investigation of their sources, *Journal of Atmospheric and Solar-Terrestrial Physics*, *63*, 899-914, doi:10.1016/S1364-6826(00)00202-9.

Nett, H., G. Perron, M. Sanchez, A. Burgess, and P. Mosner (2002), MIPAS in-flight calibration and processor verification, in *ENVISAT Calibration Review - Proc. of the European Workshop, 9 - 13 September 2002, ESTEC, Noordwijk, The Netherlands, CD-ROM*, vol. SP-520, edited by H. Sawaya-Lacoste, ESA Publications Division, ESTEC, Postbus 299, 2200 AG Noordwijk, The Netherlands.

Newell, P. T., K. M. Lyons, and C. Meng (1996), A large survey of electron acceleration events, *J. Geophys. Res.*, *101*, 2599-2614, doi:10.1029/95JA03147.

Newell, P. T., R. A. Greenwald, and J. Michael Ruohoniemi (2001), The role of the ionosphere in aurora and space weather, *Reviews of Geophysics*, *39*, 137-150, doi:10.1029/1999RG000077.

Niro, F. (2011), Mipas mission plan, *ESA Technical Note ENVI-SPPA-EOPG-TN-11-0006*, (Issue 1, Version 0).

Nozawa, S., Y. Ogawa, A. Brekke, T. Tsuda, C. M. Hall, H. Miyaoka, J. Kurihara, T. Abe, and R. Fujii (2006), EISCAT observational results during the DELTA campaign, *Earth, Planets, and Space*, *58*, 1183-1191.

Oelhaf, H. (2008), Mipas mission plan, *ESA Technical Note ENVI-SPPA-EOPG-TN-07-0073*, (Issue 4, Version 3).

Payan, S., et al. (2009), Validation of version-4.61 methane and nitrous oxide observed by MIPAS, *Atmos. Chem. Phys.*, *9*, 413-442.

Pellegrini, A. (2003), Envisat-1 products specifications, *PO-RS-MDA-GS-2009, ESA*, (Volume 12 of MIPAS products specifications).

Picone, J., A. Hedin, D. Drob, and A. Aikin (2002), NRLMSISE-00 empirical model of the atmosphere: Statistical comparisons and scientific issues, *J. Geophys. Res.*, *107*(A12), 1468, doi:10.1029/2002JA009,430.

QWG, M. (2004), Envisat mipas monthly report, *ESA Technical Note ENVI-SPPA-EOPG-TN-04-0011*, (Issue 1).

Randel, W., et al. (2004), The sparc intercomparison of middle-atmosphere climatologies, *Journal of Climate*, *17*(5), 986-1003, doi:10.1175/1520-0442(2004)017<0986:TSIOMC>2.0.CO;2.

Raspollini, P., et al. (2006), MIPAS level 2 operational analysis, *Atmos. Chem. Phys.*, *6*, 5605-5630.

Rees, M. H. (1989), *Physics and Chemistry of the Upper Atmosphere*, Cambridge University Press.

Rees, M. H., K. Stamnes, B. A. Emery, and R. G. Roble (1983), Neutral and ion gas heating by auroral electron precipitation, *J. Geophys. Res.*, *88*, 6289-6300, doi:10.1029/JA088iA08p06289.

Remedios, J. J., R. J. Leigh, A. M. Waterfall, D. P. Moore, H. Sembhi, I. Parkes, J. Greenhough, M. P. Chipperfield, and D. Hauglustaine (2007), MIPAS reference atmospheres and comparisons to V4.61/V4.62 MIPAS level 2 geophysical data sets, *Atmos. Chem. Phys. Discuss.*, *7*, 9973-10,017.

Remsberg, E. E. (2008), On the response of Halogen Occultation Experiment (HALOE) stratospheric ozone and temperature to the 11-year solar cycle forcing, *J. Geophys. Res.*, *113*, D22304, doi:10.1029/2008JD010189.

Remsberg, E. E., et al. (2008), Assessment of the quality of the Version 1.07 temperature-versus-pressure profiles of the middle atmosphere from TIMED/SABER, *J. Geophys. Res.*, *113*, D17101, doi:10.1029/2008JD010013.

Richmond, A. (1992), Assimilative mapping of ionospheric electrodynamics, *Adv. Space Res.*, *12*(6), 59-68, doi:doi:10.1016/0273-1177(92)90040-5.

Ridolfi, M., et al. (2000), Optimized forward and retrieval scheme for MIPAS near-real-time data processing, *Appl. Opt.*, *39*(8), 1323-1340.

Rishbeth, H. (1990), A greenhouse effect in the ionosphere?, *Planetary and Space Science*, *38*, 945-948, doi:10.1016/0032-0633(90)90061-T.

Rishbeth, H., and R. G. Roble (1992), Cooling of the upper atmosphere by enhanced greenhouse gases - Modelling of thermospheric and ionospheric effects, *Planetary and Space Science*, *40*, 1011-1026, doi: 10.1016/0032-0633(92)90141-A.

Roble, R. G. (1995), Energetics of the mesosphere and thermosphere, *Geophys. Monograph*, *87*, 1-21.

Roble, R. G., and R. E. Dickinson (1989), How will changes in carbon dioxide and methane modify the mean structure of the mesosphere and thermosphere?, *Geophys. Res. Lett.*, *16*, 1441-1444.

Roble, R. G., E. C. Ridley, and R. E. Dickinson (1987), On the global mean structure of the thermosphere, *J. Geophys. Res.*, *92*(A18), 8745-8758.

Roble, R. G., J. M. Forbes, and F. A. Marcos (1987), Thermospheric dynamics during the March 22, 1979, magnetic storm. I - Model simulations. II - Comparisons of model predictions with observations, *J. Geophys. Res.*, *92*, 6045-6081, doi:10.1029/JA092iA06p06045.

Rodgers, C. D. (2000), *Inverse Methods for Atmospheric Sounding: Theory and Practice*, *Series on Atmospheric, Oceanic and Planetary Physics, F. W. Taylor, ed.*, vol. 2, World Scientific.

Rodgers, C. D., and B. J. Connor (2003), Intercomparison of remote sounding instruments, *J. Geophys. Res.*, *108*(D3), 4116, doi:10.1029/2002JD002299.

Rothman, L. S., et al. (2005), The hitran 2004 molecular spectroscopic database, *J. Quant. Spectrosc. Radiat. Transfer*, *96*, 139-204.

Rusch, D. W., and C. A. Barth (1975), Satellite measurements of nitric oxide in the polar region, *J. Geophys. Res.*, *80*, 3719, doi:10.1029/JA080i025p03719.

Rusch, D. W., J.-C. Gérard, and C. G. Fesen (1991), The diurnal variation of NO, N($^2$D), and ions in the thermosphere: A comparison of satellite measurements to a model, *J. Geophys. Res.*, *96*, 11,331-11,339.

Russell III, J. M., C. Farmer, C. Rinsland, R. Zander, L. Froidevaux, G. Toon, B. Gao, J. Shaw, and M. Gunson (1988), Measurements of odd nitrogen compounds in the stratosphere by the ATMOS experiment on spacelab 3, *J. Geophys. Res.*, *93*(D2), 1718-1736.

Russell III, J. M., et al. (1993), The halogen occultation experiment, *J. Geophys. Res.*, *98*, 10,777-10,797.

Russell III, J. M., M. G. Mlynczak, L. L. Gordley, J. Tansock, and R. Esplin (1999), An overview of the SABER experiment and preliminary calibration results, pp. 277-288.

Rybicki, G. B., and D. G. Hummer (1991), An accelerated lambda iteration method for multilevel radiative transfer. I - Non-overlapping lines with background continuum, *Astron. Astrophys*, *245*, 171-181.

Sargoytchev, S. I., S. Brown, B. H. Solheim, Y.-M. Cho, G. G. Shepherd, and M. J. López-González (2004), Spectral airglow temperature imager (SATI): a ground-based instrument for the monitoring of mesosphere temperature, *Appl. Opt.*, *43*(30), 5712-5721.

Schwartz, M. J., et al. (2008), Validation of the Aura Microwave Limb Sounder temperature and geopotential height measurements, *Journal of Geophysical Research (Atmospheres)*, *113*(D12), 15-+, doi:10.1029/2007JD008783.

Semenov, A. I. (1996), Lower thermosphere temperature regime from the emision measurements during three recent decades, *Geomagn. Aeron.*, *36*(5), 60-65.

Sharma, R. D., and J. W. Duff (1997), Determination of translational temperature of the high altitude terrestrial thermosphere from the rotational distribution of the 5.3 $\mu$m emission from NO($\nu = 1$), *Geophys. Res. Lett.*, *24*(19), 2407-2410.

Sharma, R. D., and P. P. Wintersteiner (1990), Role of carbon dioxide in cooling planetary thermospheres, *Geophys. Res. Lett.*, *17*(12), 2201-2204.

Sharma, R. D., H. Doethe, and F. von Esse (1996a), On the rotational distribution of the 5.3 $\mu$m "thermal" emission from nitric oxide in the night time terrestrial atmosphere, *J. Geophys. Res.*, *101*(A8), 17,129-17,135.

Sharma, R. D., H. Doethe, F. von Esse, V. A. Kharchenko, Y.Sun, and A. Dalgarno (1996b), Production of vibrationally and rotationally excited NO in the night time terrestrial atmosphere, *J. Geophys. Res.*, *101*(A9), 19,707-19,713.

Sharma, R. D., H. Doethe, and J. W. Duff (1998), Model of the 5.3 $\mu$m radiance from NO during the sunlit terrestrial thermosphere, *J. Geophys. Res.*, *103*, 14,753-14,768.

Sica, R. J., et al. (2008), Validation of the atmospheric chemistry experiment (ace) version 2.2 temperature using ground-based and space-borne measurements, *Atmospheric Chemistry & Physics*, *8*, 35-62.

Siskind, D., C. A. Barth, and R. Roble (1989a), The response of the thermospheric nitric oxide to an auroral storm. i - low and middle latitudes, *J. Geophys. Res.*, *94*(A12), 16,885-16,898, doi:doi:10.1029/JA094iA12p16885.

Siskind, D., C. A. Barth, D. Evans, and R. Roble (1989b), The response of thermospheric nitric oxide to an auroral storm. ii - auroral latitudes, *J. Geophys. Res.*, *94*, 16,899-16,911, doi:doi:10.1029/JA094iA12p16899.

Siskind, D. E., C. A. Barth, and D. D. Cleary (1990), The possible effect of solar soft X rays on thermospheric nitric oxide, *J. Geophys. Res.*, *95*, 4311-4317.

Siskind, D. E., C. A. Barth, and J. M. Russell III (1998), A climatology of nitric oxide in the mesosphere and thermosphere, *Adv. Space Res.*, *21*(10), 1353-1362.

Siskind, D. E., S. D. Eckermann, J. P. McCormack, M. J. Alexander, and J. T. Bacmeister (2003), Hemispheric differences in the temperature of the summertime stratosphere and mesosphere, *Journal of Geophysical Research (Atmospheres)*, *108*, 4051, doi:10.1029/2002JD002095.

Siskind, D. E., L. Coy, and P. Espy (2005), Observations of stratospheric warmings and mesospheric coolings by the TIMED SABER instrument, *Geophys. Res. Lett.*, *32*, L09804, doi:10.1029/2005GL022399.

Smith, A. K., and D. R. Marsh (2005), Processes that account for the ozone maximum at the mesopause, *J. Geophys. Res.*, *110*, D23305, doi:10.1029/2005JD006298.

Solomon, S., P. J. Crutzen, and R. G. Roble (1982), Photochemical coupling of the thermosphere and the lower atmosphere 1. odd nitrogen from 50 to 120 km, *J. Geophys. Res.*, *87*, 7206-7220.

Solomon, S. C., T. N. Woods, L. V. Didkovsky, J. T. Emmert, and L. Qian (2010), Anomalously low solar extreme-ultraviolet irradiance and thermospheric density during solar minimum, *Geophys. Res. Lett.*, *37*, L16,103, doi:10.1029/2010GL044468.

Spang, R., J. J. Remedios, L. J. Kramer, L. R. Poole, M. D. Fromm, M. Müller, G. Baumgarten, and P. Konopka (2005a), Polar stratospheric cloud observations by MIPAS on ENVISAT: detection method, validation and analysis of the northern hemisphere winter 2002/2003, *Atmos. Chem. Phys.*, *5*, 679-692.

Spang, R., J. J. Remedios, S. Tilmes, and M. Riese (2005b), MIPAS observation of polar stratospheric clouds in the Arctic 2002/2003 and Antarctic 2003 winters, *Adv. Space Res.*, *36*(5), 868-878, doi:10.1016/j.asr.2005.03.092.

Steck, T. (2002), Methods for determining regularization for atmospheric retrieval problems, *Appl. Opt.*, *41*(9), 1788-1797.

Steck, T., et al. (2008), Retrieval of global upper tropospheric and stratospheric formaldehyde ($H_2CO$) distributions from high-resolution MIPAS-Envisat spectra, *Atmospheric Chemistry & Physics*, *8*, 463-470.

Stiller, G. P. (Ed.) (2000), *The Karlsruhe Optimized and Precise Radiative Transfer Algorithm (KOPRA)*, *Wissenschaftliche Berichte*, vol. FZKA 6487, Forschungszentrum Karlsruhe.

Stiller, G. P., et al. (2005), An enhanced $HNO_3$ second maximum in the Antarctic mid-winter upper stratosphere 2003, *J. Geophys. Res.*, *110*(D20), D20303, doi:10.1029/2005JD006011.

Stiller, G. P., et al. (2007), Global distributions of $HO_2NO_2$ as observed by the Michelson Interferometer for Passive Atmospheric Sounding (MIPAS), *J. Geophys. Res.*, *112*, D09314, doi:10.1029/2006JD007212.

Stiller, G. P., et al. (2008), Global distribution of mean age of stratospheric air from mipas $sf_6$ measurements, *Atmospheric Chemistry and Physics*, *8*(3), 677-695, doi:10.5194/acp-8-677-2008.

Taylor, F. W., et al. (1993), Remote sensing of atmospheric structure and composition by pressure modulator radiometry from space: The ISAMS experiment on UARS, *J. Geophys. Res.*, *98*(D6), 10,799-10,814.

Tikhonov, A. (1963), On the solution of incorrectly stated problems and method of regularization, *Dokl. Akad. Nauk. SSSR*, *151*(3), 501-504.

Tobiska, W. K., T. Woods, F. Eparvier, R. Viereck, L. Floyd, D. Bouwer, G. Rottman, and O. R. White (2000), The SOLAR2000 empirical solar irradiance model and forecast tool, *J. Atmos. Solar-Terr. Phys.*, *62*, 1233-1250.

Vincent, R. A. (1994), Gravity-wave motions in the mesosphere and lower thermosphere observed at Mawson, Antarctica, *Journal of Atmospheric and Terrestrial Physics*, *56*, 593-602.

von Clarmann, T., and G. Echle (1998), Selection of optimized microwindows for atmospheric spectroscopy, *Appl. Opt.*, *37*(33), 7661-7669.

von Clarmann, T., et al. (2002), Intercomparison of radiative transfer codes under non-local thermodynamic equilibrium conditions, *J. Geophys. Res.*, *107*(D22), 4631, doi:10.1029/2001JD001551.

von Clarmann, T., et al. (2003a), Retrieval of temperature and tangent altitude pointing from limb emission spectra recorded from space by the Michelson Interferometer for Passive Atmospheric Sounding (MIPAS), *J. Geophys. Res.*, *108*(D23), 4736, doi:10.1029/2003JD003602.

von Clarmann, T., et al. (2003b), A blind test retrieval experiment for infrared limb emission spectrometry, *J. Geophys. Res.*, *108*(D23), 4746, doi:10.1029/2003JD003835.

von Clarmann, T., et al. (2005), Experimental evidence of perturbed odd hydrogen and chlorine chemistry after the October 2003 solar proton events, *J. Geophys. Res.*, *110*(A9), A09S45, doi:10.1029/2005JA011053.

von Clarmann, T., et al. (2007), Mipas measurements of upper tropospheric $c_2h_6$ and $o_3$ during the southern hemispheric biomass burning season in 2003, *Atmospheric Chemistry & Physics*, *7*, 5861-5872.

von Clarmann, T., et al. (2009), Retrieval of temperature $H_2O$, $O_3$, $HNO_3$, $CH_4$, $N_2O$ and $ClONO_2$ from mipas reduced resolution nominal mode limb emission measurements, *Atmos. Meas. Tech.*, *2*, 159-175.

Wang, D. Y., et al. (2005), Longitudinal variations of temperature and ozone profiles observed by MIPAS during the Antarctic stratosphere sudden warming of 2002, *J. Geophys. Res.*, *110*(D20), D20101, doi:10.1029/2004JD005749.

Wintersteiner, P. P., R. H. Picard, R. D. Sharma, J. R. Winick, and R. A. Joseph (1992), Line-by-line radiative excitation model for the non-equilibrium atmosphere: Application to $CO_2$ 15-$\mu$m emission, *J. Geophys. Res.*, *97*(D16), 18,083-18,117.

Xu, J., H.-L. Liu, W. Yuan, A. K. Smith, R. G. Roble, C. J. Mertens, J. M. Russell III., and M. G. Mlynczak (2007), Mesopause structure from Thermosphere, Ionosphere, Mesosphere, Energetics, and Dynamics (TIMED)/ Sounding of the Atmosphere Using Broadband Emission Radiometry (SABER) observations, *J. Geophys. Res.*, *112*, D09102, doi:10.1029/2006JD07711.

Zachor, A. S., and R. D. Sharma (1985), Retrieval of non-LTE vertical structure from a spectrally resolved infrared limb radiance profile, *J. Geophys. Res.*, *90*(A1), 467-475.